THÈSE EN COTUTELLE PRÉSENTÉE

POUR OBTENIR LE GRADE DE

DOCTEUR DE

L'UNIVERSITÉ DE BORDEAUX

ET VIETNAM ACADEMY OF SCIENCE AND TECHNOLOGY

ÉCOLE DOCTORALE UBX

DOCTORALE DES SCIENCES PHYSIQUES ET DE L'INGENIEUR

SPÉCIALITÉ Astrophysique, Plasma, Nucleaire

Par NGUYEN Thi Phuong

FORMATION DES PLANÈTES OBSERVÉE AVEC ALMA: PROPRIÉTÉS DU GAZ ET DE LA POUSSIÈRE DES DISQUES PROTOPLANÉTAIRES ORBITANT AUTOUR DES ÉTOILES JEUNES DE FAIBLE MASSE

Sous la direction de Anne DUTREY
et de Ngoc Diep PHAM

Soutenue le 22 Novembre 2019

Membres du jury :

Mme. Maryvonne GERIN	Directrice de Recherche, Observatoire de Paris	Président
Mme. Hideko NOMURA	Professeure, National Astronomical Observatory of Japan	Rapporteur
M. Emmanuel DARTOIS	Directeur de Recherche, Université de Paris-Sud	Rapporteur
Mme Edwige CHAPILLON	Astronome-adjoint, Institut de Radioastronomie Millimétrique	Examinateur
M. DINH Van Trung	Professeur, Institute of Physics, Hanoi	Examinateur
Mme. Anne Dutrey	Directrice de Recherche, Université de Bordeaux	Directrice de thèse
M. PHAM Ngoc Diep	Researcher, Graduate University of Science and Technology	co-Directeur de thèse

Titre : Formation des planètes observée avec ALMA: propriétés du gaz et de la poussière des disques protoplanétaires orbitant autour des étoiles jeunes de faible masse

Résumé :

Cette thèse porte sur l'étude des propriétés du gaz et de la poussière dans le disque protoplanétaire entourant l'étoile jeune triple de faible masse (~1.2 M_{Sun}) GG Tau A. Comprendre les propriétés dynamiques, physiques et chimiques des systèmes stellaires multiples est nécessaire pour comprendre comment une planète peut se former et survivre dans ces environnements complexes. Les interactions gravitationnelles, dues à la multiplicité stellaire, créent une cavité centrale dans le disque protoplanétaire, la matière (gaz et poussières) se répartissant alors près des étoiles (disques internes) et en un anneau situé au delà de la cavité. Dans la cavité, le gaz et la poussière transitent sous la forme de filaments ("streamers") qui nourrissent les disques internes permettant aux étoiles centrales (puis aux planètes) de se former.

Ce travail consiste en l'analyse de l'émission de CO (^{12}CO, ^{13}CO et $C^{18}O$) observée dans le domaine millimétrique/sub-millimétrique ainsi que des cartes de l'emission thermique de la poussière. L'émission de ^{12}CO fournit des informations sur la couche moléculaire proche de l'atmosphère du disque, ^{13}CO et $C^{18}O$, qui sont moins abondants, apportent des informations sur des couches plus profondes. L'émission de la poussière permet de caractériser les propriétés du disque de poussières autour de ce même plan.

Après avoir introduit le sujet, je présente l'analyse de la morphologie du disque de poussières et de gaz et de sa cinématique qui est dérivée de l'émission de CO. Je présente également un modèle de transfert radiatif de la partie dense du disque (l'anneau) réalisé à partir des donnés CO. La soustraction de ce modèle d'anneau aux données originales révèle l'émission ténue du gaz moléculaire située dans la cavité. Ainsi, je suis en mesure d'évaluer les propriétés des filaments de gaz à l'intérieur de cette cavité, telles que: la dynamique et les conditions d'excitation du gaz en- tourant les trois étoiles et la quantité de masse dans la cavité. Le disque externe est en rotation Keplerienne jusqu'au bord interne de l'anneau dense à ~160 ua. Le disque est relativement froid avec une température pour le gaz (CO) de 25 K et une température pour les poussières de 14 K à 200 ua environ des étoiles centrales. Les températures du gaz et de la poussière chutent très rapidement (r^{-1}). La dynamique du gaz à l'intérieur de la cavité est dominée par la rotation Keplerienne, la contribution de mouvement de chute ("infall") étant évaluée à ~10−15% de la vitesse Keplerienne. La température du gaz est de l'ordre de 40 à 80 K. La densité de colonne pour CO et la densité de H_2 le long des "streamers", proches des étoiles (environ 0.3''− 0.5''), sont de l'ordre de quelques 10^{17} cm^{-2} et 10^7 cm^{-3}, respectivement. La masse totale de gaz à l'intérieur de la cavité est de ~1.6×10^{-4} M_{Sun} et le taux d'accrétion est de l'ordre de 6.4×10^{-8} M_{Sun} yr^{-1}. Ces résultats permettent de dresser la première vision un tant soit peu complète de la physique d'un système multiple jeune capable de former des planètes.

La chimie dans l'anneau est aussi discutée. Je présente ainsi la première détection de H_2S dans un disque protoplanétaire et les détections de DCO^+, HCO^+ et $H^{13}CO^+$ dans le disque de GG Tau A. Mon analyse des observations et la modélisation chimique associée suggèrent que notre compréhension de la chimie du soufre est encore incomplète. Dans GG Tau A, la détection de H_2S a probablement été possible car le disque est plus massif (facteur $\sim 3-5$) que les autres disques sur lesquels H_2S a été recherché. Une telle masse rend le système adapté à la détection de molécules rares, faisant de lui un bon candidat pour étudier la chimie dans les disques protoplanétaires.

Mots clés : disques protoplanétaires, étoiles jeunes, GG Tau A

Title : Planetary formation seen with ALMA: gas and dust properties in protoplanetary disks around young low-mass stars

Abstract :

This thesis presents the analysis of the gas and dust properties of the protoplanetary disk surrounding the young low-mass ($\sim 1.2\ M_{Sun}$) triple star GG Tau A. Studying such young multiple stars is mandatory to understand how planets can form and survive in such systems shaped by gravitational disturbances. Gravitational interactions linked to the stellar multiplicity create a large cavity around the stars, the matter (gas and dust) being either orbiting around the stars (inner disks) or beyond the cavity (outer disk). In between, the matter is streaming ("streamers") from the outer disk onto the inner disks to feed up the central stars (and possible planets).

This work makes use of millimeter/sub-millimeter observations of rotational lines of CO (^{12}CO, ^{13}CO and $C^{18}O$) together with dust continuum maps. While the ^{12}CO emission gives information on the molecular layer close to the disk atmosphere, its less abundant isotopologues (^{13}CO and $C^{18}O$) bring information much deeper in the molecular layer. The dust mm emission samples the dust disk near the mid-plane.

After introducing the subject, I present the analysis of the morphology of the dust and gas disk. The disk kinematics is derived from the CO analysis. I also present a radiative transfer model of the ring in CO isotopologues. The subtraction of this model from the original data reveals the weak emission of the molecular gas lying inside the cavity. Thus, I am able to evaluate the properties of the gas inside the cavity, such as the gas dynamics and excitation conditions and the amount of mass in the cavity. The outer disk is in Keplerian rotation down to the inner edge of the dense ring at $\sim$160 au. The disk is relatively cold with a CO gas temperature of 25 K and a dust temperature of $\sim$14 K at 200 au from the central stars. Both CO gas and dust temperatures drop very fast ($\propto r^{-1}$). The gas dynamics inside the cavity is dominated by Keplerian rotation, with a contribution of infall evaluated as $\sim 10-15\%$ of the Keplerian velocity. The gas temperature inside the cavity is of the order of $40-80$ K. The CO column density and H_2 density along the "streamers", which are close

to the binary components (around 0.3″ − 0.5″) are of the order of a few 10^{17} cm^{-2} and 10^{7} cm^{-3}, respectively. The total mass of gas in- side the cavity is $\sim 1.6\times10^{-4}$ M_{Sun} and the accretion rate is estimated at the level of 6.4×10^{-8} M_{Sun} yr^{-1}. These new results provide the first quantitative global picture of the physical properties of a protoplanetary disk orbiting around a young low-mass multiple star able to create planets.

I also discuss some chemical properties of the GG Tau A disk. I report the first detection of H_2S in a protoplanetary disk, and the detections of DCO^+, HCO^+ and $H^{13}CO^+$ in the disk of GG Tau A. Our analysis of the observations and its chemical modelling suggest that our understanding of the S chemistry is still incomplete. In GG Tau A, the detection of H_2S has been probably possible because the disk is more massive (a factor $\sim$ 3−5) than other disks where H_2S was searched. Such a large disk mass makes the system suitable to detect rare molecules and to study cold-chemistry in protoplanetary disks.

Keywords : protoplanetary disk, young star, GG Tau A

Title: Sự hình thành hành tinh quan sát bởi ALMA: Tính chất khí và bụi trên đĩa tiền hành tinh quay quanh các ngôi sao có khối lượng thấp.

Abstract :

Chủ đề nghiên cứu của luận án là về tính chất của khí và bụi trên đ a tiền hành tinh quanh một hệ đa sao có khối lượng $\sim$1.2 M_{sun}, GG Tau A. Nghiên cứu các hệ đa sao trẻ là cần thiết để hiểu về sự hình thành và tồn tại của hệ hành tinh trong môi trường nhiễu loạn hấp dẫn. Tương tác hấp dẫn của hệ đa sao tạo nên một khoang rỗng lớn xung quanh các sao thành phần, vật chất (khí và bụi) của hệ có thể quay quanh từng sao đơn ("đ a trong") và bên ngoài khoang rỗng, xung quanh cả hệ sao ("đ a ngoài"). Ở giữa hai phần này của hệ, vật chất được truyền từ đ a ngoài vào đ a trong để nuôi dưỡng các sao ở trung tâm (hoặc có thể cả hành tinh).

Nghiên cứu của luận án sử dụng các quan sát thiên văn vô tuyến ở bước sóng millimet/dưới-millimet phát ra bởi các phân tử CO (^{12}CO, ^{13}CO và $C^{18}O$) và bụi. Phát xạ từ ^{12}CO cung cấp thông tin về lớp phân tử gần với khí quyển của đ a, các đồng phân kém phổ biến hơn (^{13}CO và $C^{18}O$) cung cấp thông tin nằm sâu hơn trong lớp phân tử của đ a. Phát xạ mm của bụi giúp nghiên cứu các tính chất trên mặt phẳng giữa của đ a.

Sau khi giới thiệu về chủ đề và đối tượng nghiên cứu, tôi trình bày về hình thái và động học của đ a khí và bụi của hệ sao. Tôi cũng trình bày mô hình truyền bức xạ của đ a ngoài sử dụng các đồng phân của CO. Đ a ngoài của hệ tuân theo chuyển động Kepler cho đến gần khoang rỗng, $\sim$160 au từ tâm sao, và tương đối lạnh. Nhiệt độ khí CO và bụi lần lượt là 25K và 14K tại khoảng cách 200au, và giảm nhanh khi khoảng cách tới tâm tăng, $T \propto r^{-1}$. Việc trừ mô hình đ a ngoài từ số liệu ban đầu biểu lộ rõ ràng hơn phát xạ yếu của các phân tử khí trong khoang rỗng. Do đó, động học

và điều kiện phát xạ của khí trong khoang rỗng có thể được đánh giá. Các phân tử khí bên trong khoang rỗng bị chi phối bởi chuyển động quay, với sự đóng góp nhỏ của chuyển động rơi được đánh giá vào cỡ 10–15% chuyển động Kepler. Nhiệt độ khí bên trong khoang rỗng trong khoảng 40–80 K, mật độ dài của khí CO và mật độ khối của H_2 lần lượt là $10^{17}cm^{-2}$ và $10^{7}cm^{-3}$. Tổng khối lượng khí trong khoang rỗng là $\sim 1.6\times10^{-4}$ M_{sun}, tốc độ truyền vật chất từ đ a ngoài vào đ a trong được tính vào khoảng $\sim 6.4\times10^{-8}$ M_{sun} yr^{-1}. Các kết quả nghiên cứu này góp phần cung cấp một bức tranh tổng quát định lượng đầu tiên về tính chất vật lý của đ a tiền hành tinh quay xung quanh một hệ đa sao trẻ có khối lượng thấp, nơi có khả năng hình thành hành tinh.

Một vài tính chất hóa học của đ a tiền hành tinh GG Tau A cũng được nghiên cứu trong luận án này. Tôi trình bày về sự phát hiện lần đầu tiên H_2S trong đ a tiền hành tinh, cũng như sự phát hiện lần đầu tiên DCO^+, HCO^+ và $H^{13}CO^+$ trong đ a GG Tau A. Kết quả phân tích số liệu thực nghiệm và mô hình hóa học cho thấy sự hiểu biết của chúng ta về hóa học các phân tử có chứa sulfur trong đ a là chưa hoàn thiện. Trong đ a tiền hành tinh GG Tau A, khả năng phát hiện được phân tử hiếm như H_2S có thể là nhờ vào khối lượng lớn của đ a (lớn hơn khoảng 3–5 lần so với các đ a tiền hành tinh nơi H_2S đã từng được tìm kiếm). GG Tau A với đ a tiền hành tinh có khối lượng lớn là thích hợp để tìm kiếm các phân tử hiếm và nghiên cứu về thành phần hóa học của đ a có nhiệt độ thấp.

Keywords: đ a tiền hành tinh, sao trẻ, GG Tau A

Laboratoire d'Astrophysicque de Bordeaux

[Université de Bordeaux - Bât. B18N, Allée Geoffroy Saint-Hilaire, Pessac, France

Deparment of Astrophysics

[Vietnam National Space Center-Build. A6, 18 Hoang Quoc Viet, Hanoi, Vietnam

Declaration of Authorship

I, NGUYEN Thi Phuong, declare that this thesis titled, "Planetary formation seen with ALMA: gas and dust properties in protoplanetary disks around young low-mass stars" and the work presented in it is my own. I confirm that the results presented in the thesis (Chapter 3, Chapter 4, Chapter 5 and Chapter 6) are my research work, which have been obtained during my training with my supervisors and colleagues at the Laboratory of Astrophysics (LAB/CNRS) and the Department of Astrophysics (DAP/VNSC). These results are published in refereed journals (Astronomy & Astrophysics, Research in Astronomy and Astrophysics).

Signed: _____

Date: _____

Acknowledgements

This thesis has been done under a joint supervision agreement between Graduate University of Science and Technology, at Department of Astrophysics of Vietnam National Space Center (DAP/VNSC) and University of Bordeaux at Laboratory of Astrophysics of Bordeaux in the team, Astrochemistry of Molecules et ORigins of planetary systems (AMOR/LAB). I spent four months of three successive years in Bordeaux working with Dr. Anne Dutrey and the rest of the year in Hanoi working with Dr. Pham Ngoc Diep. I would like to thank all people and organizations in Vietnam and in France who helped me with my thesis work.

I would like to express my deepest gratitude to my supervisors, Dr. Anne Dutrey and Dr. Pham Ngoc Diep who have introduced me to the field of radio astronomy and in particular, the star and planet formation topic, encouraged, supported and closely followed my work. They are the most important people helping me to complete this thesis, without them this thesis is impossible. On this occasion, I would like to express my heartfelt gratitude to them for all the things they have been doing to help me in my PhD training period and for my future career.

I sincerely thank Prof. Pierre Darriulat from the DAP team, who introduced me to the field of astrophysics and encouraged me to start my PhD in such a great collaboration for his guidance and great support.

I would like to express my thank to other members of the AMOR team, in particular Drs. Stephane Guilloteau and Edwige Chapillon, who have contributed to my training by teaching me about data reduction and further processing of interferometry data. I thank them for their guidance and support. A part of the data which I used in my thesis has been reduced in IRAM by Dr. Edwige Chapillon and Dr. Vincent Pietu, I thank them for the help. I thank also Dr. Liton Majumdar from Jet Propulsion Laboratory for running a chemical model of GG Tau A which I used in the thesis. I thank all of them for reading my paper manuscripts and giving me their helpful comments. I thank my colleagues at DAP team, Drs. Pham Tuyet Nhung, Pham Tuan Anh, Do Thi Hoai and Bsc Tran Thi Thai for their help in the work as well as the sympathy which we share in life.

I also thank Drs. Emmanuel Di Folco, Valentine Wakelam, Jean-Marc Hure and Franck Hersant from LAB, Dr. Tracy Beck from STSI, and Dr. Jeff Bary from Colgate University for reading my paper manuscripts and for their helpful comments to improve the quality of the papers.

I take this occasion to thank my parents and younger sister, who are always beside me, take good care of me and support my decisions. Last but not least, I thank all my friends both in Vietnam, in France and in other countries, who share their lifetime with me.

The financial support from French Embassy Excellence Scholarship Programme (for foreign students), Laboratoire d'Astrophysique de Bordeaux (under research

funding of Dr. Anne Dutrey), Vietnam National Foundation for Science and Technology Development (grant no. 103.99-2016.50 and 103.99-2018.325), Vietnam National Space Center, the World Laboratory and the Odon Vallet scholarship is acknowledged.

Hanoi & Bordeaux, 2019

Nguyen Thi Phuong

Substantial summary

Understanding how planetary systems form is a major challenge of Astrophysics in the 21st century. For this purpose, observing young low-mass stars, similar to the Sun when it was in its infancy is a necessary step. Indeed, planets form from the rotating disk of gas and dust orbiting around these young stars (also called T Tauri stars). This disk is itself a residual from the molecular cloud which has formed the central star, and so called protoplanetary disk. As a consequence, determining the physics and chemistry at play in these protoplanetary disks has become an important domain of the modern astrophysics requesting both detailed observations and sophisticated models. Thus constraining initial conditions leading to planetary systems by making relevant comparisons with planet formation models requests an observational evaluation of the physical properties (density, temperature, turbulence, etc) and chemical evolution of the gas and dust disks surrounding T Tauri stars. An important source of complexity for the observations resides in the fact that the determination of these fundamental physical parameters is strongly degenerated within a single observation. The role of the observer is therefore to define an observing strategy, e.g. by observing several molecules, which allows an accurate derivation of the physical properties by minimizing the impact of possible degeneracies. Knowing the properties of the dust (nature, size, morphology) is essential to understand the formation of planetary embryos but also the genesis of complex molecules. Many organic molecules form onto grain surfaces where gaseous molecules freeze out as soon as the temperature is cold enough (e.g. 17 K for CO) and interact with molecules already trapped onto grains. This thesis investigates the properties of the protoplanetary disk surrounding a triple low-mass stellar system, GG Tau A, using interferometric observations of trace molecules such as ^{12}CO, ^{13}CO, C^{18}O, DCO$^+$, HCO$^+$ and H_2S, and of multi-wavelength dust emission.

Chapter 1 introduces the topic and the current knowledge of protoplanetary disks. The special case of protoplanetary disks surrounding binary systems is introduced both for the theoretical studies and for the observations. The second part of the Chapter presents the known properties on the GG Tau A system.

Chapter 2 summarizes some basic points about instruments, observations and analysis methods used in the present study. It briefly introduces IRAM and ALMA interferometers, the observations carried out with these facilities and data reduction. It presents the principles of radio interferometry and deconvolution. It also recalls the bases of radiative transfer, and a radiative transfer code (DiskFit) is introduced at the end of the Chapter.

Chapter 3 is the first of three chapters that address the specific studies of the protoplanetary disk GG Tau A. The results are published in Phuong et al. (2018b). It presents an analysis of the morphology of the dust disk using 0.9 mm emission and of the morpho-kinematics of the gas emissions observed with ALMA. The studies confirm the geometry of the dust ring, with an inclination of 35° and a position angle of $\sim 7°$ as well as the sharp edge and narrow ring of the dust emission. Figure 10 shows the sky map of the dust emission, the radial dependence of the 0.9 mm

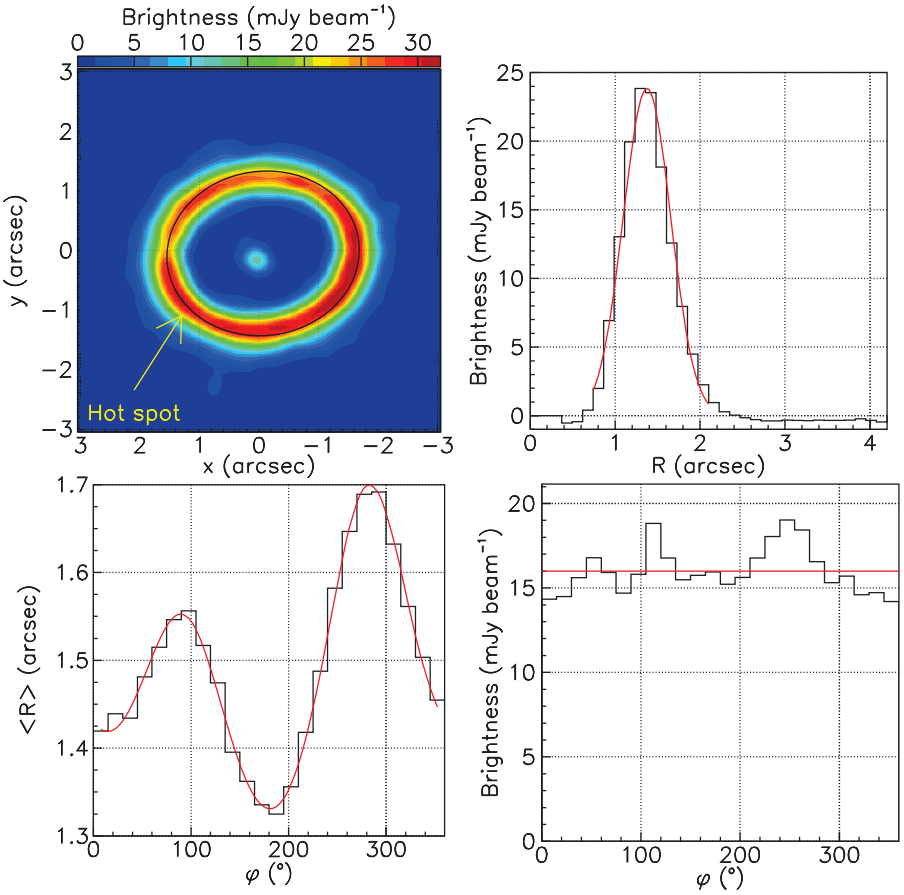

FIGURE 1: Brightness of the dust ring continuum emission. *Top left:* sky map, the black ellipse is the fit to $\langle R \rangle$ shown in the bottom left panel; the yellow arrow points to the region of the "hot spot" observed by Dutrey et al. (2014) and Tang et al. (2016) in ^{12}CO(6–5) and ^{12}CO(3–2) emissions. *Top right:* The dependence on R of the brightness averaged over position angle φ, together with the Gaussian best fit to the peak. *Bottom left:* Dependence on φ of $\langle R \rangle$ calculated in the interval $1'' < R < 2''$ (the red line is the best fit to an elliptical tilted ring offset from the origin). *Bottom right:* Dependence on φ of the disk plane continuum brightness averaged over R in the interval $1'' < R < 2''$. The red line shows the mean value of the continuum brightness.

brightness in the sky plane, and the azimuthal dependence of the mean radius $\langle R \rangle$ which reveals the tilt angle of the disk and the azimuthal dependence of the 0.9 mm brightness on the plane of the disk.

A study of ^{13}CO(3–2) emission gives an upper limit of 0.24″ (34 au) on the disk scale height at a distance of 1″ (140 au) from the central stars. The outer disk is in Keplerian rotation with a rotation velocity reaching $\sim$ 3.1 km s^{-1} at 1″ from the central stars; an upper limit of 9% (at 99% confidence level) is placed on a possible relative contribution of infall velocity. Variations of the intensity across the disk

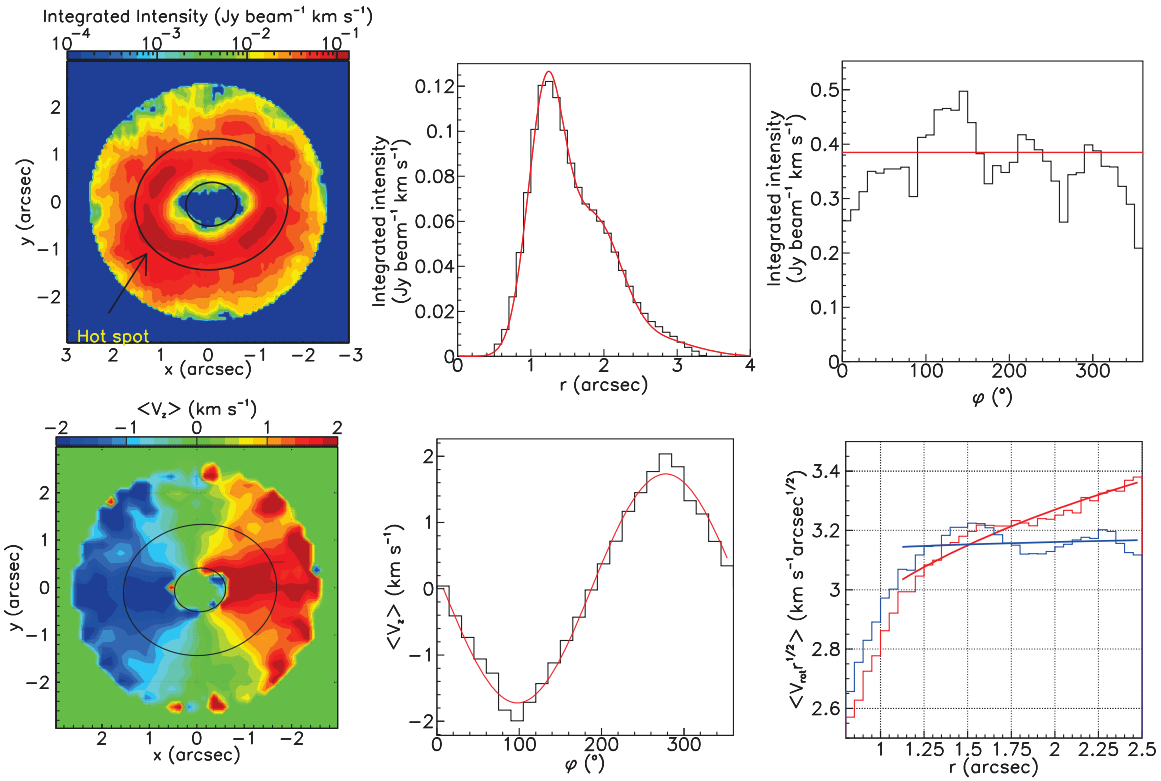

FIGURE 2: **Upper panels:** Sky map (*left*) of the ^{13}CO(3–2) integrated intensity. The black arrow shows the position of the hot spot in ^{12}CO(6–5) (Dutrey et al., 2014) and ^{12}CO(3–2) (Tang et al., 2016). Radial dependence (*middle*) of the integrated intensity azimuthally averaged in the disk plane. The red line is a fit using the same three Gaussians as in Tang et al. (2016). Azimuthal dependence (*right*) of the integrated intensity averaged across the disk ($0.54'' < r < 2''$). The red line shows the mean intensity. **Lower panels:** Sky map of the mean Doppler velocity (weighted by brightness) (*left*). Azimuthal dependence of mean line Doppler velocity weighted by brightness (*middle*). Dependence on r of $\langle V_{rot} \times r^{1/2} \rangle$ (brightness-weighted average); the lines are the best power law fits with indices -0.63 for $|\sin\omega| > 0.3$ (red) and -0.48 for $|\sin\omega| > 0.707$ (blue) (*right*).

area are studied in detail and confirm the presence of a "hot spot " in the southeastern quadrant. However several other significant intensity variations, in particular a depression in the northern direction, are also revealed. Variations of the intensity are found to be positively correlated to variations of the line width. Possible contributions to the measured line width are reviewed, suggesting an increase of the disk temperature and opacity with decreasing distance from the stars. Figure 11 (upper panels) shows the intensity map of ^{13}CO(3–2) emission, the radial and azimuthal dependence of the ^{13}CO(3–2) intensity in the plane of the gas disk. The radial dependence, described as the sum of three Gaussian functions, reveals unresolved substructures. The azimuthal dependence of the intensity shows a uniform disk with an excess of emission in the southeastern quadrant, which corresponds to

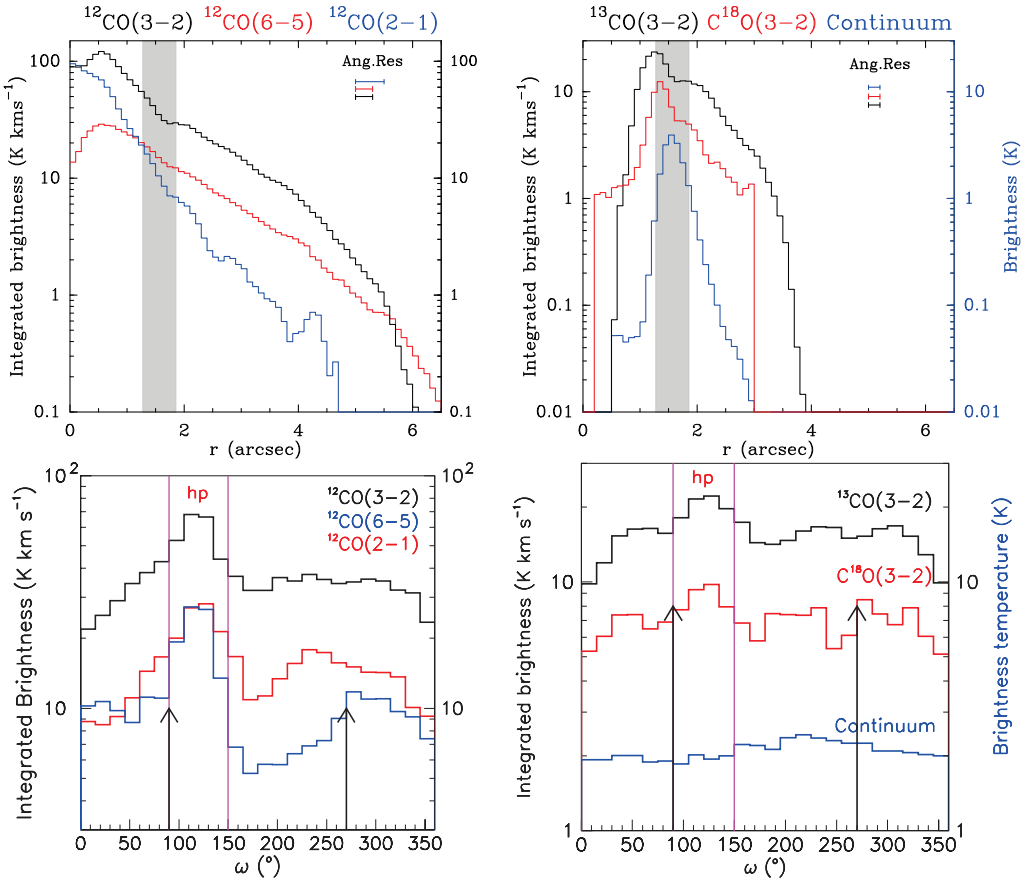

FIGURE 3: *Upper panels:* Radial dependence of the integrated brightness temperature (for line emissions) and brightness temperature (for continuum emission) in the disk plane. The grey bands show the dust ring. The horizontal sticks indicate the angular resolutions. *Lower panels:* Azimuthal dependence of the brightness temperatures integrated over the ring $1.2'' < r < 2.0''$. The left panels are for the three ^{12}CO emissions (J=6–5, 3–2 and 2–1), with CO(2–1) data taken from Dutrey et al. (2014), the right panels show the less abundant CO isotopologues (J=3–2) emissions and the continuum. Black arrows show the location of the limb brightening peaks. The magenta vertical lines show the "hot spot" location.

the "hot spot" observed in ^{12}CO(6–5) by Dutrey et al. (2014). Figure 11 (lower panels) displays the Doppler velocity map of the ^{13}CO$(3-2)$ emission, the azimuthal dependence of mean Doppler velocity $\langle V_z \rangle$ on the plane of the disk and the radial dependence of $\langle V_{\rm rot} \times r^{1/2} \rangle$. The velocity map shows the projection on the sky plane of a circular disk rotating around an axis projecting as the minor axis of the intensity elliptical disk. The azimuthal dependence of the mean Doppler velocity $\langle V_z \rangle$ is well described by a cosine function, severely constraining a possible infall contribution. The dependence of $\langle V_{\rm rot} \times r^{1/2} \rangle$ on r provides evidence for Keplerian rotation. As rotation cannot be revealed near the projection of the rotation axis, we exclude from the analysis wedges of $\pm \sim 17^\circ$ (red) and $\pm \sim 45^\circ$ (blue), the latter giving evidence

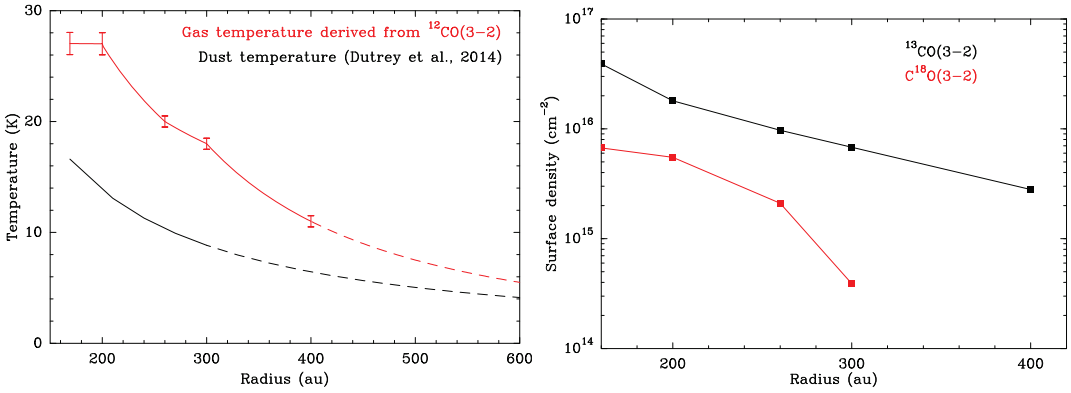

FIGURE 4: *Left:* Radial dependence of CO gas (red) and dust (black) temperatures. The gas temperature is derived from the ^{12}CO(3–2) analysis. Beyond 400 au, the CO temperature is extrapolated from the fit obtained between 300 au and 400 au. The dust temperature is taken from Dutrey et al. (2014) and extrapolated beyond a radius of 285 au. *Right:* Radial dependence of the surface densities obtained from LTE analyses of ^{13}CO(3–2) (black) and C^{18}O(3–2) (red).

for Keplerian motion with a power index of -0.48.

The second part of Chapter 3 presents an analysis of ^{12}CO(J=2–1, 3–2, and 6–5) and its isotopologues ^{13}CO(3–2) and C^{18}O(3–2). With an angular resolution better than $\sim$ 50 au, these data provide evidence for radial and azimuthal inhomogeneity of the outer disk. The azimuthal dependence of the line intensity in the plane of the disk of the ^{12}CO emissions shows the "hot spot" . It becomes less clear in the less abundant isotopologues of ^{13}CO and C^{18}O (see Figure 3).

Chapter 4 presents a radiative transfer modelling of the ^{12}CO, ^{13}CO and C^{18}O (J=3–2) emissions. The results are published in Phuong et al. (2019, submitted to A&A). This analysis is done in part in the *uv* plane in oder to reliably separate the contributions of the cavity and outer circumbinary disk. Since ^{12}CO(3–2) is optically thick and easily thermalized, we use the line emission to probe the temperature of the disk. The ^{13}CO and C^{18}O surface densities are derived assuming that the temperatures of the isotopologues are the same as for ^{12}CO emission. The temperature and surface density profiles of these lines are displayed in Figure 4.

The subtraction of the best ring model (presented above) from the original *uv* tables provides the best images of the gas emissions inside the cavity. The studies of the kinematics inside the cavity reveal an infall contribution of $\sim$ 10% $-$ 15% of the Kelperian velocity. Figure 14 displays the position-velocity diagrams and the azimuthal dependence of the de-projected Doppler velocity in 5 bins of 0.25″ each. The emissions of CO inside the cavity is defined by 6 bright blobs (see Figure 25). The column density of CO obtained from a non-LTE analysis is of the order of $\sim$ 10^{17} cm^{-2}, with the temperature between 40 and 80 K and the H_2 density of the order of 10^7 cm^{-3}. The total H_2 mass inside the cavity is of the order of $\sim$ 10^{-4} M$_\odot$ while the cumulative mass of the bright blobs is $\sim$ 10^{-5} M$_\odot$. The gas mass will

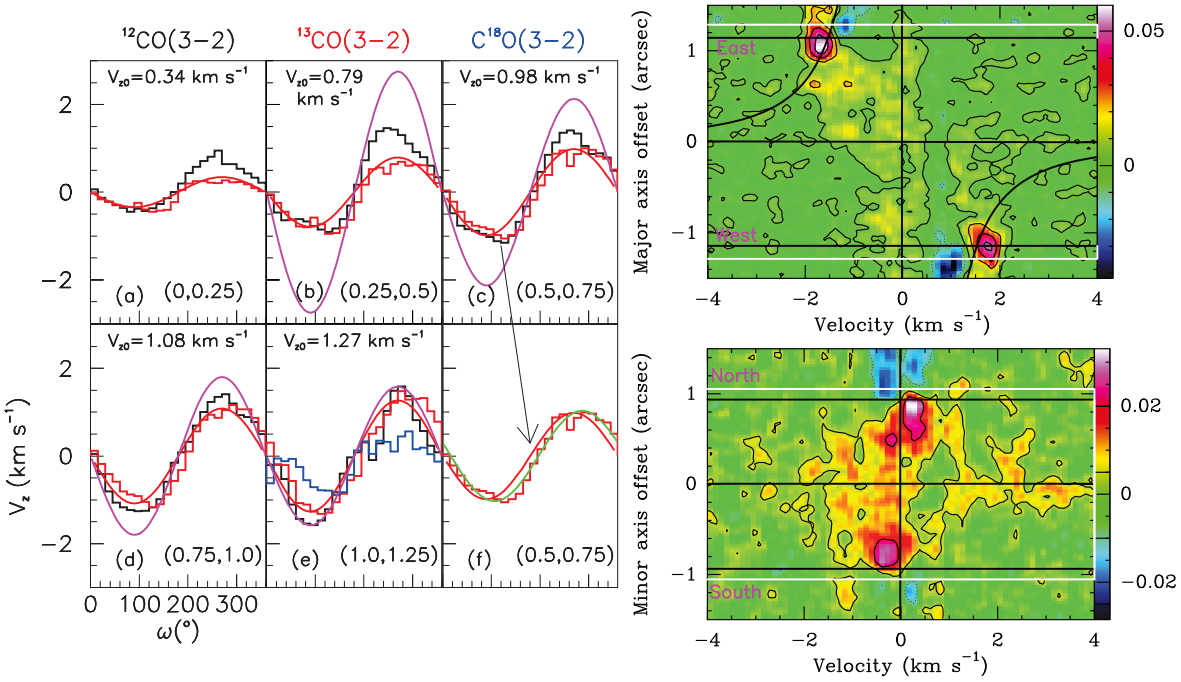

FIGURE 5: **Left:** Dependence of $\langle V_z \rangle$ (km s^{-1}) on azimuth ω (°) inside the cavity. ^{12}CO (3–2) is in black, ^{13}CO (3–2) in red and C^{18}O (3–2) in blue. The red curve is a sine fit to the ^{13}CO (3–2) data (see text). C^{18}O (3–2) data of significant intensity are only present in the bin $1.0'' < r < 1.25''$. The magenta curves show the Keplerian velocity expected around a single star of 1.36 M$_\odot$. The green curve in panel (f) shows the best fit velocity curve when infall motion is allowed. **Right:** Position-velocity diagrams of the ^{13}CO(3–2) emission inside the cavity along the major axis (upper panel) and minor axis (lower panel). The black curves show the Keplerian velocity expected around a single star of 1.36 M$_\odot$. Contour levels are spaced by 10 mJy/beam, with the zero contour omitted. The white lines indicate the position of the inner edge of the dust ring (180 au) and the black ones that of the inner radius of the gas disk (169 au).

dissipate/accrete onto the Aa disk in about 2500 years, giving an accretion rate of $\sim 6.4 \times 10^{-8}$ M$_\odot$ yr^{-1}.

Chapter 5 presents a study of the chemical content of the GG Tau A protoplanetary disk. The results are published in Phuong et al. (2018a). It presents the first detection of H_2S in a protoplanetary disk and the detection of other molecules, such as DCO^+, HCO^+, and $H^{13}CO^+$ in the outer disk of GG Tau A. Figure 16 shows the integrated intensity and velocity maps of the emissions. The DCO^+/HCO^+ ratio is measured as ~ 0.03 in the dense gas and dust disk of GG Tau A (at 250 au), a result similar to that obtained for other disks (TW Hya and LkCa 15). A crude chemical model of GG Tau A is presented and compared with observations. The detection of the rare molecule H_2S, in GG Tau A, which is not detected in other disks, such as DM Tau and LkCa 15, suggests that this massive disk may be a good testbed to

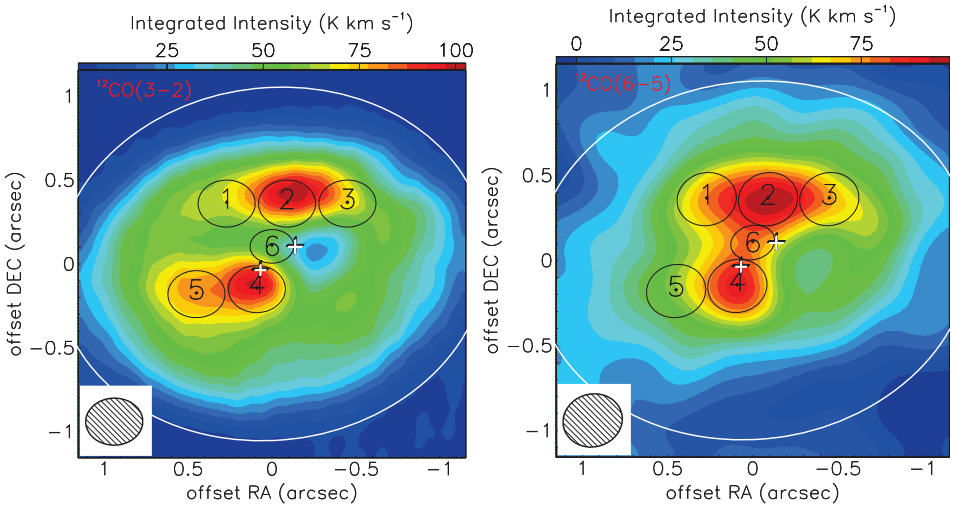

FIGURE 6: Integrated intensity of ^{12}CO(3–2) *(left)* and ^{12}CO(6–5) *(right)* and blobs location. Each blob covers an area of one beam, except for B6 which covers half of it. The color scales are in units of (K km s^{-1}). The crosses mark the position of Aa and Ab1+Ab2, and the ellipse shows the inner edge of the dust ring (180 au).

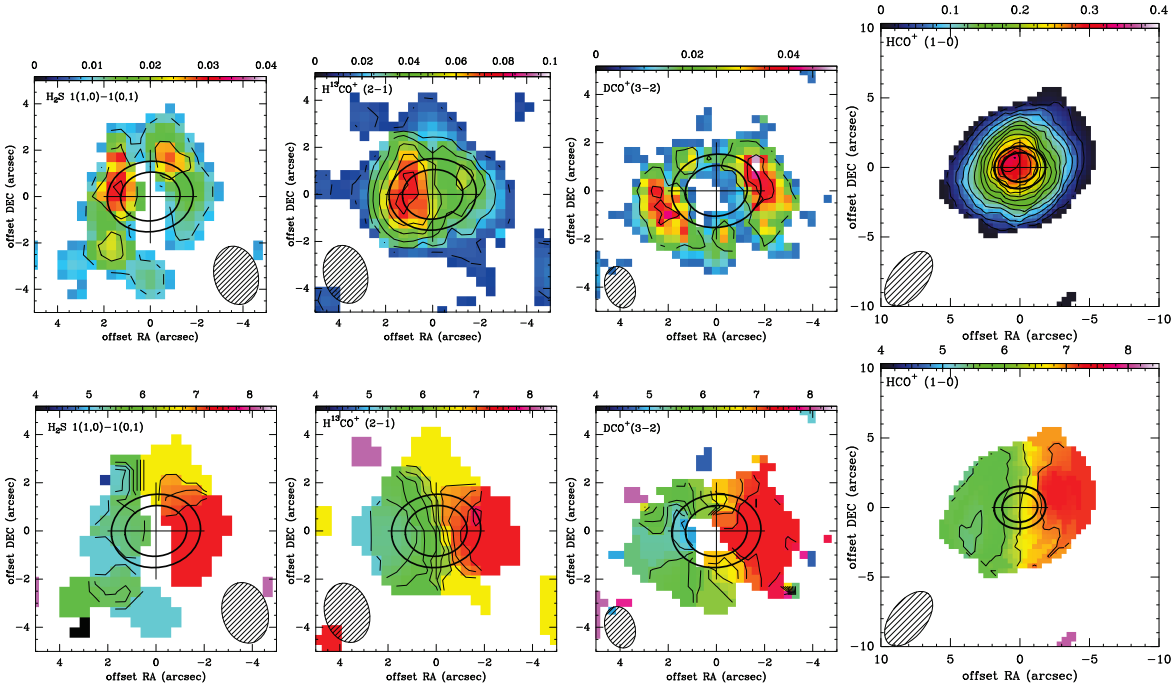

FIGURE 7: *Upper panels:* Integrated intensity maps. The color scales are in units of (Jy beam^{-1} km s^{-1}). The contour level step is 2σ. *Lower panels:* Mean velocity maps. The contour level step is 0.5 km s^{-1}. Beam sizes are indicated. The ellipses show the locations of the inner (∼180 au) and outer (∼260 au) edges of the dust ring.

study the chemical content of protoplanetary disks. I also present measurements of the abundance of these molecules relative to ^{13}CO and compare them with those

observed in the disk of LkCa 15 and in the TMC–1 molecular cloud. Upper limits to the abundance of other molecules such as, SO, SO_2,C_2S, and of c–C_3H_2, and HC_3N are also obtained.

Chapter 6 presents the general conclusion and the perspectives. Figure 26 summarizes the properties (physics, chemistry and kinematics) of the GG Tau A system and its environnement derived from the results presented in the thesis. More and more planets are presently discovered orbiting around binary and multiple stellar systems. Understanding how they form requires deep investigations of their younger counterparts such as multiple TTauri stars. In this context, the present thesis presents the most complete study performed so far.

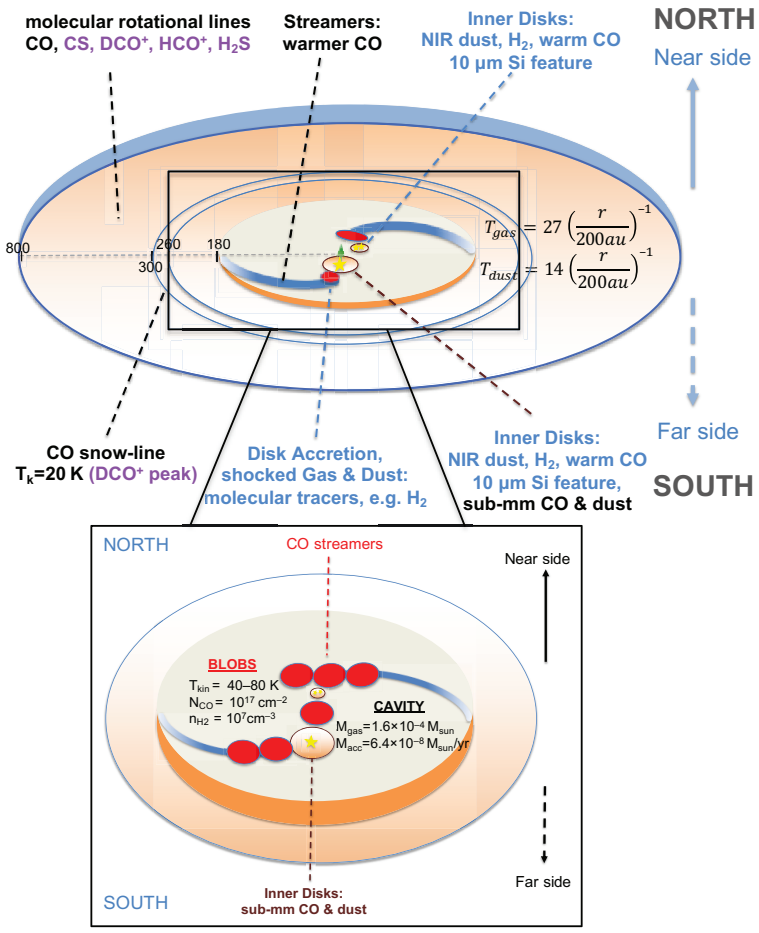

FIGURE 8: Schematics of the global properties of the GG Tau A system.

In addition, ALMA Cycle 3 and Cycle 6 observations of CN, CO and CS emissions are shown. CO data may suggest the presence of a spiral pattern, while the CN and CS data rather suggest the presence of rings. Figure 27 displays the peak brightness temperature map for CN (upper) and CS (lower) superimposed on the CO peak brightness temperature map. These data contain important information which deserves further studies.

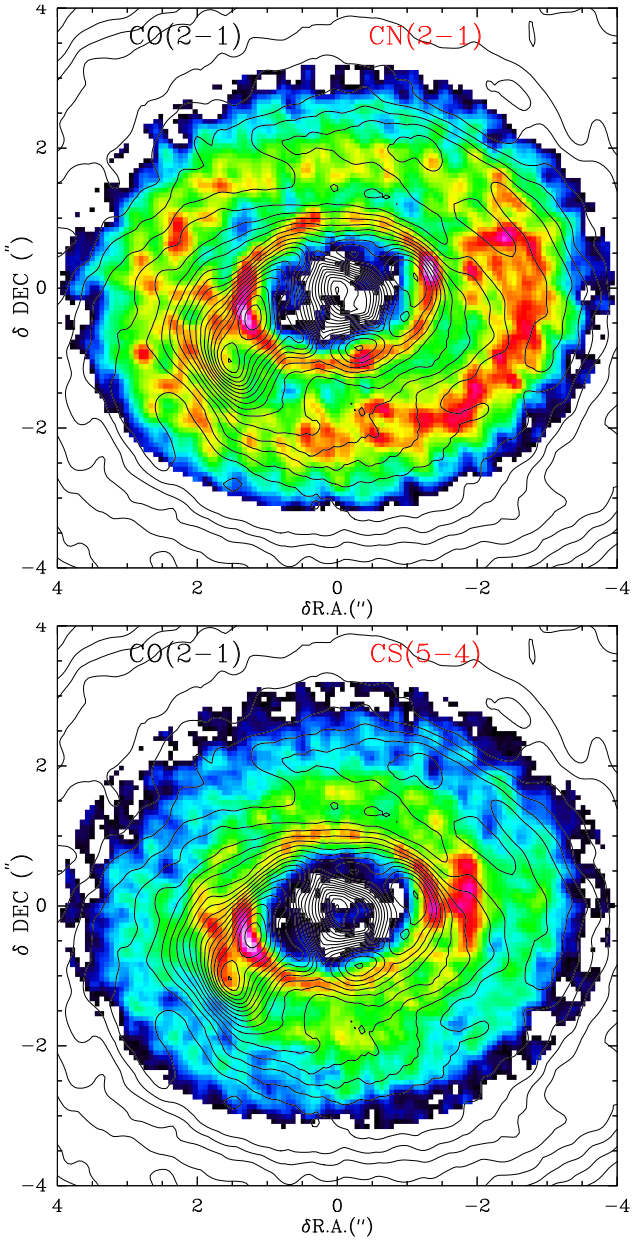

FIGURE 9: **Upper panel:** CN(2–1) peak brightness image (colour) overlaid on the CO(2–1) peak brightness in contour. **Lower panel:** CS(5–4) peak brightness image (colour) overlaid on the CO(2–1) peak brightness in contour.

Tóm tắt

Hiểu một cách cặn kẽ sự hình thành các hệ hành tinh là một thách thức lớn của vật lý thiên văn trong thế kỷ 21. Quan sát các ngôi sao trẻ có khối lượng thấp, tương tự như Mặt trời khi chúng còn ở giai đoạn sơ khai là một bước cần thiết để hiểu sự hình thành của các hệ hành tinh. Thật vậy, các hành tinh được hình thành từ đĩa khí và bụi quay quanh những ngôi sao trẻ này (được gọi là sao T Tauri). Đĩa vật chất (khí và bụi) này, một phần còn lại của đám mây phân tử nơi mà ngôi sao trung tâm hình thành, gọi là đĩa tiền hành tinh. Xác định tính chất vật lý và hóa học của đĩa tiền hành tinh đã trở thành một lĩnh vực quan trọng của vật lý thiên văn hiện đại, yêu cầu có các quan sát chi tiết và mô hình phức tạp. Do đó, ràng buộc những điều kiện ban đầu dẫn đến hình thành hệ hành tinh bằng việc so sánh với các mô hình lý thuyết yêu cầu các quan sát để có thể đánh giá tính chất vật lý (mật độ, nhiệt độ, nhiễu loạn, vv) và sự phát triển hóa học của các đĩa khí và bụi quanh sao T Tauri. Trên thực tế, việc xác định các tham số vật lý cơ bản này gặp phải hạn chế lớn với chỉ một vài quan sát đơn lẻ. Do đó, vai trò của người quan sát là xác định chiến lược quan sát phù hợp, ví dụ, quan sát một số phân tử, cho phép xác định chính xác tính chất vật lý của đĩa vật chất. Biết các tính chất của bụi (mật độ, kích thước, hình thái) là cần thiết không những để hiểu sự hình thành của phôi hành tinh mà còn để hiểu nguồn gốc hình thành các phân tử phức tạp. Các phân tử hữu cơ phức tạp có thể hình thành trên bề mặt các hạt bụi, nơi các phân tử khí đóng băng khi nhiệt độ đủ thấp (ví dụ phân tử khí CO bị đóng băng trên bề mặt của các hạt bụi ngay khi nhiệt độ đạt khoảng 17–20 K). Các phân tử khí bị dính vào bề mặt hạt bụi tương tác với nhau tạo nên các phân tử mới phức tạp hơn. Luận án này nghiên cứu các tính chất của khí và bụi trên đĩa tiền hành tinh quanh một hệ thống sao ba có khối lượng thấp, GG Tau A, sử dụng các quan sát vạch phát xạ quay của các phân tử đánh dấu như ^{12}CO, ^{13}CO, $C^{18}O$, DCO^+, HCO^+ và H_2S và phát xạ liên tục từ bụi ở nhiều bước sóng khác nhau được quan sát bởi các hệ giao thoa vô tuyến.

Chương 1 của luận án giới thiệu chủ đề nghiên cứu và các hiểu biết hiện nay về đĩa tiền hành tinh. Các nghiên cứu lý thuyết và quan sát đối với trường hợp đặc biệt của các đĩa tiền hành tinh quay xung quanh các hệ sao đôi/nhiều sao cũng được giới thiệu. Phần thứ hai của Chương 1 trình bày các hiểu biết cho đến nay về hệ thống GG Tau A.

Chương 2 trình bày một số nét cơ bản về thiết bị quan sát, các quan sát và phương pháp phân tích được sử dụng. Nội dung chương này giới thiệu ngắn gọn về hệ giao thoa vô tuyến IRAM và ALMA, các quan sát được thực hiện với các hệ giao thoa này và xử lý sơ bộ dữ liệu. Chương này cũng trình bày về nguyên tắc hoạt động của giao thoa vô tuyến và việc chuyển đổi dữ liệu cũng như một số kiến thức cơ bản về truyền bức xạ và về gói phần mềm (DiskFit) sử dụng cho việc mô hình hoá các dữ liệu quan sát được dựa trên nguyên tắc truyền bức xạ.

Chương 3 đề cập đến các kết quả nghiên cứu cụ thể về hình thái và động học của đĩa tiền hành tinh GG Tau A sử dụng quan sát phát xạ từ các đồng phân CO và bụi bởi hệ giao thoa vô tuyến ALMA. Những kết quả của nghiên cứu này được công bố trong Phuong et al. (2018b). Các nghiên cứu này xác nhận hình thái của vành bụi

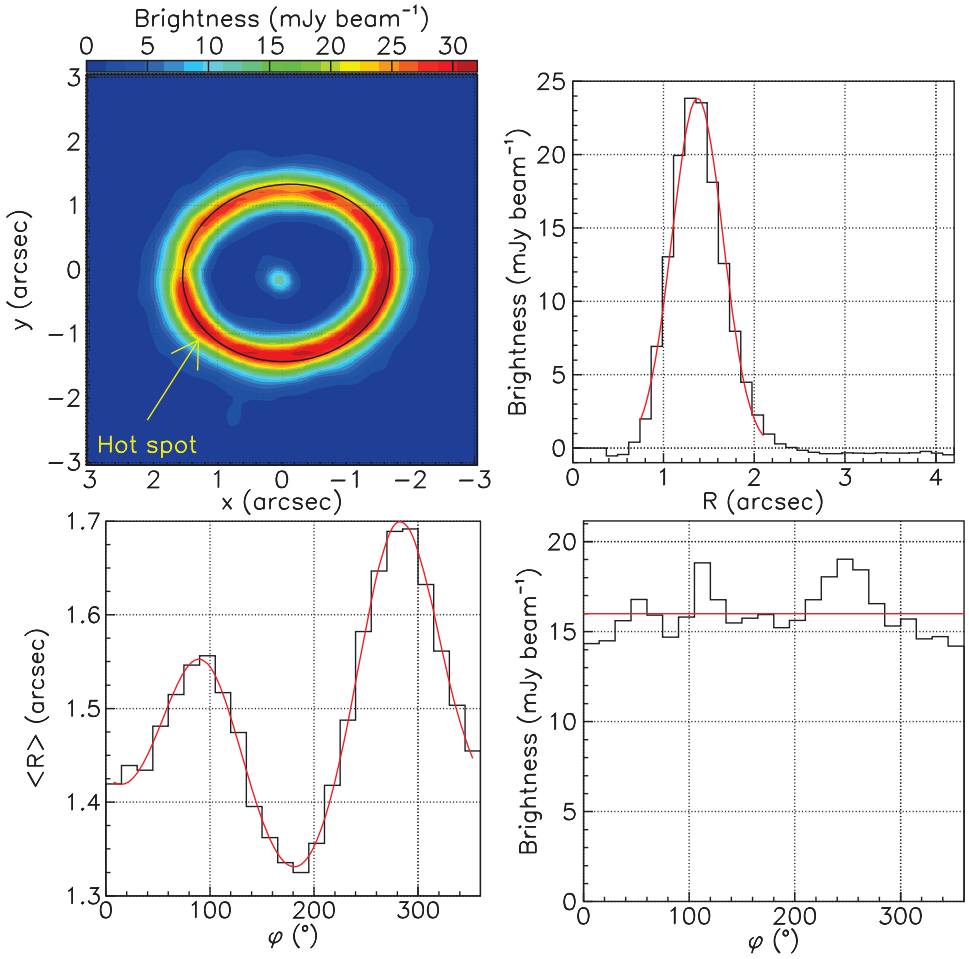

FIGURE 10: Phát xạ liên tục của vành bụi. *Từ trái sang phải và từ trên xuống dưới:* Bản đồ cường độ phát xạ, hình elip màu đen là đường khớp hàm tốt nhất giá trị trung bình của khoảng cách đến tâm sao trên mặt phẳng bầu trời $\langle R \rangle$ theo góc vị trí φ (hình dưới bên trái); mũi tên màu vàng chỉ vào vùng "điểm nóng" được quan sát bởi Dutrey et al. (2014) và Tang et al. (2016) với các phát xạ ^{12}CO(6–5) và ^{12}CO(3–2); sự phụ thuộc vào R của độ sáng tính trung bình theo φ, cùng với đường khớp hàm phù hợp nhất sử dụng hàm Gauss; sự phụ thuộc vào φ của $\langle R \rangle$ trong khoảng $1'' < R < 2''$ (đường màu đỏ là hàm khớp với hàm elip có độ nghiêng và sai lệch so với gốc toạ độ); sự phụ thuộc vào φ của độ sáng phát xạ liên tục của mặt phẳng đĩa tính trung bình trên R trong khoảng $1'' < R < 2''$. Đường màu đỏ hiển thị giá trị độ sáng trung bình phát xạ liên tục trên đĩa.

hẹp, có độ nghiêng 35° và góc vị trí $\sim 7°$ cũng như sự suy giảm mật độ nhanh chóng ở hai cạnh của vành bụi. Hình 10 (từ trái sang phải và từ trên xuống) cho thấy i) bản đồ cường độ phát xạ bụi, ii) sự phụ thuộc vào khoảng cách đến tâm sao của độ sáng trong mặt phẳng bầu trời, iii) sự phụ thuộc theo góc phương vị của bán kính trung bình $\langle R \rangle$ cho thấy góc nghiêng của đĩa và iv) sự phụ thuộc theo góc phương vị của độ sáng trên mặt phẳng đĩa.

Nghiên cứu với phát xạ ^{13}CO(3–2) cho phép chúng tôi đưa ra giới hạn trên bề

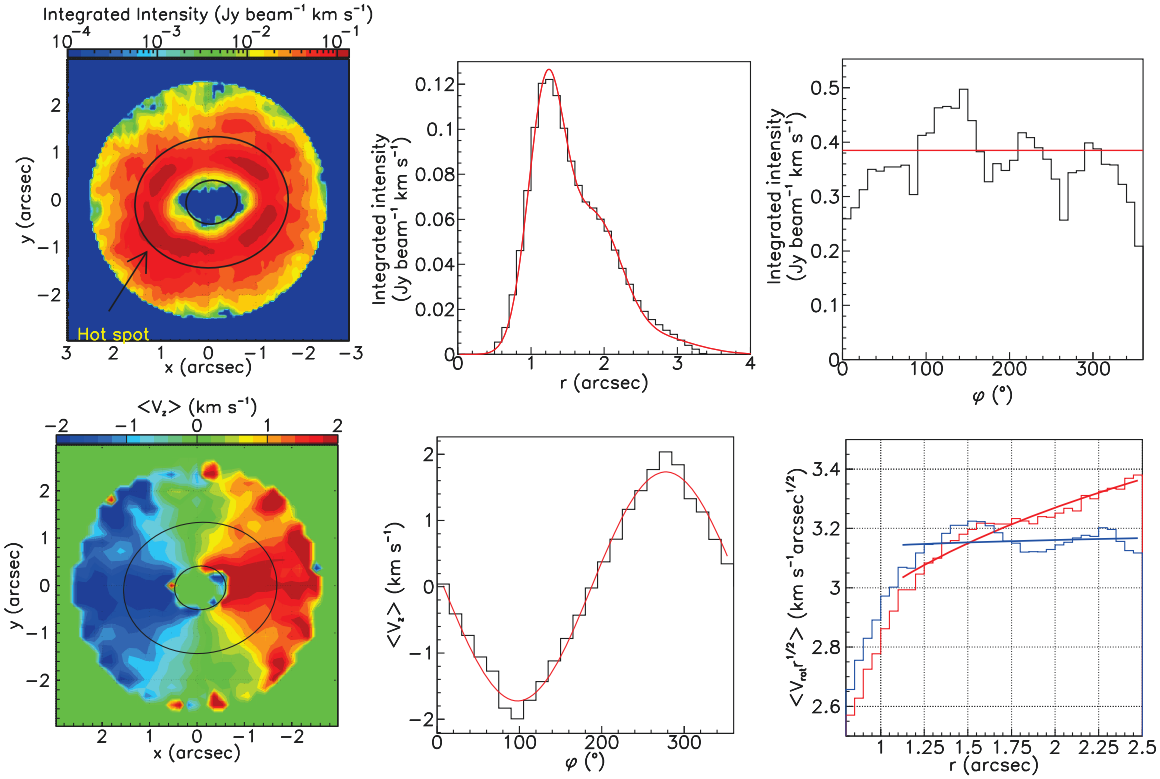

FIGURE 11: **Hình trên:** Bản đồ bầu trời của độ sáng tích phân theo vận tốc của phát xạ ^{13}CO(3–2). Mũi tên đen chỉ vào vị trí "điểm nóng" (*trái*). Sự phụ thuộc vào khoảng cách tới tâm của độ sánh tích phân, tính trung bình trên toàn mặt phẳng đĩa. Đường màu đỏ là đường khớp hàm với tổng 3 hàm Gauss giống như trong Tang et al. (2016) (*giữa*). Sự phụ thuộc theo góc phương vị của độ sáng tích phân, tính trung bình theo bán kính trên đĩa ($0,54'' < r < 2''$). Đường màu đỏ hiển thị cường độ trung bình (*phải*). **Hình dưới:** Bản đồ bầu trời của vận tốc Doppler trung bình trọng số theo độ sáng (*trái*). Sự phụ thuộc theo góc phương vị của vận tốc Doppler trung bình trọng số theo độ sáng (*giữa*). Phụ thuộc vào khoảng cách đến tâm của $\langle V_{rot} \times r^{1/2} \rangle$; các đường thẳng là đường khớp với tuyến tính bậc 1 cho chỉ số $-0,63$ (đường màu đỏ, khi giới hạn điều kiện $|\sin\omega| > 0,3$) và $-0,48$ (đường màu xanh, khi giới hạn điều kiện $|\sin\omega| > 0,707$) (*phải*).

dày đĩa tiền hành tinh này là 0,24″ (34 au) ở khoảng cách 1″ (140 au) từ tâm hệ sao. Đĩa ngoài này chuyển động theo định luật Kepler với tốc độ quay ~ 3.1 km s^{-1} tại khoảng cách 1″ (140 au) từ tâm hệ sao và giới hạn trên của vận tốc rơi so với thành phần quay là 9% (với độ tin cậy 99%). Sự biến đổi của độ sáng trên đĩa cũng được nghiên cứu chi tiết và xác nhận sự hiện diện của "điểm nóng" trong góc phần tư phía đông nam của đĩa. Kết quả phân tích số liệu cũng cho thấy tồn tại vùng phát xạ yếu hơn so với các khu vực khác ở phía bắc của đĩa. Sự biến đổi độ sáng được chỉ ra có mối tương quan với biến đổi độ rộng vạch phổ. Các yếu tố đóng góp vào việc làm rộng vạch phổ cũng được xem xét. Nghiên cứu cho thấy nhiệt độ và độ dày quang học của vạch phát xạ ^{13}CO(3–2) trên đĩa tăng khi khoảng cách tới tâm hệ sao

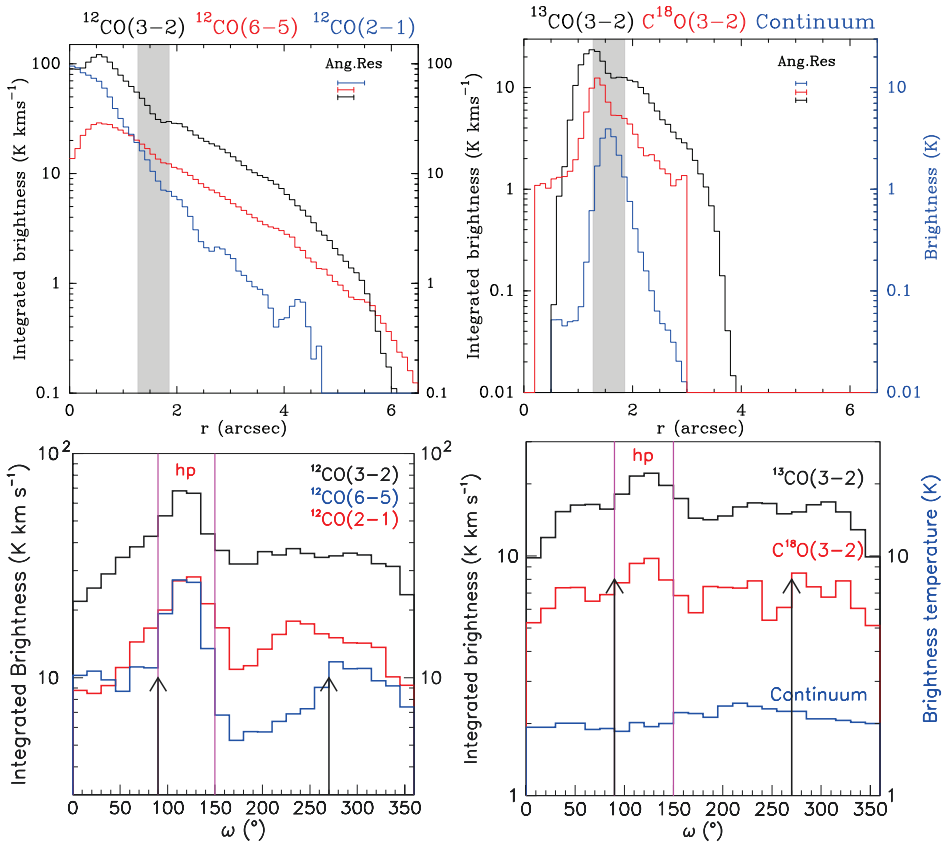

FIGURE 12: *Hình trên:* Sự phụ thuộc vào khoảng cách tới tâm của độ sáng tích phân theo vận tốc (vạch phát xạ quay của phân tử) và độ sáng (phát xạ liên tục từ bụi) trong mặt phẳng đĩa. Các đoạn thẳng nằm ngang trong hình chỉ ra độ phân giải không gian tương ứng. *Hình dưới:* Sự phụ thuộc theo góc phương vị của đại lượng tương ứng, tính trung bình trong vành $1,2'' < r < 2.0''$. Các hình bên trái là biểu đồ của ba vạch của ^{12}CO (J=6–5, 3–2 và 2–1), với dữ liệu CO(2–1) được lấy từ Dutrey et al. (2014), các hình bên phải là biểu đồ của vạch phát xạ J=3–2 của các đồng phân ít phổ biến hơn. Trong các hình phía trên, vùng màu xám đánh dấu vành bụi. Trong các hình phía dưới, mũi tên màu đen chỉ vị trí xảy ra hiệu ứng tăng cường sáng (*limb brightening*), các đường màu tím giới hạn vị trí "điểm nóng".

giảm dần. Hình 11 (hàng trên, từ trái sang phải) trình bày bản đồ độ sáng phát xạ ^{13}CO(3–2), sự phụ thuộc của độ sáng vào khoảng cách đến tâm và góc phương vị trong mặt phẳng đĩa. Sự phụ thuộc vào khoảng cách đến tâm, được mô tả là tổng của ba hàm Gauss, cho thấy các cấu trúc tinh tế chưa được phân giải với độ phân giải hiện nay của quan sát này (∼50 au). Sự phụ thuộc theo góc phương vị của độ sáng cho thấy đĩa tương đối đồng nhất có phát xạ vượt trội ở góc phần tư phía đông nam, tương ứng với "điểm nóng " được quan sát với ^{12}CO(3–2) được báo cáo trong Dutrey et al. (2014). Hình 11 (hàng dưới, từ trái sang phải) trình bày bản đồ vận tốc Doppler của phát xạ ^{13}CO(3–2), sự phụ thuộc theo góc phương vị của vận tốc Doppler trung bình $\langle V_z \rangle$ trên mặt phẳng đĩa và sự phụ thuộc vào khoảng cách đến

tâm của $\langle V_{\rm rot} \times r^{1/2} \rangle$. Bản đồ vận tốc cho thấy bằng chứng của một đĩa khí quay. Sự phụ thuộc theo góc phương vị của vận tốc Doppler trung bình $\langle V_z \rangle$ khớp tốt với hàm cos xác nhận chuyển động quay của đĩa. Sự phụ thuộc của $\langle V_{\rm rot} \times r^{1/2} \rangle$ vào r mô tả chuyển động Kepler của đĩa (nếu đĩa chuyển động theo định luật Kepler thì tích này là hằng số). Đường cong màu đỏ biểu thị phân bố của đại lượng này không tính đến vùng $\sim 17^\circ$ quanh bán trục nhỏ, khớp với hàm tuyến tính bậc 1 cho chỉ số $-0,63$ trong khi đường cong màu xanh biểu thị phân bố của đại lượng này bỏ qua vùng $\sim 45^\circ$ quanh bán trục nhỏ, cho kết quả của chỉ số khi khớp hàm là $-0,48$, hoàn toàn phù hợp với chuyển động Kepler.

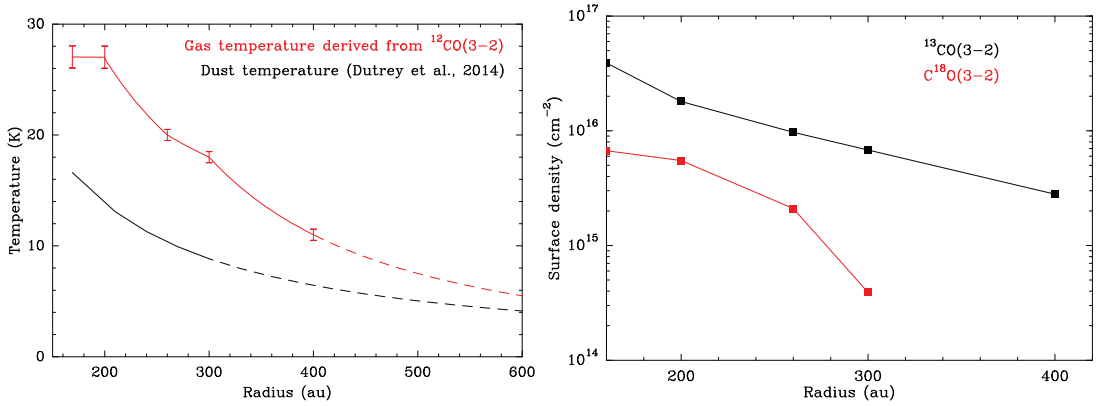

FIGURE 13: *Hình trái:* Sự phụ thuộc vào khoảng cách tới tâm của nhiệt độ khí CO (màu đỏ) và bụi (màu đen). Nhiệt độ khí được lấy từ kết quả phân tích vạch phát xạ ^{12}CO(3–2). Nhiệt độ bụi được lấy từ Dutrey et al. (2014). *Hình phải:* Sự phụ thuộc vào khoảng cách tới tâm của mật độ bề mặt của ^{13}CO(–2), C^{18}O(3–2)

Phần thứ hai của Chương 3 trình bày phân tích các vạch phát xạ phân tử ^{12}CO (J=2–1, 3–2 và 6–5) và các đồng phân của nó ^{13}CO (3–2) và C^{18}O (3–2). Với độ phân giải góc tốt hơn ~ 50 au, những dữ liệu này cho thấy bằng chứng về sự không đồng nhất theo khoảng cách tới tâm sao và góc phương vị của đĩa ngoài của hệ tiền hành tinh này. Sự phụ thuộc theo góc phương vị của cường độ phát xạ trong mặt phẳng đĩa của phát xạ ^{12}CO cho thấy sự hiện diện của "điểm nóng " ở góc phần tư đông nam. "Điểm nóng" này không thể hiện rõ trong các đồng phân ít phổ biến của CO như ^{13}CO và C^{18}O (xem Hình 19).

Chương 4 trình bày mô hình truyền bức xạ của ^{12}CO, ^{13}CO và C^{18}O (J=3–2). Kết quả nghiên cứu của chương này đã được gửi đăng trên tạp chí Astronomy & Astrophysics (Phuong et al. 2019). Công việc này được thực hiện một phần trong mặt phẳng *uv*. Để nghiên cứu phát xạ của khí từ đĩa ngoài với sự phát xạ của khí từ trong khoang rỗng một cách riêng biệt, tôi đã loại bỏ các *thành phần CLEANed* bên trong khoang rỗng $r < 160$ au từ số liệu *uv* ban đầu và phân tích dữ liệu với số liệu *uv* đã thay đổi (chỉ còn các phát xạ từ đĩa ngoài). *Thành phần CLEANed* là thành phần data-cube tốt nhất mô tả phát xạ của nguồn được sử dụng trong quá trình chuyển đổi số liệu từ mặt phẳng *uv* sang mặt phẳng bầu trời. Vì vạch phát xạ phân tử ^{12}CO(3–2) có độ dày quang học lớn và dễ bị nhiệt hóa, chúng tôi sử dụng vạch này để tính nhiệt độ của đĩa giả sử mật độ bề mặt của ^{12}CO(3–2) đủ lớn. Mật

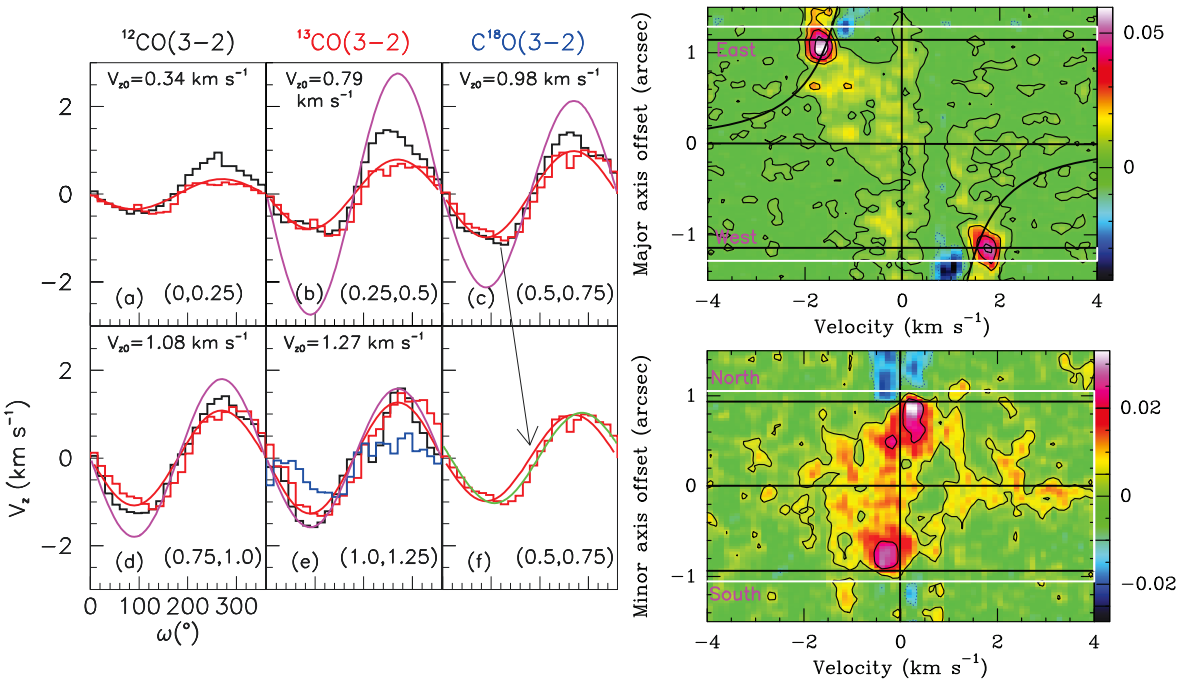

FIGURE 14: **Hình trái:** Sự phụ thuộc của $\langle V_z \rangle$ (km s^{-1}) vào góc phương vị ω (°) trong khoang rỗng. Phát xạ ^{12}CO (3–2) được biểu diễn bởi đường màu đen, ^{13}CO (3–2) màu đỏ và C^{18}O (3–2) màu xanh lam. Đường cong màu đỏ biểu diễn đường khớp hàm của phát xạ ^{13}CO (3–2) với hàm sin. Các đường cong màu tía biểu diễn đường chuyển động Kepler cho một sao đơn có khối lượng 1,36 $M_\odot$. Đường cong màu xanh lá cây trong bảng (f) biểu diễn hàm khớp với sự đóng góp của thành phần vận tốc rơi so sánh với hàm khớp chỉ bao gồm thành phần chuyển động quay, hai đường khớp được vẽ chồng lên số liệu của phát xạ ^{13}CO. **Hình phải:** Sơ đồ Vận tốc–Vị trí của phát xạ ^{13}CO(3–2) trong khoang rỗng dọc theo bán trục lớn (hình trên) và bán trục nhỏ (hình dưới). Các đường cong màu đen biểu diễn đường chuyển động Kepler quanh ngôi sao đơn có khối lượng 1,36 $M_\odot$. Các đường đồng mức tương ứng với giá trị 10 mJy beam^{-1}. Các đường thẳng màu trắng chỉ vị trí bán kính trong của vành bụi (180 au) và các đường thẳng màu đen chỉ bán kính trong của đĩa khí (169 au). Lưu ý rằng dữ liệu đã được được xoay 7° để bán trục nhỏ của đĩa hướng đến phía bắc.

độ của ^{13}CO và C^{18}O được tính khi giả sử rằng phân bố nhiệt độ theo khoảng cách tới tâm của ^{13}CO và C^{18}O giống với phân bố của ^{12}CO trong mô hình để khớp với số liệu. Sự phụ thuộc theo bán kính của nhiệt độ (khí và bụi) và mật độ bề mặt của ^{13}CO và C^{18}O được trình bày trong Hình 20.

Việc trừ mô hình "đĩa ngoài" tốt nhất (như đề cập ở trên) từ các số liệu *uv* ban đầu làm nổi bật phát xạ yếu của khí bên trong khoang rỗng. Các nghiên cứu về động học của khí trong khoang rỗng cho thấy khí trong khoang rỗng chủ yếu bị chi phối bởi chuyển động quay, với một phần đóng góp nhỏ của chuyển động rơi ($\sim 10\% - 15\%$ độ lớn của vận tốc Kelper). Hình 14 trình bày bản đồ Vận tốc–Vị trí (P-V diagram)

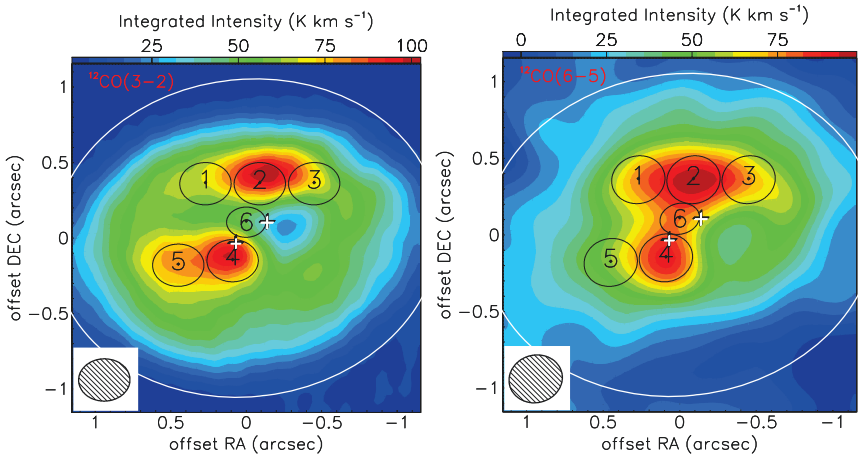

FIGURE 15: Bản đồ độ sáng tích phân theo vận tốc của ^{12}CO(3–2) *(trái)* và ^{12}CO(6–5) *(phải)* và vị trí của các vùng sáng. Mỗi vùng sáng bao phủ một diện tích beam, ngoại trừ vùng 6 chỉ bao phủ $\sim$ 50% diện tích beam. Giá trị bảng màu được thể hiện trên mỗi hình và có đơn vị là K km s^{-1}.

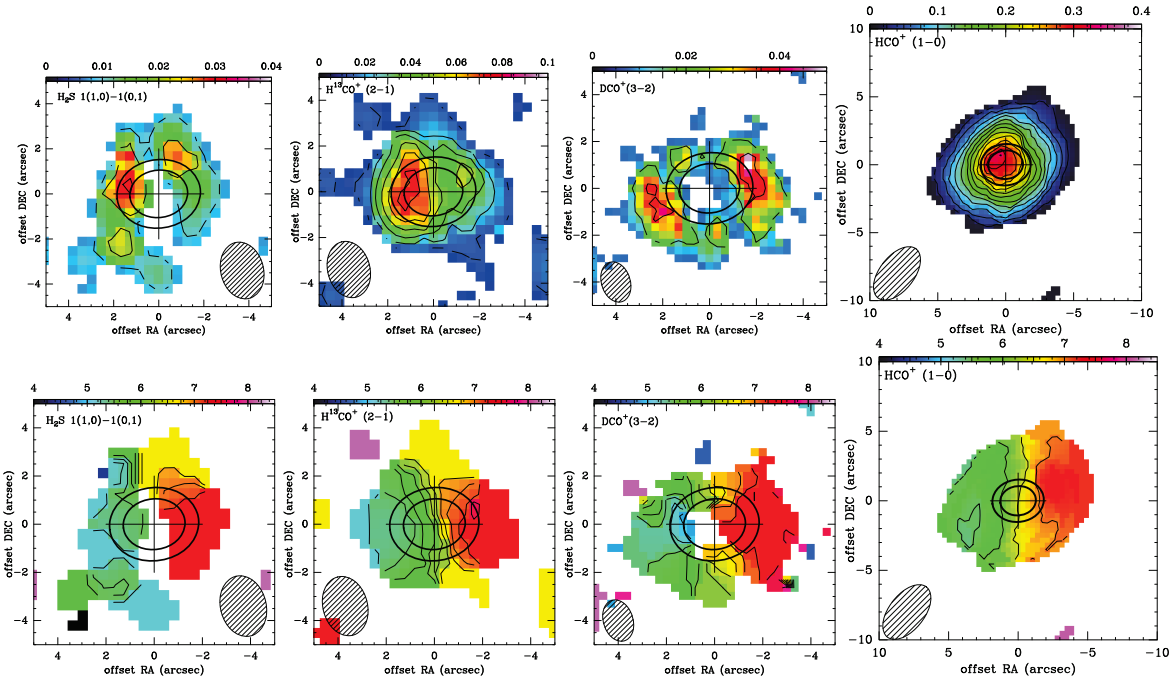

FIGURE 16: *Trên:* Bản đồ cường độ phát xạ. Thang màu được biểu diễn trong đơn vị Jy beam^{-1} km s^{-1}. Mỗi đường đồng mức tương ứng với 2σ. *Dưới:* Bản đồ vận tốc. Mỗi đường đồng mức tương ứng với 0.5 km s^{-1}. Kích thước beam được chỉ ra ở góc dưới của mỗi hình. Các đường e-lip biểu diễn vị trí của bán kính trong ($\sim$180 au) và bán kính ngoài ($\sim$260 au) của vành bụi.

và sự phụ thuộc theo góc phương vị của vận tốc Doppler trung bình trong 5 vành tròn với độ rộng mỗi vành là $0,25''$. Phần phát xạ mạnh của CO bên trong khoang

rỗng được chia ra thành 6 vùng sáng (xem Hình 25). Phân tích non–LTE cho kết quả về mật độ dài của CO trong các vùng sáng này là $\sim 10^{17}\,\mathrm{cm}^{-2}$, nhiệt độ $40 - 80\,\mathrm{K}$ và mật độ H_2 trong các vùng sáng này là $10^7\,\mathrm{cm}^{-3}$. Khối lượng H_2 trong khoang khoảng $\sim 10^{-4}\,\mathrm{M}_\odot$ trong khi tổng khối lượng của các vùng sáng là $\sim 10^{-5}\,\mathrm{M}_\odot$. Khối khí này sẽ biến mất (do bồi đắp vào đĩa trong của Aa) trong khoảng 2500 năm. Do đó, tốc độ bồi tụ vật chất được tính vào khoảng $\sim 6.4 \times 10^{-8}\,\mathrm{M}_\odot\,\mathrm{yr}^{-1}$.

Chương 5 trình bày nghiên cứu về thành phần hóa học của đĩa GG Tau A. Kết quả nghiên cứu được công bố trong Phuong et al. (2018a). Nội dung chương này trình bày việc lần đầu tiên phát hiện H_2S trong một đĩa tiền hành tinh và sự phát hiện các phân tử khác trong đĩa GG Tau A, DCO^+, HCO^+, và $H^{13}CO^+$. Hình 16 trình bày bản đồ cường độ phát xạ và vận tốc của các vạch phát xạ phân tử này. Tỷ lệ DCO^+/HCO^+ trong đĩa khí và bụi mật độ cao (ở 250 au) được đánh giá vào

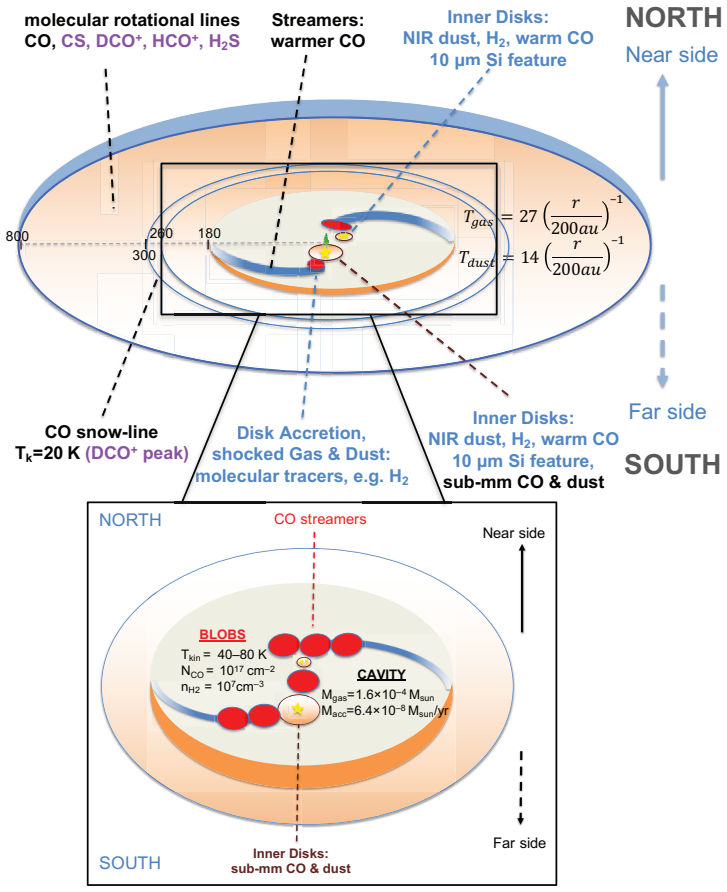

FIGURE 17: Tính chất tổng quát của hệ sao GG Tau A.

khoảng 0.03, tương tự như trong các đĩa tiền hành tinh khác (TW Hya và LkCa 15). Kết quả này bổ sung thêm bằng chứng về việc deuterium hóa xảy ra trong đĩa tiền hành tinh GG Tau A. Chương 5 cũng trình bày một mô hình hóa học đơn giản của GG Tau A và so sánh với các quan sát.

Việc H_2S được phát hiện trong GG Tau A, trong khi nó không được phát hiện trong các đĩa khác, có khối lượng thấp hơn GG Tau A khoảng 3–5 lần, như DM Tau

và LkCa 15, cho thấy rằng đĩa tiền hành tinh với khối lượng lớn này có thể là một đối tượng tốt để nghiên cứu thành phần và sự tiến hóa hóa học trong đĩa tiền hành tinh. Tôi cũng trình bày độ phổ cập so với ^{13}CO của các phân tử này trong đĩa GG Tau A, và so sánh với đĩa LkCa 15 và trong đám mây phân tử TMC-1. Giới hạn trên mật độ bề mặt của các phân tử khác không được phát hiện trong GG Tau A, như SO, SO_2, C_2S và của *c*-C_3H_2 và HC_3N cũng được đưa ra.

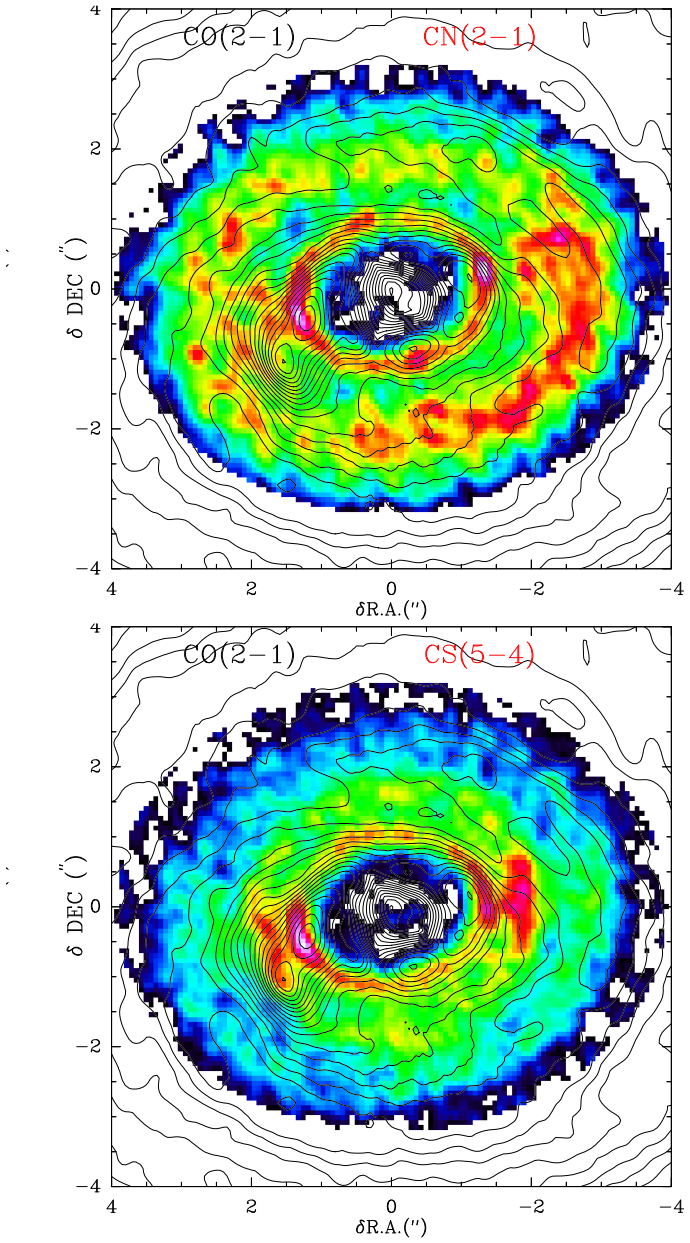

FIGURE 18: **Trên:** Bản đồ độ sáng đỉnh phát xạ của CN(2–1) (màu) chồng lên bản đồ của CO(2–1) (biểu diễn bởi các đường đồng mức). **Dưới:** Bản đồ độ sáng đỉnh phát xạ của CS(5–4) (màu) chồng lên bản đồ của CO(2–1) (các đường đồng mức).

Chương 6 trình bày kết luận và triển vọng nghiên cứu tương lai. Hình 26 tóm

tắt các thuộc tính (vật lý, hóa học và động học) của GG Tau A và môi trường xung quanh nó được nghiên cứu trong luận án này. Ngày càng có nhiều ngoại hành tinh được tìm thấy quanh các hệ sao đôi và đa sao. Do đó, việc hiểu cách chúng hình thành yêu cầu các nghiên cứu kỹ về các đối tượng trẻ hơn như các hệ đa sao T Tauri. Trong bối cảnh như vậy, luận án này trình bày một nghiên cứu đầy đủ nhất cho tới nay về tính chất của một đĩa tiền hành tinh quanh hệ đa sao T Tauri.

Quan sát ALMA ở Chu kỳ 3 (Cycle 3) và Chu kỳ 6 (Cycle 6) các vạch phát xạ CN, CO và CS được trình bày trong chương này. Dữ liệu CO mới cho thấy bằng chứng của vùng phát xạ dạng xoắn ốc ở mức độ thấp. Các quan sát từ CN và CS cho thấy cấu trúc vành, một trong số chúng trùng với các đặc trưng quan sát được từ CO (xem Hình 27). Các quan sát mới này hứa hẹn cung cấp thêm nhiều thông tin thú vị về đĩa tiền hành tinh quanh hệ sao ba GG Tau A.

Résumé substantiel

Comprendre comment se forment les systèmes planétaires est un défi majeur de l'astrophysique du 21me siècle. Pour cela observer les jeunes étoiles de faible masse, semblables au Soleil quand il avait environ un million d'années est une étape fondamentale. En effet, les planètes se forment à partir du disque de gaz et de poussières qui orbite autour de ces jeunes étoiles (également appelées étoiles TTauri). Ce disque est lui même un résidu du nuage moléculaire qui a formé l'étoile centrale, il est appelé disque protoplanétaire. En conséquence, déterminer la physique et la chimie de ces disques est devenu un domaine important de l'astrophysique qui demande à la fois des observations et des modèles sophistiqués. Contraindre les conditions initiales menant à la formation des systèmes planétaires et les comparer aux modèles passe par une évaluation observationnelle des propriétés physiques (densité, température, turbulence, etc.) et de l'évolution chimique des disques. Une source de limitation pour les observations réside dans le fait que la détermination de ces paramètres physiques fondamentaux est fortement dégénérée au sein d'une observation unique. Le rôle de l'observateur est donc de définir une stratégie d'observation, par exemple en observant plusieurs molécules, permettant une détermination précise des propriétés physiques pour minimiser l'impact des dégénérescences possibles. Connaitre les propriétés de la poussière (nature, taille, morphologie) est aussi important pour comprendre la formation des embryons planétaires mais aussi la genèse des molécules complexes. De nombreuses molécules organiques se forment sur les surfaces des grains où les molécules gazeuses condensent dès que la température devient suffisamment basse (par exemple 17 K pour le CO) pour interagir avec les molécules déjà piégées sur des grains.

Cette thèse étudie les propriétés du disque protoplanétaire entourant un système stellaire triple de faible masse, GG Tau A, en utilisant des observations interférométriques de molécules traces, telles que ^{12}CO, ^{13}CO, C^{18}O, DCO$^+$, HCO$^+$ et H_2S, et l'émission thermique de la poussière observée à plusieurs longueurs d'onde.

Le chapitre 1 présente le sujet et les connaissances actuelles sur les disques protoplanétaires. Le cas particulier des disques protoplanétaires entourant les systèmes binaires est introduit à la fois pour les aspects théoriques et pour les observations. La deuxième partie du chapitre présente les propriétés connues du système GG Tau A.

Le chapitre 2 résume quelques points fondamentaux sur les instruments, les observations et les méthodes d'analyse. Il présente brièvement les interféromètres IRAM/NOEMA et ALMA, les observations effectuées avec ces instruments et la réduction des données. Il expose également les principes de l'interférométrie radio et de la déconvolution. Il rappelle aussi les bases du transfert radiatif, et le code de transfert radiatif DiskFit est introduit à la fin du chapitre.

Le chapitre 3 est le premier des trois chapitres qui traitent de l'étude spécifique du disque protoplanétaire GG Tau A. Les résultats sont publiés dans Phuong et al.

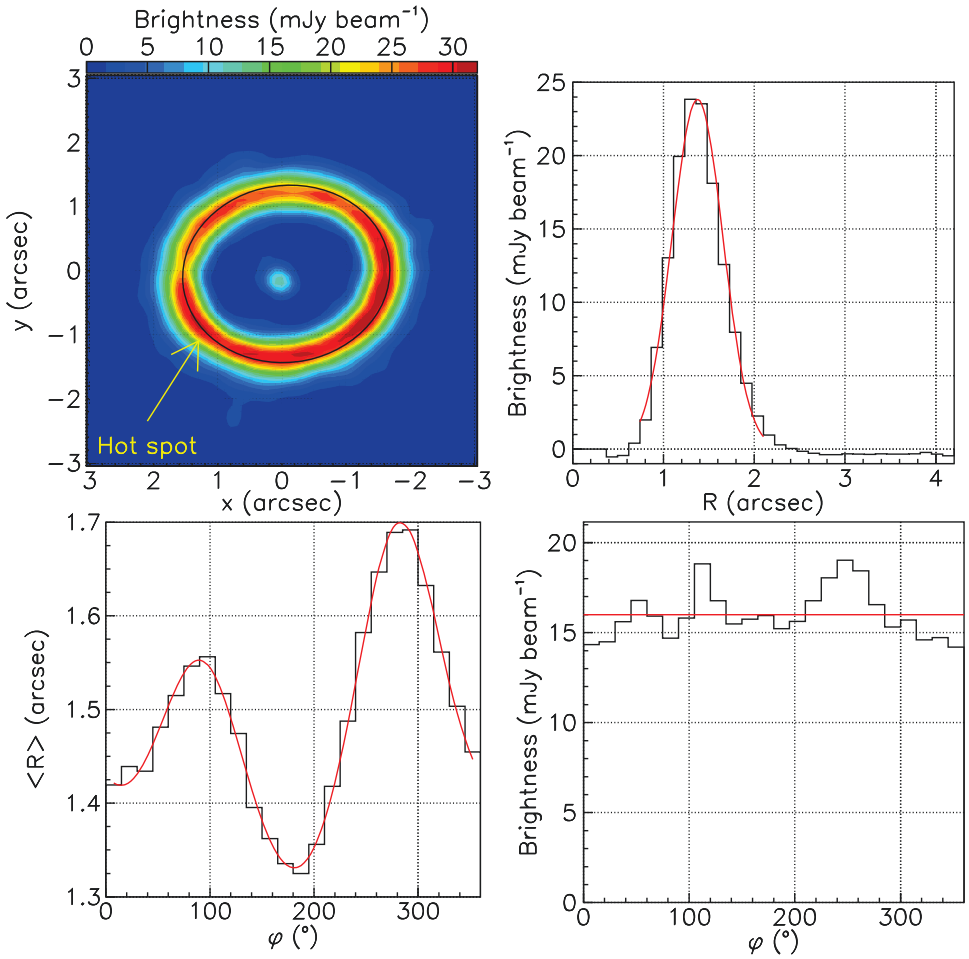

FIGURE 19: Emission continue de l'anneau de poussières. *De gauche à droite et de haut en bas:* la carte du ciel, l'ellipse noire correspond à $\langle R \rangle$ (valeur moyenne de R) indiquée dans le panneau inférieur gauche; la flèche jaune indique la région du point chaud ("hot spot") observée par Dutrey et al. (2014) et Tang et al. (2016) en ^{12}CO(6-5) et ^{12}CO(3-2); la dépendance en R de la brillance moyennée sur φ, avec le meilleur ajustement gaussien au pic; la dépendance en φ de $\langle R \rangle$ est calculée dans l'intervalle $1'' < R < 2''$ (la courbe rouge correspond le mieux à l'anneau elliptique incliné et décalé par rapport à l'origine); et la dépendance en φ de la brillance du continuum moyenné sur R dans l'intervalle $1'' < R < 2''$. La ligne rouge indique la valeur moyenne de la brillance du continuum.

(2018b). Il présente une analyse de la morphologie du disque de poussières en utilisant une carte obtenue à 0.9 mm et une étude morpho-cinématique du gaz (CO) observé avec ALMA. Les études confirment l'étroitesse de l'anneau de poussières, son inclinaison de 35° et son angle de position de $\sim$ 7° ainsi que la présence d'un bord interne net. La figure 19 montre l'émission de l'anneau de poussières, la dépendance radiale de la brillance, la dépendance azimutale pour le CO et la dépendance azimutale de la brillance à 0.9 mm.

L'étude réalisée avec ^{13}CO(3–2) donne une limite supérieure de 0.24″ (34 au) pour

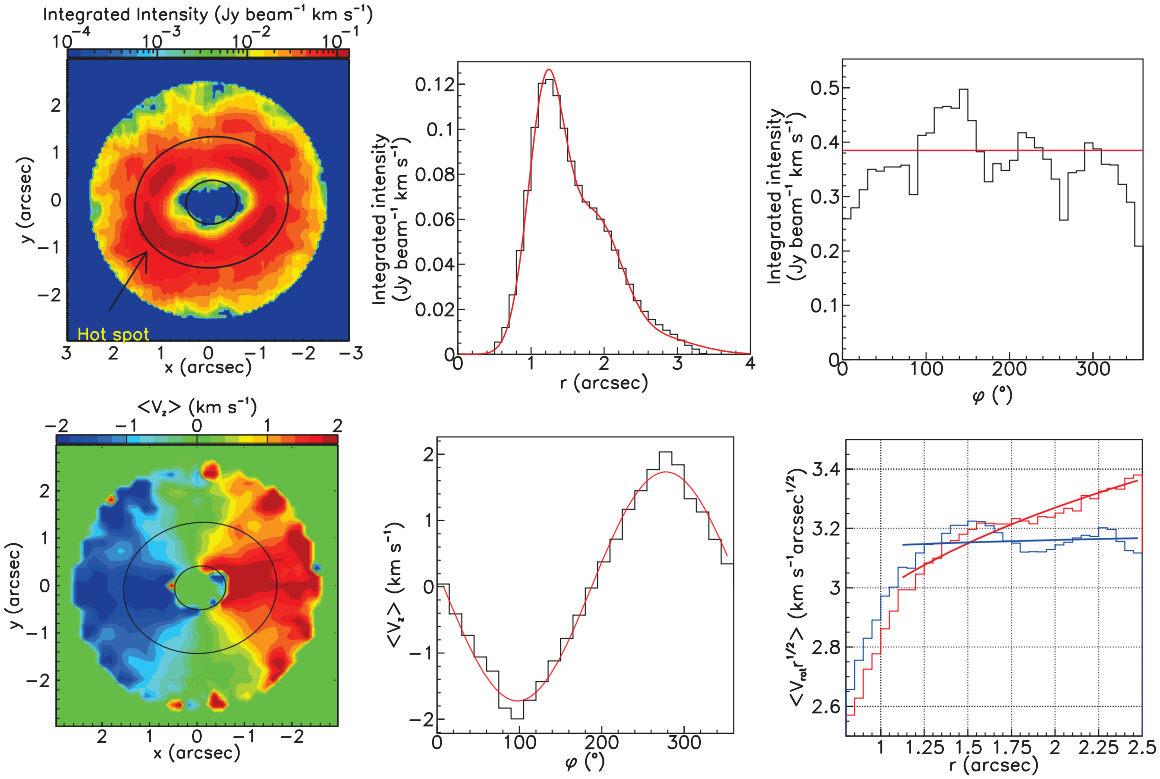

FIGURE 20: **Haut:** Carte du ciel de l'intensité intégrée de le émission de la transition ^{13}CO(3–2). La flèche noire indique la position du point chaud en ^{12}CO(6–5) (Dutrey et al., 2014) et ^{12}CO(3–2) (Tang et al., 2016) (*gauche*). Dépendance en r de l'intensité intégrée moyennée de manière azimutale dans le plan du disque. La ligne rouge est un ajustement utilisant les mêmes trois Gaussiennes que dans Tang et al. (2016) (*milieu*). Dépendance azimutale de l'intensité intégrée moyennée sur le disque ($0.54'' < r < 2''$). La ligne rouge indique l'intensité moyenne (*droite*). **Bas:** Carte du ciel indiquant la vitesse Doppler moyenne (pondérée par l'intensité) (*gauche*). Dépendance azimutale de la vitesse Doppler moyenne pondérée par l'intensité (*milieu*). Dépendance de $\langle V_{rot}\, r^{1/2} \rangle$ en fonction de r (moyenne pondérée par l'intensité); les lignes sont la meilleure loi de puissance, elle correspond aux indices -0.63 pour $|\sin\omega| > 0.3$ (rouge) et -0.48 pour $|\sin\omega| > 0.707$ (bleu) (*right*.)

l'echelle de hauteur apparente du disque à une distance de $1''$ (140 au) des étoiles centrales. Le disque externe est en rotation Keplerienne avec une vitesse de rotation atteignant ~ 3.1 km s^{-1} à $1''$ des étoiles centrales; une limite supérieure de 9 % (avec un niveau de confiance de 99%) est placée sur une possible vitesse de chute ("infall") vers les étoiles. Les variations d'intensité à travers la zone du disque sont étudiées en détail et confirment la présence d'un point chaud dans le quadrant sud-est. Plusieurs autres variations d'intensité significatives, notamment une dépression dans la direction nord, sont également révélées. La corrélation des intensités observées aux variations de la largeur de raie est aussi étudiée. Les contributions possibles à la largeur de raie mesurée sont examinées, suggérant une décroissance de la

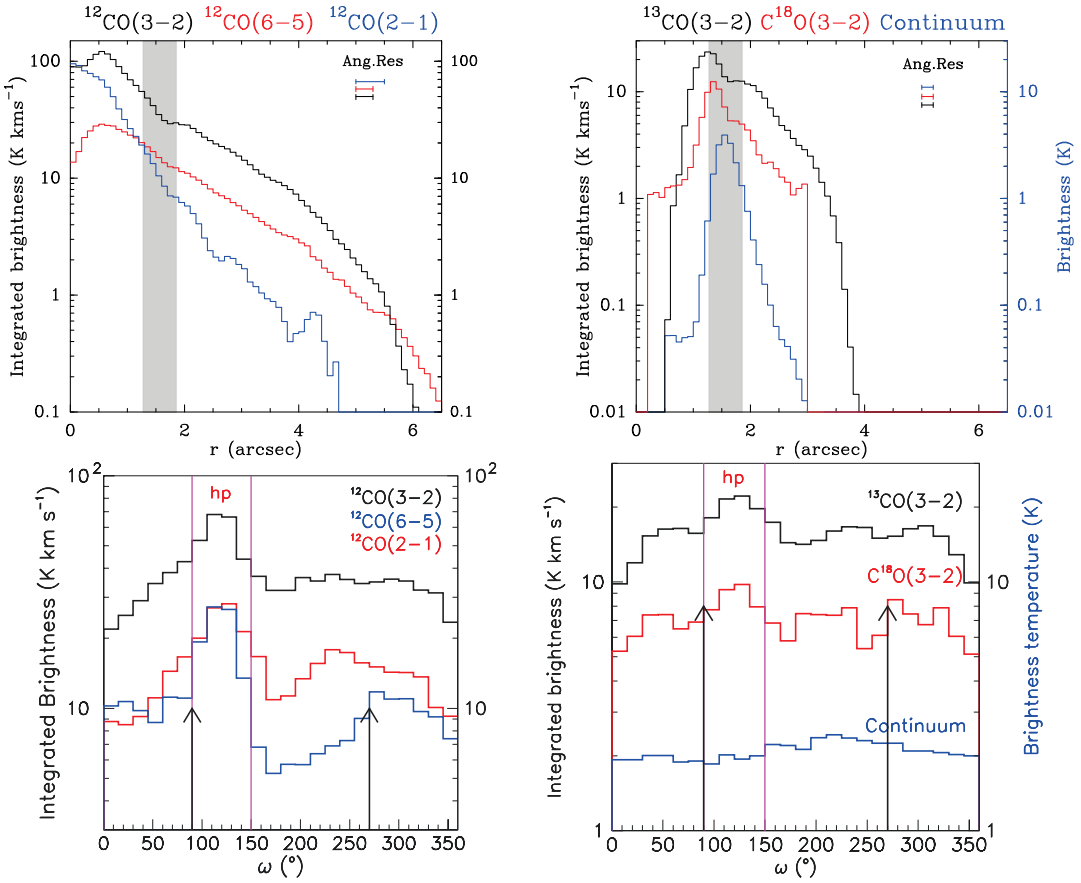

FIGURE 21: *Haut:* Dépendance radiale de la brillance de température intégrée. Les barres horizontales indiquent la résolution. *Bas:* Dépendance azimutale de la brillance de température intégrée sur l'anneau $1.2'' < r < 2.0''$. Les panneaux de gauche montrent les trois émissions de ^{12}CO (J = 6–5, 3–2 et 2–1), avec les données de CO (2–1) extraites de Dutrey et al. (2014), les panneaux du milieu montrent les émissions des isotopologues de CO moins abondants (J = 3–2) et les panneaux de droite montrent les transitions CS (7–6) et CS (3–2) et le continuum. Les flèches noires indiquent l'emplacement des pics le long du grand axe du disque. Les lignes verticales magenta dans les panneaux supérieurs indiquent le bord intérieur de l'anneau de poussières, dans les panneaux inférieurs, elles montrent l'emplacement du point chaud.

température et de l'opacité du disque avec la distance aux étoiles. La figure 20 (panneaux du haut) montre la carte d'intensité de l'émission ^{13}CO (3–2), les variations radiales et azimutales de l'intensité de ^{13}CO(3–2) . La dépendance radiale révèle des sous-structures non résolues. La dépendance azimutale de l'intensité suggère un disque uniforme avec un excès d'émission dans le quadrant sud-est (correspondant au "point chaud "observé par Dutrey et al. (2014)) et qui pourrait correspondre à une planète en formation. La figure 20 (panneaux inférieurs) montre la carte des vitesses de l'émission ^{13}CO(3–2), la dépendance azimutale de la vitesse moyenne $\langle V_z \rangle$ ainsi que la dépendance radiale du produit $\langle V_{\rm rot} \times r^{1/2} \rangle$. L'étude de la carte

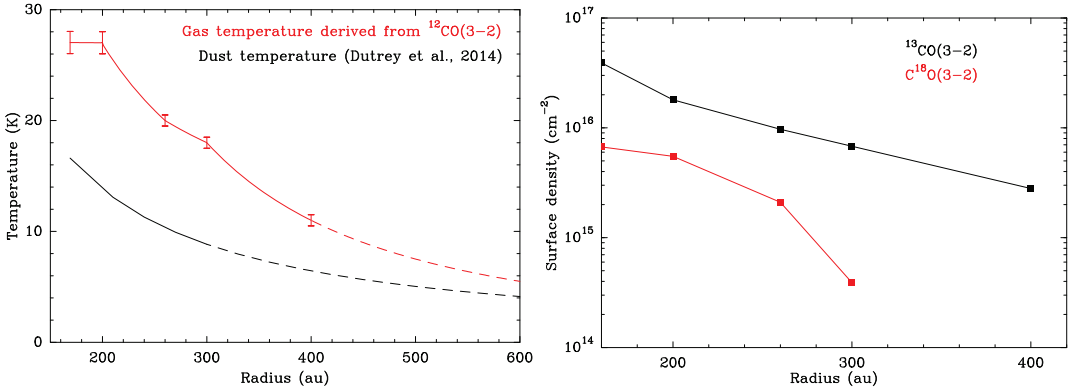

FIGURE 22: *Gauche:* Dépendance radiale de la température du gaz (CO) en rouge et des poussières en noir. La température du gaz est dérivée de l'analyse ^{12}CO $(3-2)$. La température des poussières provient de Dutrey et al. (2014). *Droite:* Dépendance radiale des densités de surface dérivées de ^{13}CO, C^{18}O (J=3 − 2) et de CS (J=7 − 6(et (J=3 − 2). La densité de surface de CS présentée est obtenue en prenant la température déduite de la poussière.

des vitesses confirme que le disque tourne autour de son axe principal. La dépendance azimutale de la vitesse moyenne $\langle V_z \rangle$ est correctement ajustée par une fonction cosinus confirmant la rotation du disque, ceci permettant également de placer une limite supérieure sur le mouvement de chute. Comme attendu, la dépendance de $\langle V_{\rm rot} \times r^{1/2} \rangle$ sur r montre que la meilleure loi de vitesse du disque est Keplerienne. La courbe bleue présente la distribution réduite à $\sim 45^\circ$ autour du petit axe, correspondant à un indice pour la vitesse de -0.48, ce qui est parfaitement Keplerien (-0.5).

La deuxième partie du chapitre 3 présente l'analyse des données ^{12}CO (J=2–1, 3–2, et 6–5) et de ses isotopologues ^{13}CO $(3-2)$ et C^{18}O $(3-2)$, et de CS (6–5) et CS (3–2). Avec une résolution lineaire supérieure à $\sim$ 50 au, ces données révèlent des inhomogénéités radiales et azimutales dans le disque externe. La dépendance azimutale de l'intensité des émissions de ^{12}CO montre le "point chaud". Il est moins visible dans les données ^{13}CO et C^{18}O et disparaît pratiquement dans les émissions de CS (voir la figure 21).

Le chapitre 4 présente une modélisation du transfert radiatif pour les données ^{12}CO, ^{13}CO et C^{18}O (J=3 − 2), et CS (J=7 − 6). Il est publié dans Phuong et al. (2019, A&A). Ce travail est partiellement effectué dans le plan de Fourier. Pour mieux séparer l'émission du gaz dans l'anneau de celle du gaz dans la cavité, j'ai procédé par itérations. J'ai d'abord étudié le disque externe et l'anneau. J'ai ensuite soustrait le meilleur modèle de l'anneau et du disque externe pour étudier le gaz dans la cavité. Puisque ^{12}CO (J=3 − 2) est optiquement épais et facilement thermalisé, cette raie permet de déterminer la température cinétique dans le disque. Les densités de surface du gaz sont ensuite déduites des données optiquement plus minces ^{13}CO et C^{18}O en utilisant la température déduite de CO. Les densités de surface de CS sont calculées

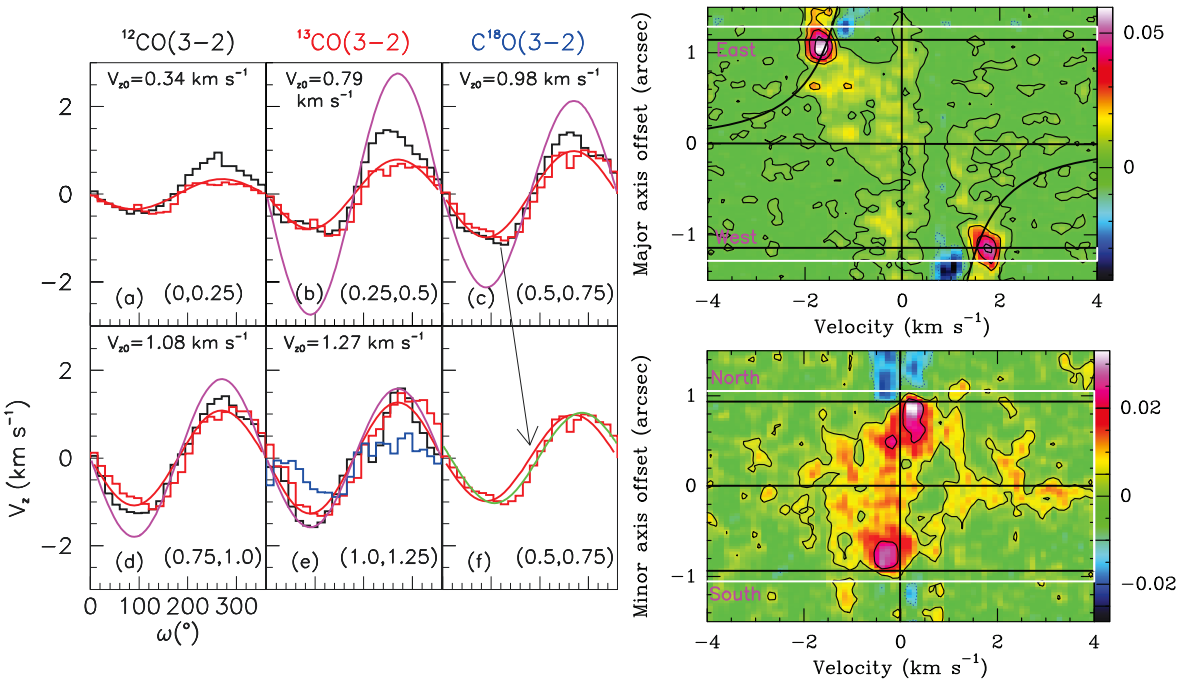

FIGURE 23: **Gauche:** Dépendance de $\langle V_z \rangle$ ($\mathrm{km\,s^{-1}}$) en fonction de l'azimut ω (°) dans la cavité. ^{12}CO(3 − 2) est en noir, ^{13}CO(3 − 2) en rouge et C^{18}O(3 − 2) en bleu. La courbe rouge est un ajustement des données ^{13}CO(3 − 2) par une fonction sinus. Nous utilisons un blanc s'il n'y a pas de bonnes données disponibles (bruit) dans le disque. La courbe magenta montre la courbe Keplerienne attendue pour une étoile centrale de 1.36 $\mathrm{M_\odot}$. **Droite:** Diagrammes position-vitesse de l'émission ^{13}CO(3–2) dans la cavité le long de l'axe principal (panneau supérieur) et de l'axe secondaire (panneau inférieur). La courbe noire montre la vitesse keplerienne attendue autour d'une étoile de 1.36 $\mathrm{M_\odot}$.

en partant de 2 hypothèses extrêmes: i) l'émission de CS provient de la même altitude que l'émission de CO et a donc son profil de température; ii) l'émission de CS provient plutôt de plus profond dans le disque (~ 1 échelle de hauteur au dessus du plan médian) et cette couche de gaz doit donc être à une température plus proche de celle de la poussière située près du plan médian. Les profils de température et de densité de surface mesurés sont résumés dans la figure 22.

La soustraction du meilleur modèle d'anneau (présenté ci-dessus) des données originales (dans le plan de Fourier) fournit les meilleures images possible des émissions de CO et CS à l'intérieur de la cavité. L'étude de la cinématique de la cavité révèle une vitesse de chute du gaz dans la cavité qui est de $\sim$ 10% − 15% de la vitesse Kepleriennne locale. La figure 23 montre les diagrammes position-vitesse et la dépendance azimutale de la vitesse déprojectée dans 5 cellules de taille $\Delta r = 0.25''$ chacun. Les émissions de CO à l'intérieur de la cavité peuvent être définies par des condensations (ou "blobs") brillantes (voir la figure 24). L'analyse non-LTE de ces condensations indique que la densité de colonne de CO est de $\sim 10^{17}\,\mathrm{cm^{-2}}$, la température varie de 40 à 80 K et la densité de H_2 est de l'ordre de $\sim 10^{7}\,\mathrm{cm^{-3}}$. La

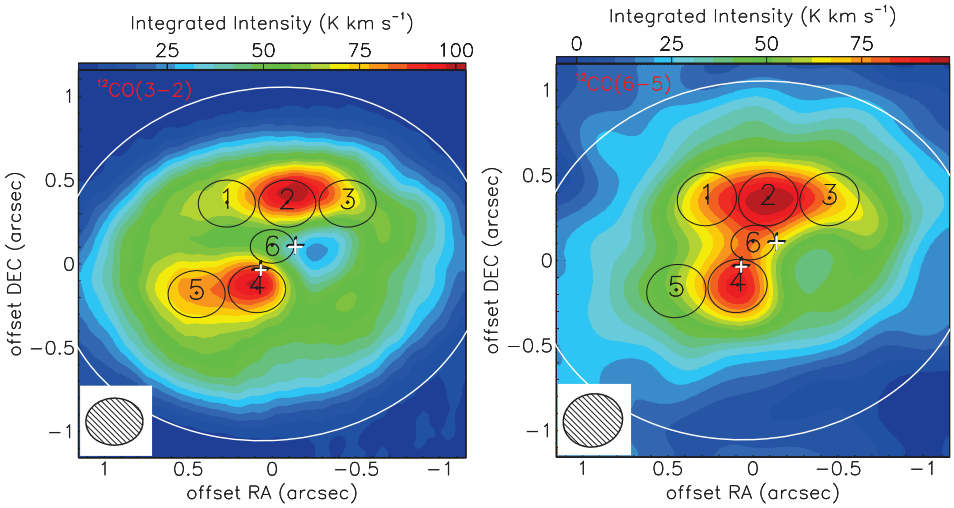

FIGURE 24: Intensité intégrée de ^{12}CO(3 − 2) *(gauche)* et ^{12}CO(6 − 5) *(droite)*. Chaque "blob" couvre un lobe interférométrique à l'exception de B6, qui ne couvre que ∼ 50% d'un lobe.

masse totale de H_2 à l'intérieur de la cavité est estimée à $\sim 10^{-4}\,M_\odot$ alors que la masse cumulée des condensations est de $\sim 10^{-5}\,M_\odot$. La masse de gaz va se dissiper / s'accréter sur le disque Aa en environ 2500 ans, cela correspond à un taux d'accrétion de $\sim 6.4 \times 10^{-8}\,M_\odot\,an^{-1}$

Le chapitre 5 présente une étude du contenu chimique du disque protoplanétaire GG Tau A. Les résultats sont publiés dans Phuong et al. (2018a). Il présente la première détection de H_2S dans un disque protoplanétaire et la détection d'autres molécules, telles que DCO^+, HCO^+, et $H^{13}CO^+$ dans le disque externe de GG Tau A. Le rapport DCO^+/HCO^+ (à 250 au) est mesuré ($\sim$ 0.03). Il est identique à ceux observés dans des disques similaires comme ceux entourant TW Hya et LkCa 15. Les abondances des molécules par rapport à ^{13}CO sont calculées et comparées à celles observées dans le disque de LkCa 15 et le nuage moléculaire TMC-1. Les deux disques ont des abondances similaires. Les limites supérieures (en densité de colonne) des autres molécules telles que, SO, SO_2,C_2S, et de *c*–C_3H_2, et HC_3N sont également présentées. Un modèle chimique du disque de GG Tau A est aussi discuté et comparé aux observations. La comparaison montre que la chimie du soufre n'est pas encore bien comprise. La détection de H_2S dans le disque de GG Tau A est facilitée par la grande masse du disque (comparée aux autres disques où H_2S a été cherché). Le disque de GG Tau A apparait comme un bon candidat pour étudier le contenu chimique des disques protoplanétaires.

Le chapitre 6 présente la conclusion générale. En particulier, la figure 26 résume les propriétés de GG Tau A et de son environnement (physique, chimie et cinématique) obtenues grâce à cette thèse. De plus en plus de planètes autour des étoiles binaires ou multiples (50% des étoiles galactiques) sont découvertes, il est important de comprendre comment ces systèmes planétaires peuvent se former et évoluer. Cette thèse y contribue en présentant l'étude la plus complète effectuée à ce jour d'un tel système stellaire.

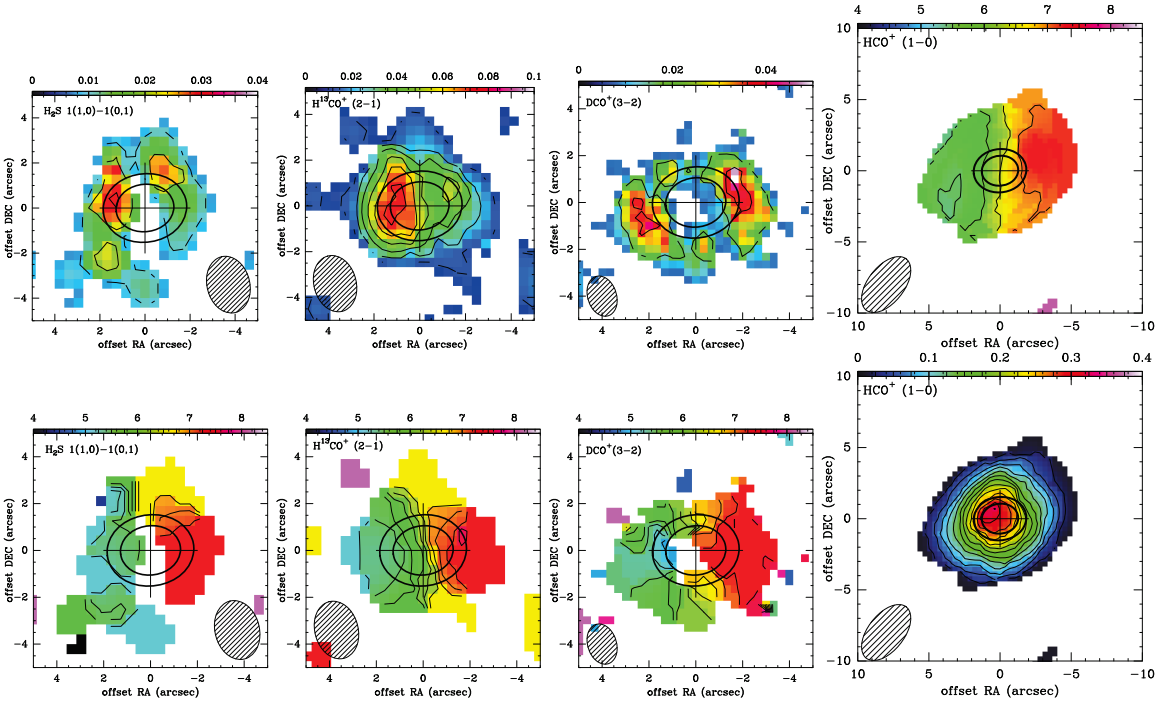

FIGURE 25: *Haut:* Cartes d'intensité intégrée. L'échelle de couleurs est dans l'unité de (Jy beam^{-1} km s^{-1}). Les contours sont à 2σ. *Bas:* Cartes des gradients de vitesse. Les contours sont par pas de 0,5 km s^{-1}. Les tailles des lobes sont indiquées. Les ellipses indiquent les rayons intérieur ($\sim$180 au) et extérieur ($\sim$260 au) de l'anneau de poussières.

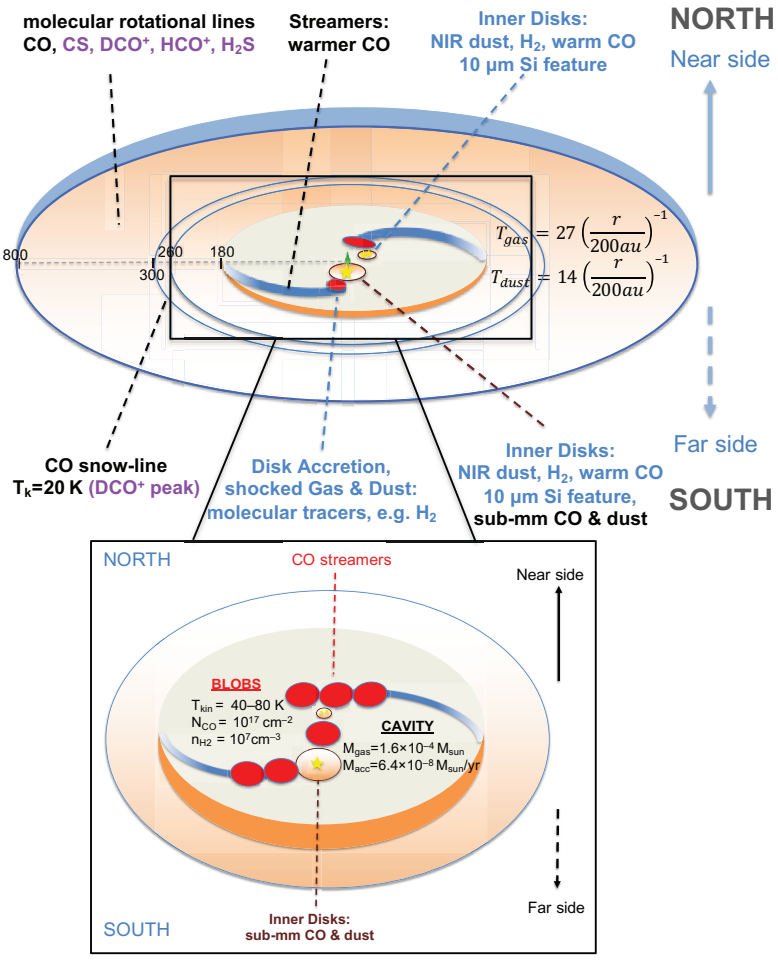

FIGURE 26: Un schéma de l'ensemble GG Tau A. Les propriétés globales sont présentées.

Puis le chapitre présente les perspectives découlant de ces résultats nouveaux et de nouvelles observations ALMA (cycle 3 et cycle 6) de CN, CO et CS non analysées. Les cartes à fort rapport signal/bruit de l'émission de CO(2–1) montrent la présence de bras spiraux à bas niveau dans la partie externe du disque. Elles pourraient être liées à des perturbations gravitationnelles dues à la présence du "point chaud" favorisant alors l'hypothèse de la planète en formation. Les nouvelles observations CN et CS font aussi apparaitre plusieurs structures annulaires dans l'anneau. L'analyse de ces nouvelles données s'avère donc très prometteuse, elle permettra en particulier de contraindre la dynamique du disque externe et de l'anneau et ses liens potentiels avec le "point chaud".

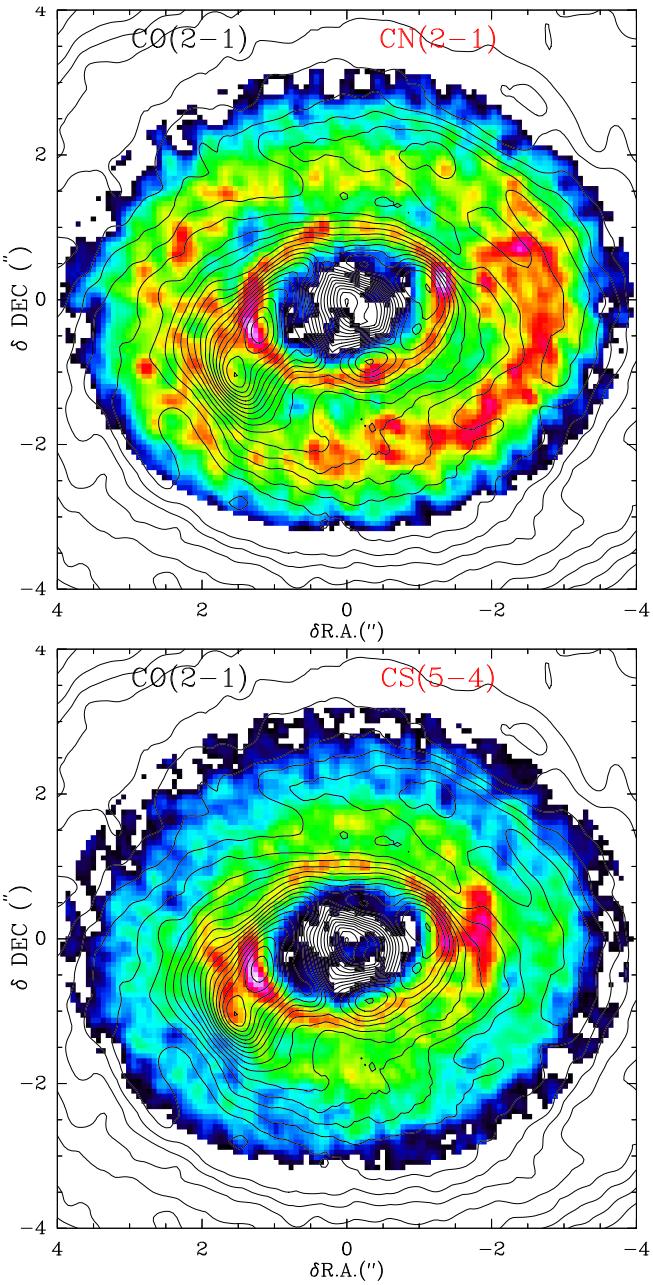

FIGURE 27: **Haut:** Superposition des cartes de brillance de CN(2–1) en couleur et de CO(2–1) en contour. **Bas:** Superposition des cartes de brillance de CS(5-4) en couleur et de CO(2–1) en contour

Contents

Declaration of Authorship i

Acknowledgements iii

Substantial summary v

1 Introduction 1

1.1 Overview . . . 1
1.2 The disk structure . . . 2
1.2.1 Density profile . . . 4
Vertical structure . . . 4
Radial structure . . . 5
1.2.2 Temperature profile . . . 6
1.3 Planet formation in protoplanetary disks . . . 7
1.3.1 The formation of planets . . . 7
1.3.2 Interaction between the planets and disks . . . 8
1.4 Gas composition of protoplanetary disks . . . 8
1.4.1 Gas in the inner disk . . . 9
1.4.2 Gas in the outer disk . . . 9
1.5 Observing the dust in protoplanetary disks . . . 10
1.6 Protoplanetary disks around binary and multiple systems . . . 13
1.6.1 Theoretical considerations . . . 13
1.6.2 Summary: what to observe? . . . 14
1.7 GG Tau A - an interesting binary system . . . 15
1.7.1 Existing observations . . . 16
The stars . . . 16
The circumbinary disk . . . 17

The circumstellar disks . . . 18
The cavity and "streamers" . . . 18
The hot spot . . . 19
1.7.2 Simulations of the GG Tau A system . . . 20
Radiative transfer simulation . . . 20
Hydrodynamical simulation . . . 21

2 Observations, data reduction and radiative transfer 23
2.1 Radio interferometry . . . 23
2.1.1 General . . . 23
2.1.2 Imaging and deconvolution . . . 26
Imaging . . . 26
Fourier Transform . . . 27
Weighting and Tapering . . . 27
Deconvolution . . . 29
2.1.3 ALMA and NOEMA interferometers . . . 29
ALMA, the Atacama Large Millimeter/submillimeter Array . 29
NOEMA, the NOrthern Extended Millimeter Array . . . 30
2.2 GG Tau A observations with interferometry . . . 31
2.2.1 ALMA observations . . . 31
2.2.2 NOEMA observations . . . 31
2.3 Data reduction . . . 32
2.3.1 The ALMA data reduction . . . 32
Continuum emission and proper motion . . . 32
Line emissions . . . 34
2.3.2 The NOEMA data reduction . . . 37
2.4 Data analysis strategy . . . 38
2.4.1 Radiative transfer equation . . . 38
2.4.2 DiskFit . . . 40

3 Morphology and kinematics of the disk surrounding GG Tau A 43
3.1 Introduction . . . 43
3.2 Geometry of the dust ring . . . 44

3.2.1 Morphology of the dust ring . . . 44
3.3 Morphology and kinematics of the gas disk obtained from observations of the ^{13}CO(3–2) emission . . . 46
3.3.1 Morphology . . . 46
General features . . . 46
Disk thickness and integrated intensity variations across the disk: generalities . . . 50
3.3.2 Kinematics . . . 54
Keplerian rotation . . . 54
Line width . . . 56
3.4 Multiline studies . . . 59
3.4.1 Radial and azimuthal dependence of the emission of CO isotopologues across the disk . . . 59
3.4.2 CO gas kinematics in the outer disk . . . 62
3.4.3 The "hot spot" . . . 64
3.5 Summary . . . 66
3.A Channel maps . . . 68

4 Gas properties from the outer disk to the central cavity 69
4.1 Local Thermal Equilibrium Modelling of the circumbinary disk . . . 69
4.1.1 Continuum fit . . . 69
4.1.2 CO isotopologues . . . 70
4.1.3 Discussion . . . 73
Temperature distribution in the outer disk . . . 73
Gas distribution and homogeneity of the outer ring . . . 75
4.2 Analysis of the gas inside the cavity . . . 75
4.2.1 The dynamics inside the cavity . . . 75
4.2.2 Gas properties . . . 76
4.2.3 Evaluation of the mass of gas contained in the cavity . . . 81
4.2.4 Discussion . . . 82
Gas kinematics . . . 82
Gas temperature . . . 83
Amount of gas . . . 83
Mass accretion rate . . . 84

4.3 Summary . . . 84
4.A Best ring model results reveal the emission inside the cavity . . . 86
4.B χ^2 maps on excitation condition parameters plane . . . 87

5 Chemical content of GG Tau A **89**
5.1 Published survey . . . 89
5.1.1 Results . . . 89
5.1.2 Comparison between observations and chemical model predictions . . . 92
Observed column density . . . 92
Predicted column density from the chemical model . . . 92
5.1.3 Discussion . . . 94
5.2 Summary . . . 98
5.A Channel maps . . . 99

6 Conclusion and Perspectives **101**
6.1 Conclusion . . . 101
6.1.1 Gas properties in the outer disk . . . 101
6.1.2 Gas inside the cavity . . . 103
6.2 New Observations . . . 104
6.2.1 CO observations . . . 104
6.2.2 CN observations . . . 104
6.2.3 CS observations . . . 106
6.3 Comparative study of the new observations and perspectives . . . 109

A Papers and Accepted proposals **111**

Bibliography **169**

List of Figures

1 Brightness of the dust ring continuum emission. *Top left:* sky map, the black ellipse is the fit to $\langle R \rangle$ shown in the bottom left panel; the yellow arrow points to the region of the "hot spot" observed by Dutrey et al. (2014) and Tang et al. (2016) in ^{12}CO(6–5) and ^{12}CO(3–2) emissions. *Top right:* The dependence on R of the brightness averaged over position angle φ, together with the Gaussian best fit to the peak. *Bottom left:* Dependence on φ of $\langle R \rangle$ calculated in the interval $1'' < R < 2''$ (the red line is the best fit to an elliptical tilted ring offset from the origin). *Bottom right:* Dependence on φ of the disk plane continuum brightness averaged over R in the interval $1'' < R < 2''$. The red line shows the mean value of the continuum brightness. vi

2 **Upper panels:** Sky map (*left*) of the ^{13}CO(3–2) integrated intensity. The black arrow shows the position of the hot spot in ^{12}CO(6–5) (Dutrey et al., 2014) and ^{12}CO(3–2) (Tang et al., 2016). Radial dependence (*middle*) of the integrated intensity azimuthally averaged in the disk plane. The red line is a fit using the same three Gaussians as in Tang et al. (2016). Azimuthal dependence (*right*) of the integrated intensity averaged across the disk ($0.54'' < r < 2''$). The red line shows the mean intensity. **Lower panels:** Sky map of the mean Doppler velocity (weighted by brightness) (*left*). Azimuthal dependence of mean line Doppler velocity weighted by brightness (*middle*). Dependence on r of $\langle V_{rot} \times r^{1/2} \rangle$ (brightness-weighted average); the lines are the best power law fits with indices -0.63 for $|\sin\omega| > 0.3$ (red) and -0.48 for $|\sin\omega| > 0.707$ (blue) (*right*). vii

3 *Upper panels:* Radial dependence of the integrated brightness temperature (for line emissions) and brightness temperature (for continuum emission) in the disk plane. The grey bands show the dust ring. The horizontal sticks indicate the angular resolutions. *Lower panels:* Azimuthal dependence of the brightness temperatures integrated over the ring $1.2'' < r < 2.0''$. The left panels are for the three ^{12}CO emissions (J=6–5, 3–2 and 2–1), with CO(2–1) data taken from Dutrey et al. (2014), the right panels show the less abundant CO isotopologues (J=3–2) emissions and the continuum. Black arrows show the location of the limb brightening peaks. The magenta vertical lines show the "hot spot" location. viii

4 *Left:* Radial dependence of CO gas (red) and dust (black) temperatures. The gas temperature is derived from the ^{12}CO(3–2) analysis. Beyond 400 au, the CO temperature is extrapolated from the fit obtained between 300 au and 400 au. The dust temperature is taken from Dutrey et al. (2014) and extrapolated beyond a radius of 285 au. *Right:* Radial dependence of the surface densities obtained from LTE analyses of ^{13}CO(3–2) (black) and C^{18}O(3–2) (red). ix

5 **Left:** Dependence of $\langle V_z \rangle$ (km s^{-1}) on azimuth ω (°) inside the cavity. ^{12}CO (3–2) is in black, ^{13}CO (3–2) in red and C^{18}O (3–2) in blue. The red curve is a sine fit to the ^{13}CO (3–2) data (see text). C^{18}O (3–2) data of significant intensity are only present in the bin $1.0'' < r < 1.25''$. The magenta curves show the Keplerian velocity expected around a single star of 1.36 M$_\odot$. The green curve in panel (f) shows the best fit velocity curve when infall motion is allowed. **Right:** Position-velocity diagrams of the ^{13}CO(3–2) emission inside the cavity along the major axis (upper panel) and minor axis (lower panel). The black curves show the Keplerian velocity expected around a single star of 1.36 M$_\odot$. Contour levels are spaced by 10 mJy/beam, with the zero contour omitted. The white lines indicate the position of the inner edge of the dust ring (180 au) and the black ones that of the inner radius of the gas disk (169 au). x

6 Integrated intensity of ^{12}CO(3–2) *(left)* and ^{12}CO(6–5) *(right)* and blobs location. Each blob covers an area of one beam, except for B6 which covers half of it. The color scales are in units of (K km s^{-1}). The crosses mark the position of Aa and Ab1+Ab2, and the ellipse shows the inner edge of the dust ring (180 au). xi

7 *Upper panels:* Integrated intensity maps. The color scales are in units of (Jy beam^{-1} km s^{-1}). The contour level step is 2σ. *Lower panels:* Mean velocity maps. The contour level step is 0.5 km s^{-1}. Beam sizes are indicated. The ellipses show the locations of the inner ($\sim$180 au) and outer ($\sim$260 au) edges of the dust ring. xi

8 Schematics of the global properties of the GG Tau A system. xii

9 **Upper panel:** CN(2–1) peak brightness image (colour) overlaid on the CO(2–1) peak brightness in contour. **Lower panel:** CS(5–4) peak brightness image (colour) overlaid on the CO(2–1) peak brightness in contour. xiii

10 Phát xạ liên tục của vành bụi. *Từ trái sang phải và từ trên xuống dưới:* Bản đồ cường độ phát xạ, hình elip màu đen là đường khớp hàm tốt nhất giá trị trung bình của khoảng cách đến tâm sao trên mặt phẳng bầu trời $\langle R \rangle$ theo góc vị trí φ (hình dưới bên trái); mũi tên màu vàng chỉ vào vùng "điểm nóng" được quan sát bởi Dutrey et al. (2014) và Tang et al. (2016) với các phát xạ ^{12}CO(6–5) và ^{12}CO(3–2); sự phụ thuộc vào R của độ sáng tính trung bình theo φ, cùng với đường khớp hàm phù hợp nhất sử dụng hàm Gauss; sự phụ thuộc vào φ của $\langle R \rangle$ trong khoảng $1'' < R < 2''$ (đường màu đỏ là hàm khớp với hàm elip có độ nghiêng và sai lệch so với gốc toạ độ); sự phụ thuộc vào φ của độ sáng phát xạ liên tục của mặt phẳng đĩa tính trung bình trên R trong khoảng $1'' < R < 2''$. Đường màu đỏ hiển thị giá trị độ sáng trung bình phát xạ liên tục trên đĩa. xv

11 **Hình trên:** Bản đồ bầu trời của độ sáng tích phân theo vận tốc của phát xạ ^{13}CO(3–2). Mũi tên đen chỉ vào vị trí "điểm nóng" (*trái*). Sự phụ thuộc vào khoảng cách tới tâm của độ sánh tích phân, tính trung bình trên toàn mặt phẳng đĩa. Đường màu đỏ là đường khớp hàm với tổng 3 hàm Gauss giống như trong Tang et al. (2016) (*giữa*). Sự phụ thuộc theo góc phương vị của độ sáng tích phân, tính trung bình theo bán kính trên đĩa ($0,54'' < r < 2''$). Đường màu đỏ hiển thị cường độ trung bình (*phải*). **Hình dưới:** Bản đồ bầu trời của vận tốc Doppler trung bình trọng số theo độ sáng (*trái*). Sự phụ thuộc theo góc phương vị của vận tốc Doppler trung bình trọng số theo độ sáng (*giữa*). Phụ thuộc vào khoảng cách đến tâm của $\langle V_{rot} \times r^{1/2} \rangle$; các đường thẳng là đường khớp với tuyến tính bậc 1 cho chỉ số $-0,63$ (đường màu đỏ, khi giới hạn điều kiện $|\sin\omega| > 0,3$) và $-0,48$ (đường màu xanh, khi giới hạn điều kiện $|\sin\omega| > 0,707$) (*phải*). xvi

12 *Hình trên:* Sự phụ thuộc vào khoảng cách tới tâm của độ sáng tích phân theo vận tốc (vạch phát xạ quay của phân tử) và độ sáng (phát xạ liên tục từ bụi) trong mặt phẳng đĩa. Các đoạn thẳng nằm ngang trong hình chỉ ra độ phân giải không gian tương ứng. *Hình dưới:* Sự phụ thuộc theo góc phương vị của đại lượng tương ứng, tính trung bình trong vành $1,2'' < r < 2.0''$. Các hình bên trái là biểu đồ của ba vạch của ^{12}CO (J=6–5, 3–2 và 2–1), với dữ liệu CO(2–1) được lấy từ Dutrey et al. (2014), các hình bên phải là biểu đồ của vạch phát xạ J=3–2 của các đồng phân ít phổ biến hơn. Trong các hình phía trên, vùng màu xám đánh dấu vành bụi. Trong các hình phía dưới, mũi tên màu đen chỉ vị trí xảy ra hiệu ứng tăng cường sáng (*limb brightening*), các đường màu tím giới hạn vị trí "điểm nóng". xvii

13 *Hình trái:* Sự phụ thuộc vào khoảng cách tới tâm của nhiệt độ khí CO (màu đỏ) và bụi (màu đen). Nhiệt độ khí được lấy từ kết quả phân tích vạch phát xạ ^{12}CO(3–2). Nhiệt độ bụi được lấy từ Dutrey et al. (2014). *Hình phải:* Sự phụ thuộc vào khoảng cách tới tâm của mật độ bề mặt của ^{13}CO(–2), C^{18}O(3–2) xviii

14 **Hình trái:** Sự phụ thuộc của $\langle V_z \rangle$ ($\mathrm{km\,s^{-1}}$) vào góc phương vị ω (°) trong khoang rỗng. Phát xạ ^{12}CO (3–2) được biểu diễn bởi đường màu đen, ^{13}CO (3–2) màu đỏ và C^{18}O (3–2) màu xanh lam. Đường cong màu đỏ biểu diễn đường khớp hàm của phát xạ ^{13}CO (3–2) với hàm sin. Các đường cong màu tía biểu diễn đường chuyển động Kepler cho một sao đơn có khối lượng 1,36 $M_\odot$. Đường cong màu xanh lá cây trong bảng (f) biểu diễn hàm khớp với sự đóng góp của thành phần vận tốc rơi so sánh với hàm khớp chỉ bao gồm thành phần chuyển động quay, hai đường khớp được vẽ chồng lên số liệu của phát xạ ^{13}CO. **Hình phải:** Sơ đồ Vận tốc–Vị trí của phát xạ ^{13}CO(3–2) trong khoang rỗng dọc theo bán trục lớn (hình trên) và bán trục nhỏ (hình dưới). Các đường cong màu đen biểu diễn đường chuyển động Kepler quanh ngôi sao đơn có khối lượng 1,36 $M_\odot$. Các đường đồng mức tương ứng với giá trị 10 $\mathrm{mJy\,beam^{-1}}$. Các đường thẳng màu trắng chỉ vị trí bán kính trong của vành bụi (180 au) và các đường thẳng màu đen chỉ bán kính trong của đĩa khí (169 au). Lưu ý rằng dữ liệu đã được được xoay 7° để bán trục nhỏ của đĩa hướng đến phía bắc. . . . xix

15 Bản đồ độ sáng tích phân theo vận tốc của ^{12}CO(3–2) *(trái)* và ^{12}CO(6–5) *(phải)* và vị trí của các vùng sáng. Mỗi vùng sáng bao phủ một diện tích beam, ngoại trừ vùng 6 chỉ bao phủ $\sim$ 50% diện tích beam. Giá trị bảng màu được thể hiện trên mỗi hình và có đơn vị là $\mathrm{K\,km\,s^{-1}}$. . xx

16 *Trên:* Bản đồ cường độ phát xạ. Thang màu được biểu diễn trong đơn vị $\mathrm{Jy\,beam^{-1}\,km\,s^{-1}}$. Mỗi đường đồng mức tương ứng với 2σ. *Dưới:* Bản đồ vận tốc. Mỗi đường đồng mức tương ứng với 0.5 $\mathrm{km\,s^{-1}}$. Kích thước beam được chỉ ra ở góc dưới của mỗi hình. Các đường e-lip biểu diễn vị trí của bán kính trong ($\sim$180 au) và bán kính ngoài ($\sim$260 au) của vành bụi. xx

17 Tính chất tổng quát của hệ sao GG Tau A. xxi

18 **Trên:** Bản đồ độ sáng đỉnh phát xạ của CN(2–1) (màu) chồng lên bản đồ của CO(2–1) (biểu diễn bởi các đường đồng mức). **Dưới:** Bản đồ độ sáng đỉnh phát xạ của CS(5–4) (màu) chồng lên bản đồ của CO(2–1) (các đường đồng mức). xxii

19 Emission continue de l'anneau de poussières. *De gauche à droite et de haut en bas:* la carte du ciel, l'ellipse noire correspond à $\langle R \rangle$ (valeur moyenne de R) indiquée dans le panneau inférieur gauche; la flèche jaune indique la région du point chaud (''hot spot'') observée par Dutrey et al. (2014) et Tang et al. (2016) en ^{12}CO(6-5) et ^{12}CO(3-2); la dépendance en R de la brillance moyennée sur φ, avec le meilleur ajustement gaussien au pic; la dépendance en φ de $\langle R \rangle$ est calculée dans l'intervalle $1'' < R < 2''$ (la courbe rouge correspond le mieux à l'anneau elliptique incliné et décalé par rapport à l'origine); et la dépendance en φ de la brillance du continuum moyenné sur R dans l'intervalle $1'' < R < 2''$. La ligne rouge indique la valeur moyenne de la brillance du continuum. xxv

20 **Haut:** Carte du ciel de l'intensité intégrée de le émission de la transition ^{13}CO(3–2). La flèche noire indique la position du point chaud en ^{12}CO(6–5) (Dutrey et al., 2014) et ^{12}CO(3–2) (Tang et al., 2016) (*gauche*). Dépendance en r de l'intensité intégrée moyennée de manière azimutale dans le plan du disque. La ligne rouge est un ajustement utilisant les mêmes trois Gaussiennes que dans Tang et al. (2016) (*milieu*). Dépendance azimutale de l'intensité intégrée moyennée sur le disque ($0.54'' < r < 2''$). La ligne rouge indique l'intensité moyenne (*droite*). **Bas:** Carte du ciel indiquant la vitesse Doppler moyenne (pondérée par l'intensité) (*gauche*). Dépendance azimutale de la vitesse Doppler moyenne pondérée par l'intensité (*milieu*). Dépendance de $\langle V_{rot}\, r^{1/2} \rangle$ en fonction de r (moyenne pondérée par l'intensité); les lignes sont la meilleure loi de puissance, elle correspond aux indices -0.63 pour $|\sin\omega| > 0.3$ (rouge) et -0.48 pour $|\sin\omega| > 0.707$ (bleu) (*right*.) . . . xxvi

21 *Haut:* Dépendance radiale de la brillance de température intégrée. Les barres horizontales indiquent la résolution. *Bas:* Dépendance azimutale de la brillance de température intégrée sur l'anneau $1.2'' < r < 2.0''$. Les panneaux de gauche montrent les trois émissions de ^{12}CO (J = 6–5, 3–2 et 2–1), avec les données de CO (2–1) extraites de Dutrey et al. (2014), les panneaux du milieu montrent les émissions des isotopologues de CO moins abondants (J = 3–2) et les panneaux de droite montrent les transitions CS (7–6) et CS (3–2) et le continuum. Les flèches noires indiquent l'emplacement des pics le long du grand axe du disque. Les lignes verticales magenta dans les panneaux supérieurs indiquent le bord intérieur de l'anneau de poussières, dans les panneaux inférieurs, elles montrent l'emplacement du point chaud. xxvii

22 *Gauche:* Dépendance radiale de la température du gaz (CO) en rouge et des poussières en noir. La température du gaz est dérivée de l'analyse ^{12}CO (3 − 2). La température des poussières provient de Dutrey et al. (2014). *Droite:* Dépendance radiale des densités de surface dérivées de ^{13}CO, C^{18}O (J=3 − 2) et de CS (J=7 − 6(et (J=3 − 2). La densité de surface de CS présentée est obtenue en prenant la température déduite de la poussière. xxviii

23 **Gauche:** Dépendance de $\langle V_z \rangle$ (km s^{-1}) en fonction de l'azimut ω (°) dans la cavité. ^{12}CO(3 − 2) est en noir, ^{13}CO(3 − 2) en rouge et C^{18}O(3 − 2) en bleu. La courbe rouge est un ajustement des données ^{13}CO(3 − 2) par une fonction sinus. Nous utilisons un blanc s'il n'y a pas de bonnes données disponibles (bruit) dans le disque. La courbe magenta montre la courbe Keplerienne attendue pour une étoile centrale de 1.36 M$_\odot$. **Droite:** Diagrammes position-vitesse de l'émission ^{13}CO(3–2) dans la cavité le long de l'axe principal (panneau supérieur) et de l'axe secondaire (panneau inférieur). La courbe noire montre la vitesse keplerienne attendue autour d'une étoile de 1.36 M$_\odot$. xxix

24 Intensité intégrée de ^{12}CO(3 − 2) *(gauche)* et ^{12}CO(6 − 5) *(droite)*. Chaque "blob" couvre un lobe interférométrique à l'exception de B6, qui ne couvre que ∼ 50% d'un lobe. xxx

25 *Haut:* Cartes d'intensité intégrée. L'échelle de couleurs est dans l'unité de (Jy beam^{-1} km s^{-1}). Les contours sont à 2σ. *Bas:* Cartes des gradients de vitesse. Les contours sont par pas de 0,5 km s^{-1}. Les tailles des lobes sont indiquées. Les ellipses indiquent les rayons intérieur (∼180 au) et extérieur (∼260 au) de l'anneau de poussières. xxxi

26 Un schéma de l'ensemble GG Tau A. Les propriétés globales sont présentées. xxxii

27 **Haut:** Superposition des cartes de brillance de CN(2–1) en couleur et de CO(2–1) en contour. **Bas:** Superposition des cartes de brillance de CS(5-4) en couleur et de CO(2–1) en contour xxxiii

1.1 Schematic of the formation process of protoplanetary disks and of the corresponding Spectral Energy Distributions. The figure is adapted from Greene (2001) and Dauphas and Chaussidon (2011). 1

1.2 Schematic picture of the flared and layered structure of a protoplanetary disk. The left hand side of the picture shows the distribution and evolution of the dust. The right hand side shows the molecular distribution and the dominant chemical processes in each layer. The figure is taken from Henning and Semenov (2013). 3

1.3 **Upper panels:** Gas (*left*) and dust (*right*) density distributions in protoplanetary disks. **Lower panels:** Gas (*left*) and dust (*right*) temperature distributions in protoplanetary disk. The four distributions are the result of a model calculation. The Figure is adapted from Cleeves, Bergin, and Adams (2014). 3

1.4 Chemical composition of protoplanetary disks: tracers and instruments. The figure is taken from van Dishoeck (2014). 9

1.5 Submillimeter spectroscopy of molecular rotational lines in the chemically rich, nearby TW Hydra disk. These observations, made with the Submillimeter Array (SMA), are at a range of resolutions, shown in the lower left corner of each panel. (Williams and Cieza, 2011). 11

1.6 Intensity maps of 1.25 mm dust emission from protoplanetary disks observed in DSHARP (Andrews et al., 2018). 12

1.7 **Left:** Two-dimensional representation of the Roche potential of two stars with a mass ratio of 1 to 4 with its five Lagrangian points. The bold line represents the edge of the Roche lobe. Reproduced from Frank, King, and Raine (2002). **Middle & Right:** Hydrodynamical simulations of the binary systems Kepler 34 and Kepler 35 (Pierens and Nelson, 2013b). x and y are given in au, the density decreases from red to blue. 14

1.8 A schematic picture of a typical binary T Tauri system showing its components and associated gas and dust emissions. A possible planet in formation is shown opening a gap in the circumbinary disk (Dutrey et al., 2016). 15

1.9 **Upper left panel:** Intensity map of the 1.3 mm continuum emission and velocity maps of the ^{13}CO(2–1) line emission at $v = 5.55$ (blue contours), 6.30 (white contours) and 7.05 km s^{-1} (red contours) (Guilloteau, Dutrey, and Simon, 1999). **Upper right panel:** NIR image from scattered light emission obtained by Roddier et al. (1996). **Lower left panel:** The triple star system and the circumstellar warm dust, as observed by Di Folco et al. (2014). The spectra show silicate emission at 10 μm observed in Aa and Ab (Skemer et al., 2011). **Lower right panel:** Intensity map of CO(6–5) emission (green) superimposed on the map of dust emission at mm wavelength (yellow contours) and at NIR (white contours), and the emissions of H_2 at FUV (dark blue) and at NIR (red). The figures are from Dutrey et al. (2016). 17

1.10 Intensity map of CO(6–5) emission. The spectra shown in the two inserts display the CO(6–5) emission at the hot spot location (east) and onto Aa (Dutrey et al., 2016). 19

1.11 The H-band observations of GG Tau A. The number (1)–(6) indicate the remarkable features. The Figure is taken from Brauer et al. (2019) 20

1.12 **Left:** The dust mass density distribution of the GG Tau A model. **Right:** Polarized intensity map of GG Tau A simulated with circumstellar disks as described in the text. The figure is taken from Brauer et al. (2019). 21

1.13 An example of hydrodynamical simulation of the GG Tau A system. The simulation is for a system with a major axis of 62 au and eccentricity of $e = 0.3$ (Nelson and Marzari, 2016). 21

2.1 Two-element inteferometer. 24

2.2 Interferometric coordinate transformation in interferometer measurement. *Upper*: In image (l, m, v) plane, *Lower*: In a Fourier or (u, v) plane. 25

2.3 Schematic diagram of the **CLEAN** process 27

2.4 The ALMA Compact Array. 30

2.5 The NOrthern Extended Millimeter Array equipped with 10 antennas. 30

2.6 Time dependence of the water vapour level measured near each antenna during 2 blocks of observations on Sep 25th and 30th, 2016. The curves are polynomial fits to the means. 33

2.7 uv coverage of the ALMA observations of GG Tau A Cycle 3 observations. The red and black colours correspond to data that were observed on Sep 25th and 30th, 2016 (*left*). The corresponding dirty beam is shown in the (*right*) panel. 33

2.8 Continuum intensity map. The beam size is indicated at the lower left corner. The color scale is in units of Jy beam^{-1}. 35

2.9 Channel map of the unmasked regions (shown in red) of ^{13}CO(3–2) emission, where the SNR exceeds the applied threshold. 36

3.1 Brightness of the dust ring continuum emission. *Left*: sky map; the black ellipse is the fit to $\langle R \rangle$ shown in Figure 3.3; the yellow arrow points to the region of the hot spot observed by Dutrey et al. (2014) and Tang et al. (2016) in ^{12}CO(6–5) and ^{12}CO(3–2) emissions. *Middle and right*: projections on the x and y axes of the central source brightness integrated over y and x respectively. The lines show Gaussian best fits. 44

3.2 Continuum brightness of the dust ring emission projected on the x (left) and y (middle) axes and integrated over y and x respectively. The right panel shows its distribution as a function of R, averaged over φ, together with the Gaussian best fit to the peak. In all three panels pixels having $R' < 0.5''$ are excluded. 45

3.3 Continuum emission. *Left:* Dependence on φ of $< R >$ calculated in the interval $1'' < R < 2''$. The red line is the best fit to an elliptical tilted ring offset from the origin (see text). *Right:* Dependence on φ of the disk plane continuum brightness averaged over R in the interval $1'' < R < 2''$. The red line shows the mean value. 46

3.4 *Left:* Line brightness distribution (Jy beam^{-1}); the red curve is a Gaussian fit to the noise peak. *Right:* Doppler velocity spectrum weighted by brightness and integrated over $8'' \times 8''$ (blue); the red histogram is obtained from the original by symmetry about the origin. 47

3.5 *Left:* Sky map of the ^{13}CO$(3-2)$ integrated intensity. The black arrow shows the position of the hot spot in ^{12}CO$(6-5)$ (Dutrey et al., 2014) and ^{12}CO$(3-2)$ (Tang et al., 2016). *Right:* Sky map of the mean Doppler velocity (weighted by brightness) excluding the region contained in the scaled-down ellipse shown in the left panel. In both panels $R < 2.5''$ and the black ellipses are the best fit to the distribution of $< R >$ in the continuum data and its scaled-down version (by a factor 3). 47

3.6 Line emission. *Left* and *middle:* Continuum brightness (blue, arbitrary normalisation) and line integrated intensity (red) projected on the x (left) and y (middle) axes in the region of $r > 0.54''$. *Right:* r-dependence of the integrated intensity averaged azimuthally in the disk plane. The red line is a fit using the same three Gaussians as in Tang et al. (2016). 48

3.7 Line emission. *Left:* Mean value of R, $< R >$, weighted by the brightness across the disk over the interval $0.54 < r < 2$ arcsec. The red line is the result of the fit described in the text. *Middle:* Dependence on φ of the mean line Doppler velocity (brightness-weighted); the red line is the result of the fit described in the text. *Right:* Dependence on φ of the disk plane integrated intensity averaged across the disk ($0.54'' < r < 2''$). The red line shows the mean value. 49

3.8 Geometry. *Left*: in the (y, z) plane; *middle*: in the sky plane (x, y); *right*: in the disk plane (x, ζ) 49

3.9 Integrated intensity map in the sectors used for the study of the disk thickness. 51

3.10 Disk thickness. Dependence on r (upper panels) and on R (lower panels) of the line integrated intensity averaged in 60° wide angular sectors centred on the ellipse axes. In each case, the leftmost panel is for minor-axis sectors and the rightmost panel for major-axis sectors. The central values of ω (upper panels) and φ (lower panels) are indicated in the inserts for each sector. 52

3.11 ^{13}CO$(3-2)$ map in the disk plane of the difference between the integrated intensity and its value averaged over ω at the same r. The black circles show the maxima of the Gaussians describing the mean radial integrated intensity distribution, r=1.22″ and 1.87″ respectively. The red circle corresponds to the mean value of r in the dust map (1.62″). 53

3.12 Distributions on ω (left) and r (right) of the Doppler velocity respectively averaged over $0.8 < r < 3.2$ arcsec and over ω. In the left panel, the line shows the best fit result, of the form $-1.43 \sin\omega + 0.05 \cos\omega$ km s^{-1}. 54

3.13 *Left:* Dependence on r of $\langle V_{rot} \times r^{1/2} \rangle$ (brightness-weighted average); the lines are the best power law fits with indices -0.63 for $|\sin\omega| > 0.3$ (red) and -0.48 for $|\sin\omega| > 0.707$ (blue). *Middle:* Dependence on ω of $\langle V_{rot} \rangle$ (averaged in the interval $0.8'' < r < 2.5''$) calculated using the nominal origin of coordinates on the sky plane (black histogram) or by shifting the origin by $\pm 0.06''$ in either x or y (red and blue histograms). *Right:* De-projected map of $\langle V_{rot} \times r^{1/2} \rangle$ ($|\sin\omega| > 0.3$). . . 55

3.14 Dependence of the brightness on the difference dV_z between measured values of V_z their mean values in the pixel. Summing is over all pixels in the interval $0.8'' < r < 2.5''$. The curve is a Gaussian fit. . 56

3.15 *Left:* Dependence on ω of the integrated intensity for $1.3'' < r < 1.7''$ (blue), $1.7'' < r < 2.1''$ (red) and $2.1'' < r < 2.5''$ (black); *Middle:* dependence on ω of the value of $\langle V_z \rangle$ in each of the three r-intervals (black histograms); here, $\langle V_z \rangle$ has been divided by 1.46, 1.27 and 1.18 km s^{-1} respectively, making the three histograms nearly identical; the red curve is a sine wave. *Right:* dependence of σ_{vz} on ω, for each r-interval separately; in each r-ω bin, a Gaussian fit is performed to the peak of the V_z spectrum, giving a σ-value that averages to respectively 0.258, 0.210 and 0.181 km s^{-1}; the plotted histograms are normalized to these respective average values; in addition, for clarity, they are shifted up by respectively 0, 0.5 and 1. The red curve, a sixth degree polynomial fit to the distribution of the central r-interval, is shown to guide the eye. In the left and right panels the arrows point in the direction of increasing r and indicate remarkable features: the black arrow shows the hot spot as defined from the left panel, the blue and red arrows show peaks of the line width as defined from the right panel. 58

3.16 Correlation between the normalized relative fluctuations of the line width $\Delta\sigma$ and the integrated intensity Δf (see text). The line is the best fit to the data, $\Delta\sigma = 0.32\Delta f$. The blue points are for $105° < \omega < 165°$ (hot spot). 59

3.17 *Upper panel:* ^{13}CO(3–2) integrated intensity map (left, contour spacing of 0.01 Jy/beam km s^{-1} (3 σ) with zero level omitted) and velocity map (right). *Lower panel:* C^{18}O(3–2) integrated intensity map (left, contour spacing of 0.01 Jy/beam km s^{-1}, 2 σ) and velocity map (right). The beams are indicated in the lower left corner of each intensity map. The contour level spacing in velocity maps is 0.5 km s^{-1}. The continuum has been subtracted. The white ellipses indicate the inner and outer edges of the dust ring. 60

3.18 *Upper panels:* Radial dependence of the integrated brightness temperature in the disk plane. In the right panel, the continuum histogram shows the brightness temperature. The horizontal sticks indicate the angular resolutions. The grey bands delineate the dust ring. In the lower panels. *Lower:* The azimuthal dependence of the same quantities averaged over the ring $1.2'' < r < 2.0''$. The left panels display the three ^{12}CO emissions (J=6–5, 3–2 and 2–1), the latter being taken from Dutrey et al. (2014); the right panels show the less abundant CO isotopologues (J=3–2) emissions. Black arrows show the location of the limb brightening peaks and magenta lines show the "hot spot" location. 61

3.19 Distribution of the difference between the measurements of the mean Doppler velocity in a same pixel for ^{12}CO (3–2) vs ^{13}CO (3–2) (left) and for ^{12}CO (3–2) vs ^{12}CO (6–5) (right). 62

3.20 Dependence on r of $V_{rot} \times r^{1/2}$ (weighted by the brightness and averaged in r bins of 0.15″) of ^{12}CO(3–2) (black), ^{13}CO(3–2) (red) and C^{18}O(3–2) (blue) emissions. The horizontal bars indicate the radial range over which the mean value is calculated for each transition. The grey shaded area cover the dense dust ring. 63

3.21 Sky maps of intensities measured in the ring $1'' < r < 2''$ for ^{12}CO(3–2) (left), ^{13}CO(3–2) (middle) and ^{12}CO(6–5) (right). The lines show the eight regions used to draw Table 3.3. 64

3.22 Sky maps of the difference between the measured intensity and its azimuthal average at the same radius for each of ^{12}CO(3–2) (left), ^{13}CO(3–2) (middle) and ^{12}CO(6–5) (right). The circle $x^2 + y^2 = 1$ arcsec^2 is excluded. Stars locate the Dutrey et al. (2014) "hot spot". 65

3.23 Channel maps of ^{13}CO(3–2), Beam 0.22″ × 0.16″, PA=16°. The noise level is 2.4 mJy beam^{-1}. The colour scale is indicated in the upper right panel. The cross is centred on the centre of the map. 68

3.24 Channel maps of C^{18}O(3–2), Beam 0.19″ × 0.14″, PA=19°. The noise level is 4.8 mJy beam^{-1}. The colour scale is indicated in the upper right panel. The cross is centred on the centre of the map. 68

4.1 Integrated intensity of (residual) emissions after subtracting the best disk models. *Upper left panel:* ^{12}CO(3–2). The restoring beam of $0.34'' \times 0.28'', \mathrm{PA} = -89°$ is indicated in the lower left corner. *Upper right panel:* ^{13}CO(3–2). The restoring beam is $0.22'' \times 0.16'', \mathrm{PA} = 16°$. *Lower panel:* C^{18}O(3–2). The restoring beam is $0.19'' \times 0.14'', \mathrm{PA} = -167°$. The contour level is 5σ for ^{12}CO(3–2) map and 3σ for ^{13}CO(3–2), and C^{18}O(3–2) maps . The ellipses show the inner and outer edges of the dust ring at 180 au and 260 au. 72

4.2 Radial dependence of CO gas (red) and dust (black) temperature. The gas temperature is the best fit to the present data, extrapolated beyond 400 au using the power law found between 300 and 400 au. The dust temperature is from Dutrey et al. (2014) up to 300 au, extrapolated further out. 73

4.3 Comparison of the surface densities from the LTE analysis. 74

4.4 Dependence of $\langle V_z \rangle$ ($\mathrm{km\,s^{-1}}$) on azimuth ω (°) inside the cavity. ^{12}CO (3–2) is in black, ^{13}CO (3–2) in red and C^{18}O (3–2) in blue. The red curve is a fit of a sine function to the ^{13}CO (3–2) data (see text). C^{18}O (3–2) data of significant intensity are only present in the bin $1.0'' < r < 1.25''$. The magenta curves show the Keplerian velocity expected around a single star of 1.36 $\mathrm{M_\odot}$. The green curve in panel (f) shows the best fit velocity curve when infall motion is allowed. 77

4.5 Position-velocity diagrams of the ^{13}CO(3–2) emission in the cavity along the major axis *(left)* and minor axis *(right)*. The black curves show the expected Keplerian velocity around a single star of 1.36 $\mathrm{M_\odot}$. Contour levels are spaced by 10 mJy/beam, with the zero contour omitted. The white lines indicate the position of the dust ring inner edge (180 au) and the black lines that of the gas disk inner radius (169 au). 78

4.6 Integrated intensity map of ^{12}CO(3–2) *(left)* and ^{12}CO(6–5) *(right)* and blobs position and sizes. 78

4.7 From top to bottom, ^{12}CO, ^{13}CO and C^{18}O J=3–2 maps. *Left:* Integrated intensity map. *Middle:* Best ring model intensity map. *Right:* Emission inside cavity measured as the difference between observations and ring model. 86

4.8 χ^2 maps in the (n_{H2}, CD), (n_{H2}, T_{ex}) and (CD, T_{ex}) planes calculated for ^{12}CO J=6–5 and J=3–2 *(left)*, for ^{12}CO J=6–5 and J=3–2 and ^{13}CO J=3–2 *(right)*. Upper panels are for blob B1, central panels for B2 and lower panels for B3. 87

4.9 χ^2 maps in the (n_{H2}, CD), (n_{H2}, T_{ex}) and (CD, T_{ex}) planes calculated for ^{12}CO J=6–5 and J=3–2 *(left)*, for ^{12}CO J=6–5 and J=3–2 and ^{13}CO J=3–2 *(right)*. Upper panels are for blob B4, central panels for B5 and lower panels for B6. 88

5.1 **Upper panels:** Integrated intensity map of H_2S 1(1,0)–1(0,1) (*left*) and $H^{13}CO^+$(2–1) (*right*) emissions. The colour scale at the top is in units of Jy beam^{-1} km s^{-1}, the contour levels step is 2σ. **Lower panels:** Velocity map of H_2S 1(1,0)–1(0,1) (*left*) and $H^{13}CO^+$(2–1) (*right*) emissions. The colour scale at the top is in units of km s^{-1}, the contour levels step is 0.5 km s^{-1}. 90

5.2 **Upper panels:** Integrated intensity map of DCO^+(3–2) (*left*) and HCO^+(1–0) (*right*) emissions. The colour scale at the top is in units of Jy beam^{-1} km s^{-1}, the contour levels step is 2σ. **Lower panels:** Velocity map of DCO^+(3–2) (*left*) and HCO^+(1–0) (*right*) emissions. The colour scale at the top is in units of km s^{-1}, the contour levels step is 0.5 km s^{-1}. 91

5.3 Best model of H_2S, CS, DCO^+, and HCO^+ in the GG Tau A ring derived from Nautilus. The z/H ratio (which measures the scale height) is shown vs. surface density. 94

5.4 Best model of CCS, c-C_3H_2, HC_3N, SO, and SO_2 in the GG Tau A ring, derived from Nautilus, using our best knowledge of the GG Tau disk. The z/H ratio (which measures the scale height) is shown vs. surface density. 95

5.5 Channel maps of H_2S 1(1,0) - 1(0,1) emission. The colour scale is in units of Jy beam^{-1}. The contour spacing is 5 mJy beam^{-1} which corresponds to 1σ or 0.04 K. The beam (2.55″ × 1.90″, PA=14°) is shown in the lower corner of each channel map. 99

5.6 Channel maps of $H^{13}CO^+$ (2-1) emission. The colour scale is in units of Jy beam^{-1}. The contour spacing is 12 mJy beam^{-1} which corresponds to 2σ or 0.11 K. The beam (2.50″ × 1.85″, PA=15°) is shown in the lower conner of each channel map. 99

5.7 Channel maps of DCO^+ (3-2) emission. The colour scale is in units of Jy beam^{-1}. The contour spacing is 18 mJy beam^{-1} which corresponds to 2σ or 0.22 K. The beam (1.76″ × 1.23″, PA=17°) is shown in the lower conner of each channel map. 100

5.8 Channel maps of HCO^+ (1-0) emission. The colour scale is in units of Jy beam^{-1}. The contour spacing is 25 mJy beam^{-1} which corresponds to 2σ or 0.33 K. The beam (4.57″ × 2.55″, PA=−38°) is shown in the lower conner of each channel map. 100

6.1 Schematic summary of the observations and analyses of the GG Tau A system presented in the thesis. 102

6.2 Schematic summary of the gas properties inside the GG Tau A cavity. 103

6.3 CO(2–1) line emission. *Left:* Integrated intensity map (Jy beam^{-1} km s^{-1}). The contour level is 25 mJy beam^{-1} km s^{-1}, which is about eight times the rms noise level of $\sim$ 3 mJy beam^{-1} km s^{-1}. *Right:* Velocity map (km s^{-1}). The contour spacing is 0.5 km s^{-1}. The colour scales are shown on the top. 105

6.4 CO(2–1) line emission. Map of the peak brightness temperature (K). The colour scale is shown on the top and contour spacing is of 1.5 K . 105

6.5 CN(3–2) line emission. *Left:* Integrated intensity map (Jy beam^{-1} km s^{-1}). *Right:* Velocity map (km s^{-1}). 106

6.6 CN(2–1) line emission. *Left:* Integrated intensity map (Jy beam^{-1} km s^{-1}). The contour level is 5 mJy beam^{-1} km s^{-1}, about three times the rms noise level of $\sim$ 1.5 mJy beam^{-1} km s^{-1}. *Right:* Velocity map (km s^{-1}). The contour spacing is 0.5 km s^{-1}. Colour scales are shown on top. . 107

6.7 CN(2–1) line emission. Map of the peak brightness temperature (K). The colour scale is shown on top and the contour spacing is 1 K . . . 107

6.8 CS(5–4) line emission. *Left:* Integrated intensity map (Jy beam^{-1} km s^{-1}). The contour level is 5 mJy beam^{-1} km s^{-1}, about three times the rms noise level of $\sim$ 1.5 mJy beam^{-1} km s^{-1}. *Right:* Velocity map (km s^{-1}). The contour spacing is 0.5 km s^{-1}. Colour scales are shown on top. . 108

6.9 Peak brightness temperature (K) map of CS(5–4) emission. The colour scale is shown on top and the contour spacing is 1 K 108

6.10 *Upper panel:* Map of the CN(2–1) peak brightness temperature (colour) overlaid over that of CO(2–1) shown as contours. *Lower panel:* Map of the CS(5–4) peak brightness temperature (colour) overlaid over that of CO(2–1) shown as contours 110

List of Tables

1.1 Main characteristics of GG Tau 16

2.1 ALMA and NOEMA observations of GG Tau A. 37

3.3 *rms* values ($\mathrm{km\,s^{-1}}$) of the line widths measured in each of 8 regions depicted in Figure 3.21. 65

3.4 Line properties in the hot spot ellipse and its symmetric with respect to the origin of coordinates (GG Tau A) 65

4.1 System geometric and kinematic parameters 70

4.2 Dust ring parameters 70

4.3 Temperature of ^{12}CO(3–2) and surface density of ^{13}CO(3–2) and C^{18}O(3–2) - nominal model after CLEANed component removal at $r < 160$ au. 74

4.4 Infall and rotation velocity of the gas inside the cavity. 76

4.5 Blob positions with maximum brightness temperatures and their corresponding velocities for CO transitions. 79

4.6 Brighter blobs properties 80

4.7 Mass of gas inside the cavity 81

5.1 GG Tau A parameters 92

5.2 Observed and predicted surface densities of detected molecules ($\mathrm{cm^{-2}}$) 93

5.3 Observed and predicted surface densities of non-detected molecules ($\mathrm{cm^{-2}}$) 93

5.4 Molecular abundance relative to ^{13}CO ($X_{[mol]}/X_{[^{13}CO]} \times 10^5$) 96

Chapter 1

Introduction

1.1 Overview

Stars form from small fractions of the dust and gas contained in relatively dense and cool molecular clouds. Once a protostar core has condensed, a disk forms around it as a consequence of angular momentum conservation. In the early phase of star formation, the disk rapidly funnels material onto the central protostar, but as the surrounding molecular gas gets depleted, the accretion rate decreases and a small quantity of material remains in the disk that will live a few million years, allowing planets to form (hence the name "protoplanetary" disks).

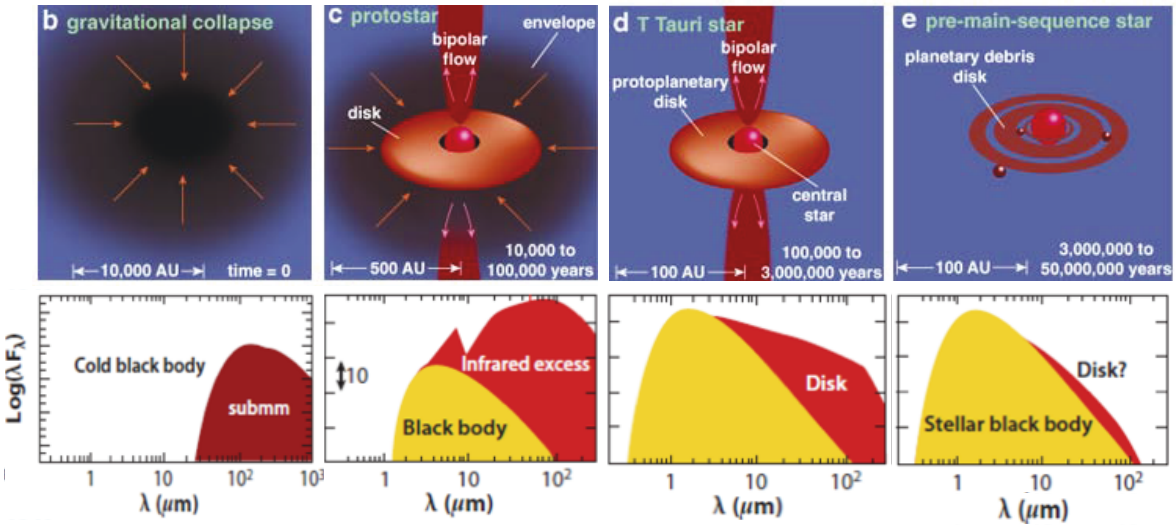

FIGURE 1.1: Schematic of the formation process of protoplanetary disks and of the corresponding Spectral Energy Distributions. The figure is adapted from Greene (2001) and Dauphas and Chaussidon (2011).

Young Stellar Objects (YSOs) cover a broad range of temperatures, hot in the central protostar and cold in the outer disk; they radiate over a wide range of wavelengths, from microns to millimetres: they can be observed with infrared and radio telescopes. Depending on the value of the slope of the Spectral Energy Distribution (SED) α_{IR} between about 2 and 25μm, one distinguishes between four classes of

YSOs: 0, I, II and III (Lada and Wilking, 1984; Lada, 1987; Andre, Ward-Thompson, and Barsony, 1993). Figure 1.1 summarises the main properties of YSOs, the evolution of their morpho-kinematics and of the SED. Of course, YSOs cannot be uniquely defined by their SED class: in particular, Robitaille et al. (2006) have shown that a face-on Class II YSO has a similar SED as an average Class I object, while an edge-on Class I YSO may have the same characteristics as a Class 0 one. The reason is that YSOs with highly inclined disks are strongly obscured and can be misinterpreted as more embedded and hence, less evolved objects. Therefore, it is essential to observe and resolve a YSO at multiple wavelengths in order to fully characterize its evolutionary stage.

Studies of exo-planets have shown that planets cover a broad range of both orbit parameters and chemical composition. These are related to the properties of the protoplanetary disks from which they are born. Therefore, the study of the gas and dust properties of protoplanetary disks reveals the mechanisms governing the formation of planets and the features that they display. Moreover, recent exo-planet surveys carried out with the Kepler Space Telescope reveal that planets can form and survive in binary systems, whether in circumbinary or circumstellar orbits (Welsh et al., 2012). The formation conditions in these systems differ from those around single stars. Theoretical studies of disk evolution predict that a T Tauri binary, at an age of about 1 Myr, should be surrounded by two inner disks, located inside the Roche lobes and an outer ring or disk located outside the outer Lindblad resonances (Artymowicz et al., 1991). For a binary system of low or moderate eccentricity, the stable zone is typically located beyond the 3:1 or 4:1 resonances (Artymowicz and Lubow, 1994). The outer radii of these inner disks, as well as the inner radius of the circumbinary (outer) disk, are defined by tidal truncation.

1.2 The disk structure

Forming from molecular clouds, protoplanetary disks are made up of 99% gas and 1% dust. H_2 is the most abundant species, followed by He and trace molecules such as CO, CS, ... (e.g. $X(CO/H_2)=8 \times 10^{-4}$, $X(CS/H_2)=1 \times 10^{-8}$, Ohishi, Irvine, and Kaifu, 1992). Inside disks, the temperature is governed by dust, which is directly heated by radiation from the central star and accretion shocks (matter falling down from the inner disk onto the star, see Figure 1.2).

Studies of protoplanetary disks show that they are flared and display important vertical and radial density and temperature gradients. The external layer is directly illuminated by the stellar UV radiation and dominated by photo-dissociation reactions, while molecules stick to dust grains in the cold internal mid-plane. Figure 1.2 shows a schematic of a flared and layered disk and Figure 1.3 shows the distribution of gas and dust density and temperature within such a disk.

The following descriptions of the structure of a protoplanetary disk (density and temperature profiles) are mostly taken and summarized from Armitage and Valencia (2010), I will only cite specific articles when needed.

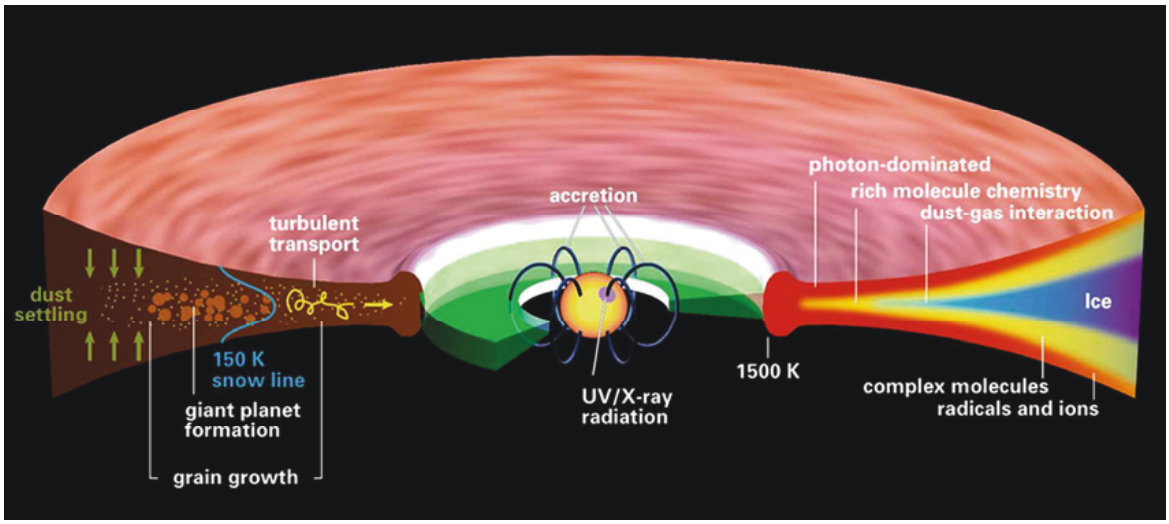

FIGURE 1.2: Schematic picture of the flared and layered structure of a protoplanetary disk. The left hand side of the picture shows the distribution and evolution of the dust. The right hand side shows the molecular distribution and the dominant chemical processes in each layer. The figure is taken from Henning and Semenov (2013).

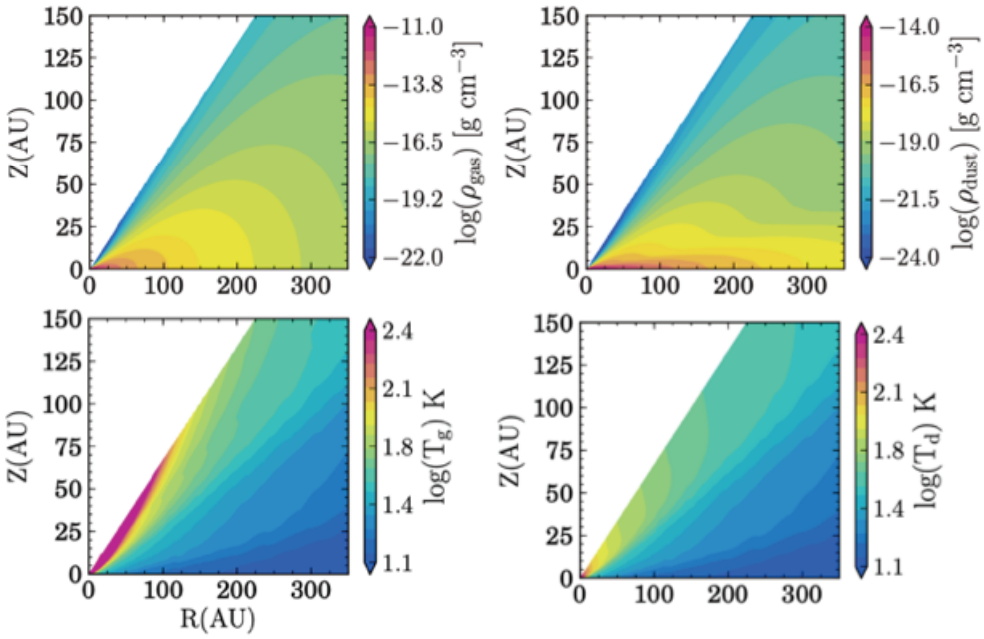

FIGURE 1.3: **Upper panels:** Gas (*left*) and dust (*right*) density distributions in protoplanetary disks. **Lower panels:** Gas (*left*) and dust (*right*) temperature distributions in protoplanetary disk. The four distributions are the result of a model calculation. The Figure is adapted from Cleeves, Bergin, and Adams (2014).

1.2.1 Density profile

Vertical structure

As a first good approximation a disk can be modelled as an optically thick disk heated by stellar radiation and supported by gas pressure in hydrostatic equilibrium. One can then approximate the optically thick interior of the disk as isothermal, with sound velocity c_s and pressure $P = \rho\, c_s^2$. The sound velocity is related to temperature via $c_s^2 = k_B T/\mu m_H$, where k_B is Boltzmann's constant, m_H the mass of a hydrogen atom.

In cylindrical coordinates, the condition for vertical hydrostatic equilibrium is,

$$\frac{dP}{dz} = -\rho\, g_z = -\frac{GM_\star}{r^2+z^2}\sin\theta \times \rho \tag{1.1}$$

where $M_\star$ is the stellar mass, and $\sin\theta = z/r$. For $z \ll r$,

$$g_z = \frac{GM_\star z}{r^3} \simeq \Omega^2 z \tag{1.2}$$

where $\Omega = \sqrt{GM_\star/r^3}$ is the Keplerian orbital velocity at the midplane, then:

$$c_s^2 \frac{d\rho}{dz} = -\Omega^2 \rho z \tag{1.3}$$

which integrates to give,

$$\rho(z) = \rho_0 \exp[-z^2/2h^2] \tag{1.4}$$

where ρ_0 is the density at mid-plane and $h = c_s/\Omega_K$ is the vertical scale height of the disk.

Defining the surface density as $\Sigma = \int \rho\, dz$, the central density is,

$$\rho_0 = \frac{1}{\sqrt{2\pi}}\frac{\Sigma}{h} \tag{1.5}$$

The above equations define the vertical structure of the simplest disk model (isothermal, with Gaussian density profile). If the temperature is not uniform, the density departs from a Gaussian profile. If the disk is accreting, the gravitational potential energy, which is thermalized in the optically thick interior, requires a vertical temperature gradient $dT/dz < 0$ in order to be transported to the disk photosphere and radiated out. Integration of Equation 1.1 gives

$$\rho = \rho_0 \exp[\frac{r^2}{h^2}((1+z^2/r^2)^{-1/2} - 1)] \tag{1.6}$$

When h/r does not exceed ~ 0.05, protoplanetary disks are geometrically thin and the density profile is Gaussian to a very good approximation. It is only when

disk winds extend beyond $z \sim r$, and when the disk is massive, $M_{disk}/M_\star > 0.5\,h/r$, that the effect of the vertical gravity gradient needs to be taken into account.

Radial structure

In the radial direction, the gravitational attraction by the star is counteracted by the pressure force (in the case of the gas) and by the centrifugal force; the combined hydrostatic and centrifugal equilibrium equation reads

$$\frac{v^2}{r} = \frac{GM_\star}{r^2} + \frac{1}{\rho}\frac{\partial p}{\partial r} \tag{1.7}$$

As the pressure decreases outward, $\partial p/\partial r < 0$, implying $v < v_{Kepler}$. In disks, the gas is moving around the central protostar slower than the dust and planets, a result of the contribution of the pressure term. The gradient is small and can be approximated by:

$$\begin{aligned} \frac{v^2}{r} \approx \Omega^2 r - c_s^2/r = \Omega^2 r(\,1 - \frac{c_s^2}{\Omega^2 r^2}\,) = \Omega^2 r(\,1 - \frac{h^2}{r^2}\,) \\ v = v_{Kepler}\sqrt{1 - \frac{h^2}{r^2}} \end{aligned} \tag{1.8}$$

The deviation from strict Keplerian rotation, $v_{Kepler} = \sqrt{GM_\star/r}$ is of the order of $(h/r)^2$ and its value is small. For a disk having $h/r = 0.03$ at 1 au,the velocity differs from Keplerian by only 0.25% (Armitage and Valencia, 2010).

Dust particles grow inside the disks, and large particles dynamically decouple from the gas and move toward the mid-plane. As a consequence, we have larger particles near the mid-plane and smaller particles further out vertically. Contrary to gas molecules, they are not affected by the radial pressure gradient that causes the mismatch in velocity: as a result, they develop a differential velocity with respect to the gas that causes aerodynamic drag. Assuming an axisymmetric vertically isothermal disk supported against gravity by gas pressure, the vertical density profile of the disk in equilibrium can then be written as:

$$r\Omega_{g(r,z)}^2 = \frac{GM_\star}{(r^2+z^2)^{3/2}}z + \frac{1}{\rho}\frac{\partial p}{\partial r} \tag{1.9}$$

where $\Omega_{g(r,z)}$ is the gas angular velocity.

A disk is often characterized by the values of the power indices p and q describing the radial profiles of the surface density and of the temperature, $\Sigma \propto r^{-p}$ and $T \propto r^{-q}$. The angular velocity of the gas at equilibrium is approximated by:

$$r\Omega^2_{g(r,z)} \approx \Omega_{K,mid}[1 - \frac{1h^2}{4r^2}(q + 2p + 3 + q\frac{h^2}{r^2})] \tag{1.10}$$

where $\Omega_{K,mid}$ is the mid-plane Keplerian value; the vertical dependence of the Keplerian velocity reads

$$\Omega_K \approx \Omega_{K,mid}(1 - \frac{3}{4}\frac{z^2}{r^2}) \tag{1.11}$$

The deviation from Keplerian rotation in this case becomes,

$$\Omega_g - \Omega_K \approx -\frac{1h^2}{4r^2}(q + 2p + 3 + q\frac{h^2}{r^2})\Omega_{K,mid} \tag{1.12}$$

The Keplerian velocity depends on the enclosed disk mass M_{disk} as

$$v'_K \approx v_K(1 + \frac{M_{disk}}{M_\star})^{1/2} \tag{1.13}$$

1.2.2 Temperature profile

We consider here the case where the dust opacity is high enough for the disk to be optically thick to both stellar radiation and to its own re-emitted radiation, which displays therefore a thermal spectrum. It is then a pure geometry problem to determine how much stellar radiation each annulus of the disk intercepts, and what equilibrium temperature, T, is obtained.

We consider the temperatures of gas and dust on the surface layer of the disk. Surface layers being both optically thin and of low density, one needs to account explicitly for the heating and cooling processes and to allow for the possibility that dust and gas are too weakly coupled to maintain the same temperature.

A disk whose temperature is set by stellar irradiation is said to be "passive ". We write the radial dependence of the temperature of the blackbody disk emission as $F(r)$. Modelling the star as a sphere of radius R and constant brightness I, we use spherical coordinates centred on the star. The stellar flux passing through a sphere of radius r is,

$$F = \int I_\star \sin\theta \cos\phi d\Omega \tag{1.14}$$

where $d\Omega$ is the solid angle element. Solving the above equation for the flux coming from the upper half of the star, meaning $-\pi/2 < \phi < \pi/2$ and $0 < \theta < \sin^{-1}(R_\star/R)$ and substituting $d\Omega = sin\theta\, d\theta\, d\phi$ one obtains,

$$F = I_\star[\sin^{-1}(R_\star/r) - (R_\star/r)\sqrt{1 - (R_\star/r)^2}] \tag{1.15}$$

A star with effective temperature $T_\star$ has brightness $I_\star = (1/\pi)\sigma T_\star^4$, where σ is the Stefan-Boltzman constant. Setting F equal to the one-side disk emission $\sigma\, T_{disk}^4$ the temperature profile is given by,

$$\left(\frac{T_{disk}}{T_\star}\right)^4 = \frac{1}{\pi}[\sin^{-1}(R_\star/r) - (R_\star/r)\sqrt{1-(R_\star/r)^2}] \tag{1.16}$$

In the approximation where geometrically $(R_\star/r) \ll 1$, we obtain $T_{disk} \propto r^{-3/4}$ for the power-law temperature profile of a flat, thin and passive disk. This implies a radial dependence of the sound velocity of the form, $c_s \propto r^{-3/8}$, and a disk thickness $(h/r) \propto r^{1/8}$. We therefore predict that the disk becomes geometrically thicker ("flaring") at larger radii.

More detailed calculations of dust emission from passive disks require considerations of two additional physical effects: the effect of the disk thickness as measured by the gas scale height increasing to larger radii, and the effect of small dust grains that are directly exposed to stellar radiation emitting as dilute rather than true blackbodies, with a higher temperature. An illustrative analytic model that incorporates these effects was developed by Chiang and Goldreich (1997) by considering a disk with surface density $\Sigma = 10^3(r/1\,\mathrm{au})^{-3/2}\,\mathrm{g\,cm^{-2}}$ around a star having $M_\star = 0.5\,M_\odot$, $T = 4000\,\mathrm{K}$, and $R_\star = 2.5\,R_\odot$. Within about 100 au, their solution reproduces only half of the bolometric luminosity of the disk emitted as a blackbody at the temperature $T \approx 150(r/1\,\mathrm{au})^{-3/7}\,\mathrm{K}$. This solution uses a two-layer approximation to dust continuum radiative transfer for a passive, hydrostatic disk. The full radiative transfer solution requires numerical treatment.

1.3 Planet formation in protoplanetary disks

1.3.1 The formation of planets

The first step toward planet formation is the growth of interstellar dust particles into larger aggregates and eventually planetesimals. Dust grains are thought to grow from sub-μm sizes to μm size particles in the dense regions of molecular clouds and cores, but the growth from micron size particles to pebbles and kilometre size bodies must occur in the high densities reached in the mid-planes of protoplanetary disks.

The evolution of solids inside a circumstellar disk is governed by transport and collisional processes, which are strongly related. Transport processes typically depend on particle size, hence on the collisional evolution of the particles, while in turn, collisions between particles are driven by dynamics.

Interstellar dust particles of size $0.1 - 1\mu m$ are in Brownian motion and feel the friction with the gas inside protoplanetary disks. The smaller dust particles, when colliding at the proper velocity, stick together and grow in size: dust grains of sizes

smaller than $10\mu m$ interact with each other, stick together and grow. Larger grains, of sizes $100 - 800\mu m$, when colliding with smaller grains, bounce away if the latter is larger than 10μm. Two equal-size particles larger than 1 mm generally fragment when they collide but may also experience various types of interaction with some of the final products being larger than the original particles. In particular, owing to mass-transfer, a meter-size rock can grow in collisions if the partner is smaller than 200μm. Windmark et al. (2012) state that the key to growing large bodies is therefore to sweep through smaller particles faster than one can get eroded or fragmented.

In protoplanetary disks, the snow-line defines the distance from the central star beyond which ices of molecular compounds condense while metals stay in the gas phase. The snow-line marks the transition between the inner warmer regions where terrestrial rocky planets can form to the cooler outer region where Jovian gaseous planets can form.

1.3.2 Interaction between the planets and disks

When a planet forms inside a protoplanetary disk, its gravitational field exerts a tidal torque on the gas and dust in the disk. This allows for angular momentum transfer between planet and disk and results in the migration of the planet. The density wave launched by the planet modifies the density of the disk and may open a gap in the disk surface density. Its radius, width and level of gas/dust depletion carry information about the planet properties. Viscosity affects both the width and the depth of the gap. Numerical simulations show that the width of the gap depends on the planet mass M_p and the orbital radius R_p (Crida and Morbidelli, 2007) as:

$$W \sim C \times R_p \times \left(\frac{M_p}{3M_\star}\right)^{1/3} \tag{1.17}$$

1.4 Gas composition of protoplanetary disks

To simplify, the chemistry of protoplanetary disks can be divided into two regions, the inner (warm) and outer (cold) disks. The transition is defined by the snow-line location (see Section 1.3). Two important snow-line locations are defined by H_2O (~ 100 K) or CO (~ 20 K). The contents of the inner disk are best characterized by IR spectroscopy whereas the outer disk is the domain of (sub)mm observations.

Figure 1.4 shows a schematic view of a standard protoplanetary disk with various molecules tracing different regions of the disk. The left hand side of the figure shows the corresponding instruments suitable for such studies.

1.4.1 Gas in the inner disk

The inner region of protoplanetary disks (< 30 au)is resolved by IR observations but mostly limited to continuum emission and is unresolved in the (sub)mm domain for molecular line observations. Using VLTI long-baseline interferometer measurements, Kraus et al. (2009) detected the near-IR emission from a Herbig Ae star, resolving the circumstellar environment down to distances from the central star smaller than 1 au. Herschel observations of molecular lines such as H_2O, CO, [O I], OH, CH^+ and [C II] from T Tauri and Herbig Ae/Be disks are reported by several authors (Meeus et al., 2012; Riviere-Marichalar et al., 2012; Riviere-Marichalar et al., 2013; Fedele et al., 2012). Thermo-chemical models with a disk structure derived from continuum observations suggest that these lines probe internal as well as external disk layers (e.g. Woitke et al., 2010; Bruderer et al., 2012).

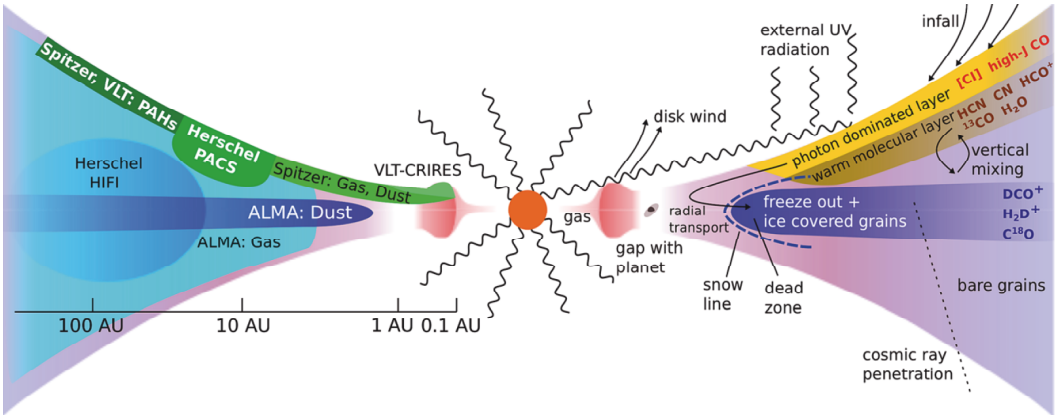

FIGURE 1.4: Chemical composition of protoplanetary disks: tracers and instruments. The figure is taken from van Dishoeck (2014).

1.4.2 Gas in the outer disk

Thanks to high sensitivity interferometer arrays such as ALMA and NOEMA, the gas content of nearby protoplanetary disks starts to be imaged. Recently, two major projects have studied the chemistry of protoplanetary disks: Chemistry In Disk (CID) using the IRAM 30-m telescope and NOEMA and DISCS using the Submillimeter Array (SMA). They have shown how different molecules trace different physical and chemical conditions. For example, ^{12}CO, the most abundant molecule after H_2, is a good tracer of temperature while its less abundant isotopologues, ^{13}CO, $C^{18}O$, $C^{17}O$, or other molecules such as CS, are good tracers of density, in particular when probing high density environments. HCO^+, N_2H^+ and CH^+ are used to study ionization; HD, DCO^+, DCN, H_2D^+ are used to trace deuterium; CN, HCN, HNC are good photochemistry tracers. The outer region of protoplanetary disks displays a flared and layered structure with important vertical and radial gradients of temperature and density.

Each layer of the outer disk hosts different chemical reactions in different physical conditions, resulting in different chemical compositions. The external layer, directly illuminated by stellar and interstellar radiation, is referred to as photon dominated region (PDRs) hosting PDR-like chemistry. In this layer, photochemistry is particularly important and depends on the strength and shape of the radiation field. T Tauri stars emit intense non-thermal UV radiation from the accretion shock, while the hotter Herbig Ae/Be stars produce larger amount of thermal UV radiation. For example, at a distance of about 100 au from the central star, a T Tauri star produces a total UV flux of $\sim 100 - 1000\, G_0$ compared with $10^5\, G_0$ for a Herbig Ae/Be star, G_0 being the value of the interstellar radiation flux (ISRF) as estimated by Habing and Draine, 10^8 photon $cm^{-2}\, s^{-1}$. Photodissociation acts differently on different molecules. For example, Lyman α photons selectively dissociate HCN and H_2O molecules, while CO and H_2 are unaffected. The latter are instead dissociated by the FUV radiation at wavelengths of 91 and 110 nm respectively.

The internal layer adjacent to the external layer is shielded from the stellar and interstellar radiation field and has temperatures of $\sim 30 - 70$ K, warm enough to allow gas-phase and gas-grain reactions to proceed. Therefore, this layer is referred to as "molecular layer". The temperature of $30 - 70K$ is warm enough to protect CO gas from freeze-out while H_2O stays frozen onto dust grains, removing oxygen from the gas phase: the mean C/O ratio is high, close to unity or even higher, leading to C-based chemistry in the molecular layer. Deeper inside the disk, in the midplane, where *mm* and *cm* size dust grains settle, the disk temperature is even lower, resulting in molecular freeze-out on grain surfaces: the CO freeze-out temperature is ~ 17 K. For example, the CO snowline in the disk of HD 163296 appears at ~ 150 au from the central star (Qi et al., 2011; Mathews et al., 2013a).

In the mm/sub-mm domain, several molecules have been detected in T Tauri disks; CO, ^{13}CO, $C^{18}O$, $C^{17}O$, CN, CS, H_2CO, CCH, DCN, HCO^+, $H^{13}CO^+$, DCO^+, N_2H^+, HC_3N, CH_3CN, HD, C_3H_2, C_2H_2, OH, SO, CH^+, N_2D^+, NH_3, CH_3OH, $H^{13}CN$, $HC^{15}N$, $C^{15}N$, HCOOH and H_2CS (Dutrey, Guilloteau, and Guelin, 1997; Thi et al., 2001; Qi et al., 2008; Dutrey et al., 2011; Chapillon et al., 2012; Bergin et al., 2013; Qi et al., 2013; Huang and Öberg, 2015; Öberg et al., 2015; Walsh et al., 2016; Guilloteau et al., 2016; Salinas et al., 2016; Guzmán et al., 2015; Hily-Blant et al., 2017; Favre et al., 2018; Le Gal et al., 2019). Figure 1.5 shows an example of observed molecules in TW Hya, an archetype of a protoplanetary disk around a single star.

1.5 Observing the dust in protoplanetary disks

For decades, the properties of the dust in protoplanetary disks have been studied using the associated Spectral Energy Distributions (SED). For example, Beckwith et al. (1990) studied 86 pre-main-sequence stars in the Taurus-Auriga star forming region; their study, using the IRAM 30 m telescope at 1.3 mm wavelength has produced important information on the evolution of disks in star forming regions.

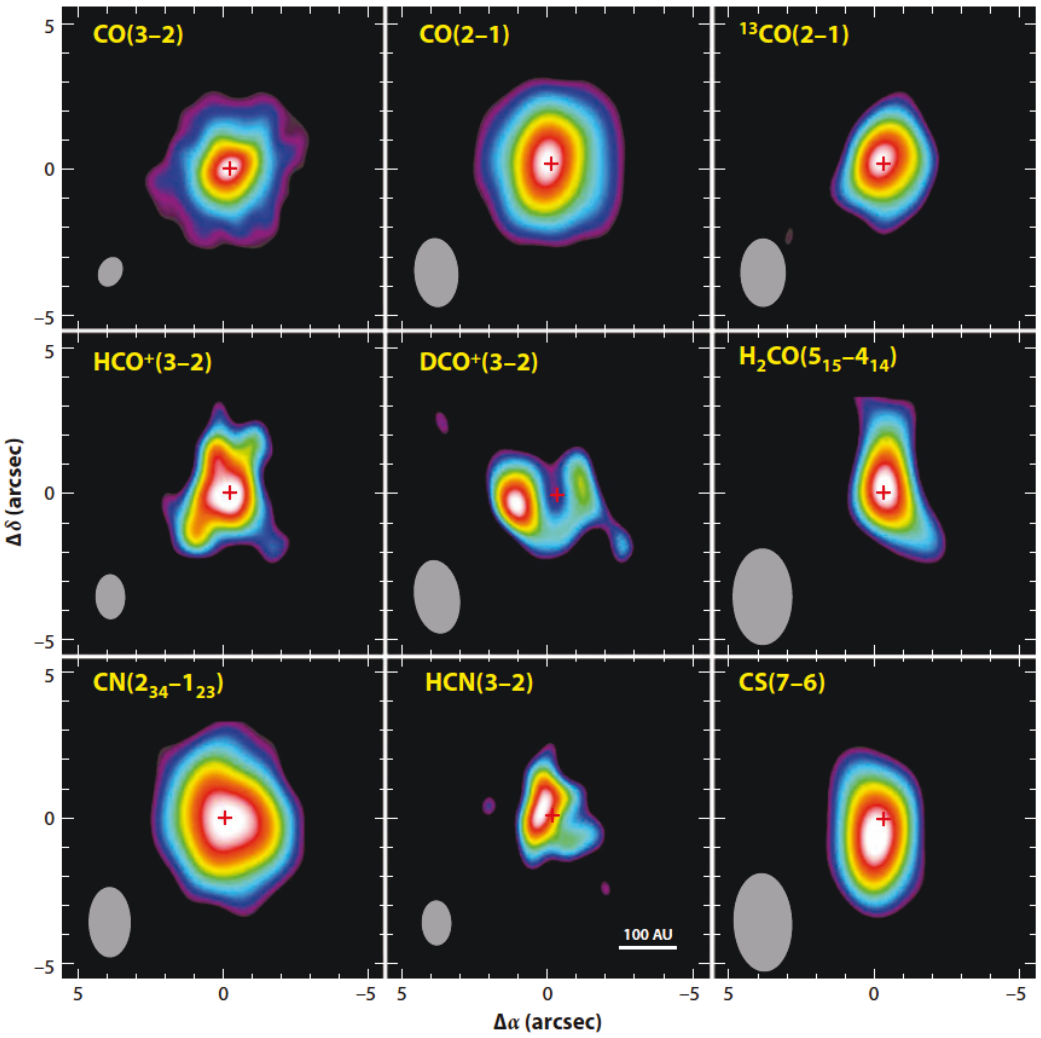

FIGURE 1.5: Submillimeter spectroscopy of molecular rotational lines in the chemically rich, nearby TW Hydra disk. These observations, made with the Submillimeter Array (SMA), are at a range of resolutions, shown in the lower left corner of each panel. (Williams and Cieza, 2011).

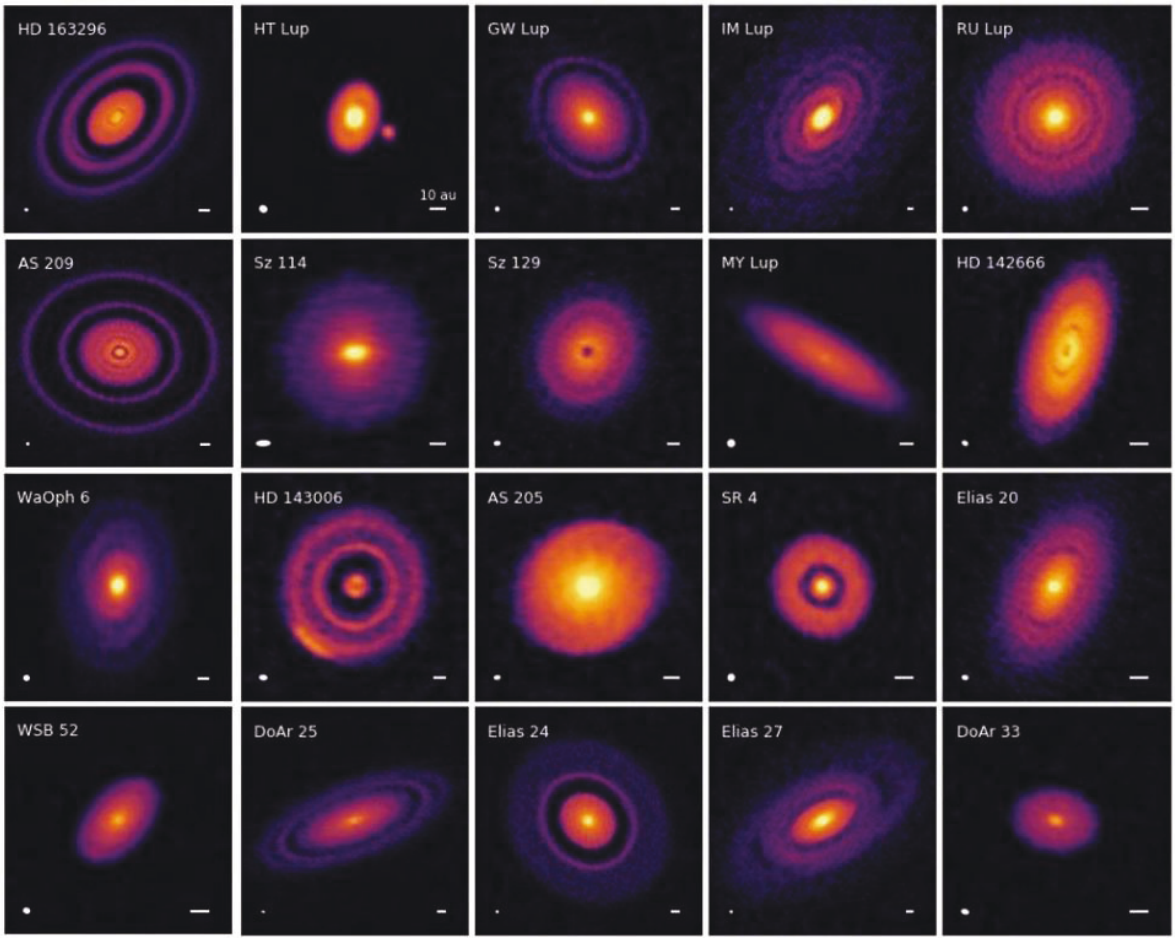

FIGURE 1.6: Intensity maps of 1.25 mm dust emission from protoplanetary disks observed in DSHARP (Andrews et al., 2018).

High resolution interferometers have added significant results: such is the case of the DSHARP (ALMA Large Program: Disk Substructures at High Angular Resolution Project, PI: Sean M. Andrews) project that mapped the dust of protoplanetary disks using ALMA. It surveyed a sample of twenty nearby protoplanetary disks at 1.25 mm wavelength. As illustrated in Figure 1.6, it revealed ubiquitous detailed substructures (with angular resolution of 35 mas or 5 au) at disk radii ranging between 5 au and 150 au. The most common pattern is made of concentric bright rings separated by dark gaps. Spiral features are less common; they are seen in single host stars (IM Lup, Elias 27, and WaOph 6), with complex patterns superimposed on rings and gaps, and in multiple stars (HT Lup and AS 205), the disks around the primary stars showing clear double-arm spirals, indicating a strong dynamical interaction.

Azimuthal inhomogeneity is rare in this sample, only seen in HD 143006 and, very weakly, in HD 163296. The sizes and amplitudes of the rings suggest that they are formed by dust being trapped into axi-symmetric gas pressure bumps.

A recent series of hydrodynamics simulations by Zhang et al. (2018) suggest that dynamical interactions between low-mass planets (sub-Jupiter) and the local disk material are plausible explanations of the observed ring/gap substructures.

1.6 Protoplanetary disks around binary and multiple systems

1.6.1 Theoretical considerations

On average, about 30% of stars form in binary or multiple systems (Reipurth et al., 2007). In multiple systems, in addition to viscosity (possibly caused by turbulences or magnetic fields), the gravity tidal process is the major actor in shaping the close-by stellar environment (Artymowicz et al., 1991). When the binary periodicity is a multiple of the disk rotation periodicity, resonances play an important role. In summary, binary disk coupling, as angular momentum transport, proceeds through viscous and resonant torques, the latter being dominant (e.g. Artymowicz and Lubow, 1994).

Models of disk evolution predict that a binary T Tauri aged 1 Myr should be surrounded by two inner circumstellar (CS) disks, located inside the Roche lobes rotating around the individual components and an outer circumbinary (CB) ring or disk located outside the $L2$ and $L3$ Lagrangian points (see Figure 1.7) and in Keplerian rotation around the binary system (Artymowicz et al., 1991). The outer radius of the CS disks and the inner radius of CB disk are tidally truncated. The inner radius of the CB disk is defined by the outer Lindblad resonance beyond which the gravitational potential becomes undisturbed, at a distance of ~ 2 major-axes of the binary orbit. Lubow and Artymowicz (1997) have shown that the inner radius of the CB disk depends on the eccentricity of the binary system and increases with it.

Hydrodynamical simulations show the complex environment of binary systems. For example, Pierens and Nelson (2013a) modelled two systems, Kepler 34 and Kepler 35, which have a mass ratio of about unity but very different eccentricities, 0.52 for the former and 0.14 for the latter (see Figure 1.7). In both systems, the CB disk is offset with respect to the centre of mass of the binary because the binary has transferred part of its eccentricity to the CB disk. In a second paper, Pierens and Nelson (2013b) have shown that eccentricity plays a more important role in shaping the environment than the mass ratio does, the CB disk eccentricity being independent from the mass ratio of the central binary. The simulations also show accretion arms ("streamers") fuelling material from the CB into the CS disks.

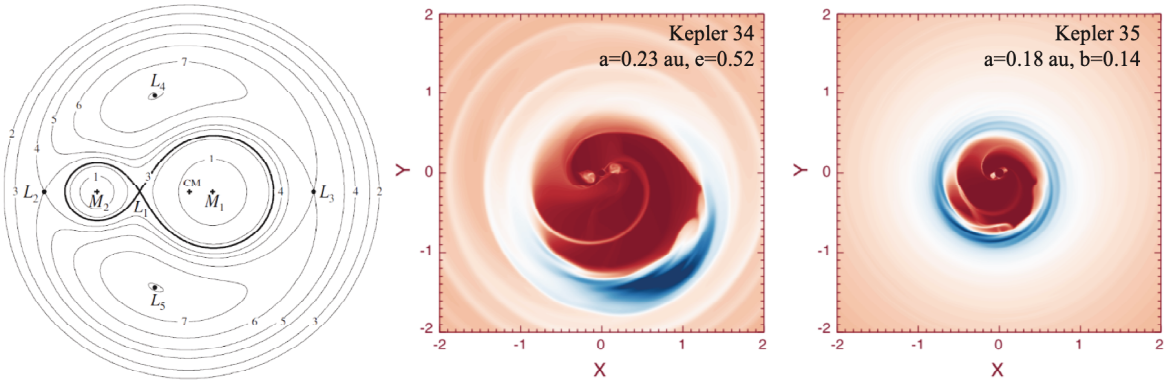

FIGURE 1.7: **Left:** Two-dimensional representation of the Roche potential of two stars with a mass ratio of 1 to 4 with its five Lagrangian points. The bold line represents the edge of the Roche lobe. Reproduced from Frank, King, and Raine (2002). **Middle & Right:** Hydrodynamical simulations of the binary systems Kepler 34 and Kepler 35 (Pierens and Nelson, 2013b). x and y are given in au, the density decreases from red to blue.

1.6.2 Summary: what to observe?

The arguments developed in the previous sections have shown what can be observed in an archetypal binary T Tauri system such as GG Tau: i) the circumstellar disks rotating around the individual components, ii) the cavity and the "streamers" feeding gas from the outer disk onto the inner disks, and iii) the circumbinary ring or disk. CB disks have been observed around several close binary systems and found to be rather similar to the circumstellar disks observed around single stars. But only a few circumbinary disks have been observed around wide binaries, with separations between 10 and 100 au, such as GG Tau A (Dutrey, Guilloteau, and Simon, 1994; Guilloteau, Dutrey, and Simon, 1999; Dutrey et al., 2014; Tang et al., 2016), UY Aur (Close et al., 1998; Duvert et al., 1998), and L 1551 NE (Takakuwa et al., 2014; Takakuwa et al., 2017); in such cases, "streamers" and circumstellar discs have been observed (Dutrey et al., 2014; Tang et al., 2014; Takakuwa et al., 2014; Takakuwa et al., 2017). Figure 1.8 shows a schematic illustration of the environment

of a typical young binary system, indicating the origin of gas and dust emissions expected from the disk.

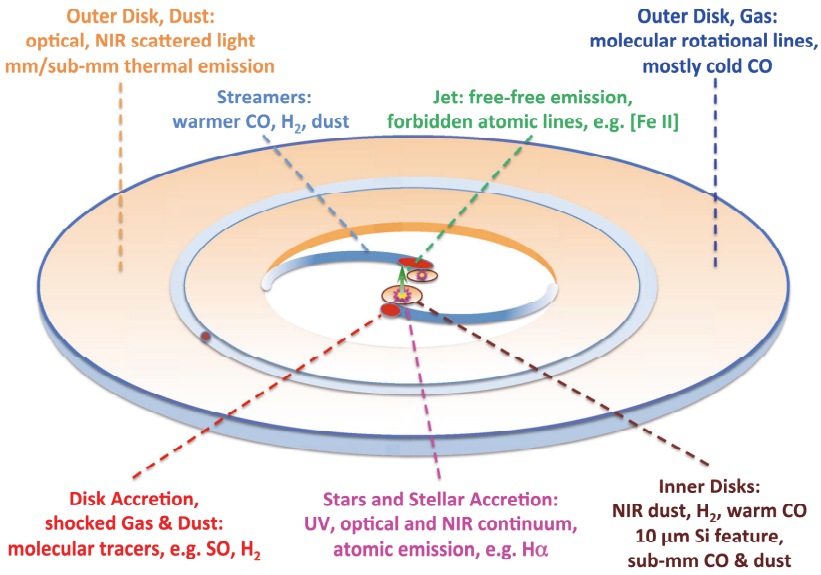

FIGURE 1.8: A schematic picture of a typical binary T Tauri system showing its components and associated gas and dust emissions. A possible planet in formation is shown opening a gap in the circumbinary disk (Dutrey et al., 2016).

Many open questions remain in the study of protoplanetary disks around multiple systems, such as:

- Gas kinematics in the gravitationally perturbed cavity.
- The formation of circumstellar disks in the gravitationally perturbed environment.
- Gas and dust properties and gas kinematics in conditions favourable for the forming of planets.

1.7 GG Tau A - an interesting binary system

GG Tau A is one of the few disks for which all features relevant to the dynamics of a multiple protostar system have been observed and measured. They include the close environment of the protostars (within 30 au), the circumbinary disk, the cavity and the "streamers ". A very detailed review of the properties of the triple system is given in Dutrey et al. (2016).

1.7.1 Existing observations

The stars

Leinert et al. (1991), using a near infrared speckle interferometer, discovered that GG Tau is a hierarchical quadruple system in the Taurus-Auriga star forming region, with two binaries GG Tau A in the north and GG Tau B in the south, separated by $10''$ (1400 au). The northern component, GG Tau A is resolved as a binary, GG Tau Aa and GG Tau Ab, with a separation of 35 au. The southern component, GG Tau B is another binary, GG Tau Ba and GG Tau Bb, separated by $\sim$ 200 au. The system has then be studied by several teams at different wavelengths (infrared, mid-infrared, visible, (sub) mm) and with different instruments. Table 1.1 summarises the main characteristics of the system. The northern component, GG Tau A is more massive and has been studied in more detail than GG Tau B. Some detailed information about GG Tau A, which is the main object studied in this thesis, is summarised below.

TABLE 1.1: Main characteristics of GG Tau

	GG Tau A	GG Tau B	
Spectral index	Aa: K7 Ab: M0.5	Ba: M5 Bb: M7	White et al. (1999)
Mass	Aa: $0.78 \pm 0.1\, M_\odot$ Ab: $0.68 \pm 0.03 M_\odot$	Ba: $0.12 \pm 0.02 M_\odot$ Bb: $0.044 \pm 0.006 M_\odot$	White et al. (1999)
	Ab1: $0.6 \pm 0.03 M_\odot$ Ab2: $0.30 \pm 0.05 M_\odot$		Di Folco et al. (2014)
Major axis	32.4 au		Beust and Dutrey (2005)
Eccentricity	0.34		Beust and Dutrey (2005)

In the 1990s, GG Tau A was found to be surrounded by a dense gas and dust ring extending from 180 au to 260 au and an outer Keplerian disk reaching out to 800 au (Dutrey, Guilloteau, and Simon, 1994). Using CO emission observations, Guilloteau, Dutrey, and Simon (1999) evaluated the dynamical mass of the system as $1.28 \pm 0.07\, M_\odot$, consistent with the mass derived from HST observations by White et al. (1999), $1.46 \pm 0.1\, M_\odot$ (the derived spectral indices are K7 for GG Tau Aa and M0.5 for GG Tau Ab). Hartigan and Kenyon (2003) analyzed spectrocopy data from HST, derived spectral types M0 for GG Tau Aa and M2 for GG Tau Ab, resulting in a binary mass of 0.98 $M_\odot$ ($M_{Aa} = 0.60\, M_\odot$ and $M_{Ab} = 0.38\, M_\odot$). Recently, Di Folco et al. (2014) discovered that GG Tau Ab is in fact itself a binary, Ab1/Ab2, separated by 4.5 au, with an orbital period of 16 years (see Figure 1.10 lower left panel) making GG Tau A a triple system. The measured IR flux gives the spectral type of the third component, GG Tau Ab2, as M3, adding 0.3 $M_\odot$ to the system, making the spectral mass consistent with the dynamical mass derived by Guilloteau, Dutrey, and Simon (1999) using ^{13}CO(2–1) observations from the IRAM array.

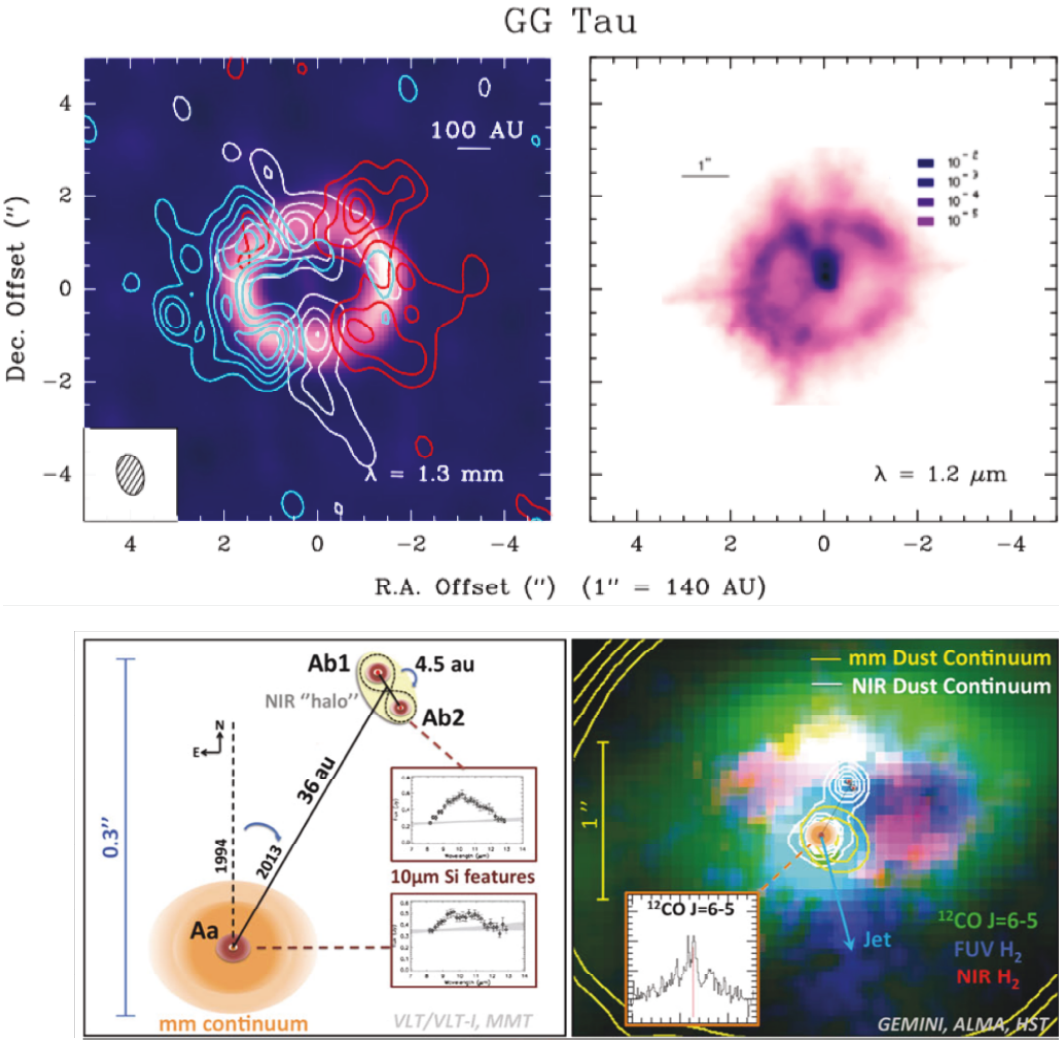

FIGURE 1.9: **Upper left panel:** Intensity map of the 1.3 mm continuum emission and velocity maps of the ^{13}CO(2–1) line emission at $v = 5.55$ (blue contours), 6.30 (white contours) and 7.05 km s^{-1} (red contours) (Guilloteau, Dutrey, and Simon, 1999). **Upper right panel:** NIR image from scattered light emission obtained by Roddier et al. (1996). **Lower left panel:** The triple star system and the circumstellar warm dust, as observed by Di Folco et al. (2014). The spectra show silicate emission at 10 μm observed in Aa and Ab (Skemer et al., 2011). **Lower right panel:** Intensity map of CO(6–5) emission (green) superimposed on the map of dust emission at *mm* wavelength (yellow contours) and at NIR (white contours), and the emissions of H_2 at FUV (dark blue) and at NIR (red). The figures are from Dutrey et al. (2016).

The circumbinary disk

The circumbinary disk surrounding GG Tau A has been observed by several teams: Skrutskie et al. (1993) using the Nobeyama single dish telescope; Kawabe et al.

(1993), using the Nobeyama Milliliter Array to observe the CO(1–0) emission; Simon and Guilloteau (1992) using the IRAM interferometer to observe the dust emission, Dutrey, Guilloteau, and Simon (1994) and Guilloteau, Dutrey, and Simon (1999) to observe CO, ^{13}CO and dust emissions. More recently ALMA observations of the CO gas and dust emissions have been reported at high angular resolution of $\sim$ 50 au, by Dutrey et al. (2014) and Tang et al. (2016). These observations revealed that the outer disk is made of a dense gas and dust ring, extending from 180 au to 260 au (containing 70% of the total disk mass of 0.15 $M_\odot$), and an outer CO gas disk reaching out to 800 au. Guilloteau, Dutrey, and Simon (1999) evaluated the ^{13}CO gas temperature in the disk as $\sim 20(r/300\,\mathrm{au})^{-0.9}$ K, while the dust temperature was derived from multi-wavelength dust emissions at 0.45, 1.3 and 3.4-mm and found of the order of $\sim 14(r/200\,\mathrm{au})^{-1.1}$ K (Dutrey et al., 2014).

The circumstellar disks

The material surrounding the protostars was first described by Guilloteau, Dutrey, and Simon (1999) using the 1.3-mm continuum emission observed with the IRAM interferometer. They measured an unresolved flux of about 10 mJy toward the central stars. Later, with better angular resolution of 0.45″, Piétu et al. (2011) at 267 GHz, Dutrey et al. (2014) at 690 GHz with an angular resolution of 0.3″ and Tang et al. (2016) at 330 GHz with an angular resolution of $\sim$ 0.35″ have confirmed that the emission is centred on the Aa star. Dutrey et al. (2014) observed the inner disk orbiting Aa using CO(6–5) and continuum observations; they evaluate the mass of the circumstellar disk as at least 10^{-3} $M_\odot$; assuming an accretion rate of $10^{-8}\,M_\odot\,yr^{-1}$, the Aa disk would dissipate in less than $3.10^4 - 10^5$ years, without external replenishment. Yang et al. (2017) observations in H-band also revealed the presence of a circumstellar disk around Aa. The emission of silicate grains at wavelengths between 5 and 34 μm, detected using Spitzer/IRS, has been reported and analysed by Forrest et al. (2004) and Sargent et al. (2006) and Furlan et al. (2006). A model using 252 K astrosilicate grains suggests that the emission emanates from the inner regions ($r \sim 1$ au) of the circumstellar disk(s). The presence of two distinct silicate features in the first spatially resolved MMTAO observations of Skemer et al. (2011) demonstrates that at least two CS disks are present.

The cavity and "streamers"

The earlier measurement of the radius of GG Tau A cavity, at 1.3 mm wavelength, has been later confirmed by NIR scattered light observations using the Canada-France-Hawii Telescope (CFHT) by Roddier et al. (1996) (see Figure 1.10 upper right panel); they measured a radius of 180 au, larger than theoretically expected ($\sim$ 80 au, or twice the major-axis of the binary orbit Artymowicz et al., 1991); the cavity has been observed to host both diffuse gas and dust. NIR scattered light images show some low brightness emission inside the dynamically cleared area (Roddier et al., 1996; Itoh et al., 2002). Several H_2 lines have been also observed, providing evidence for

material in-falling onto the inner CS disks (Thi et al., 2001; Beck et al., 2012). Yang et al. (2017) observed a northern "streamer" arc close to Ab in a scattered light image. The maps of CO(2–1), (3–2) and (6–5) observed by IRAM and ALMA interferometers also show significant amount of emissions inside the cavity; the position of the peak brightness in CO(2–1) and (6–5) emissions coincides with that of hot H_2 emission ($\sim$ 1500 K) observed by Beck et al. (2012) (see Figure 1.10 lower right panel). Using a non-LTE radiative transfer code to analyse the CO data, these authors obtain a temperature at the peak position of the order of 35 to 70 K.

The hot spot

Dutrey et al. (2014) have shown the presence of a south-eastern hot spot on the outer edge of the dense ring, at a distance of $\sim$ 260 au from the central stars, both in CO(2–1) and CO(6–5) emissions. They estimated the temperature of the hot spot to be 40 K, a factor 2 higher than in its surroundings. The authors suggested that it might signal the presence of an unknown (already formed) embedded companion that is still actively accreting material from the circumbinary disk. The possible presence of a planet is still an open question.

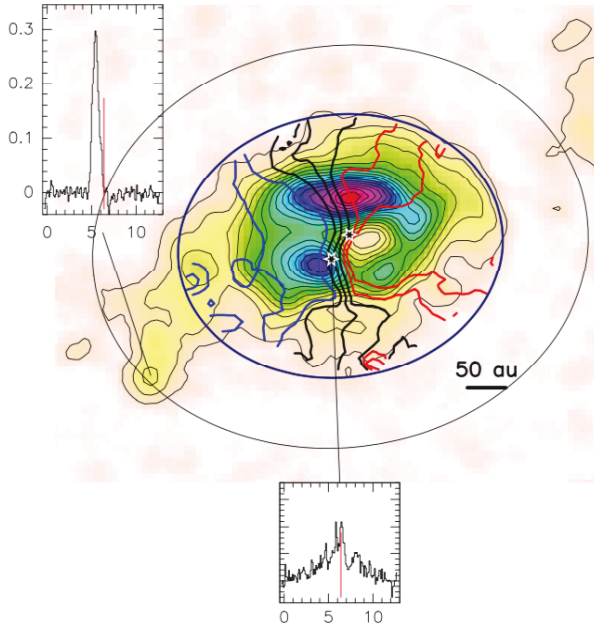

FIGURE 1.10: Intensity map of CO(6–5) emission. The spectra shown in the two inserts display the CO(6–5) emission at the hot spot location (east) and onto Aa (Dutrey et al., 2016).

1.7.2 Simulations of the GG Tau A system

Radiative transfer simulation

In order to reconstruct the observation features of GG Tau A at infrared wavelengths, Brauer et al. (2019) used the Monte-Carlo code POLARIS (Reissl et al. 2016; Brauer et al. 2017) to model dust emission. The most recent infrared observations of GG Tau A reported by Yang et al. (2017) shows the circumstellar disks around both Aa and Ab (see Figure 1.11). The authors identified 6 remarkable positions seen in most GG Tau A IR images (Duchêne et al., 2004).

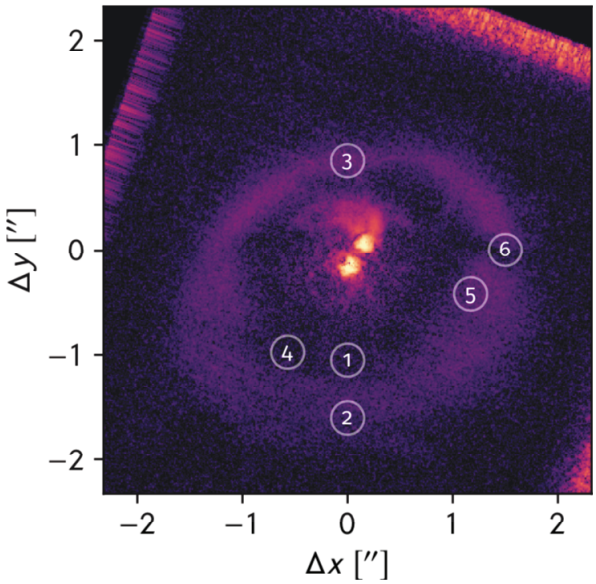

FIGURE 1.11: The H-band observations of GG Tau A. The number (1)–(6) indicate the remarkable features. The Figure is taken from Brauer et al. (2019)

Their model consists of three stars GG Tau Aa, Ab1 and Ab2 with Ab1 and Ab2 considered as a binary. All star properties (such as, effective temperature, luminosity, visual extinction, inclination, position angle and size of the circumstellar/circumbinary disks) are taken from the literature. The power index describing the radial distributions of the density in the circumstellar disks is assumed to be the same as for minimum mass solar nebulae (Hayashi, 1981). Compact, homogeneous and spherical grains are taken to consist of 62.5% silicate and 37.5% graphite. The grain size distribution reaches up to 0.5 μm in the disk mid-plane.

The model favours circumstellar disks around Aa and Ab1 coplanar with the circumbinary disk, but perpendicular to it around Ab2. The Spectral Energy Distribution and polarization intensity agree well with observations. Figure 1.12 left shows the dust mass distribution of their model and Figure 1.12 right shows their best result.

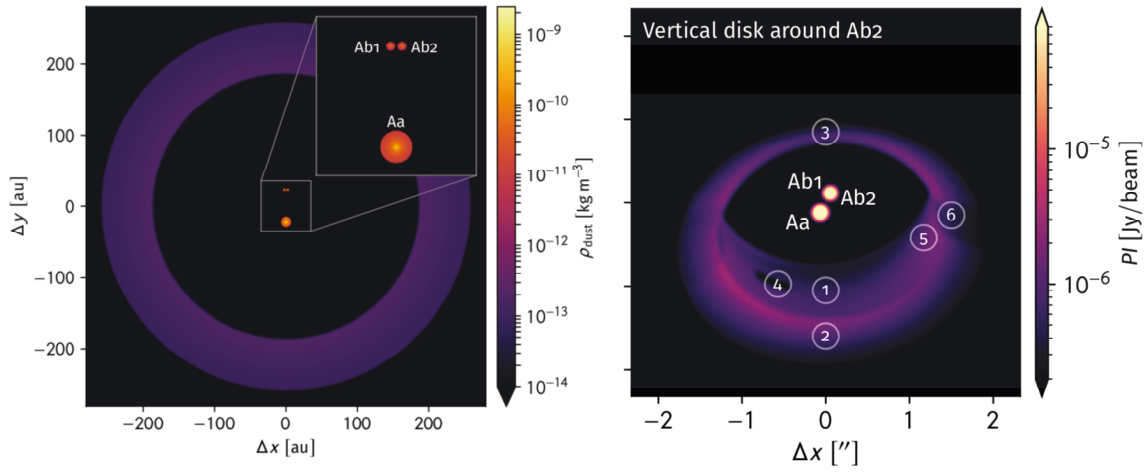

FIGURE 1.12: **Left:** The dust mass density distribution of the GG Tau A model. **Right:** Polarized intensity map of GG Tau A simulated with circumstellar disks as described in the text. The figure is taken from Brauer et al. (2019).

Hydrodynamical simulation

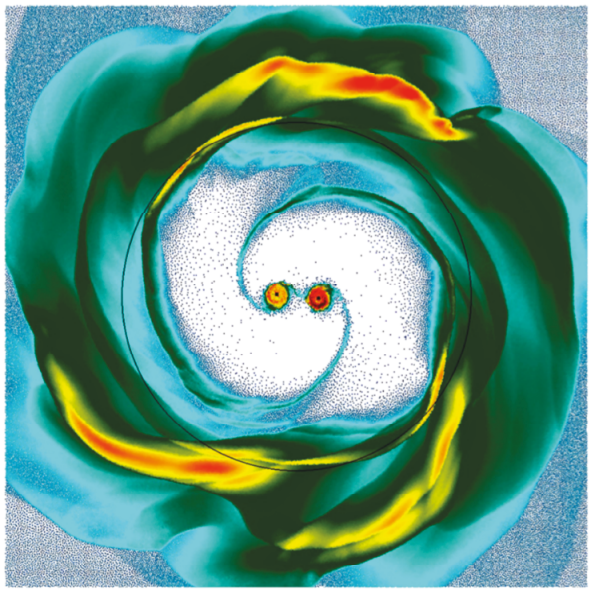

FIGURE 1.13: An example of hydrodynamical simulation of the GG Tau A system. The simulation is for a system with a major axis of 62 au and eccentricity of $e = 0.3$ (Nelson and Marzari, 2016).

Nelson and Marzari (2016) using the VINE code (Wetzstein et al., 2009) have simulated the evolution of a binary system based on GG Tau A observations. They ignore the binarity of GG Tau Ab. The initial conditions (density, temperature) were chosen to be the same as the observations reported by Guilloteau, Dutrey, and Simon (1999). To study the respective impact of the morphology of the dense ring and

of the low density outer disk, the authors perform two series of simulations: 1) the whole mass (0.12 $M_\odot$) is contained in the dense ring and 2) 70% of mass is contained in the dense ring, the rest being in the outer disk. They find that after 3 orbits ($\sim$ 6500 years) the total mass transport is $\sim$ 15% in the first model and $\sim$ 5% in the second model. Using this mass transport rate and an outer disk mass of $\sim 0.04\,M_\odot$, they find that the entire disk could be generated this way in less than 10^4 years. Finally, they found that both self-gravity and tidal truncation should contribute to the formation of spiral patterns (see Figure 1.13). They interpret the sharp features of the ring as the manifestation of such a spiral structure, the low density outer disk being an excretion disk created by the outward mass flux generated by the spiral arms as they propagate outwards. They conclude that GG Tau A is a coplanar system with eccentricity of $e = 0.3$ and major axis of $a = 62au$.

Chapter 2

Observations, data reduction and radiative transfer

2.1 Radio interferometry

2.1.1 General

A radio telescope is characterised by

i) the sensitivity, the ability to measure weak sources of radio emission, proportional to the area and efficiency of the antenna and the sensitivity of the radio receiver used to amplify and detect the signal and

ii) the angular resolution, the ability to distinguish two neighbour sources, namely fine details in the sky; it is approximately equal to the ratio between the wavelength of observation (λ) and the diameter of the antenna (D) ($\theta = \lambda/D$). This implies that larger telescopes provide better images but building a large single dish has some limitations, in particular in terms of installation, movement, etc. Interferometers make it possible to cope with these difficulties while providing much better resolution than single dish telescopes.

An interferometer measures the interference pattern produced by multiple apertures. An interferometer has N antennas providing $N(N-1)/2$ baselines that give independent information and therefore produce much more detailed images than a single dish telescope. In other words, a radio interferometer can be thought of as a single telescope with a very large but incompletely-filled aperture, of diameter equal to the maximum spacing, or baseline, between any two of its components. This large "synthesized" aperture is only sampled at the locations at which an element exists, and this is aided by the rotation of the Earth which effectively moves the elements with respect to the source being observed, hence increasing the sampling. The size of the "synthesized" aperture dictates the resolution or ("beam size") of the array; the larger the aperture, the smaller the resolution.

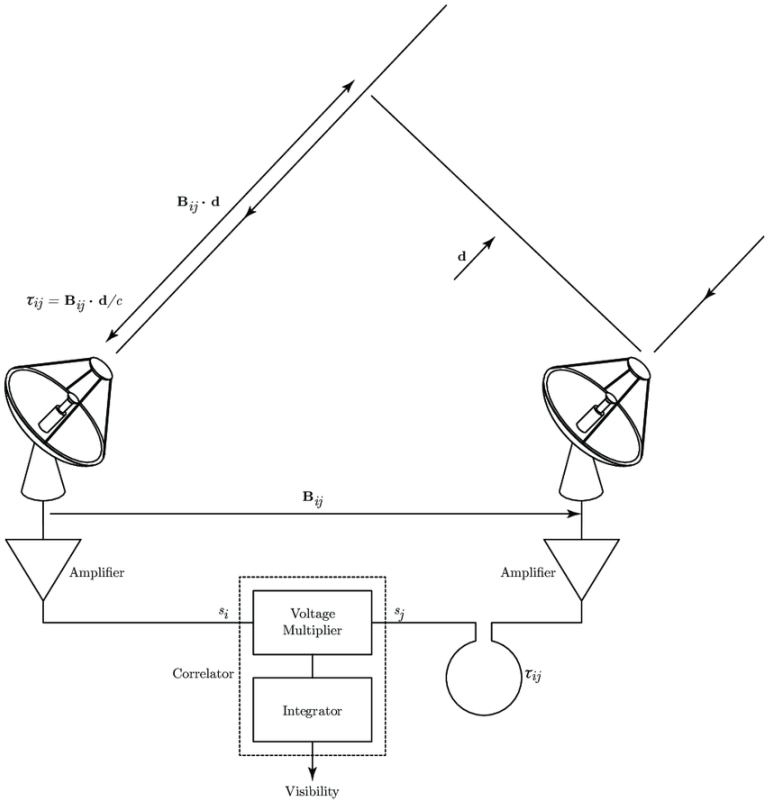

FIGURE 2.1: Two-element inteferometer.

The interference pattern measures the *complex visibility* which has the form of a Fourier transform:

$$V = |V|e^{i\Phi_V} = \int_{Sky} A(\sigma)I(\sigma)e^{-2\pi\nu\mathbf{b}.\sigma/c}d\Omega \tag{2.1}$$

where σ is the unit vector along the pointing direction, $\mathbf{b}$ is the baseline vector, A is the antenna power pattern, and I is the sky brightness distribution.

Let (u, v, w) be the coordinates of the baseline vector, in units of the observing wavelength ν, in a frame of the delay tracking vector $\vec{d_0}$, and (l, m, z) are the coordinates of the source vector $\vec{d}$ in this frame. Then

$$\begin{aligned} \nu\mathbf{B}.\mathbf{d}/c &= ul + vm + wz \\ \nu\mathbf{B}.\mathbf{d_0}/c &= w \\ z &= \sqrt{1 - l^2 - m^2} \\ \text{and } d\Omega &= \frac{dldm}{z} = \frac{dldm}{\sqrt{1 - l^2 - m^2}} \end{aligned} \tag{2.2}$$

Thus,

$$V(u,v,w) = \int\int A(l,m)I(l,m)e^{-2i\pi(ul+vm+w(\sqrt{1-l^2-m^2}-1))}\frac{dldm}{\sqrt{1-l^2-m^2}} \tag{2.3}$$

With $I(l,m) = 0$ when $x^2+y^2 \geq 1$ If (x,y) are sufficiently small, we can make the approximation

$$(\sqrt{1-l^2-m^2}-1)w \simeq \frac{1}{2}(x^2+y^2)w \simeq 0 \tag{2.4}$$

and Eq (2.3) becomes

$$V(u,v) = \int\int A'(l,m)I(l,m)e^{-2i\pi(ul+vm)dldm} \tag{2.5}$$

with $A'(l,m) = A(l,m)/\sqrt{1-l^2-m^2}$

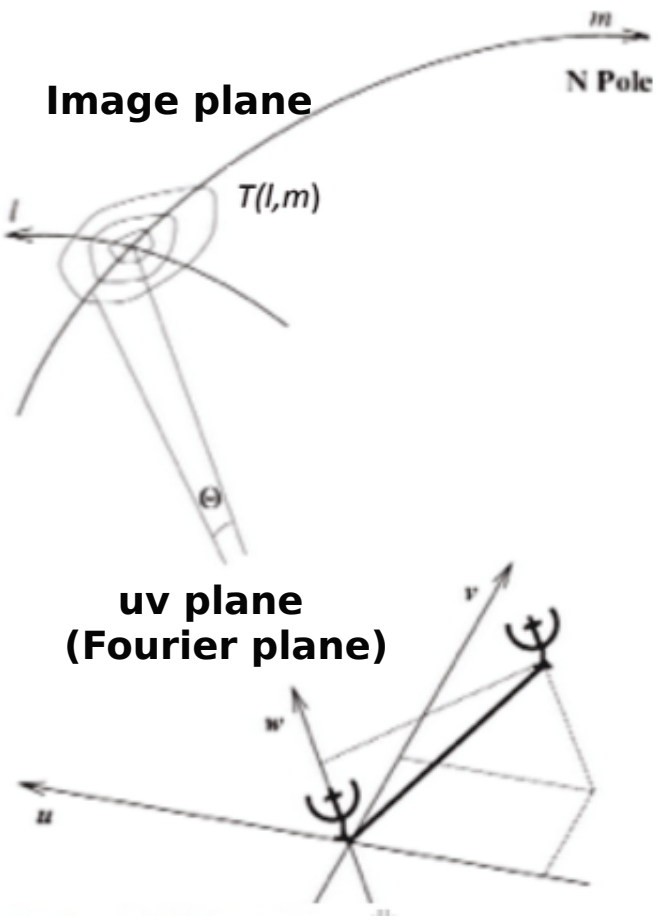

FIGURE 2.2: Interferometric coordinate transformation in interferometer measurement. *Upper*: In image (l,m,v) plane, *Lower*: In a Fourier or (u,v) plane.

The interference pattern is directly related to the source brightness $I(l,m)$. In particular, for small fields of view, the complex visibility, $V(u,v)$ is the $2D$ Fourier

transform of the brightness on the sky, $I(l,m)$ mutiplied by the antenna power pattern $A(l,m)$. Deconvolution techniques then must be applied to recover the true sky brightness distribution.

2.1.2 Imaging and deconvolution

Imaging

An interferometer measures the visibility function

$$V(u,v) = \int\int A(l,m)I(l,m)e^{-2i\pi(ul+vm)}dldm \tag{2.6}$$

over an ensemble of points $(u_i,v_i), i = 1,n$ where $A(l,m)$ is the power pattern of the antennas and $I(l,m)$ the sky brightness distribution. The ensemble of the visibility measurements is called a uv table.

The imaging process consists in determining as well as possible the sky brightness $I(x,y)$. Since Equation (2.6) is a convolution, the imaging process will involve deconvolution techniques.

Let $S(u,v)$ be the sampling (or spectral sensitivity) function defined over the ensemble of the n baseline for which there exists a visibility measurement

$$\begin{aligned} S(u,v) \neq 0 \leftrightarrow \exists i \in 1,nsuchthat(u_i,v_i) = (u,v) \\ S(u,v) = 0 \leftrightarrow \exists i \in 1,nsuchthat(u_i,v_i) \neq (u,v) \end{aligned} \tag{2.7}$$

The spectral sensitivity function S contains information on the relative weights of each visibility, usually derived from noise predicted from the system temperature, antenna efficiency, integration time and bandwidth.

We define

$$I_w(x,y) = \int\int S(u,v)W(u,v)V(u,v)e^{2i\pi(ul+vm)}dudv \tag{2.8}$$

where $W(u,v)$ is an arbitrary *weighting function*. Since the Fourier Transform of a product of two functions is the convolution of the Fourier Transform of the function, $I_w(l,m)$ can be identified with

$$I_w(l,m) = (A(l,m)I(l,m)) * *(D_w(l,m)) \tag{2.9}$$

where

$$D_w(l,m) = \int\int S(u,v)W(u,v)e^{2i\pi(ul+vm)}dudv = S\hat{W} \tag{2.10}$$

is called the *dirty beam*, and is directly dependent on the choice of *weighting function* W, as well as on the spectral sensitivity function S. $I(l,m)$ is usually call dirty image.

Fourier Transform, which allows to directly derive I_w from the measured visibilities V and spectral sensitivity function S, and **Deconvolution**, which allows to derive the sky brightness I from I_w, are thus two key issues in imaging.

Fourier Transform

The simplest approach would be to directly compute sin and cos functions for all combinations of visibilites and pixels in the image (Direct Fourier Transform). However, this process is straight but slow. In practice, we use Fast Fourier Transform (FFT) because of its definite speed advantage. This method requires to regrid the visibilities on a regular grid to be able to perform a $2-D$ FFT. This gridding process will introduce some distortion in the dirty image and dirty beams, which should be corrected.

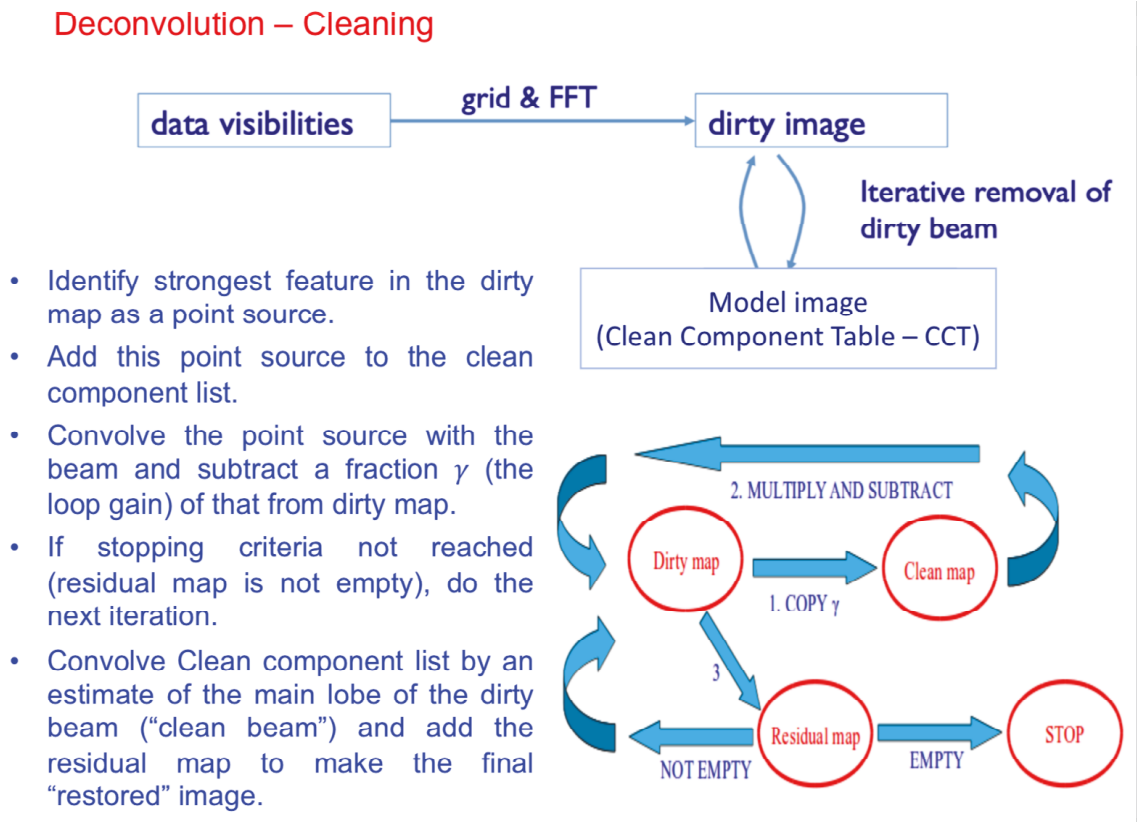

FIGURE 2.3: Schematic diagram of the **CLEAN** process

Weighting and Tapering

At the uv table creation, the sampling function is defined as

$$S(u,v) = \frac{1}{\sigma^2(u,v)} \tag{2.11}$$

where the noise σ is computed from system temperature, bandwidth, integration time, and system efficiency (including quantization and decorrelation)

$$\sigma(u,v) = \frac{J_I \, T_{sys}}{\eta_Q \sqrt{2\Delta\nu \, t_{int}}} \tag{2.12}$$

where J_I is the antenna temperature to flux density conversion factor: $J_I = 2k/\eta_A \, A$ The weights $W(u,v)$ can be freely chosen. The selection of weights is usually decomposed in two slightly different processes, called *Weighting* and *Tapering*.

- **Weighting** deals with the local variations of weights for each grid cell after the gridding process
- **Tapering** consists in apodizing the uv coverage by $T(u,v) = exp(-(u^2 + v^2)/t^2)$ where t is a tapering distance. This is corresponding to smoothing the data in the image plane (convolution by a Gaussian). This process can give less weight to long baselines, so degrading angular resolution.

Depending on science goal, one can choose to use different weighting type: Natural weighting, Uniform weighting or Robust weighting. Their main properties, advantages and disadvantages are summarized below:

- **Natural weighting**

  $W(u,v) = 1/\sigma^2$ in occupied (u,v) cells, where σ^2 is the noise variance, and $W(u,v) = 0$ everywhere else.

  It maximizes point source sensitivity.

  Generally, it gives more weight to short baselines (low spatial frequencies), so angular resolution is degraded.

- **Uniform weighting**

  $W(u,v)$ is inversely proportional to the local density of (u,v) points. The sum of weights in a (u,v) cell is a constant and 0 for empty cells.

  It fills the (u,v) plane more uniformly and the dirty beam sidelobes are lower.

  It gives more weight to long baselines (high spatial frequencies), so angular resolution is enhanced.

  It downweights some data, so the point source sensitivity is degraded.

  It also can create troubles with sparse sampling: cells with few data points have same weight as cells with many data points.

- **Robust (Briggs) weighting**

  Variant of uniform weighting that avoids giving too much weight to (u,v) cells with low natural weight.

The software implementations differ: $W(u,v) = \frac{1}{\sqrt{1+S_N^2/S_{thresh}^2}}$; S_N is the natural weight of the cell and S_{thresh} is a threshold.

With a high threshold, the weighting is chosen to be natural, with a low threshold, the weighting is chosen to be uniform.

An adjustable parameter allows for continuous variation between maximum point source sensitivity and high resolution.

Deconvolution

The first imaging step leads to a convolution equation whose solution is the convolution product of the sky brightness distribution (apodized by the interferometer primary beam) by the dirty beam.

To derive the astronomically meaningful image, i.e ideally the sky brightness, a deconvolution is required. Deconvolution is always a non-linear process, and requires to impose some contraints on the solution, or in other words to add some information, to better select plausible solutions.

The standard deconvolution technique, **CLEAN** relies on such a qualitative constraint: it assumes that the sky brightness is essentially an ensemble of point sources. The algorithm which derives from such an assumption is straightforward. It is a simple "matching pursuit".

Schwartz (1978) showed that the Clean algorithm is equivalent to a least squares fit of sinusoids to visibilities in the case of no noise.

2.1.3 ALMA and NOEMA interferometers

Among existing radio interferometers, ALMA – the Atacama Large Millimeter/submillimeter Array – is the most powerful in the world and NOEMA – the NOrthern Extended Millimeter Array – is the most advanced in the Northern Hemisphere.

ALMA, the Atacama Large Millimeter/submillimeter Array

ALMA, the Atacama Large Millimeter/submillimeter Array, is a (sub)millimetre interferometer installed on the Chajnantor plateau in the Atacama Desert of northern Chile, at 5000 m above sea level. ALMA consists of 66 high-precision antennas: fifty 12 m diameter antennas in the main Array (12 m Array), twelve 7 m diameter antennas in the 7 m Array (ALMA Compact Array –ACA), and four 12 m diameter antennas in the Total Power Array. ALMA covers the frequency range of 31–950 GHz, corresponding to wavelengths of 9.6 to 0.3 mm. The antennas can be arranged into 10 configurations, yielding projected baselines ranging from about 15 m to 16 km.

With the longest baseline of 16 km, ALMA can produce images with angular resolution of $\sim 0.01''$. With high sensitivity and angular resolution, ALMA has opened a new window for answering many major scientific questions.



FIGURE 2.4: The ALMA Compact Array.

NOEMA, the NOrthern Extended Millimeter Array

NOEMA, the NOrthern Extended Millimeter Array, is a (sub)mm array located in the French Alps on the wide and isolated Plateau de Bure at an altitude of 2550 m, previously known as Plateau de Bure Interferometer, the PdBI array which included six 15 m-diameter antennas. NOEMA is being upgraded with the goal to double the



FIGURE 2.5: The NOrthern Extended Millimeter Array equipped with 10 antennas.

number of antennas from six to twelve and to upgrade the receiver from 3 bands of 8 GHz width to 4 bands of 16 GHz width in each polarisation mode. Ultimately, the correlator will cover 2 frequency bands of 16 GHz per polarisation. NOEMA will be able to cover the frequency range of 70 to 375 GHz, corresponding to wavelengths of 3 to 0.8 mm. With twelve movable antennas, NOEMA will reach a maximal baseline of 1.6 km, providing images with an angular resolution as high as $\sim 0.1''$. Currently, NOEMA operates with 10 antennas, all equipped with new receivers.

At the Taurus or Rho Ophiuchi distance (150 pc which is the distance of closest low-mass star forming regions, with the exception of TW Hya), such instruments are mandatory to observe small and weak sources such as protoplanetary disks of size $0.5 - 3''$. At 150 pc, $1''$ is 150 au or about 5 times the size of Solar System (Neptune-Sun is $\sim$30 au). The distance of Jupiter to the Sun is $\sim 0.03''$ at the same distance.

2.2 GG Tau A observations with interferometry

2.2.1 ALMA observations

GG Tau A has been observed in three operation cycles of the ALMA interferometer: Cycle 0 (2011), Cycle 1 (2012) and Cycle 3 (2015).

Cycle 0 observations: Observations were carried out in Band 9 on August 13th, 2012 with 22 antennas, providing projected baselines ranging from 20 m to 344 m. The spectral band was chosen to cover the emission of the molecular line CO(6–5) and the continuum underneath. Dutrey et al. (2014) give details about observations and data reduction.

Cycle 1 observations: Observations were carried out in Band 7 on November 18th and 19th, 2013 with 29 antennas, providing projected baselines ranging from 15 m to 1282 m. The frequency setup covered the lines of ^{12}CO(3–2) and ^{13}CO(3–2) and CS(7–6). Details about these observations are given in Tang et al. (2016).

Cycle 3 observations: Observations were carried out in Band 7 on September 25th and 30th, 2016 in configuration C40–6 with 39 antennas, providing projected baselines ranging from 16 m to 3049 m. Spectral line windows of 58.6 MHz width were chosen to cover the lines of ^{13}CO(3–2) and C^{18}O(3–2) and CS(7–6) with a channel width of $\sim$0.14 MHz ($\sim$ 0.1 km s^{-1}). The continuum was observed around 330.15 GHz and 342.00 GHz. These are described in detail in the present chapter.

2.2.2 NOEMA observations

GG Tau A has been observed by NOEMA and by the PdBI for about two decades in order to study the morphology and kinematics, the gas and dust properties and the chemical content of the disk. I list below observations that are presented in the thesis.

HCO$^+$(1–0) was observed between Jan 1997 and Apr 1997 with six antennas. Details about the observations can be found in Guilloteau, Dutrey, and Simon (1999).

DCO$^+$ (3–2) was observed with the PdBI interferometer in December 2013 and April 2014 with six antennas. The total on-source integration time was $\sim$ 5 hours.

Baselines ranging between 15 m and 176 m provide a beam of $1.76'' \times 1.23''$, PA=17°. Phase and amplitude calibrations were performed using QSO 0507+179 and 0446+112, while the flux calibration was carried out using QSO 3C84 (flux 10.3 Jy at 216.1 GHz) and MWC 349 (flux 1.6 Jy at 216.1 GHz).

H_2S 1(1,0)-1(0,1) & $H^{13}CO^+$ (2-1): Observations were carried out on 23 December, 2017 using the D configuration with nine antennas. The total on-source integration time was 5.2 hours. Baselines ranging between 24 m and 176 m provide a beam of $2.50'' \times 1.9''$, PA=15°. Phase and amplitude calibrations were performed using QSO B0507+179 and B0446+113. Flux calibration was carried out using QSO MWC349 as a reference (flux 1.4 Jy at 170.3 GHz). The full 7.74 GHz upper and lower sidebands of the new PolyFiX correlator were covered at 2 MHz channel spacing. The emission of molecular lines of H_2S 1(1,0)-1(0,1), $H^{13}CO^+$ (2-1), and also of CCS, SO_2, SO, HC_3N, and c-C_3H_2 have been observed with high spectral resolution (62.5 kHz).

2.3 Data reduction

2.3.1 The ALMA data reduction

The ALMA Cycle 0 and Cycle 1 observations have been reduced and reported in Dutrey et al. (2014) and Tang et al. (2016). For the present thesis, I use the available *uv*-tables to produce clean images with different beam sizes, suitable for each specific study. For example, the CO(6–5) data collected in Cycle 0 and the CO(3–2) data collected in Cycle 1 were reduced using GILDAS[1] to get a beam size of $0.35'' \times 0.31''$, PA=104° and $0.34'' \times 0.28''$, PA=$-89°$ respectively.

Here, I describe in some detail the reduction of the Cycle 3 observations that was made in Bordeaux in May, 2017. The observations were made in two blocks, under good weather conditions. Figure 2.6 shows the time variation of the water vapour level during the two observation blocks. The two blocks have been merged and calibrated using the standard ALMA calibration script in the CASA[2] software package (Version 4.7.0). The phase and bandpass calibrator is QSO J0510+1800. The amplitude/flux are calibrated using J0522-3627. The calibrated data were re-gridded in velocity to the LSR frame using the "cvel" task, and exported through UVFITS format to the GILDAS package for imaging and de-convolution. Figure 2.7 shows the Fourier coverage.

Continuum emission and proper motion

Continuum emission is observed in two windows, one centred at 330.15 GHz and the other at 342.00 GHz. As the 330.15 GHz continuum window includes emission

[1] https://www.iram.fr/IRAMFR/GILDAS/
[2] https://casa.nrao.edu

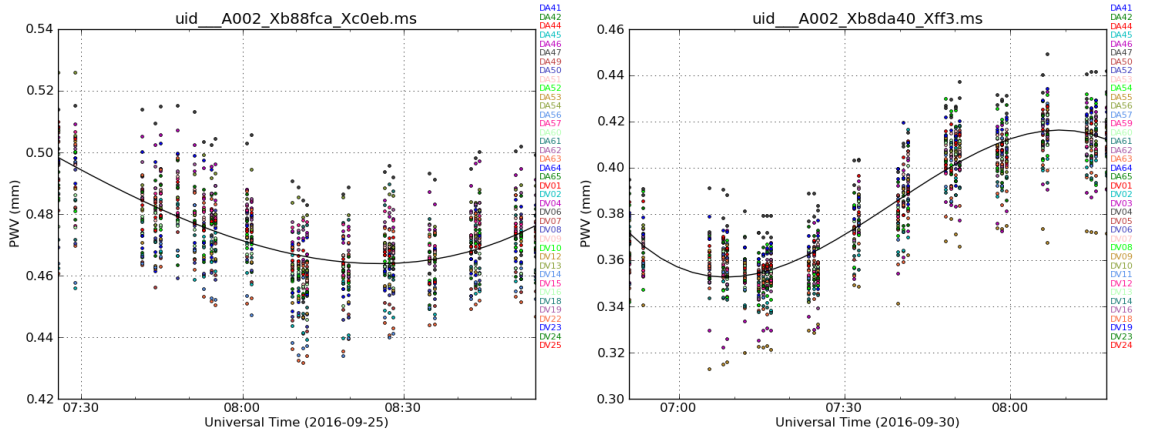

FIGURE 2.6: Time dependence of the water vapour level measured near each antenna during 2 blocks of observations on Sep 25th and 30th, 2016. The curves are polynomial fits to the means.

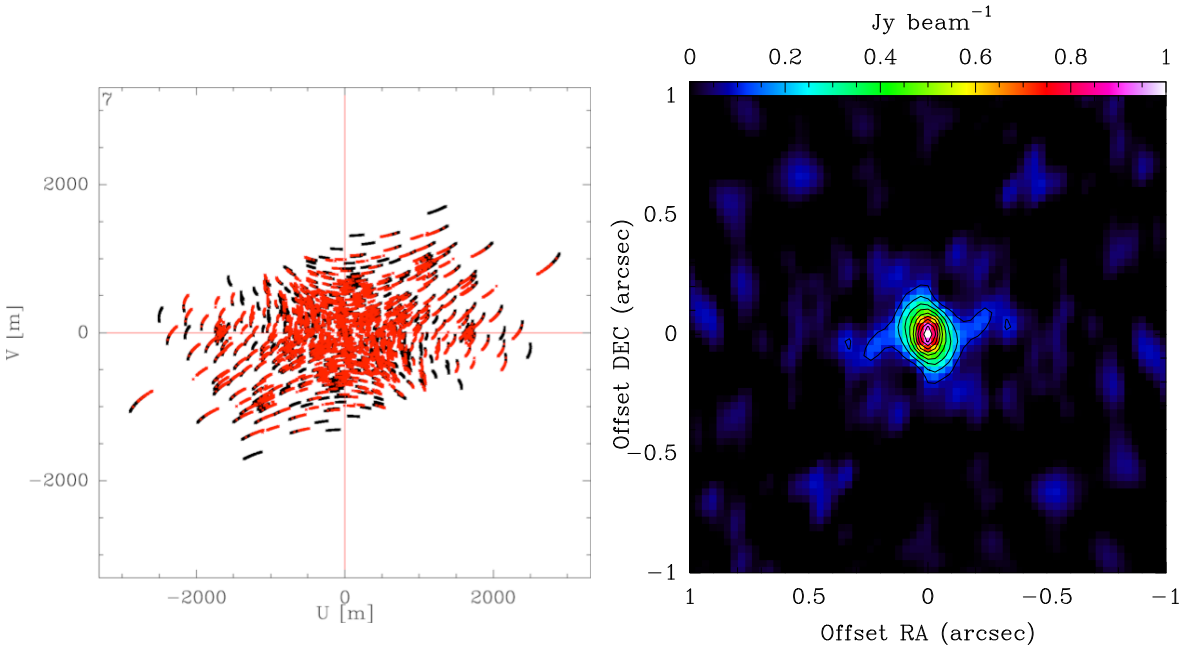

FIGURE 2.7: *uv* coverage of the ALMA observations of GG Tau A Cycle 3 observations. The red and black colours correspond to data that were observed on Sep 25th and 30th, 2016 (*left*). The corresponding dirty beam is shown in the (*right*) panel.

lines of HNCO and CH_3CN, these were flagged by the *uv_filter* task in GILDAS and their weights and visibilities were set to zero. The continuum *uv* data sets were produced using the *uv_continuum* task which rescales all visibilities and u, v coordinates to the mean observing frequency, and concatenates the resulting (single-channel) visibilities into a *uv* data set. The continuum was self-calibrated using the *selfcal* task in GILDAS. Self-calibration means that the source itself is used to calibrate the instrument when it is bright enough (Signal-to-Noise Ratio, SNR, greater

than 100).

Proper motion

The origin of coordinates at RA=4h 32m 30.3s and DEC=17° 31′ 40″ corresponds to year 2000. GG Tau has significant proper motion: Ducourant et al. (2005) quote [17, −19] mas per year, while Frink et al. (1997) quote [11, −28] mas per year. These measurements essentially refer to GG Tau Aa, which is the brightest of the three stars. They need to be corrected in order to obtain the proper motion of the centre of mass of the system, which we assume to be in the centre of the continuum ring. We fitted the continuum emission as the sum of a Gaussian (for the circumstellar disk around Aa) and an elliptical ring (for the dust ring) in the *uv* plane (Guilloteau, Dutrey, and Simon, 1999; Piétu et al., 2011). The apparent motion of the ring gives a proper motion of [9, −23] mas per year, that we applied to all our data set, meaning we recenter all the images on the center of the ring.

Continuum imaging

The DIRTY beam and DIRTY map have been produced with a pixel size of 0.05″ × 0.05″, and a map size of 512 × 512 pixels using the task *uv_map* which inverse Fourier transforms the visibility data (*uv*–data) and creates a raw image data cube. The CLEAN image was then produced by deconvolving the Point-Spread Function from the DIRTY image using Hogbom algorithm and natural weighting (Hogbom and Brouw, 1974). Deconvolution was done down to a threshold of about one rms noise level. The obtained beam size is 0.19″ × 0.13″, PA=12°. Figure 2.8 shows the clean image of the continuum at 330 GHz.

Line emissions

We use the centre of the continuum image as origin of coordinates for the study of the line emissions, meaning that we apply the proper motion of [9, −23] mas per year to ^{13}CO(3–2), C^{18}O(3–2) and CS(7–6) *uv* tables. The data are self-callibrated using *uv_cal* task in GILDAS which applies a calibration gain table obtained from the continuum self-calibration to a *uv* table.

^{13}CO(3–2) The ^{13}CO(3–2) emission was observed in Cycle 1 and again in Cycle 3 with the 12-m Array and the same spectral resolution of 0.1 km s^{-1}. We merged the two *uv* tables using the *uv_merge* task in GILDAS, which merges two *uv* tables of identical spectral characteristics to form a single output *uv* table.

CS(7–6): The CS(7–6) emission was observed in Cycle 1 with channel spacing of $\sim$ 0.4 km s^{-1}, and in Cycle 3 with channel spacing of $\sim$ 0.1 km s^{-1}. We resampled Cycle 3 observations to have the same channel spacing as for Cycle 1 observation and then merged both *uv* tables using *uv_merge* task in GILDAS. These data will be analyzed together with CS(5–4) data observed in Cycle 6 (2018).

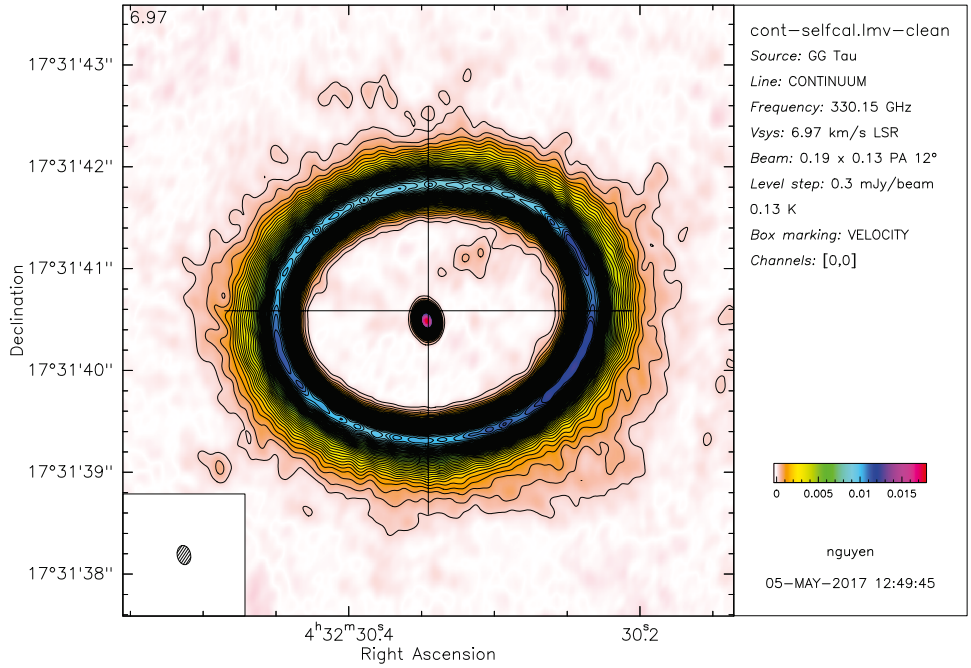

FIGURE 2.8: Continuum intensity map. The beam size is indicated at the lower left corner. The color scale is in units of Jy beam^{-1}.

C^{18}O(3–2): The C^{18}O(3–2) emission was observed only in Cycle 3 with a channel spacing of $\sim 0.1\,\mathrm{km\,s^{-1}}$.

For each molecular line emission, we produced two sets of data, with and without continuum subtraction. The continuum was subtracted using the *uv_subtract* task in GILDAS which fits a constant to the real and imaginary parts of the visibility data of the line-free (i.e. continuum only) channels in each spectral window and subtracted that contribution from the original *uv* table.

In each *uv* table, the DIRTY beam and DIRTY map have been obtained using a pixel size of 0.03×0.03 arcsec^2, and a map size of 1024×1024 pixels, the visibilities being weighted with either natural or robust weighting (R_{Briggs}=0.3). We CLEANed the images down to a threshold of about one *rms* noise level.

To reduce the bias of the non-linearity process of deconvolution, we clean only the area where the emission is exceeding some threshold (i.e a few times higher than the rms noise level) in the individual channel map. Traditionally, astronomers choose to clean either the whole map or in the area of strong emission define from the integrated DIRTY image. The Figure 2.9 shows an example of such masking in some channel maps of ^{13}CO(3–2) data.

The data have been analyzed either in the *uv* plane or in the image plane, depending on the goal. We present their maps (integrated intensity and velocity) in the following chapter.

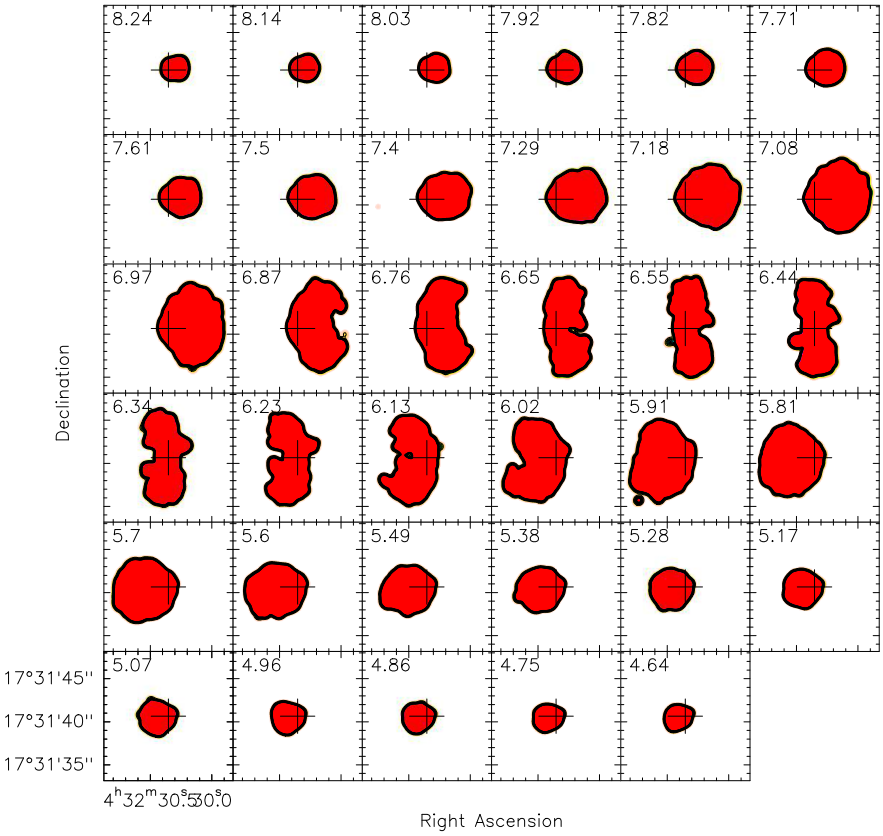

FIGURE 2.9: Channel map of the unmasked regions (shown in red) of ^{13}CO(3–2) emission, where the SNR exceeds the applied threshold.

2.3.2 The NOEMA data reduction

In an attempt to study S-bearing species in the GG Tau A system, we searched for H_2S, SO, SO_2 and C_2S in the disk (2015, project S15AV and 2017, project W17BA). The data have been reduced in Grenoble in March 2017 (S15AV) and in December 2017 (W17BA) and have been calibrated using the pipeline in GILDAS.

We checked the pipeline calibration report and redid the individual calibration for each baseline when needed. In the observations, we included lines of H_2S 1(1,0)–1(0,1), $H^{13}CO^+$ (2–1), and also of CCS, SO_2, SO, HC_3N, and c-C_3H_2. We have detected the H_2S 1(1,0)–1(0,1) and $H^{13}CO^+$(2–1) with SNR$\geq$5, while the other lines remained undetected. The imaging and deconvolution of H_2S 1(1,0)–1(0,1) and $H^{13}CO^+$ (2–1) have been done with natural weighting using *Hogbom* algorithm and cleaned down to about one rms noise level. The *uv* tables of detection and non–detection lines are then used for further analysis. The maps of the detected line emissions are presented in the following Chapter 5.

Table 2.1 lists all the existing GG Tau data that have been observed using the ALMA, PdBI and NOEMA interferometers.

TABLE 2.1: ALMA and NOEMA observations of GG Tau A.

(1)	(2)	(3)	(4)	(5)
		ALMA observations		
^{12}CO(6–5)	691.473	$0.35'' \times 0.31''$, PA=104°	0.11	ALMA#2011.0.00059.S
^{12}CO(3–2)	345.795	$0.34'' \times 0.28''$, PA=−89°	0.11	ALMA#2012.1.00129.S
C^{18}O(3–2)	329.330	$0.19'' \times 0.14''$, PA=19°	0.11	ALMA#2015.1.00224.S
^{13}CO(3–2)	330.588	$0.22'' \times 0.16''$, PA=15∘	0.11	ALMA#2012.1.00129.S ALMA#2015.1.00224.S
CS(7–6)	324.883	$0.23'' \times 0.16''$, PA=−161°	0.43 0.11	ALMA#2012.1.00129.S ALMA#2015.1.00224.S
		NOEMA observations		
HCO^+(1–0)	89.188	$4.57'' \times 2.55''$, PA=−38°	0.30	PdBI: 1997
DCO^+(3–2)	216.112	$1.76'' \times 1.23''$, PA=17°	0.10	NOEMA:X06B
$H^{13}CO^+$(2–1)	173.507	$2.50'' \times 1.90''$, PA=15°	0.25	NOEMA:W17BA
H_2S 1(1,0)–1(0,1)	168.763	$2.50'' \times 1.90''$, PA=15°	0.25	NOEMA:W17BA

Note. **(1)**–Transition, **(2)**–Frequency (GHz), **(3)**–Beam, **(4)**–Spectral resolution ($\mathrm{km\,s^{-1}}$), **(5)**–Facilities and project code

2.4 Data analysis strategy

I have preformed two different types of analysis:

1) In order to study the morphology and kinematics of the system, I work in the *image*-plane limiting the study to measurements of the effective emissivity (namely ignoring issues of scale height, of flaring, of optical thickness and of temperature and assuming the source to be a thin disk). The goal of this study is to determine the global properties of the system.

2) In addition, I performed a radiative transfer modelling of the circumbinary disk with the aim to study molecular density and temperature profiles of the outer disk and to reveal as well as possible the gas emission inside the cavity of the system. These studies use a radiative transfer code to mimic a flaring protoplanetary disk with vertical and radial gradients of gas/dust density and temperature. The model is built in the *image*-plane and compared with the observations in *uv*-plane in order to avoid the non-linear effects introduced by the deconvolution process.

The following section, Section 2.4.1, introduce the radiative transfer equation and its solutions in Local Thermal Equilibrium (LTE) and non-LTE conditions as used in the radiative transfer code DiskFit (Section 2.4.2).

2.4.1 Radiative transfer equation

The specific intensity I_ν, defined as the amount of energy passing through a surface normal to the path, per unit of time, surface, bandwidth (measured in frequency units) and solid angle is conserved along its path as long as no local absorption or emission process takes place; it is evaluated along the direction of motion. The transfer equation for radiation propagating over a distance ds can then be written as

$$\frac{dI_\nu}{ds} = j_\nu - \alpha_\nu I_\nu \tag{2.13}$$

where j_ν and α_ν are the emission and absorption/extinction coefficients respectively.

Defining the optical depth as $d\tau_\nu = \alpha_\nu ds$ and the source function $S_\nu = j_\nu/\alpha_\nu$, the equation (2.13) can be re-written as:

$$\frac{dI_\nu}{d\tau} = -I_\nu + S_\nu \tag{2.14}$$

Both dust and gas can contribute to emission and absorption of radiation. The dust emission and absorption are given by:

$$\begin{aligned} j_\nu^{dust} &= \alpha_\nu^{dust} B_\nu(T_{dust}) \\ \alpha_\nu^{dust} &= \kappa_\nu \rho_{dust} \end{aligned} \tag{2.15}$$

where $B_\nu(T_{dust})$ is the Planck function of a black body emission at the dust temperature T_{dust}, κ_ν is the dust opacity, and ρ_{dust} is the density of the dust. The emission and absorption of the molecular gas is due to the spectral line transition between an upper level u and a lower lever l with energy $h\nu$,

$$\begin{aligned} j_\nu^{gas} &= \frac{h\nu}{4\pi} n_u A_{ul} \Phi(\nu) \\ \alpha_\nu^{gas} &= \frac{h\nu}{4\pi} (n_l B_{lu} - n_u B_{ul}) \Phi(\nu) \end{aligned} \tag{2.16}$$

where n_i is the level population of the level i, A_{ij} and B_{ij} are the Einstein coefficients (Wilson, Rohlfs, and Hüttemeister, 2009) for the transition from level i to level j, and $\Phi(\nu)$ is the normalised line profile of the transition.

$$\begin{aligned} B_{ul} &= \frac{c^3}{8\pi h\nu^3} A_{ul} \\ B_{lu} &= \frac{g_u}{g_l} B_{ul} = \frac{g_u}{g_l} \frac{c^3}{8\pi h\nu^3} A_{ul} \end{aligned} \tag{2.17}$$

where g_i is the statistical weight of level i.

For optically thick emissions and assuming Local Thermal Equilibrium (LTE), the specific intensity is equal to the Planck black body brightness distribution independently of the material:

$$I_\nu = B_\nu(T) \tag{2.18}$$

In many cases, molecular emissions are non-LTE, even in the case of CO molecules: although the excitation seems always to be close to LTE, there exists a level J (J > 3) for which the value of the Einstein A coefficient is large enough for the population to be subthermal. Solving radiative transfer problems in non-LTE conditions is difficult because of the interdependence of the molecular level populations and the local radiation field, requiring iterative solution methods and making some simplifying assumptions.

If we only take into account the global properties of the medium, the calculation can be greatly simplified by introducing a *geometrically averaged escape probability* β, the probability that a photon will escape the medium from where it was created. This probability depends only on the optical depth τ and is related to the intensity within the medium, and independent of the radiation field. It can be written as,

$$\overline{J_{\nu_{ul}}} = S_{\nu_{ul}}(1 - \beta) \tag{2.19}$$

For a given direction, defined by the direction cosine, μ, and frequency, ν, the optical depth τ is:

$$\tau(\nu, r, \mu) = \int \alpha(r, s, \mu) \phi(\nu - \nu_0 + \frac{v_0}{c} s \frac{dv_s}{ds}) ds \tag{2.20}$$

where α is the standard absorption coefficient, and ϕ is the normalized line shape function (a Gaussian function in most cases).

Assuming the value of the gradient dv_s/ds to be a constant a_0, and writing $x = \nu - \nu_0 + \frac{\nu_0}{c} a_0 \frac{s}{c}$, the optical depth τ can be expressed as

$$\tau(\nu, r, \mu) = \alpha(r) \frac{c}{a_0 \nu_0} \int \phi(x) dx \tag{2.21}$$

The escape probability averaged over the line and solid angle is,

$$\beta(r) = \int \int \phi(x) \exp(-\tau(x, r, \mu)) d\mu \, dx \tag{2.22}$$

Changing the variable $y = \int \phi(x) dx$ and using normalization $\int \phi(x) dx = 1$, we obtain,

$$\beta = \frac{1}{2} \int \frac{1 - \exp(-\tau(r, \mu))}{\tau(r, \mu)} d\mu \tag{2.23}$$

where $\tau(r, \mu) = (\alpha(r)c)/v_0 a(r, \mu)$

For a plane parallel geometry (slab):

$$\beta_{slab} = \frac{1 - e^{-3\tau}}{3\tau} \tag{2.24}$$

In a static, spherically symmetric and homogeneous medium, $dv(r)/dr = 0$, the escape probability becomes:

$$\beta_{sphere} = \frac{1.5}{\tau} [1 - \frac{2}{\tau^2} + (\frac{2}{\tau} + \frac{2}{\tau^2}) e^{-\tau}] \tag{2.25}$$

When there exists a velocity gradient that is large compared to the width of the velocity distribution at a given point, the LVG (Large Velocity Gradient) approximation, first introduced by Sobolev (1957) can be used. In this case:

$$\beta_{LVG} = \frac{1}{\tau} \int_0^\tau e^{-\tau'} d\tau' = \frac{1 - e^{-\tau}}{\tau} \tag{2.26}$$

2.4.2 DiskFit

DiskFit is a radiative transfer code which simulates dust and molecular line (CO,CS, ...) observations of a disk at mm/sub-mm wavelength. It models a flared disk with piece-wise radial power laws for the temperatures and surface densities. It produces a disk image, that can be compared with observations and solves the radiative transfer equation by a simple step by step integration along the line of sight (z) for a grid

of projected position (x, y) at each point z_i.

$$J_{i+1}(\nu) = (S_i - J_i(\nu)) \times (1 - exp(-d\tau_i)) + J_i(\nu) \tag{2.27}$$

This image is then Fourier transformed to the uv-plane in order to allow for a direct comparison with the observed visibilities. The difference between the predicted model visibilities and the observed ones is minimized using a modified Levenberg–Marquardt method, and the error bars are derived from the covariance matrix.

$$\chi^2 = \frac{\Sigma_i[(Re_{\mathrm{obs_i}} - Re_{\mathrm{mod_i}})^2 + (Im_{\mathrm{obs_i}} - Im_{\mathrm{mod_i}})^2]}{\Sigma\, i} \tag{2.28}$$

In DiskFit, a protoplanetary disk is characterised by the following parameters:

5 parameters to describe the disk geometry:

X_0, Y_0	(radian)	the star position
V_{disk}	(km s^{-1})	the LSR (systemic) velocity of the disk
PA	($^\circ$)	the position angle of the projection of the disk axis on the sky plane
i	($^\circ$)	the inclination of the disk w.r.t the sky plane

8 parameters to describe the relevant physical quantities: The rotation velocity (V), temperature (T), surface density (Σ), and pressure scale height (h) that control the line emission are parameterized using radial power laws:

$$a(r) = a_0(r/R_a)^{-e_a} \tag{2.29}$$

where a_0 and e_a correspond to the values taken by $a(r)$ at the reference radius R_a. Here, a stands for $V, T, \Sigma,$ and h)

The scale height, h is used to calculate the Gaussian density distribution $n(r, z)$:

$$n(r,z) = \frac{\Sigma(r)}{h(r)\sqrt{\pi}} \exp\left[-\left(z/h(r)\right)^2\right] \tag{2.30}$$

2 parameters to describe the edges of the disk: The outer, R_{out} and inner R_{in} radii of the emission region.

2 parameters to describe the line profile: The local line width, dV, and a radial power index e_v used to model the effect of turbulence.

Additional information about DiskFit can be found in (Dartois, Dutrey, and Guilloteau, 2003; Piétu, Dutrey, and Guilloteau, 2007). I had the opportunity to contribute to the development of a more friendly interface for DiskFit users.

Chapter 3

Morphology and kinematics of the disk surrounding GG Tau A[1]

3.1 Introduction

The present section studies the morphology and kinematics of the GG Tau A system using ALMA observations of (sub)millimeter emissions from the dust (continuum), and from various CO isotopologues. They include a first set of ALMA Cycle 1 observations of the dust emission at 0.9 mm and of the ^{13}CO(3–2) emission with an angular resolution of 0.35″, the latter exploring detailed properties of the gas disk, such as scale height at the inner edge, azimuthal dependence of the emission, Keplerian rotation of the gas, contribution of infalling gas toward the circumbinary disk. Possible contributions to the measured line width are discussed together with their correlation to the morpho-kinematics, suggesting an increase of the disk temperature and opacity when approaching the stars.

A second set of ALMA observations (Cycle 3) is used to refine the study of the ^{13}CO(3–2) emission using a better angular resolution ($\sim$ 0.15″) and to observe emissions from the ^{12}CO(3–2). Together with archived observations of ^{12}CO(6–5), and ^{12}CO(2–1), these data allow for a detailed investigation of the properties and morpho-kinematics of the outer disk. The radial dependence of the emission reveals inhomogeneity structures at the angular resolution of 0.15″ and its azimuthal dependence displays important differences between different molecules, which are critically discussed.

[1]The content of this Chapter is mostly adapted from 2 papers:
1) Phuong, N.T.; Diep, P.N.; Dutrey, A.; Chapillon, E.; Darriulat, P.; Guilloteau, S.; Hoai, D.T; Nhung, P.T; Tang, Y-W; Thao, N.T.; Tuan-Anh, P., 2018RAA, 18, 31P, DOI: 10.1088/1674-4527/18/3/31
2) Phuong, N.T.; Dutrey, A.; Diep, P.N; Guilloteau, S.; Chapillon, E.; Di Folco, E.; Tang, Y-W.; Pietu, V.; Bary, J.; Beck, T.; Hersant, F.; Hoai, D.T.; Hure, J.M.; Nhung, P.T.; Pierens, A.; Tuan-Anh, P., 2019, submitted to A&A

3.2 Geometry of the dust ring

3.2.1 Morphology of the dust ring

Figure 3.1 (left) maps the brightness of the 0.9 mm emission. It shows an elliptical ring surrounding a central source. The right panels show the projections on the x (right ascension offset) and y (declination offset) axes of the central source intensity integrated over y and x respectively. Gaussian fits give mean values of $0.06''$ and $-0.13''$ and FWHM values of $0.40''$ and $0.33''$ in x and y respectively, comparable to the beam size of ($0.39'' \times 0.29''$): the central source is unresolved.

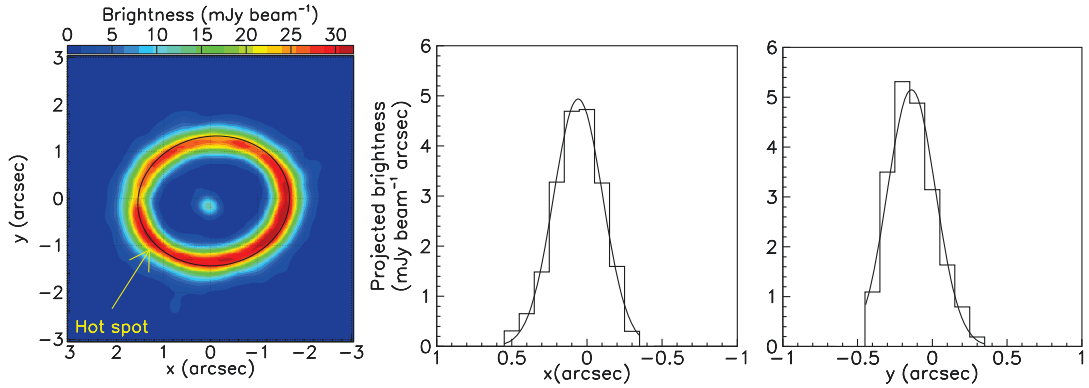

FIGURE 3.1: Brightness of the dust ring continuum emission. *Left*: sky map; the black ellipse is the fit to $\langle R \rangle$ shown in Figure 3.3; the yellow arrow points to the region of the hot spot observed by Dutrey et al. (2014) and Tang et al. (2016) in ^{12}CO(6–5) and ^{12}CO(3–2) emissions. *Middle and right*: projections on the x and y axes of the central source brightness integrated over y and x respectively. The lines show Gaussian best fits.

Figure 3.2 (left) displays the x and y projections of the continuum brightness integrated over y and x respectively. It requires the distance R' to the central source to exceed $0.5''$ ($R' = \sqrt{(x-0.06)^2 + (y+0.13)^2}$), thereby excluding its contribution. The corresponding mean values of x and y are $-0.05''$ and $-0.09''$ respectively, showing that the ring is shifted north-west by $\sim 0.12''$ with respect to the central source. The position and width measurements illustrated in Figure 3.1 and Figure 3.2 are accurate to be better than $0.02''$, using the residual of the fits to estimate measurement errors: they are dominated by systematics rather than simply by thermal noise. However, the angular separation between GG Tau Aa and Ab is $0.25''$: depending on what is being talked about, the position of the "centre" may vary by some $\pm 0.1''$. Figure 3.2 (right) displays the dependence on $R = \sqrt{x^2 + y^2}$ of the continuum brightness averaged over position angle $\varphi = 90^\circ - tan^{-1}(y/x)$ (measured counter-clockwise from north), again excluding the central source by requiring $R' > 0.5''$. A Gaussian fit to the peak gives a mean of $1.45'' \pm 0.02''$ and a σ of $0.27'' \pm 0.02''$ where the uncertainties account for the dependence on the interval of R over which the fit is performed. Retaining a σ value of $0.27''$ and subtracting the beam size in quadrature gives a de-convolved FWHM of $0.53'' \pm 0.04''$. Tang et al.

(2016) quote a value of 0.54″ for a square box fit, becoming 0.51″ for a Gaussian fit, in excellent agreement with the present result.

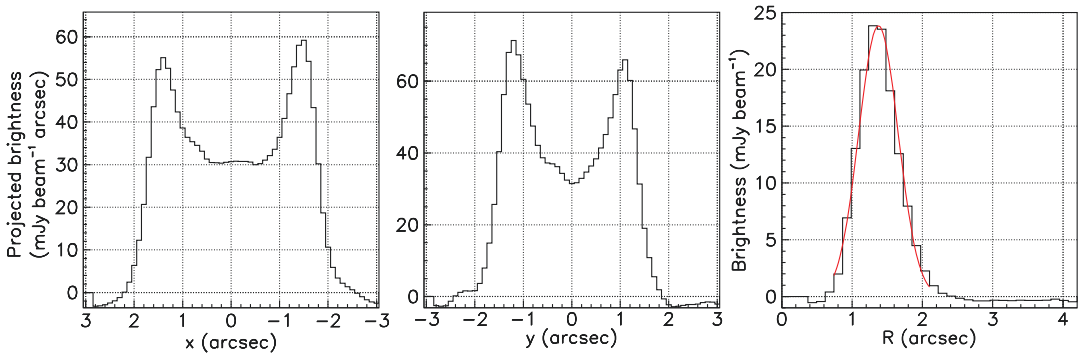

FIGURE 3.2: Continuum brightness of the dust ring emission projected on the x (left) and y (middle) axes and integrated over y and x respectively. The right panel shows its distribution as a function of R, averaged over φ, together with the Gaussian best fit to the peak. In all three panels pixels having $R' < 0.5''$ are excluded.

Figure 3.3 (left) displays the dependence on φ of the mean value of R, $\langle R \rangle$, weighted by the radial average of the brightness across the ring over the interval $1'' < R < 2''$. A fit of the dependence of $\langle R \rangle$ on φ as an ellipse of semi-major and semi-minor axes a_0 and b_0 and offset by Δx and Δy has been made to first order in the offsets and in the ellipticity:

$$R = \left[\frac{\cos^2(\varphi - \varphi_0)}{a_0^2} - 2\frac{\Delta x}{\sqrt{a_0 b_0}} \frac{\cos(\varphi - \varphi_0)}{a_0^2} + \frac{\sin^2(\varphi - \varphi_0)}{b_0^2} - 2\frac{\Delta y}{\sqrt{a_0 b_0}} \frac{\sin(\varphi - \varphi_0)}{b_0^2} \right]^{-1/2} \tag{3.1}$$

It gives $a_0 = 1.62''$ and $b_0 = 1.38''$, position angle of the major axis $\varphi_0 = 97°$ and small offsets $\Delta x = -0.07''$ and $\Delta y = -0.05''$, at the level of measurement uncertainties. This confirms the good centreing of the ring on the origin of coordinates and the aspect ratio corresponds to a tilt with respect to the sky plane $\theta = \cos^{-1}(1.38/1.62) = 32° \pm 4°$ of a circular ring about the rotated (by 7.0°) x axis.

These results confirm the values quoted by Tang et al. (2016): 1.63″ instead of 1.62″ for a_0, 7.5° instead of 7.0° for the position angle and 36.4° instead of 32° for the tilt with respect to the sky plane, the latter being measured to no better than ±4°. The values quoted for the tilt by Dutrey et al. (2014) are $37° \pm 1°$ for ^{12}CO(6–5) and $35.0° \pm 0.2°$ for the dust. Figure 3.3 (right) displays the dependence on position angle φ of the continuum brightness averaged over R in the interval $1'' < R < 2''$. Here we have used the fact that the ratio between the beam area in the sky plane and its de-projected value in the disk plane is equal to $\langle R \rangle / a_0$. In the disk plane the brightness is uniform over the disk circumference and equal to 16.0 mJy beam^{-1} to within ±8.5% (rms).

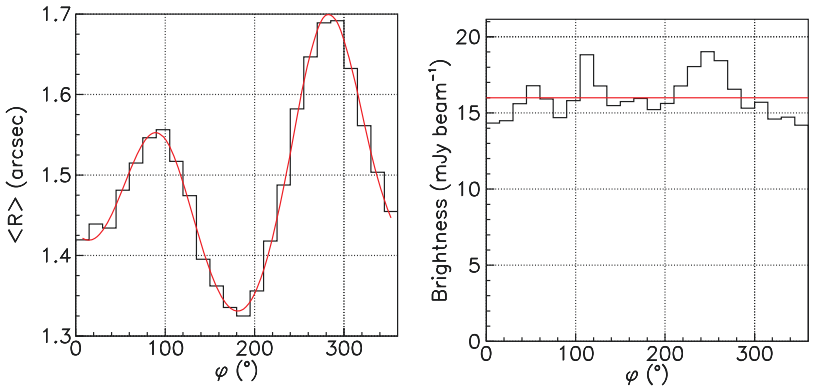

FIGURE 3.3: Continuum emission. *Left:* Dependence on φ of $< R >$ calculated in the interval $1'' < R < 2''$. The red line is the best fit to an elliptical tilted ring offset from the origin (see text). *Right:* Dependence on φ of the disk plane continuum brightness averaged over R in the interval $1'' < R < 2''$. The red line shows the mean value.

3.3 Morphology and kinematics of the gas disk obtained from observations of the ^{13}CO(3–2) emission

3.3.1 Morphology

General features

Figure 3.4 (left) displays the brightness distribution over the data cube elements. A Gaussian fit to the noise peak gives a mean of -0.19 mJy beam^{-1} and a σ of 7.2 mJy beam^{-1} (0.56 K). Figure 3.4 (right) displays the Doppler velocity (V_z) spectrum integrated over $8'' \times 8''$, with a double-horn profile typical of a rotating volume. It is centred to better than 0.1 km s^{-1}. In what follows, throughout the Chapter, we restrict the Doppler velocity range to $|V_z| < 2$ km s^{-1} unless specified otherwise.

Figure 3.5 displays the sky maps of the velocity-integrated brightness, or integrated intensity (left), and of the mean Doppler velocity (right). The map of the integrated intensity shows a clear disk of gas surrounding the central stars and having morphology similar to the dust morphology, indicating a concentric circular gas disk having the same inclination as the dust ring on the sky plane. It displays no central emission, with an abrupt inner cut-off at $1''$; there is no significant emission inside an ellipse scaled down from the dust ellipse by a factor 3, meaning a de-projected radius of $1.62''/3 = 0.54''$. The velocity map excludes the region inside the scaled-down ellipse where noise dominates. It displays a clear velocity gradient along the major axis of the ellipse, as expected from rotation of the tilted disk about its axis. Note that an infalling (rather than rotating) gas would display instead a gradient along the minor axis of the ellipse. In general adding some infall motion would cause the axis of the velocity gradient to deviate from the major axis, the more so the larger the relative contribution of infall.

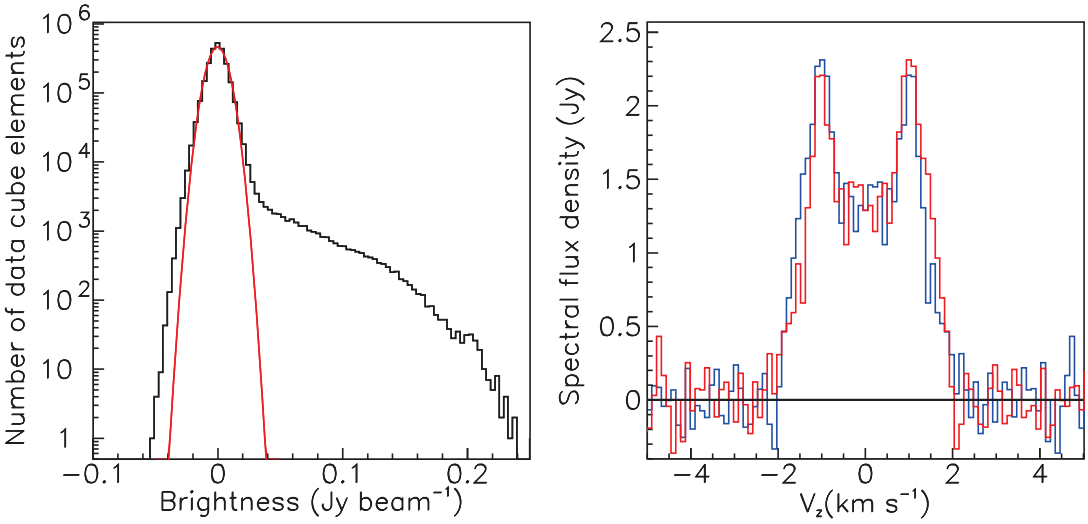

FIGURE 3.4: *Left:* Line brightness distribution (Jy beam^{-1}); the red curve is a Gaussian fit to the noise peak. *Right:* Doppler velocity spectrum weighted by brightness and integrated over $8'' \times 8''$ (blue); the red histogram is obtained from the original by symmetry about the origin.

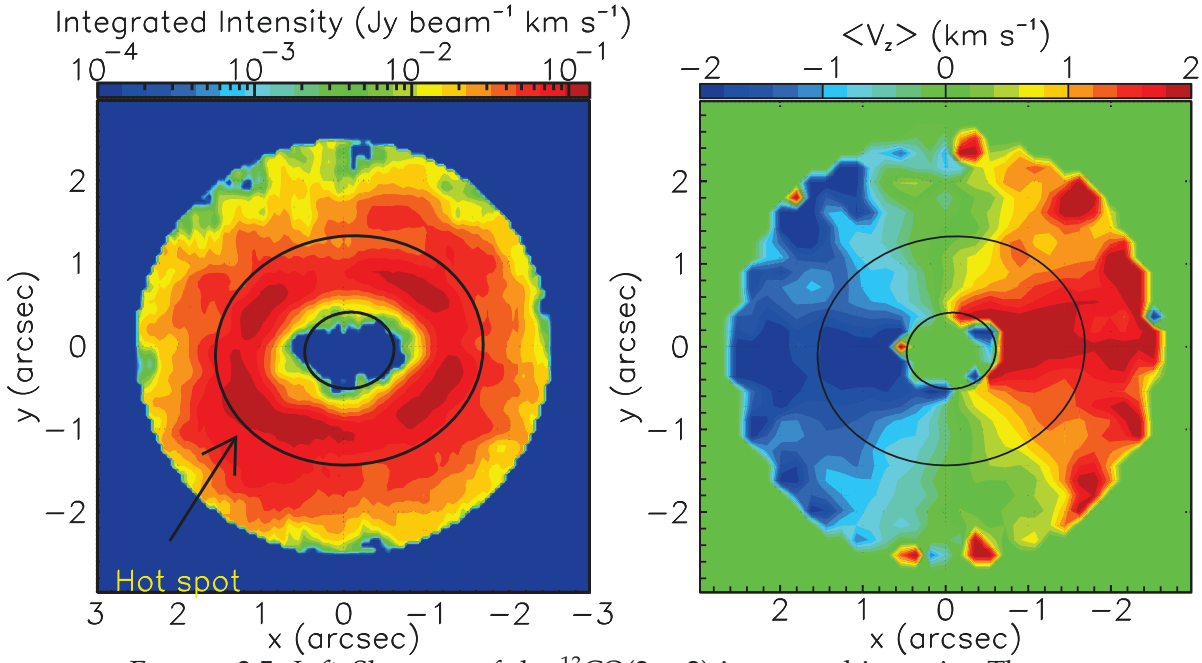

FIGURE 3.5: *Left:* Sky map of the ^{13}CO$(3-2)$ integrated intensity. The black arrow shows the position of the hot spot in ^{12}CO$(6-5)$ (Dutrey et al., 2014) and ^{12}CO$(3-2)$ (Tang et al., 2016). *Right:* Sky map of the mean Doppler velocity (weighted by brightness) excluding the region contained in the scaled-down ellipse shown in the left panel. In both panels $R < 2.5''$ and the black ellipses are the best fit to the distribution of $< R >$ in the continuum data and its scaled-down version (by a factor 3).

Figure 3.6 shows the projections on the x and y axes and r-dependence, averaged over $\varphi = 90^\circ - \tan^{-1}(y/x)$, of the integrated intensity, where r is the de-projected value of R in the disc plane (see Figure 3.8). Here, de-projection assumes a tilt angle of 32° and a position angle of the disk axis of 7°, as for the dust. In all panels we exclude the central region where noise dominates by requiring $r > 0.54''$. When compared with the dust (continuum) ring, the gas (line) ring is broader and peaks at smaller radii. The mean values of x and y are $0.02''$ and $-0.10''$ respectively. A fit to the integrated intensity distribution as a function of r as a sum of three Gaussians is shown in the right panel of the figure. The means and widths of the Gaussians are fixed to the values obtained by Tang et al. (2016) when fitting the western half of the gas disc.

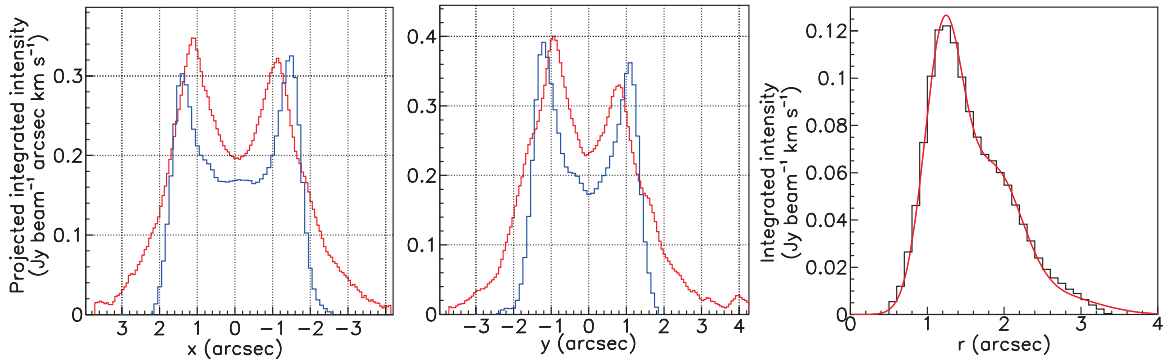

FIGURE 3.6: Line emission. *Left* and *middle:* Continuum brightness (blue, arbitrary normalisation) and line integrated intensity (red) projected on the x (left) and y (middle) axes in the region of $r > 0.54''$. *Right:* r-dependence of the integrated intensity averaged azimuthally in the disk plane. The red line is a fit using the same three Gaussians as in Tang et al. (2016).

Figure 3.7 displays the mean value of R, $< R >$, weighted by the brightness across the ring over the interval $0.54'' < r < 2''$. A fit of the dependence of $< R >$ on φ as an ellipse gives semi-major and semi-minor axes $a_0 = 1.45''$ and $b_0 = 1.19''$, position angle of the major axis $\varphi_0 = 97.8^\circ$ and small offsets $\Delta x = 0.02''$ and $\Delta y = 0.07''$. The position angle and aspect ratio (0.82 instead of 0.85) are very similar to the dust result, but the size of the ellipse is scaled down by a factor 87%. The tilt angle is now 35°, compared with 32° for the dust.

Another estimate of the tilt geometry is obtained from the map of the mean Doppler velocity (Figure 3.7, middle). In a ring defined as $0.54'' < r < 2''$, a fit of the form $< V_z >= V_0 - \Delta V \cos(\varphi - \varphi_0)$ gives $V_0 = 0.05$ km s^{-1}, $\Delta V = 1.73$ km s^{-1} and $\varphi_0 = 97.8^\circ$, again in excellent agreement with the value obtained from the dust fit, $\varphi_0 = 97.0^\circ$; this provides evidence against a significant infall contribution. The values quoted by Dutrey et al. (2014) are $97^\circ \pm 2^\circ$ for ^{12}CO$(6-5)$ and $96.5^\circ \pm 0.2^\circ$ for the dust. The value of ΔV, 1.73 km s^{-1} corresponds to a mean rotation velocity of $\Delta V / \sin\theta \sim 3.3$ km s^{-1}. Figure 3.7 (right) displays the dependence on φ of the disk plane integrated intensity averaged across the ring in the interval $0.54'' < r < 2''$. It

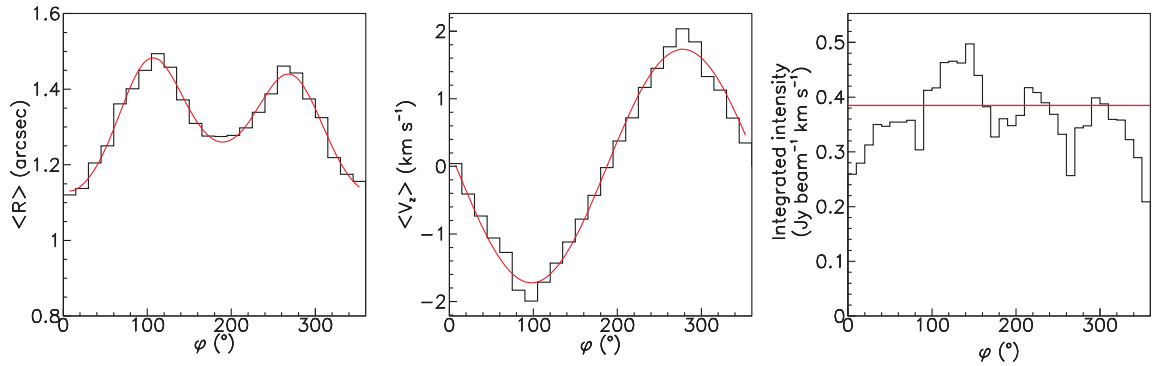

FIGURE 3.7: Line emission. *Left:* Mean value of R, $< R >$, weighted by the brightness across the disk over the interval $0.54 < r < 2$ arcsec. The red line is the result of the fit described in the text. *Middle:* Dependence on φ of the mean line Doppler velocity (brightness-weighted); the red line is the result of the fit described in the text. *Right:* Dependence on φ of the disk plane integrated intensity averaged across the disk ($0.54'' < r < 2''$). The red line shows the mean value.

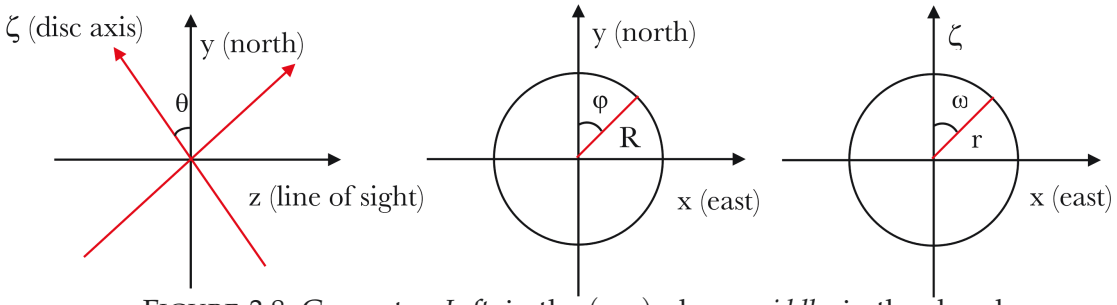

FIGURE 3.8: Geometry. *Left*: in the (y, z) plane; *middle*: in the sky plane (x, y); *right*: in the disk plane (x, ζ)

has a mean value of 0.39 Jy beam^{-1} km s^{-1} and fluctuates around it with an rms of 17%, showing a significant excess at the south-east quadrant ($\varphi = 100° - 150°$). Table 3.1 summarises the geometry parameters of the dust and ^{13}CO(3 − 2) emissions.

TABLE 3.1: Geometry parameters.

		Projection on x and y		Ellipse fitted to $\langle R \rangle$ vs φ					
		$\langle x \rangle$ ($''$)	$\langle y \rangle$ ($''$)	a_0 ($''$)	b_0 ($''$)	φ_0 (°)	Δx ($''$)	Δy ($''$)	θ (°)
Dust	Central source	0.06	−0.13	-	-	-	-	-	-
	Ring	−0.05	−0.09	1.62	1.38	97.0	−0.07	−0.05	32
^{13}CO(3-2)	Disk	0.02	−0.01	1.45	1.19	97.8	0.02	0.07	35

Disk thickness and integrated intensity variations across the disk: generalities

In the following two sections we use new coordinates obtained from those of the preceding sections by a rotation of angle 8° about the z axis. To within 1°, this brings the new x axis on the major axes of the ellipses found in the preceding sections as best describing the φ dependence of both $\langle R \rangle$ and the Doppler velocity. Moreover, unless otherwise explicitly specified, we assume a tilt $\theta = 35°$ of the disk plane as a reasonable compromise between values obtained in both earlier and the present studies, for both gas and dust observations. In practice, we use 99×99 pixels of $0.06'' \times 0.06''$ on the sky map, covering $(99 \times 0.06'') \times (81 \times 0.0733'') \sim 6'' \times 6''$ in the disk plane ($0.0733'' = 0.06''/\cos 35°$). To each pixel (x, y) we associate disk coordinates $\zeta = y/\cos\theta, r = \sqrt{x^2 + \zeta^2}$ and $\omega = 90° - tan^{-1}(\zeta/x)$. Here disk plane and disk coordinates are simply defined by this transformation, implying no assumption on the disk being actually thin and flat.

Estimate of the disk thickness obtained from the sharpness of the disk inner edge Tang et al. (2016) have commented on the sharpness of the inner edge of the $^{13}CO(3-2)$ emission and on the smallness of the vertical temperature gradient, the inner edge of the disk being directly exposed to stellar light and casting a shadow on the outer disk. Here, we compare the value of the smearing of the inner edge of the disk map near the major axis of the ellipse with its value near the minor axis. To a good approximation, the effect of disk thickness essentially cancels for the former while, for the latter, it scales with the product of the disk thickness by the sine of the tilt angle. The optical thickness of the line is not expected to strongly affect this result. We consider four angular sectors in the disk plane, each 60° wide and centred on the axes of the ellipse (see Figure 3.9). In each sector, we study the radial dependence of the integrated intensity, both in the disk plane (r) and in the sky plane (R).

The result is displayed in Figure 3.10. In order to evaluate the sharpness of the inner edge of the gas disk, we fit a Gaussian to the rise of each distribution, between $0.5''$ and $1.5''$ in r. In R, we use the same interval of $0.5''$ to $1.5''$ for the sectors centred on the major axis of the ellipse but a scaled-down (by a factor $\cos 35°$=0.82) interval of $0.41''$ to $1.23''$ for the sectors centred on the minor axes in order to account for the effect of the tilt. The mean and σ values (dispersions, a factor 2.35 smaller than FWHM values also commonly quoted in the literature) obtained for the Gaussian best fits are listed in Table 3.2.

The r–distributions show identical σ values, to within ± 10 mas, in the four angular sectors. A contribution from the disk thickness would cause these values to be larger in the minor-axis sectors than in the major-axis sectors: it is already clear that a significant contribution from the disk thickness is excluded. At variance with the distributions as a function of r, the distributions as a function of R show significantly different σ values for the major-axis sectors, $\sim 0.33''$, and the minor-axis sectors, $\sim 0.28''$, a factor 85% smaller. Similarly, the ratio between the mean values of the Gaussians (listed as "scaling factor" in the table) are equal for the two sectors

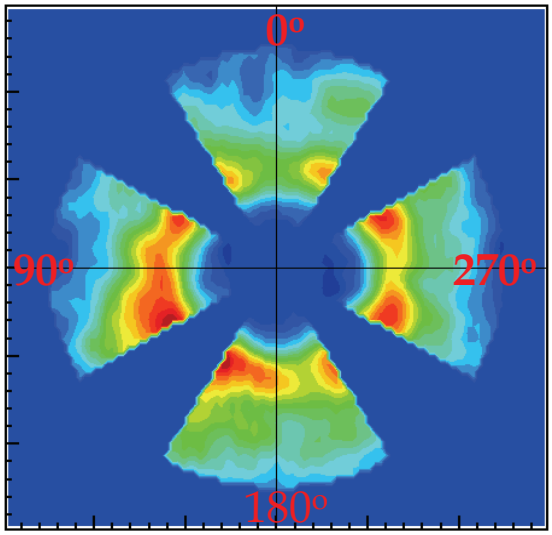

FIGURE 3.9: Integrated intensity map in the sectors used for the study of the disk thickness.

TABLE 3.2: Estimating the thickness of the gas disk from the sharpness of its inner edge projected on the sky plane. All values (except the scaling factors) are in arcsec.

		North	East	South	West
r fit	$\langle r \rangle$	1.15	1.31	1.24	1.34
	σ	0.32	0.34	0.33	0.32
R fit	$\langle R \rangle$	0.99	1.29	1.08	1.32
	σ	0.28	0.34	0.28	0.32
R fit, beam subtracted	σ	0.24	0.31	0.24	0.29
R fit, de-projected	Scaling factor	0.86	0.98	0.87	0.99
	σ	0.29	0.31	0.29	0.29

of a same axis of the ellipse, but again 85% smaller for sectors centred on the minor axis than for those centred on the major axis. The latter are very slightly smaller than unity, as expected from the 60° angular widths of the sectors. The consistency between these numbers suggests an interpretation of the σ values measured in the R distributions as the sum of three terms added in quadrature: i) a beam contribution of 0.14″ on both the minor- and major-axis sectors (calculated from the known beam parameters); ii) a contribution from the intrinsic smearing of the disk emission, σ_0, caused by effects such as density variations and contributing in each sector a value σ_0 scaled down by the scaling factors listed in the table; iii) an additional contribution σ_1 due to the disk thickness and contributing only to the minor-axis sectors. After subtraction of the beam contribution and correction for de-projection, one obtains values of σ of 0.29″ for the minor-axis sectors and $\sim$ 0.30″ for the major-axis sectors. A contribution σ_1 due to the disk thickness would cause the former to exceed the

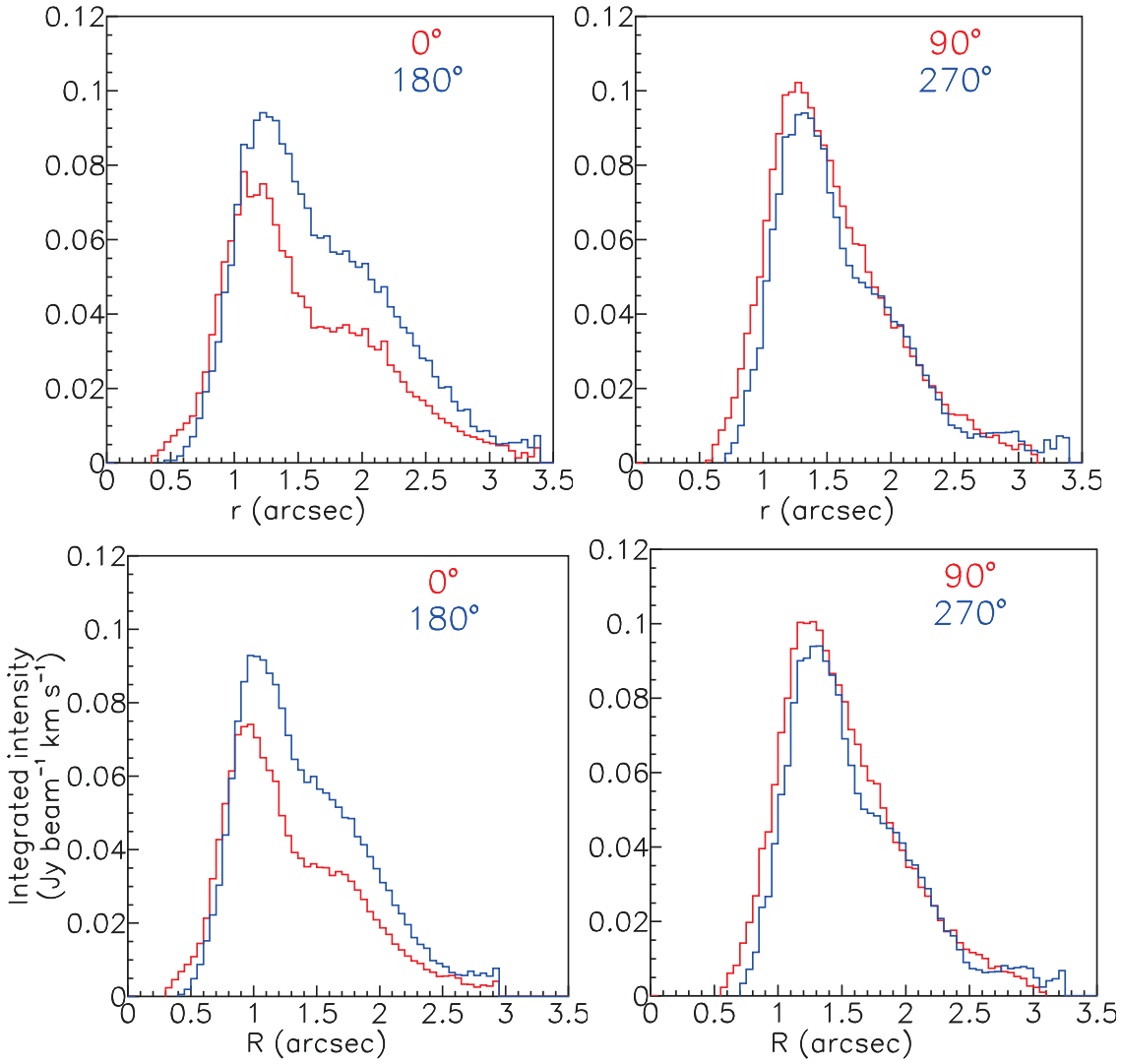

FIGURE 3.10: Disk thickness. Dependence on r (upper panels) and on R (lower panels) of the line integrated intensity averaged in 60° wide angular sectors centred on the ellipse axes. In each case, the leftmost panel is for minor-axis sectors and the rightmost panel for major-axis sectors. The central values of ω (upper panels) and φ (lower panels) are indicated in the inserts for each sector.

latter, at variance with what is observed. From the consistency between the numbers, we estimate an uncertainty of $\sim 0.02''$ on the Gaussian σs. To 95% confidence level (2σ) we obtain an upper limit for σ_1 of $\sqrt{(0.29+2\times0.02)^2-0.30^2} = 0.14''$, corresponding to a scale height $H(r) \sim 0.14/\sin 35° = 0.24''$ (34 au) at $r \sim 1''$ (140 au) where the Keplerian velocity is ~ 3 km s^{-1}; at 30 K, the sound velocity is ~ 0.5 km s^{-1} and hydrostatic equilibrium implies $H(r) = 0.5/3 = 0.17''$ compared with the $0.24''$ upper limit obtained above. We have checked that this result is independent of the width of the angular sectors (using 40° instead of 60° lowers the Gaussian σ's by $\sim 0.01''$). Depending on the interval chosen to calculate the Gaussian σ's

lower values of the σ_1 upper limit may be obtained, as low as 0.10″ instead of 0.14″. We conservatively prefer to retain the latter value as our final result.

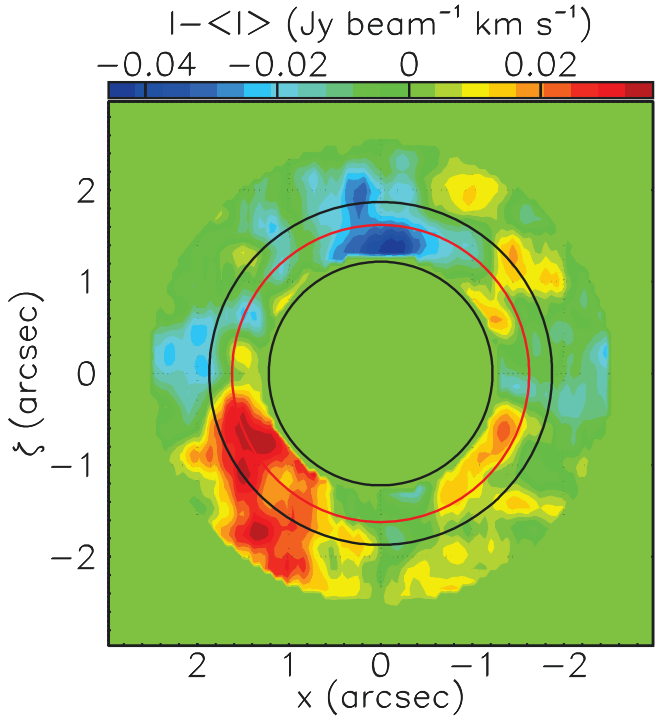

FIGURE 3.11: ^{13}CO(3 − 2) map in the disk plane of the difference between the integrated intensity and its value averaged over ω at the same r. The black circles show the maxima of the Gaussians describing the mean radial integrated intensity distribution, r=1.22″ and 1.87″ respectively. The red circle corresponds to the mean value of r in the dust map (1.62″).

Integrated intensity variations across the disk In order to better understand the nature of the integrated intensity variations displayed in Figure 3.7 (right), we display in Figure 3.11 the map in the disk plane of the difference between the measured integrated intensity and its value averaged over ω at the same value of r (as obtained from Figure 3.6, right). This map provides a measure of the lack of rotational symmetry of the integrated intensity in the disk plane. It gives strong evidence for an excess associated with the "hot spot" observed by Dutrey et al. (2014) and Tang et al. (2016) and for a northern depression of similar amplitude. Both excess and depression reach their maxima at a distance from the central stars corresponding to the gap between the maxima of the two first Gaussians describing the mean radial distribution of the integrated intensity (these Gaussians peak at r=1.22″ and 1.87″ respectively). It is also in this gap that the continuum dust emission peaks (at $r = 1.62''$). However, both excess and depression extend to larger values of r, particularly the former that extends out to $r \sim 2.5''$.

3.3.2 Kinematics

Keplerian rotation

Calling V_{rot} and V_{fall} the components of the disk plane velocity respectively perpendicular and parallel to the disk radius, the Doppler velocity reads $V_z = \sin\theta(V_{rot}\sin\omega + V_{fall}\cos\omega)$ for each data-cube element (x, y, V_z). To a good approximation, V_{fall} can be neglected and we can calculate $V_{rot} = V_z(\sin\theta\sin\omega)^{-1}$ for each data-cube element, leaving for later the task to reveal a possible small V_{fall} contribution. V_{rot} becomes trivially singular along the ζ axis. We require accordingly $|\sin\omega|$ to exceed 0.3 when calculating V_{rot}. As $\sin^{-1}(0.3) = 17.5°$, this is not much of a loss.

Figure 3.12 displays the dependence on ω and r of V_z averaged (using brightness as weight) over $0.8'' < r < 2.5''$ and over ω respectively. Averaging V_z requires some care in dealing with the noise: the interval used for averaging must be symmetric with respect to the mean value obtained as a result, which requires relaxing the condition $|V_z| < 2\ \mathrm{km\,s^{-1}}$ usually applied in the analysis. The ω-dependence is perfectly described by a sine wave of amplitude $1.43\ \mathrm{km\,s^{-1}}$. Adding a cosine term does not change the coefficient of the sine term and insignificantly improves the value of χ^2. Its amplitude is $0.05\ \mathrm{km\,s^{-1}}$, only 2.6% of the amplitude of the $\sin\omega$ term, corresponding to a shift of 1.9° in ω. As a check of the correctness of the procedure, we compare this result with what is obtained when requiring a 3-σ cut on each data-cube element; the amplitudes of the sine and cosine waves become 1.40 and $0.04\ \mathrm{km\,s^{-1}}$ respectively.

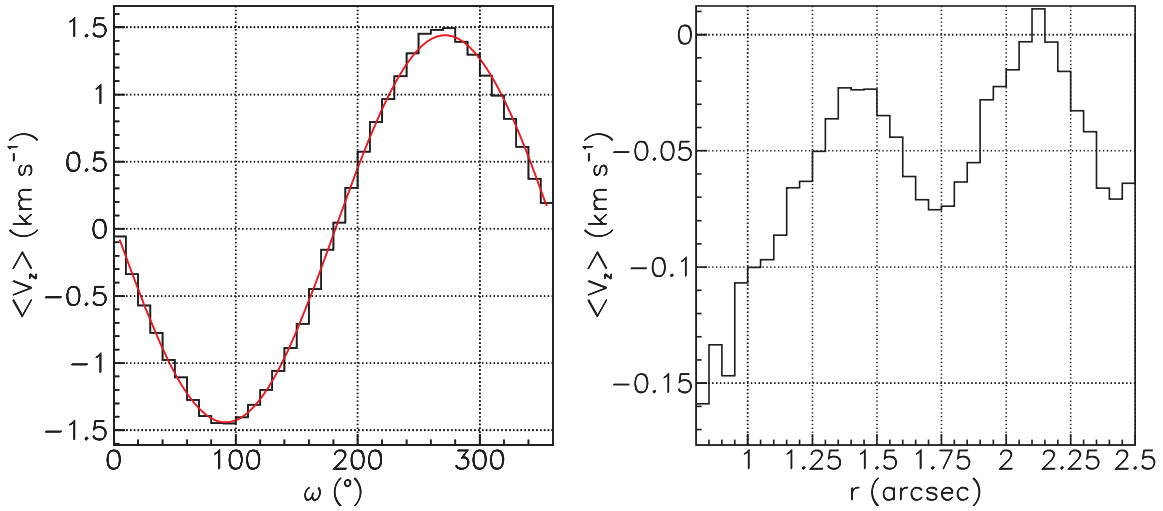

FIGURE 3.12: Distributions on ω (left) and r (right) of the Doppler velocity respectively averaged over $0.8 < r < 3.2$ arcsec and over ω. In the left panel, the line shows the best fit result, of the form $-1.43\sin\omega + 0.05\cos\omega\ \mathrm{km\,s^{-1}}$.

Assuming a 3° uncertainty on ω, corresponding to half a beam sigma at a distance of $1.3''$, we obtain a 3-σ upper limit (99% confidence level) of 9% on the ratio

V_{fall}/V_{rot}. As a function of r, averaging over ω would cause $\langle V_z \rangle$ to cancel if symmetry with respect to the ζ axis were perfect. It is indeed found very small, at the level of 0.05 km s^{-1} as soon as r exceeds the peak of the radial integrated intensity distribution at $r \sim 1.3''$.

Similarly, the dependence on ω and r of V_{rot} averaged respectively (using brightness as weight) over $0.8'' < r < 2.5''$ and over ω ($|\sin\omega| > 0.3$) is displayed in Figure 3.13. The left panel shows the distribution of $\langle V_{rot} \times r^{1/2} \rangle$ on r, which would be constant if the rotation were Keplerian. A fit in the interval $1.1'' < r < 2.5''$ gives a power index of -0.63 instead of the Keplerian -0.5 and $< V_{rot} >= 3.0$ km s^{-1} at $r = 1''$. The middle panel illustrates the difficulty to measure V_{rot} reliably due to its singularity on the ζ axis. As remarked earlier, the binarity of the central star prevents the position of the "center"to be defined to better than some $\pm 0.1''$ (more exactly such a definition requires modelling properly the binary configuration). Shifting the origins of x and y on the sky map by 1 pixel size (± 0.06 arcsec) changes the value of ω and therefore of V_{rot}. The result displayed in the middle panel shows the importance of the effect. As a result, increasing the $|\sin\omega|$ cut from 0.3 to 0.707 ($\sin 45^\circ$) makes the $< V_{rot} \times r^{1/2} >$ distribution Keplerian with a power index of -0.51 instead of -0.63, the rotation velocity at $r = 1''$ increasing from 3.0 to 3.1 km s^{-1} (left panel). We show in the right panel the map of $V_{rot}\, r^{1/2}$ in the disk plane. It is uniform except for increases near the ω limits in the north-west and south-east directions. These are largely artefacts due to the difficulty of calculating reliably V_{rot} near the ζ axis. Note that Dutrey et al. (2014) quote a V_{rot} value of 3.4 ± 0.1 km s^{-1} for ^{12}CO(6-5) emission with an index of -0.5 ± 0.1 at $r = 100$ au; this corresponds to 2.9 km s^{-1} at $r = 1''$, consistent with the 3.0 km s^{-1} observed here for ^{13}CO(3-2) emission.

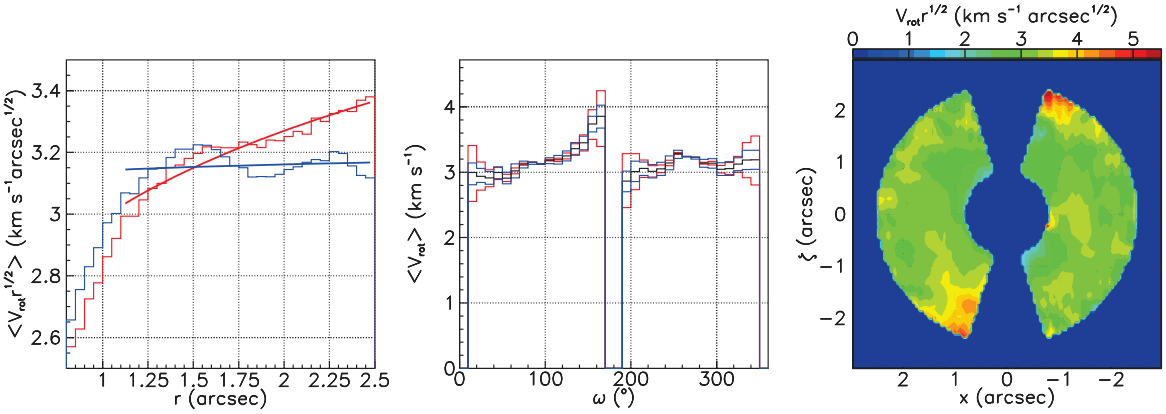

FIGURE 3.13: *Left:* Dependence on r of $\langle V_{rot} \times r^{1/2} \rangle$ (brightness-weighted average); the lines are the best power law fits with indices -0.63 for $|\sin\omega| > 0.3$ (red) and -0.48 for $|\sin\omega| > 0.707$ (blue). *Middle:* Dependence on ω of $\langle V_{rot} \rangle$ (averaged in the interval $0.8'' < r < 2.5''$) calculated using the nominal origin of coordinates on the sky plane (black histogram) or by shifting the origin by $\pm 0.06''$ in either x or y (red and blue histograms). *Right:* De-projected map of $\langle V_{rot} \times r^{1/2} \rangle$ ($|\sin\omega| > 0.3$).

Line width

Figure 3.14 displays the dependence of the brightness on the difference dV_z between the values of V_z measured in a given pixel and their mean values in that same pixel. The mean is calculated using brightness as a weight and the histogram is summed over all pixels in the interval $0.8'' < r < 2.5''$. A Gaussian fit gives a σ-value of 0.23 km s^{-1}.

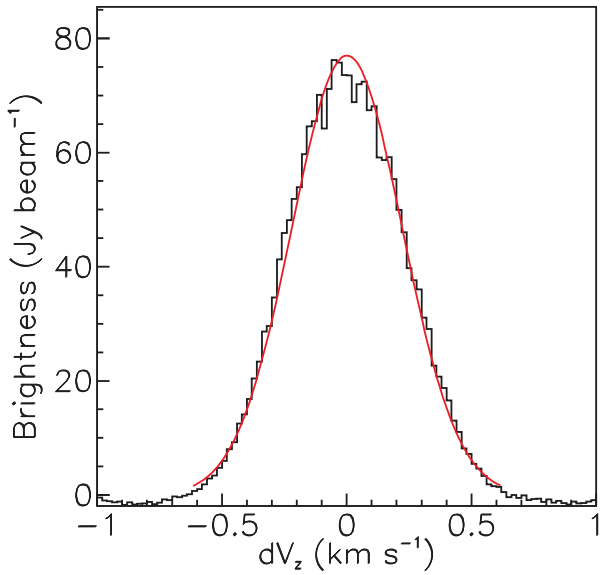

FIGURE 3.14: Dependence of the brightness on the difference dV_z between measured values of V_z their mean values in the pixel. Summing is over all pixels in the interval $0.8'' < r < 2.5''$. The curve is a Gaussian fit.

Several quantities, added in quadrature, are expected to contribute to σ_{vz}: Keplerian shear σ_K associated with both beam size and disk thickness, the instrumental resolution σ_I and the thermal broadening σ_T, possibly including a turbulence contribution (Teague et al., 2016), and opacity broadening, σ_τ.

Averaged over ω, the Keplerian shear at $r = 1.5''$ reads, from the derivative of a power law, $\sigma_K = 0.6\langle|V_z|\rangle\sigma_r/r$ where 0.6 stands for the power index of the radial V_{rot} distribution (it would be 0.5 in a pure Keplerian case). Here, σ_r is the sum in quadrature of the σ's of beam, $0.21''$, and of the disk thickness multiplied by $\tan\theta = 0.7$, $0.11''$. Hence, $\sigma_r \sim \sqrt{0.21^2 + 0.11^2} = 0.24''$ and
$\sigma_K = 0.6 \times \sin(35^\circ) \times 3.1 \times 1.5^{-0.6} \times (2/\pi) \times \sigma_r/1.5 = 0.09$ km s^{-1}. Taking the FWHM of the instrumental resolution as one velocity bin gives $\sigma_I \sim 0.05$ km s^{-1}. Thermal broadening proper reads $\sqrt{2kT/M_{co}}$ where k is Boltzmann constant, T the temperature and M_{co} the mass of the ^{13}CO molecule; at $T = 18$ K (Tang et al., 2016) it amounts again to some 0.10 km s^{-1}. Opacity tends to flatten the line profile and its effect is an effective broadening of $\sim \sqrt{ln(\tau)}$, where τ is the line opacity (Piétu, Dutrey, and Guilloteau, 2007). Tang et al. (2016) show that ^{13}CO(3-2) and ^{12}CO(3-2)

have similar brightness, implying that $\tau(^{13}\mathrm{CO})$ is significantly above unity. Using both ^{13}CO(3-2) and ^{12}CO(3-2), we estimate its value to be $\tau \sim 10$, meaning an effective broadening of $\sim$1.5 and a joint contribution of ~ 0.15 km s^{-1} for thermal and opacity broadening. A possible additional source of broadening could be the effect of noise. However, using a 3-σ cut to select the data, which must underestimate the measured value of σ_{vz}, we obtain 0.20 instead of 0.23 km s^{-1}, showing that noise can be neglected within our estimated uncertainty of $\pm$0.03 km s^{-1}.

Adding the estimated contributions in quadrature gives a total contribution of $\sqrt{0.05^2 + 0.09^2 + 0.15^2} = 0.18$ km s^{-1} compared with 0.23 ± 0.03 km s^{-1} measured: there is not much room left for additional contributions and turbulence is small (highly subsonic) in this disk.

Important additional information on the line width can be obtained from a study of the variations of σ_{vz} over the disk plane. To this end we consider three r intervals, 0.4″ wide, covering between 1.3″ and 2.5″ and 24 ω-intervals, 15° wide, covering between 0 and 360°. The dependence on ω of the integrated intensity is shown in Figure 3.15 (left) for each r-interval separately. The hot spot sticks out at values of ω that increase from $\sim$ 120° in the low r-interval to $\sim$ 150° in the high r-interval. The middle panel shows the dependence on ω of the normalized value of V_z averaged in each r-ω bin separately; more precisely a fit of the form $\langle V_z \rangle = -a \sin\omega - b\cos\omega$ is performed in each r-ω bin separately and the normalization is made by dividing each of the three distributions by the corresponding value of a (respectively 1.46, 1.27 and 1.18 km s^{-1}, namely $\sim$ 1.78 km s^{-1} divided by $\langle r \rangle^{1/2}$). The values of b are between 0.02 and 0.03 km s^{-1} and can be neglected: all three normalized histograms are well described by a sine wave. The right panel displays the dependence on ω of σ_{vz}: in each r-ω interval the σ of a Gaussian fit to the peak of the Doppler velocity spectrum is plotted after normalization to its value averaged over ω in the corresponding r-interval (0.258, 0.210, and 0.181 km s^{-1} respectively).

As a function of ω, the line width fluctuates relatively less than the integrated intensity. Moreover, there is no sign of a sine wave contribution that would signal the effect of Keplerian shear, confirming the conclusion that was reached above. While the "hot spot" dominates the variations of the integrated intensity, its presence is barely visible as an increase of the line width; conversely, sharper line width excesses at $\omega \sim 60°$ and 320° are visible on the velocity-integrated distribution as less marked excesses. The depressions at $\omega \sim 0°$, 90° and 270° are also associated with lower values of the line width. The correlation between σ_{vz} and fluctuations of the integrated intensity f is illustrated in Figure 3.16. In each (r, ω) bin we define $\Delta\sigma$ and Δf as the difference between the values of σ_{vz} and f and their mean in the r interval: $\Delta\sigma = \sigma_{vz} / < \sigma_{vz} > -1$ and $\Delta f = f / < f > -1$. A clear positive correlation is evidenced from the best linear fit, $\Delta\sigma = 0.32\,\Delta f$. Note that the correlation is even slightly stronger if one excludes the hot spot region, the corresponding Pearson coefficients being respectively 0.25 and 0.32. From the low-r interval to the high-r interval the ω-averaged line width (σ) decreases by a factor 0.70 while the amplitude of the V_z sine wave decreases only by a factor 0.81. A possible explanation may be

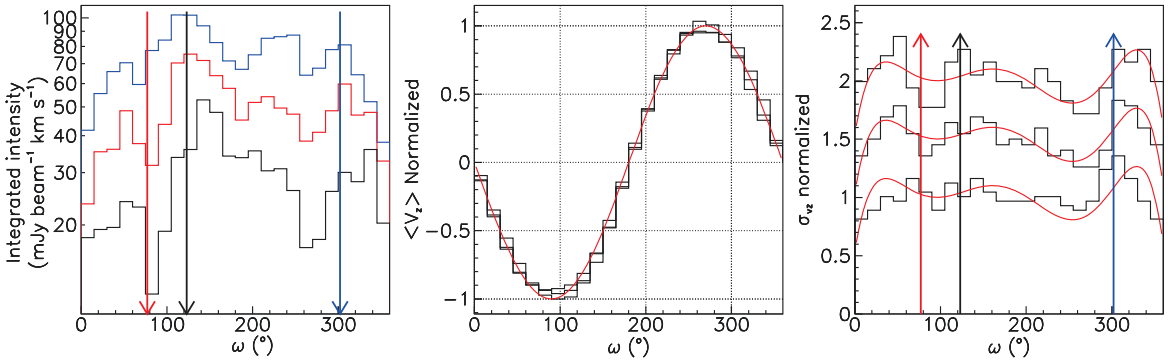

FIGURE 3.15: *Left:* Dependence on ω of the integrated intensity for $1.3'' < r < 1.7''$ (blue), $1.7'' < r < 2.1''$ (red) and $2.1'' < r < 2.5''$ (black); *Middle:* dependence on ω of the value of $\langle V_z \rangle$ in each of the three r-intervals (black histograms); here, $\langle V_z \rangle$ has been divided by 1.46, 1.27 and 1.18 km s^{-1} respectively, making the three histograms nearly identical; the red curve is a sine wave. *Right:* dependence of σ_{vz} on ω, for each r-interval separately; in each r-ω bin, a Gaussian fit is performed to the peak of the V_z spectrum, giving a σ-value that averages to respectively 0.258, 0.210 and 0.181 km s^{-1}; the plotted histograms are normalized to these respective average values; in addition, for clarity, they are shifted up by respectively 0, 0.5 and 1. The red curve, a sixth degree polynomial fit to the distribution of the central r-interval, is shown to guide the eye. In the left and right panels the arrows point in the direction of increasing r and indicate remarkable features: the black arrow shows the hot spot as defined from the left panel, the blue and red arrows show peaks of the line width as defined from the right panel.

an increase of the temperature and opacity with decreasing r. An increase of temperature and opacity from (T, τ)=(18 K, 5) at $r \sim 2.3$ arcsec to (36 K, 10) at $r \sim 1.5$ arcsec would imply an effective thermal broadening increasing from ~ 0.13 km s^{-1} to about 0.21 km s^{-1}. Adding in quadrature σ_K and σ_I contributions of respectively 0.09 and 0.05 km s^{-1} would give respectively 0.15 and 0.23 km s^{-1}, compared with 0.18 and 0.26 km s^{-1} being measured.

The fact that the ω-dependence of $\langle V_z \rangle$ is very well described by a simple sine wave in each of the three intervals implies that the observations are consistent with V_{rot} being independent of ω. It shows again that the fluctuations of $V_{rot}\, r^{1/2}$ observed in Figure 3.12 are affected by very large uncertainties. Indeed, very good fits to the measured V_z sky map are obtained by assuming a purely Keplerian rotation velocity. On the contrary, we estimate that the uncertainty attached to both $\langle V_z \rangle$ and σ_{vz} is of the order of only 0.02 km s^{-1}, making the discussion of the line width in terms of σ_{vz} more reliable than in terms of V_{rot} dispersion.

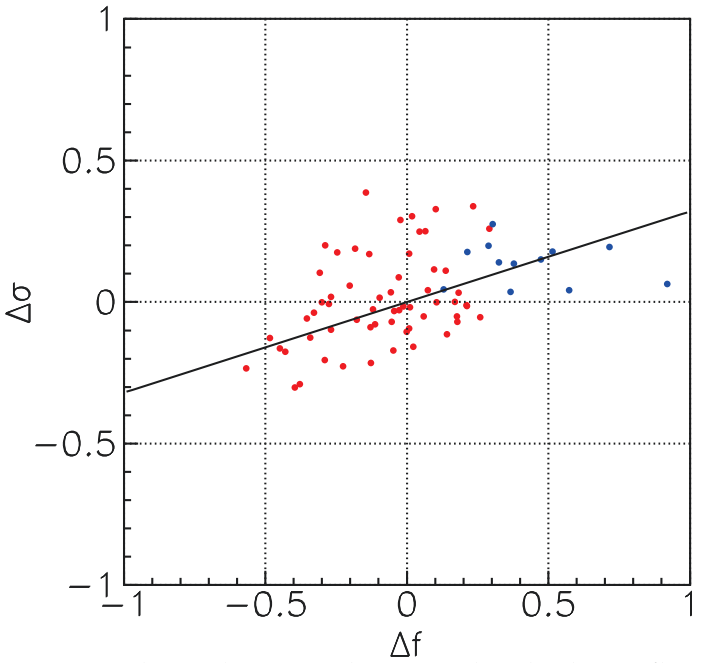

FIGURE 3.16: Correlation between the normalized relative fluctuations of the line width $\Delta\sigma$ and the integrated intensity Δf (see text). The line is the best fit to the data, $\Delta\sigma = 0.32\Delta f$. The blue points are for $105° < \omega < 165°$ (hot spot).

3.4 Multiline studies

3.4.1 Radial and azimuthal dependence of the emission of CO isotopologues across the disk

The Section uses observations of (sub)millimetre emissions of different molecules: ^{12}CO(6–5), ^{12}CO(3–2), ^{12}CO(2–1), ^{13}CO(3–2) and C^{18}O(3–2). The ^{12}CO(6–5), ^{12}CO(3–2) and ^{12}CO(2–1) data have been reported in Dutrey et al. (2014) and Tang et al. (2016).

Figure 3.17 shows the integrated intensity and velocity maps of ^{13}CO(3–2) (left) and C^{18}O(3–2) (right). In these figures, the continuum has been subtracted. The velocity maps suggest rotation inside the disk.

The ^{13}CO(3–2) emission extends out to 550 au, while the C^{18}O(3–2)emission is mostly visible in the dense ring.

Figure 3.18 (upper panels) shows the radial profile of all the integrated emission for all lines after de-projection to the disk plane. The de-projection has been done assuming a position angle of the minor disk axis of 7° and an inclination of 35°.

The ^{12}C^{16}O emission covers a broad region around the central binary, $r \leq 6''$ (800 au), peaking at the centre. Some of the differences between the three CO transitions may result from calibration effects and different uv coverages. In particular, short spacings are missing in the CO$(6-5)$ transition data because of the high frequency, making it less sensitive to extended structures.

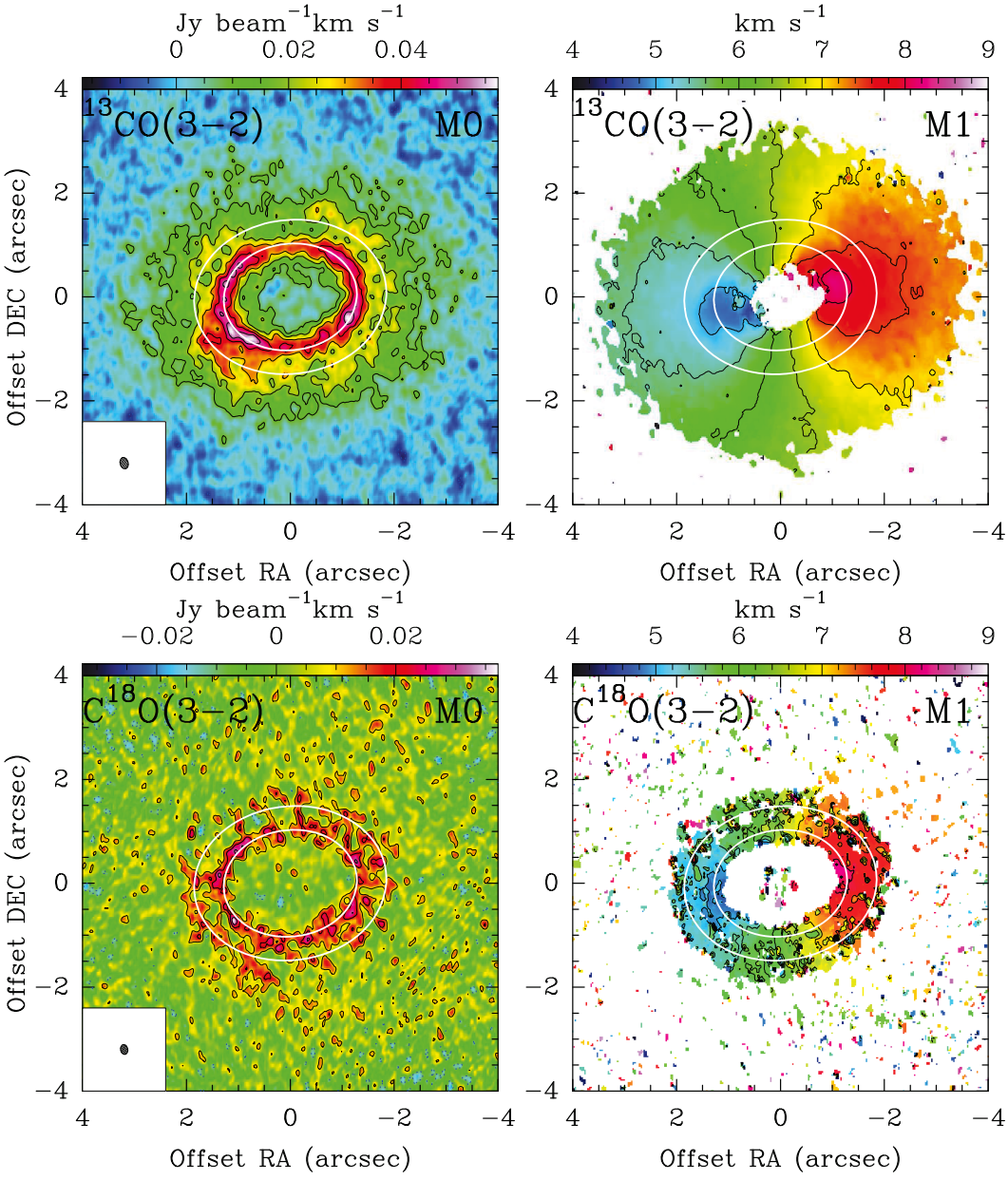

FIGURE 3.17: *Upper panel:* ^{13}CO(3–2) integrated intensity map (left, contour spacing of 0.01 Jy/beam km s^{-1} (3 σ) with zero level omitted) and velocity map (right). *Lower panel:* C^{18}O(3–2) integrated intensity map (left, contour spacing of 0.01 Jy/beam km s^{-1}, 2 σ) and velocity map (right). The beams are indicated in the lower left corner of each intensity map. The contour level spacing in velocity maps is 0.5 km s^{-1}. The continuum has been subtracted. The white ellipses indicate the inner and outer edges of the dust ring.

Figure 3.18 (lower panels) displays the azimuthal dependence (in the disk plane) of the peak brightness and velocity integrated brightness in the ring ($1.2'' \leq r \leq 2''$) for CO, ^{13}CO, C^{18}O, and the 0.85 mm continuum emissions. The azimuth ω in the disk mid-plane is measured counter-clockwise from the minor axis (north). The

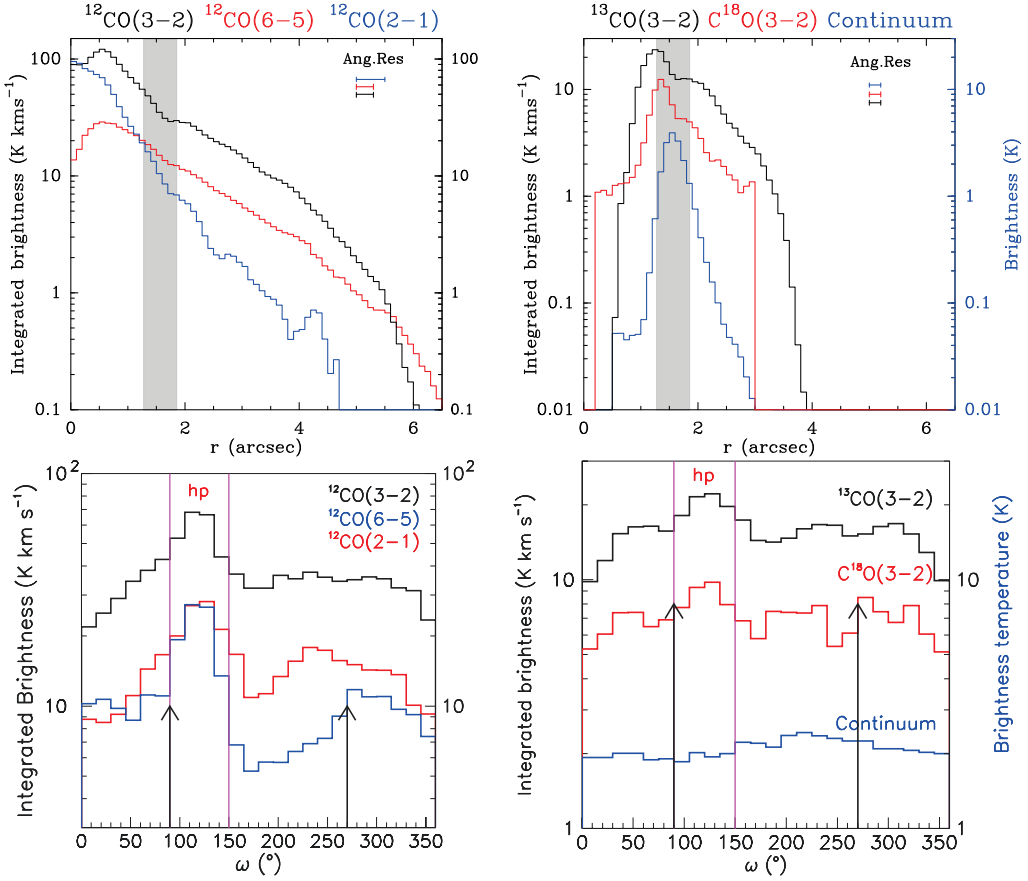

FIGURE 3.18: *Upper panels:* Radial dependence of the integrated brightness temperature in the disk plane. In the right panel, the continuum histogram shows the brightness temperature. The horizontal sticks indicate the angular resolutions. The grey bands delineate the dust ring. In the lower panels. *Lower:* The azimuthal dependence of the same quantities averaged over the ring $1.2'' < r < 2.0''$. The left panels display the three ^{12}CO emissions (J=6–5, 3–2 and 2–1), the latter being taken from Dutrey et al. (2014); the right panels show the less abundant CO isotopologues (J=3–2) emissions. Black arrows show the location of the limb brightening peaks and magenta lines show the "hot spot" location.

significant enhancement in the south-eastern quadrant for $^{12}C^{16}O$ corresponds to the "hot spot" observed by Dutrey et al. (2014), that may reveal a possible planet in formation (labelled "hp" for " hypothetical planet" in the figure). The "hot spot" is much less visible in the other CO isotopologues.

In Figure 3.18 we also notice the existence of two peaks in CO isotopologues. Their azimuth does not exactly correspond to the location of the limb brightening effects (at 90 and 270°, in the disk reference frame) that naturally result from the increased velocity coherence length in an inclined rotating disk.

3.4.2 CO gas kinematics in the outer disk

We expect different emissions to display identical Doppler velocity distributions in a given pixel to the extent that the radial ranges probed along the line of sight are the same. To check on this, Figure 3.19 compares the mean Doppler velocities measured in a same pixel for different lines. Each pixel contribution is weighted by the geometrical mean $(I_1 I_2)^{1/2}$ of the velocity integrated intensities I_1 and I_2 measured in the pixel for each of the two lines. The mean values of the central velocity are indeed very small, -0.02 and 0.01 km s^{-1}; their σ's are 0.08 and 0.15 km s^{-1} for ^{12}CO(3–2) vs ^{13}CO(3–2) and ^{12}CO(3–2) vs ^{12}CO(6–5) respectively.

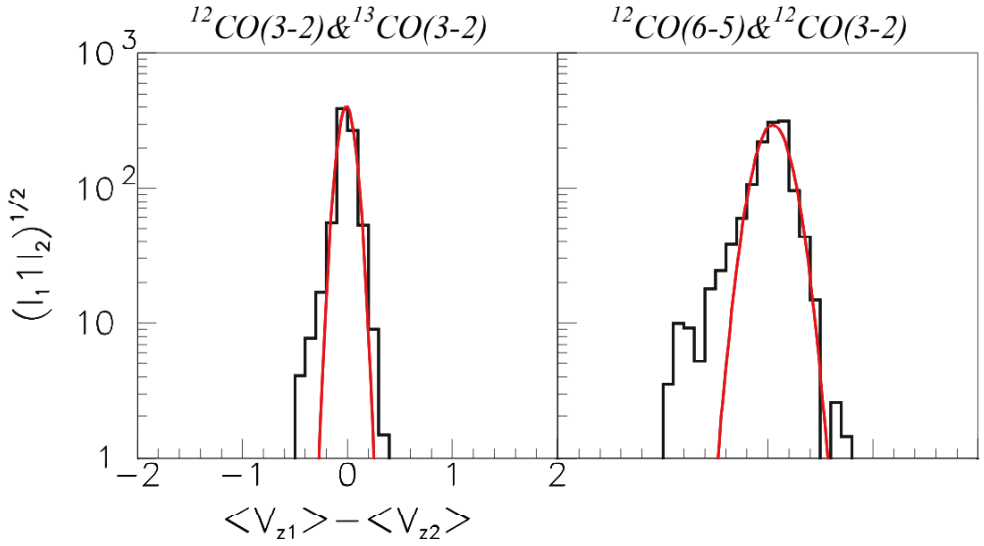

FIGURE 3.19: Distribution of the difference between the measurements of the mean Doppler velocity in a same pixel for ^{12}CO (3–2) vs ^{13}CO (3–2) (left) and for ^{12}CO (3–2) vs ^{12}CO (6–5) (right).

These figures show remarkable overall agreement of the mean Doppler velocities between the three sets of observations, to better than 0.02 km s^{-1} on average, and more generally between all line observations. This is different from what is observed for the intensity of the emission. Indeed, the latter depends on the excitation energy, on the gas temperature, on the optical thickness and is sensitive to azimuthal

inhomogeneity. On the contrary the rotation velocity is the same for all as long as the regions probed along the line of sight are the same. For example, comparing the ^{12}CO(3 − 2) and ^{13}CO(3 − 2) data, we find that they can accommodate a $\sim 0.06''$ shift in y, meaning some 10 au vertically (i.e. parallel to the disk axis), but not much more. Moreover, a remarkable result is that the dominance of rotation extends inside the ring as will be shown in the following Chapter.

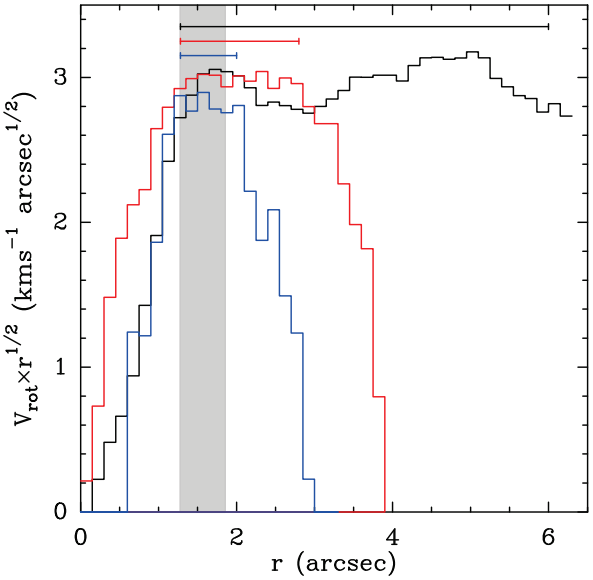

FIGURE 3.20: Dependence on r of $V_{rot} \times r^{1/2}$ (weighted by the brightness and averaged in r bins of $0.15''$) of ^{12}CO(3–2) (black), ^{13}CO(3–2) (red) and C^{18}O(3–2) (blue) emissions. The horizontal bars indicate the radial range over which the mean value is calculated for each transition. The grey shaded area cover the dense dust ring.

We calculate the rotation velocity $V_{rot} = V_z(\sin\theta \sin\omega)^{-1}$ for each data cube element separately, neglecting a possible in-fall contribution on the basis of the results obtained in the preceding section and excluding the region $|\sin\omega| < 0.707$. The result is illustrated in Figure 3.20, which shows the dependence of $\langle V_{rot} \times r^{1/2} \rangle$ on r, which should be constant for the three CO isotopologues if the rotation is Keplerian. There is a good overall agreement between the three isotopes, showing that the outer ring and disk are in Keplerian rotation beyond about 180 au. Constant fits to these histograms perform in a radial range where the SRN is large enough, give $V_{rot} \approx 2.94\,\mathrm{km\,s^{-1}}$, standard deviation ($\sigma$) of $0.14\,\mathrm{km\,s^{-1}}$ of the residuals from the mean for CO, $2.98\,\mathrm{km\,s^{-1}}$ ($\sigma = 0.04\,\mathrm{km\,s^{-1}}$) for ^{13}CO and $2.81\,\mathrm{km\,s^{-1}}$ ($\sigma = 0.07\,\mathrm{km\,s^{-1}}$) for C^{18}O, at $\approx 1.0''$. The formal errors on these mean values will be 2 to 3 times smaller, depending on the number of independent points, which is not a simple value given our averaging method. The CO data show deviations from the mean which are not random, since they occur on a radial scale of $\approx 0.8''$, more than twice the resolution.

We conservatively use the standard deviation as the error on the mean, and derive a mean weighted value of $2.94 \pm 0.03\,\mathrm{km\,s^{-1}}$ for the Keplerian speed at $1''$, i.e.

$3.48 \pm 0.04\,\mathrm{km\,s^{-1}}$ at 100 au, in agreement with previous, less precise determinations (e.g. Dutrey et al. (2014) found $3.4 \pm 0.1\,\mathrm{km\,s^{-1}}$). Taking into account the uncertainty on the inclination, $\pm 2°$, this corresponds to a total stellar mass of $1.36 \pm 0.07\,\mathrm{M_\odot}$.

3.4.3 The "hot spot"

Figure 3.21 displays the sky maps of the intensities measured in the ring $1'' < r < 2''$, where the "hot spot" is present. All three emissions display a south-eastern excess for $120° < \omega < 210°$, which corresponds to the "hot spot" position in Dutrey et al. (2014) and Tang et al. (2016). But they also show an excess at opposite azimuth (not at the same radius as the "hot spot"): it suggests distinguishing between four quadrants centred on 15°, 105°, 195° and 285° respectively. Moreover, the excess is limited to lower values of r in the western quadrant while it is tailing to higher values of r in the eastern quadrant. Accordingly, we split each quadrant in two regions, $1'' < r < 1.5''$ and $1.5'' < r < 2''$ respectively. The line profiles display no difference between the 4 quadrants of a same sub-ring. Table 3.3 lists the associated line widths (*rms* values), which are indeed equal within errors.

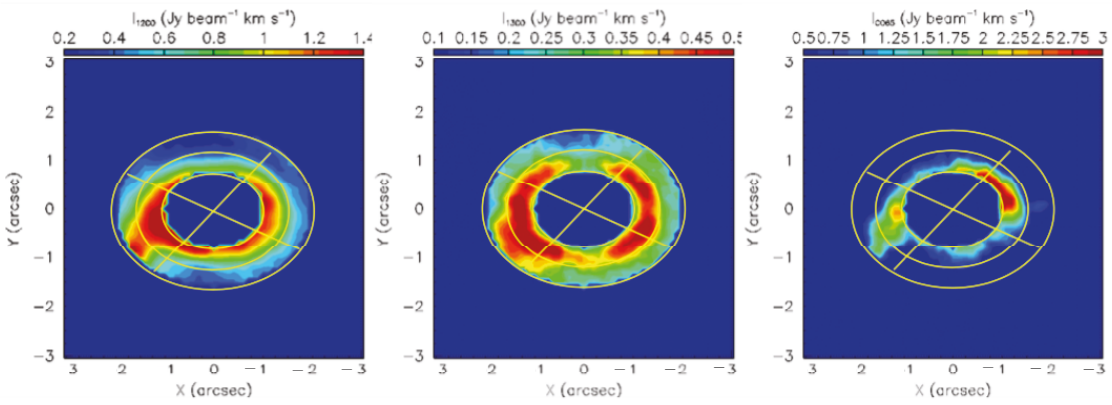

FIGURE 3.21: Sky maps of intensities measured in the ring $1'' < r < 2''$ for ^{12}CO(3–2) (left), ^{13}CO(3–2) (middle) and ^{12}CO(6–5) (right). The lines show the eight regions used to draw Table 3.3.

However, a different picture emerges if we account for the strong radial dependence of the intensity by mapping, for each pixel, the difference between the measured intensity and the mean intensity measured at that radius (averaged over azimuth). Then, as illustrated in Figure 3.22, much better evidence for the hot spot is revealed. The east-west excess (or north-south depression) revealed in Figure 3.21 for $1'' < r < 1.5''$ is therefore probably unrelated to the "hot spot" but rather a geometrical effect associated with the disk thickness. However, Figure 3.22 also provides clear evidence for a northern depression, which is as deep as the hot spot is high.

TABLE 3.3: *rms* values ($\mathrm{km\,s^{-1}}$) of the line widths measured in each of 8 regions depicted in Figure 3.21.

	Transition	$[60°, 150°]$*	$[150°, 240°]$	$[240°, 330°]$	$[-30°, 60°]$
$1'' < r < 1.5''$	^{12}CO $(3-2)$	0.36	0.40	0.39	0.39
	^{13}CO $(3-2)$	0.24	0.25	0.25	0.23
	^{12}CO $(6-5)$	0.24	0.26	0.39	0.31
$1.5'' < r < 2''$	^{12}CO $(3-2)$	0.28	0.28	0.33	0.28
	^{13}CO $(3-2)$	0.21	0.19	0.21	0.20
	^{12}CO $(6-5)$	0.26	0.16	0.17	0.14

*"hot spot" region

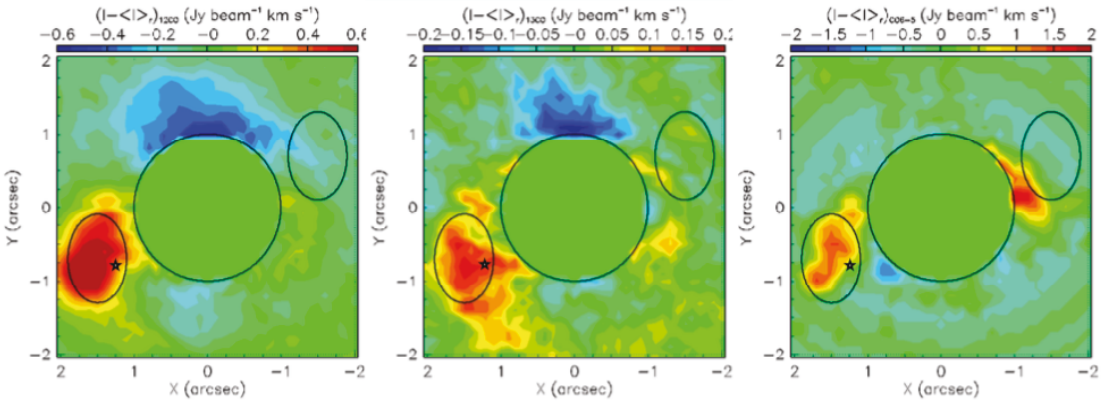

FIGURE 3.22: Sky maps of the difference between the measured intensity and its azimuthal average at the same radius for each of ^{12}CO(3–2) (left), ^{13}CO(3–2) (middle) and ^{12}CO(6–5) (right). The circle $x^2 + y^2 = 1\,\mathrm{arcsec}^2$ is excluded. Stars locate the Dutrey et al. (2014) "hot spot".

TABLE 3.4: Line properties in the hot spot ellipse and its symmetric with respect to the origin of coordinates (GG Tau A)

	Hot spot ellipse		Diametrically opposite ellipse	
	$\langle V_z \rangle$	$rms(\langle V_z \rangle)$	$\langle V_z \rangle$	$rms(\langle V_z \rangle)$
	$(\mathrm{km\,s^{-1}})$		$(\mathrm{km\,s^{-1}})$	
^{12}CO $(3-2)$	-1.3	0.27	1.1	0.38
^{13}CO $(3-2)$	-1.3	0.22	1.1	0.24
^{12}CO $(6-5)$	-1.2	0.25	1.6	0.28

Defining the "hot spot" region as an ellipse centred at $(x, y) = (1.5, -0.7)$ with semi-axes of $(0.4'', 0.6'')$, we compare in Table 3.4 the line widths measured in the "hot spot" ellipse and in the diametrically opposite ellipse centred at $(x, y) = (-1.5, 0.7)$.

Our analysis suggest that there is no detectable excess of turbulence at the "hot spot" location.

3.5 Summary

The present analysis contributes additional information to the morphology and kinematics of the gas and dust disk surrounding the GG Tau A triple protostar. It reveals the presence of concentric dust and gas rings sharing a same axis projecting on the sky plane $\sim 7^\circ$ east of north. In the approximation where both rings are flat and thin, their inclination angles with respect to the sky plane are respectively 32° and 35°. The gas ring is broader than the dust ring and peaks at smaller distance (typically 87%) to the central stars. The de-projected radial dependence of the line emission displays maxima at $\sim 1.2''$ and $1.9''$ from the central stars, bracketing the mean dust ring radius of $\sim 1.6''$. It cuts-off sharply at a mean distance of ~ 1 arcsec, cancelling completely below ~ 0.54 arcsec. Azimuthal *rms* variations of the dust and gas emissions in the disk plane are measured at the respective levels of $\sim \pm 9\%$ and $\pm 17\%$. Strong evidence is obtained for the rotation of the tilted gas disk about its axis dominating the kinematics.

A detailed study of the properties of the gas disk has been presented, adding significant new contributions to the earlier analyses of Tang et al. (2016). From the azimuthal dependence of the sharpness of the inner edge of the disk, a 95% confidence level upper limit of $0.24''$ (34 au) has been placed on its scale height $H(r)$ at a distance of $1''$ (140 au) from the central stars. At 30 K, hydrostatic equilibrium would imply $H(r)/r \sim 0.17''$, consistent with this observation.

Variations of the integrated intensity across the disk area have been studied in detail and found to confirm the presence of a hot spot in the south-eastern quadrant. However several other significant fluctuations, in particular a depression in the northern direction, have also been revealed. On average, the *rms* relative azimuthal variation of the integrated intensity reaches $\sim 17\%$. The radial dependence of the integrated intensity is modulated with enhancements at $r \sim 1.2''$ and $1.9''$, bracketing the dust ring ($\sim 1.6''$). It is also between these radial integrated intensity enhancements that both the hot spot and the northern depression are observed to peak (their effects nearly cancelling each other when averaged over ω).

The study of the gas kinematics has given evidence for a strong dominance of rotation about the disk axis. The Doppler velocity gradient being perpendicular to the projection of the disk axis on the sky plane allows placing a 99% confidence upper limit of 9% on the ratio between a possible infall velocity and the rotation velocity. The difficulty of evaluating reliably the rotation velocity close to the sky plane projection of the disk axis has been discussed. Taking it in proper account, the rotation is observed to be Keplerian with a power index of ~ -0.51 across most of the disk area. At $r = 1''$, the rotation velocity reaches $\sim 2.94 \pm 0.03$ km s^{-1}, i.e. 3.48 ± 0.04 km s^{-1} at 100 au, in agreement with previous, less precise determinations (e.g. Dutrey et al. (2014) quoted 3.4 ± 0.1 km s^{-1} at 100 au). Taking into account the uncertainty on the inclination, this corresponds to a total stellar mass of 1.36 ± 0.06 M$_\odot$. No significant correlation has been found between the azimuthal inhomogeneity of the rotation velocity and of the observed integrated intensity (hot spot and northern depression) but a radial modulation of the rotation velocity reminiscent of that observed for the

intensity has been observed, with maxima at $\sim 1.4''$ and $\sim 2.1''$.

The dependence of the linewidth on r and ω has been studied. It shows little dependence on ω but increases from 0.18 $\mathrm{km\,s^{-1}}$ to 0.26 $\mathrm{km\,s^{-1}}$ when r decreases from $2.3''$ to $1.5''$. As the contributions of Keplerian shear and instrumental spectral resolution taken together should not exceed some 0.11 $\mathrm{km\,s^{-1}}$, a possible explanation may be a factor 2 decrease of the disk surface temperature and opacity, reaching respectively 36 K and 10 at $r = 1.5''$. Relative variations of the line width over the disk area have been found to be correlated with relative variations of the integrated intensity, the former being about a third of the latter. At least qualitatively, this result would also support the presence of a temperature gradient, the CO(3–2) emission ladder peaking at temperatures higher than the average disk temperature.

3.A Channel maps

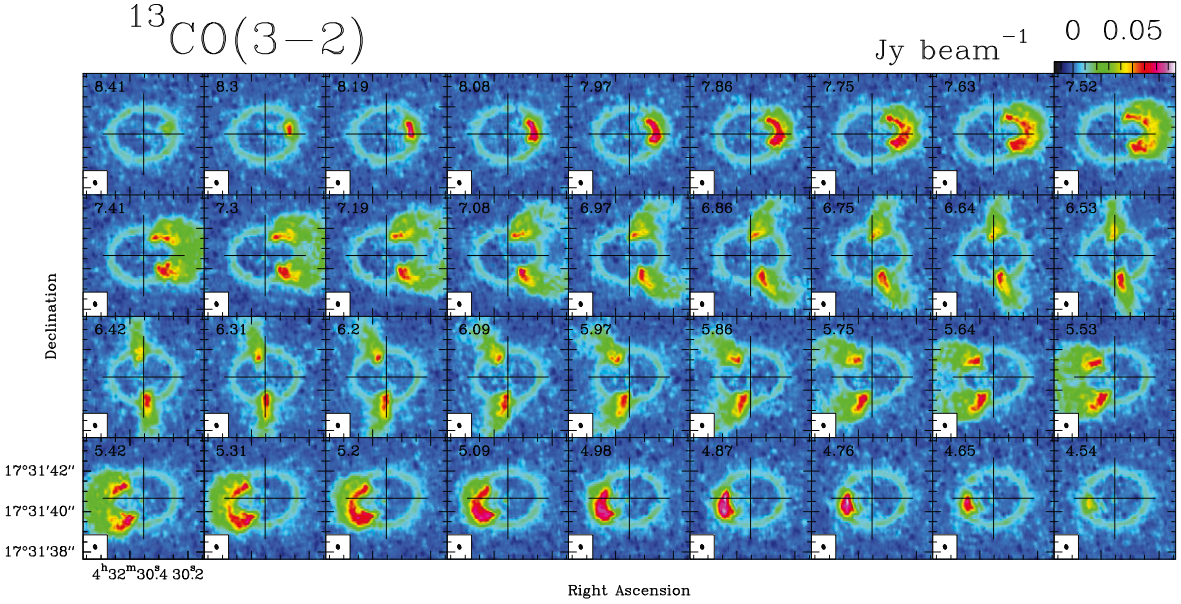

FIGURE 3.23: Channel maps of ^{13}CO(3–2), Beam 0.22″ × 0.16″, PA=16°. The noise level is 2.4 mJy beam^{-1}. The colour scale is indicated in the upper right panel. The cross is centred on the centre of the map.

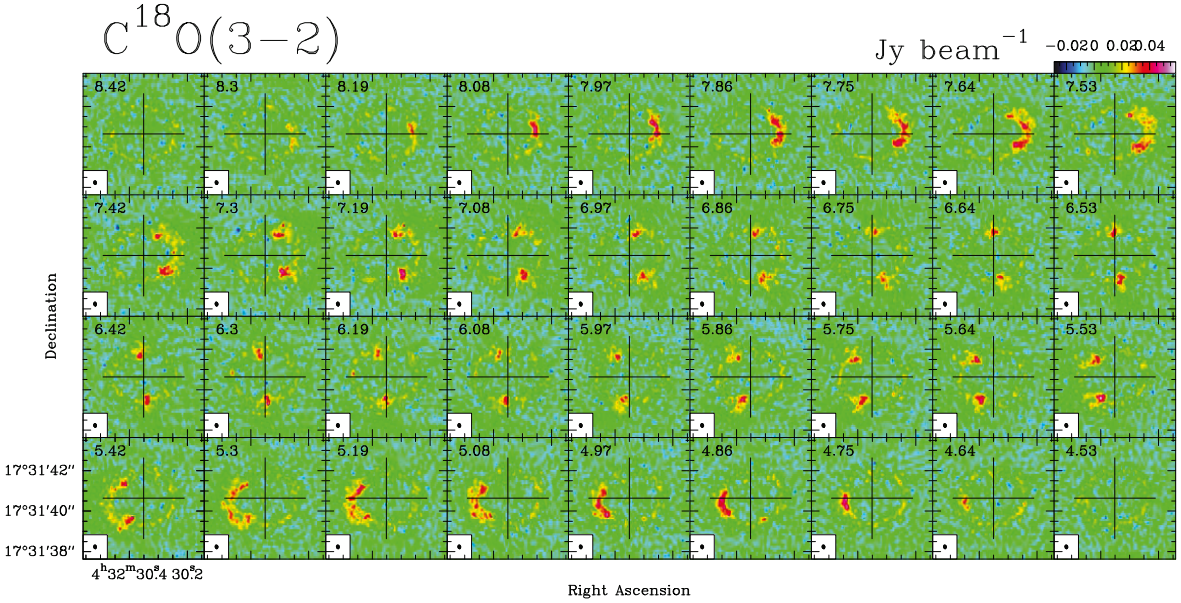

FIGURE 3.24: Channel maps of C^{18}O(3–2), Beam 0.19″ × 0.14″, PA=19°. The noise level is 4.8 mJy beam^{-1}. The colour scale is indicated in the upper right panel. The cross is centred on the centre of the map.

Chapter 4

Gas properties from the outer disk to the central cavity[1]

This Chapter presents the study of the gas properties in the ring, the outer disk and inside the cavity of GG Tau A using ALMA observations of the (sub)mm CO (^{12}CO,^{13}CO, C^{18}O) emissions. A radiative transfer modelling of the outer disk using DiskFit in Local Thermal Equilibrium (LTE) condition is presented, providing information about the molecular surface density and the gas temperature profile in the circumbinary disk. The morpho-kinematics of the gas inside the cavity is studied using observations of CO emissions which are analysed assuming non-LTE conditions. I also discuss the total amount of gas and the accretion rate inside the cavity.

4.1 Local Thermal Equilibrium Modelling of the circumbinary disk

4.1.1 Continuum fit

The CO emission being at least partially optically thick, I cannot simply separate the contribution of CO and continuum emissions (Weaver, Isella, and Boehler, 2018). To determine the continuum properties, we fitted the continuum using the broadband, line-free, spectral window data following the procedure described in Dutrey et al. (2014). The radial dependence of the emission of the circumstellar disk of Aa is fitted as a Gaussian and subtracted. The radial dependence of the emission of the ring is then fitted using a simple power law distribution for the surface density and the temperature with sharp inner and outer edges, assuming a spatially constant dust absorption coefficient that depends on frequency $\kappa_\nu = \kappa_{\nu 0}(\nu/\nu_0)$ (see also Table 4.2). The results of the common fit performed using 1.3 mm and 0.8 mm data

[1]The content of this Chapter is mostly adapted from the paper:
1) Phuong, N.T.; Dutrey, A.; Diep, P.N; Guilloteau, S.; Chapillon, E.; Di Folco, E.; Tang, Y-W.; Pietu, V.; Bary, J.; Beck, T.; Hersant, F.; Hoai, D.T.; Hure, J.M.; Nhung, P.T.; Pierens, A.; Tuan-Anh, P., 2019, submitted to A&A

are summarised in Table 4.2. The 1.3 mm continuum emission is from Dutrey et al. (2014).

The goal of this continuum modelling is that residual emission after model fitting becomes small compared to the noise level in the spectral line data, so that the continuum does not introduce any significant bias in the combined fit for spectral lines described in the next Section. Adjusting only the surface density is enough for this. The residuals, such as those due to the azimuthal variations, or the shallow outer edge of the brightness distribution, are well below 1 K in brightness.

TABLE 4.1: System geometric and kinematic parameters

Parameter	Value	
(x_0, y_0)	(0,0)	Center of dust ring
$PA(^\circ)$	7	PA of disk rotation axis
$i(^\circ)$	-35	Inclination
$V_{\rm LSR}$ (km s^{-1})	6.40	Systemic velocity
V_0 (km s^{-1})	3.37	Keplerian Rotation velocity at 100 au
dV (km s^{-1})	0.3	Local line width

Note. The values are taken as fixed value which are derived from the available literatures.

TABLE 4.2: Dust ring parameters

Parameter	Value	
Inner radius (au)	193	Dutrey et al. (2014)
Outer radius (au)	285	
Abs. Coefficient K_ν (cm$^2/g$)	$0.02 \times (\nu/230\text{GHz})$	Dutrey et al. (2014)
Temperature (K)	$14 \times (r/200\,\text{au})^{-1}$	Dutrey et al. (2014)
Surface density (cm^{-2})	$5.6\ 10^{24} \times (r/200\,\text{au})^{-1.4}$	Fitted

This continuum model is then used to fit the uv table containing both the line and continuum observations.

4.1.2 CO isotopologues

We first analyze the CO isotopologue data without subtracting the continuum. The parameters labelled as "fixed" in Tables 4.1 and 4.2 are used as fixed input parameters of the model.

Tang et al. (2016) showed that the radial profile of the intensity of the ^{13}CO emission could be reasonably well described by a superposition of 3 Gaussians (see their Figure 3c). Thus, assuming a single power law radial profile is not a good approximation for the CO emissions. Therefore, we fit the data assuming piece-wise, continuous power laws (linear in log-log space) for the surface density and temperature.

The parameters of the Gaussian decomposition from Tang et al. (2016) are used to define the radial knots, at 160, 200, 260, 300 and 400 au for ^{12}CO and ^{13}CO data. For the case of C^{18}O we use 4 knots at 160, 200, 260, 300 au because of its lesser extension.

While the outer disk can be modelled as Keplerian, this is not the case for the gas inside the cavity, which, however, contributes to a significant fraction of the total CO emission. In the image plane, there is no clear separation for the gas between the ring and the cavity, contrary to the continuum emission. Moreover, when fitting inside the *uv*-plane, one cannot separate the contribution of the cavity from that of the outer disk. To cope with this difficulty, we first subtract the clean components located inside the cavity (up to a radius of 160 au) from the original *uv* tables (this also removes the continuum contribution of Aa) and the modified *uv* tables are then modelled with a Keplerian disk truncated at short radii (see Chapter 2, Figure 2.3 for the description of deconvolution process and the Clean components definition).

The following strategy has been adopted to combine the information provided by the ^{12}CO and ^{13}CO data. In a first step, we estimate the radial distribution of the temperature by fitting the ^{12}CO line using a given assumed value of the surface density. The value of this surface density is not critical, as long as it is large enough to produce sufficient optical thickness. We then use the temperature profile derived from ^{12}CO to fit the ^{13}CO data and determine the associated surface density, taking advantage of the lower optical thickness of this line. The ^{12}CO surface density is then obtained by simply scaling the ^{13}CO surface density by the known isotopic ratio ^{12}CO/^{13}CO (70, Milam et al., 2005). Two iterations are enough for the process to converge. The method makes the implicit assumption that the ^{12}CO and ^{13}CO layers are at the same temperature. This hypothesis is consistent with the results obtained by Tang et al. (2016), who found that the vertical temperature gradient around 200-400 au should be small in order to reproduce the observed ^{12}CO/^{13}CO line ratio.

A common inner radius of 169 au is applied to all molecular distributions. This radius is here only to obtain a good model for the ring and outer disk: it should not be interpreted as the physical gas edge of the cavity. Constraining the inner gas edge is not possible because of the clean component removal, which may contaminate the emissions around 160 au. The outer radii are evaluated for each isotopologue separately. The small difference between our adopted Keplerian rotation law and that suggested by the analysis in Chapter 3 has negligible impact on the fitted parameters (within the error bars).

I obtained this way a common model of the ring and outer disk which gives a satisfactory description of the emission of the different CO isotopologues. Subtracting this model from the original data gives us the emissions inside the cavity. Figure 4.1 maps the residuals from the original *uv* data after subtraction of the contributions of the best fit outer disk model and of the Aa continuum emission.

As expected, most of the left-over emission comes from the cavity for the ^{12}CO and ^{13}CO emissions. As the model does not allow for azimuthal inhomogeneities, they are enhanced in the residuals of the ring and outer disk. The best fit results are

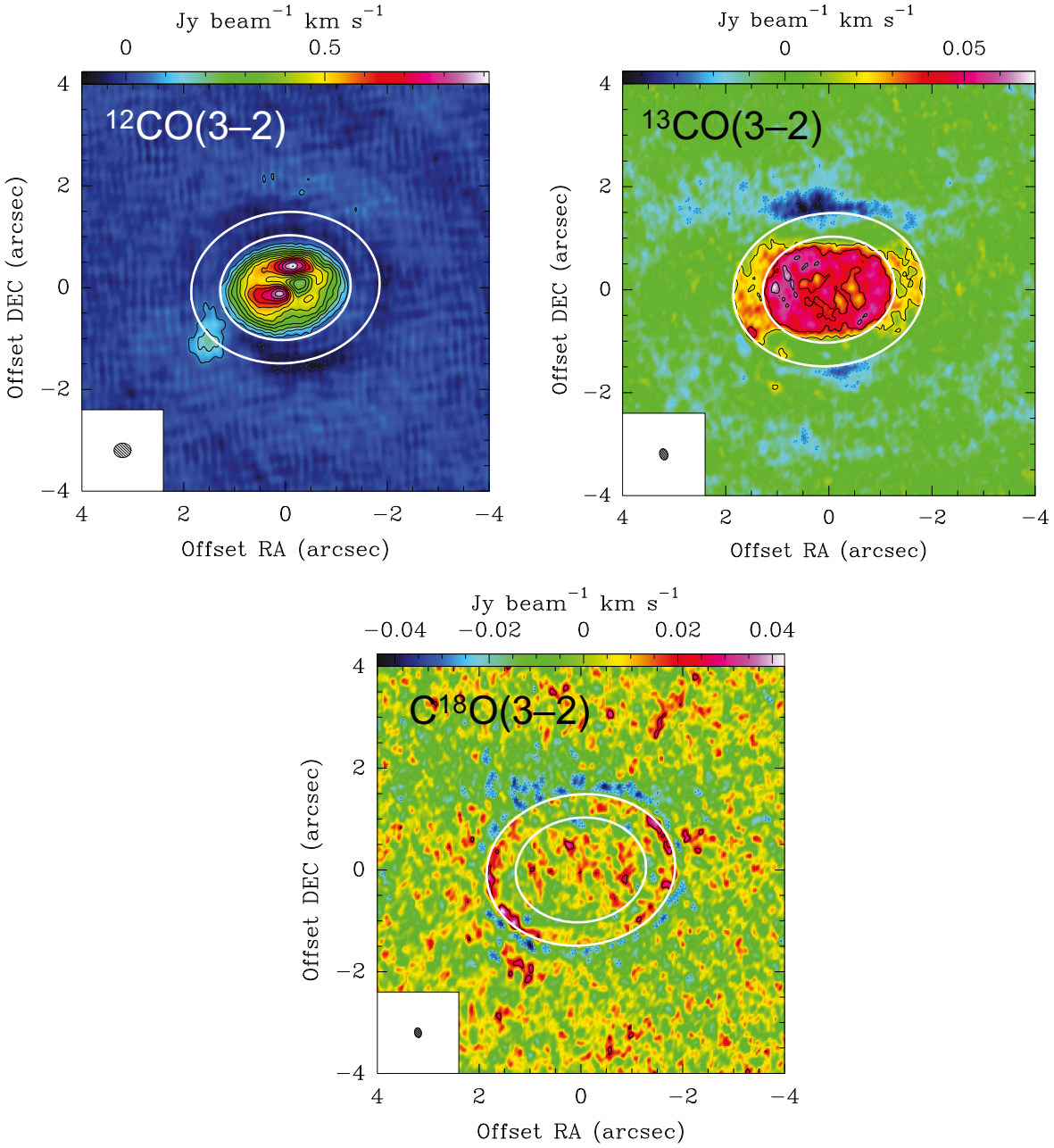

FIGURE 4.1: Integrated intensity of (residual) emissions after subtracting the best disk models. *Upper left panel:* ^{12}CO(3–2). The restoring beam of $0.34'' \times 0.28'', \mathrm{PA} = -89^\circ$ is indicated in the lower left corner. *Upper right panel:* ^{13}CO(3–2). The restoring beam is $0.22'' \times 0.16'', \mathrm{PA} = 16^\circ$. *Lower panel:* C^{18}O(3–2). The restoring beam is $0.19'' \times 0.14'', \mathrm{PA} = -167^\circ$. The contour level is 5σ for ^{12}CO(3–2) map and 3σ for ^{13}CO(3–2), and C^{18}O(3–2) maps . The ellipses show the inner and outer edges of the dust ring at 180 au and 260 au.

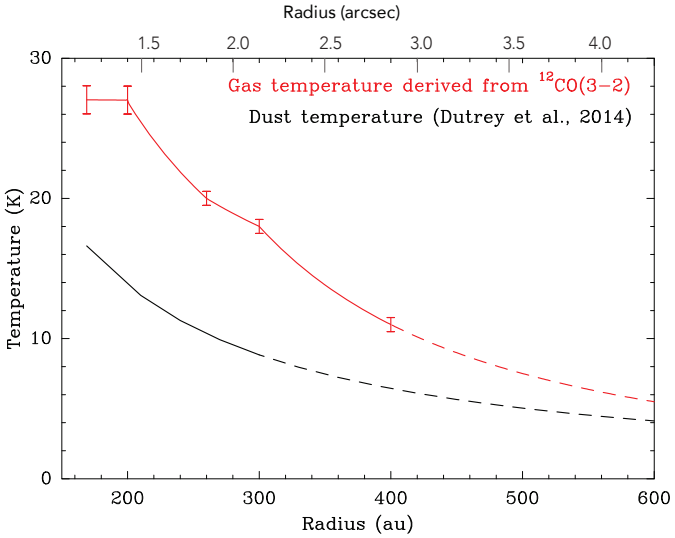

FIGURE 4.2: Radial dependence of CO gas (red) and dust (black) temperature. The gas temperature is the best fit to the present data, extrapolated beyond 400 au using the power law found between 300 and 400 au. The dust temperature is from Dutrey et al. (2014) up to 300 au, extrapolated further out.

illustrated in Figures 4.2 and 4.3, and listed in Table 4.3. The uncertainties have been estimated from the dispersion of results obtained in the process of searching for the best fit. They are of the order of 1 to 2 K on the temperatures and of 20% to 30% on the surface densities. An important and robust result is the strong decrease of the gas temperature with increasing distance from the stars, from $\sim$ 27 K at 180 au to $\sim$ 11 K at 400 au. Assuming constant flaring ($h(r)$ proportional to r) we obtain scale heights at $r = 200$ au of 24 au for ^{12}CO(3–2) and 23 au for ^{13}CO(3–2). In hydrostatic equilibrium, this corresponds to a temperature of $\sim$ 15 K, consistent with the dust temperature obtained by Dutrey et al. (2014). The final fits use a fixed value of the ratio $h(r)/r = 24/200 = 0.12$. The values obtained for the outer disk radii are $\sim$370 au for C^{18}O(3–2), $\sim$550 au for ^{13}CO(3–2) and > 600 au for ^{12}CO(3–2), the latter two values being poorly constrained by the fit due to the steep radial decrease of the temperature.

4.1.3 Discussion

Temperature distribution in the outer disk

The present analysis confirms that most of the outer disk of GG Tau A is very cold (see Figure 4.2), giving a gas temperature in agreement with the value of 20 K at 300 au obtained by Guilloteau, Dutrey, and Simon (1999) from ^{13}CO data. The agreement between these two values derived from independent ^{12}CO and ^{13}CO analysis supports the assumption of a limited vertical temperature gradient in the CO layer, as already noted by Tang et al. (2016). A power law fit to the radial dependence of

TABLE 4.3: Temperature of ^{12}CO(3–2) and surface density of ^{13}CO(3–2) and C^{18}O(3–2) - nominal model after CLEANed component removal at $r < 160$ au.

(1) r (au)	(2) T_k (K)	(3) (K)	(4) (K)	(5) ^{13}CO 10^{15} cm^{-2}	(6) C^{18}O 10^{15} cm^{-2}	(7)) Ratio
160	27.2	0.17	[26,28]	39 ± 2	6.7 ± 0.6	5.8 ± 0.8
200	27.4	0.11	[25,28]	18 ± 1	5.5 ± 0.4	3.3 ± 0.4
260	19.7	0.07	[19,21]	9.7 ± 0.3	2.1 ± 0.1	4.6 ± 0.4
300	18.0	0.03	[17,19]	6.8 ± 0.1	0.39 ± 0.02	17 ± 1
400	10.7	0.02	[10,11]	2.8 ± 0.03	–	–

Note. (1) Knot radius. (2) Temperature derived from ^{12}CO(3–2) and (3) its formal error from the fit and (4) estimated confidence interval from the minimizations. (5-6) molecular column density, (7) ^{13}CO/C^{18}O surface density ratio.

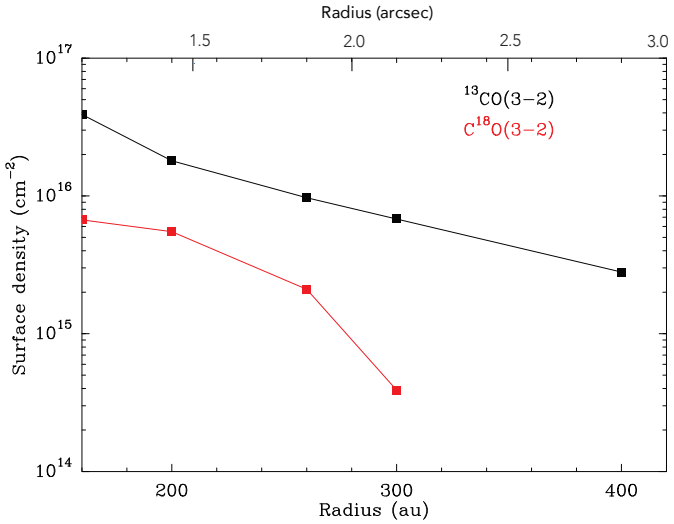

FIGURE 4.3: Comparison of the surface densities from the LTE analysis.

the temperature gives a power index between -1.0 and -1.3, in agreement with the value of -1 obtained by Guilloteau, Dutrey, and Simon (1999). From the analysis of the continuum images at wavelengths between 3 and 0.45 mm, Dutrey et al. (2014) measured a similar power index for the dust temperature, characteristic of the large grains that the mid-plane is hosting. The steep radial decrease of the temperature is most likely due to the stellar light being blocked by the inner dense ring, the outer regions of the disk being in its shadow.

Gas distribution and homogeneity of the outer ring

The model gives a surface density ratio between ^{13}CO and C^{18}O of $\sim$ 17 beyond 300 au, 2.5 times larger than the nominal isotopic ratio of 7 (Milam et al., 2005; Wilson, 1999), suggesting selective photodissociation (van Dishoeck and Black, 1988), but also confirming that in the outer disk the emissions are optically thin. On the contrary, inside the densest part of the ring (200 $-$ 260 au), the measured ratio is of the order of 3 $-$ 5. Chemical effects such as selective photodissociation and fractionation that occurs through isotope exchange between CO and C^+ (Watson, Anicich, and Huntress, 1976) and enhances ^{13}CO at temperatures about 20–30 K, would both tend to enhance this ratio above the double isotopic (^{16}O/^{18}O)/(^{12}C/^{13}C) ratio. Thus the simplest explanation for a low value is partially optically thick ^{13}CO(3–2) emission. However, our model should account for the opacity if the disk was as smooth as assumed. Hence, we conclude that the GG Tau disk and ring deviates significantly from the smooth, non stratified, azimuthally symmetric structure that we adopted.

The radial dependence of the observed emission of the molecular lines, ^{13}CO(3–2) and C^{18}O(3–2), illustrated in the upper panels of Figure 3.18, does not obey a simple power law but displays some irregularities, in particular in the form of a bump near 2″. After subtracting the best fit azimuthally symmetric outer disk model, Figure 4.1 reveals important azimuthal inhomogeneity: the hot spot is enhanced in the ^{12}CO(3–2) map and in the other maps the ring and outer disk display an east-west enhancement or equivalently north-south depletion. This is particularly clear for the optically thinner transitions of C^{18}O(3–2), suggesting radial density variations in the molecular layer. The azimuthal inhomogeneity observed in Figure 4.1 is real, instrumental effects such as resulting from velocity coherence length and convolution using an elongated beam being properly accounted for by the model. All these evidences point to the existence of radial and azimuthal sub-structures that remain unresolved (at least radially) at our 30 au linear resolution.

4.2 Analysis of the gas inside the cavity

Having built a reasonable model of the ring and outer disk, we can subtract its contribution to the measured visibilities in order to obtain the contribution of the emission of the gas contained in the cavity. CLEANed maps of the residual emission have been shown in Figure 4.1. The present section studies the properties of the gas inside the cavity using the residual map.

4.2.1 The dynamics inside the cavity

Figure 4.4 displays the azimuthal dependence of $\langle V_z/sin(i)\rangle$ averaged over r in 5 rings, each 0.25″ wide, for each CO isotopologue inside the region $0 < r < 1.25''$. Azimuth and radius are defined in the disk plane. Sine wave fits to the ^{13}CO(3–2) data, of the form $V_z/\sin(i) = V_{z0}\sin\omega$, are made in each ring separately. Good fits

are obtained, indicating that the gas kinematics inside the cavity is dominated by rotation. The amplitude is however smaller than for Keplerian rotation of a thin disk, the more so at the lower values of r. The ^{12}CO(3–2) and ^{13}CO(3–2) amplitudes agree for $1'' < r < 1.25''$, but differ at the lower values of r. The C^{18}O(3–2) populate only a narrow interval of r, preventing a reliable interpretation.

Furthermore, a better fit is obtained by taking into account the contribution of infall using a radial velocity $V_z/\sin(i) = V_{fall}\cos\omega + V_{rot}\sin\omega$. The results are presented in Table 4.4: $V_{fall} > 0$ corresponds to infall motions. Table 4.4 thus indicates that the gas in the cavity is moving inwards to the centre at velocities about 0.3 km s^{-1}, which is about $10-15\%$ of the Keplerian velocity. Since infall and rotation motions have different radial dependence, the finite beamsize has different impact on the infall velocity than on the apparent rotation velocity, which, in this specific case, is small.

TABLE 4.4: Infall and rotation velocity of the gas inside the cavity.

Ring	V_{Kep} (km s^{-1})	V_{rot} (km s^{-1})	V_{fall} (km s^{-1})	$\frac{V_{fall}}{V_{rot}}$	$\frac{V_{fall}}{V_{Kep}}$
(a)	-	0.34	0.04	12%	-
(b)	-	0.79	0.21	27%	-
(c)	3.63	0.98	0.30	31%	8%
(d)	3.07	1.08	0.38	28%	12%
(e)	2.71	1.27	0.48	38%	18%

Direct evidence for infall is also presented in Figure 4.5 that shows position-velocity diagrams of the ^{13}CO$(3-2)$ emission inside the cavity along the major and minor axes of the disk. The PV diagram along the major axis shows Keplerian rotation down to the inner edge of the ^{13}CO(3–2) emission, at $\sim 1.1''$ (~ 160 au). The PV diagram along the minor axis displays a north–south asymmetry that reveals an infall contribution of some 0.2 km s^{-1} in V_z, namely $\sim 0.3-0.4$ km s^{-1} de-projected.

4.2.2 Gas properties

Using the ^{12}CO(6–5) data from Dutrey et al. (2014) and the (residual) ^{12}CO$(3-2)$ data smoothed to a similar angular resolution ($0.35'' \times 0.30''$). I identify 2 dominant features in the gas streamers (Dutrey et al., 2014) that I separate in 5 bright "blobs" for simplifying the analysis and a 6th one connecting blobs 2 and 4, brighter in CO(6–5) (see Figure 4.6). Integrated line flux and line widths were derived for each blob by fitting a Gaussian to the line profile. To determine the physical conditions, we use a non-LTE escape probability radiative transfer code implemented in DiskFit. It uses *escape probability* formulation of Elitzur (1992), $\beta = [1-\exp(-\tau)]/\tau$, a single collision partner, H_2, and Gaussian line profiles.

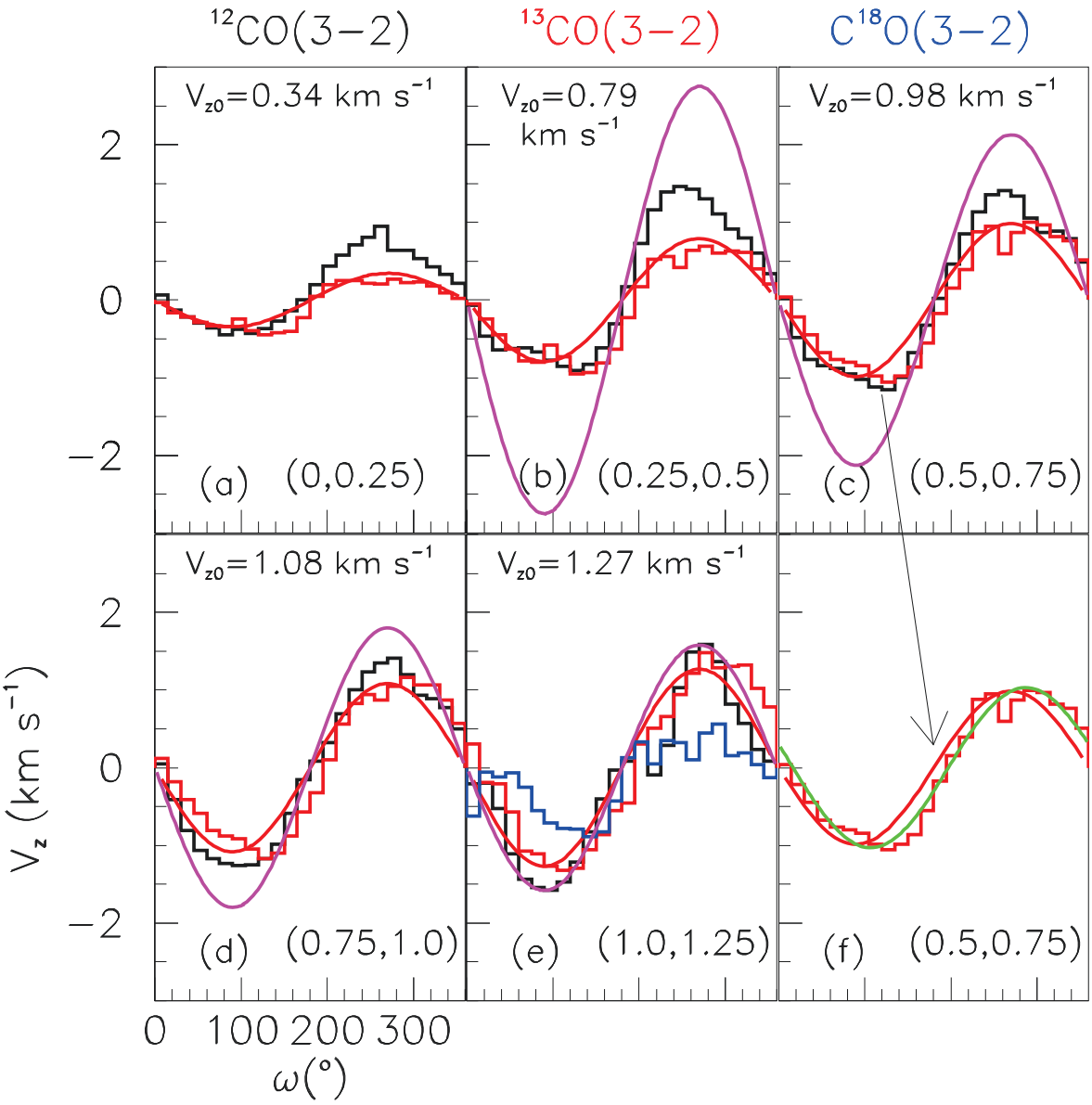

FIGURE 4.4: Dependence of $\langle V_z \rangle$ (km s^{-1}) on azimuth ω (°) inside the cavity. ^{12}CO (3–2) is in black, ^{13}CO (3–2) in red and C^{18}O (3–2) in blue. The red curve is a fit of a sine function to the ^{13}CO (3–2) data (see text). C^{18}O (3–2) data of significant intensity are only present in the bin $1.0'' < r < 1.25''$. The magenta curves show the Keplerian velocity expected around a single star of 1.36 $M_\odot$. The green curve in panel (f) shows the best fit velocity curve when infall motion is allowed.

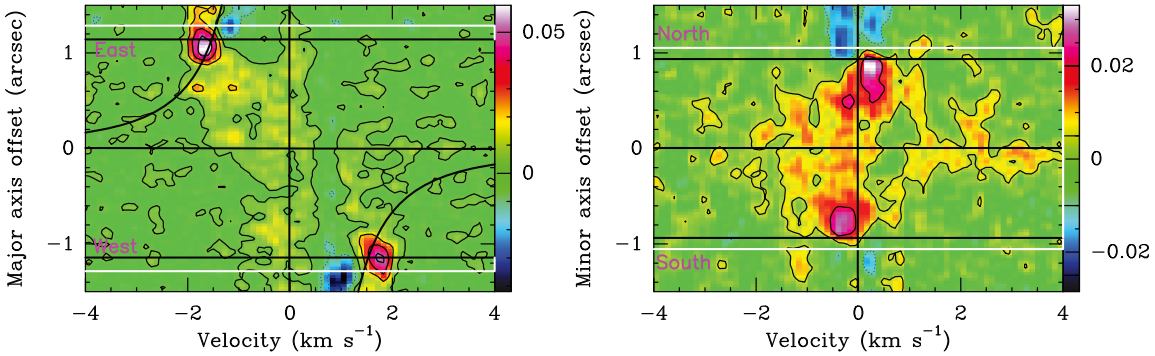

FIGURE 4.5: Position-velocity diagrams of the ^{13}CO(3–2) emission in the cavity along the major axis *(left)* and minor axis *(right)*. The black curves show the expected Keplerian velocity around a single star of 1.36 $M_\odot$. Contour levels are spaced by 10 mJy/beam, with the zero contour omitted. The white lines indicate the position of the dust ring inner edge (180 au) and the black lines that of the gas disk inner radius (169 au).

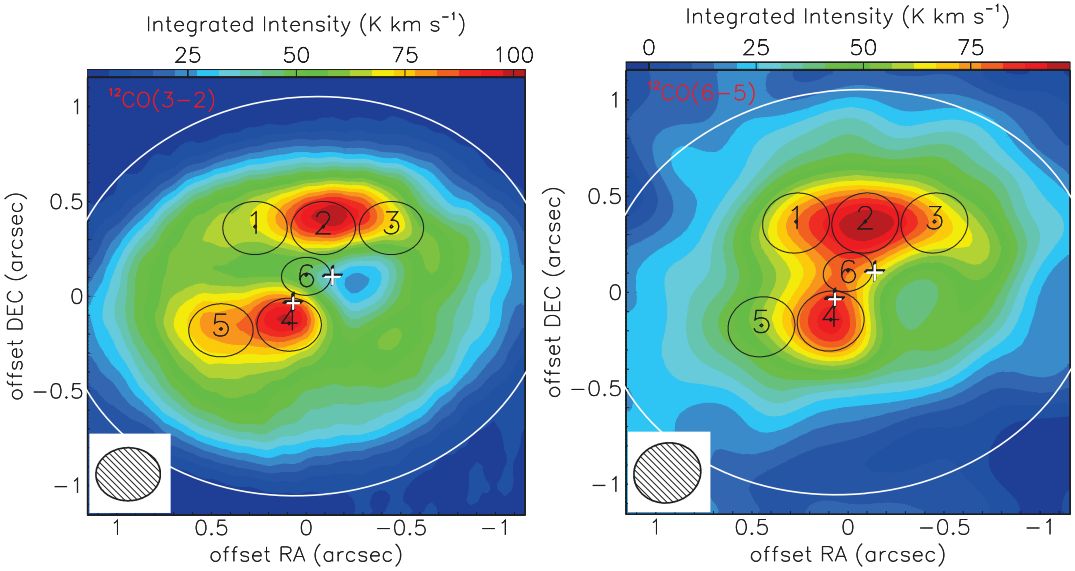

FIGURE 4.6: Integrated intensity map of ^{12}CO(3–2) *(left)* and ^{12}CO(6–5) *(right)* and blobs position and sizes.

TABLE 4.5: Blob positions with maximum brightness temperatures and their corresponding velocities for CO transitions.

Blob properites				CO(3-2)		CO(6-5)			^{13}CO(3-2)		
(1)	(2)	(3)	(4)	(5)	(6a)	(6b)	(7)	(7)	(6c)	(5)	(7)
1	$(0.27, 0.3)$	0.45	4.3	6.2	26.5	32.7	6.2	32.7	6.9	5.5	2.4
2	$(-0.09, 0.36)$	0.37	6.1	7.5	38.2	25.2	7.0	27.8	2.3	8.3	1.5
3	$(-0.45, 0.36)$	0.58	3.8	7.4	32.5	26.2	7.8	31.0	0.2	7.9	3.3
4	$(0.09, -0.15)$	0.17	–	4.7	21.4	20.5	5.3	24.2	2.3	5.4	1.7
5	$(0.45, -0.18)$	0.48	4.2	4.2	30.5	17.9	5.3	24.8	8.8	4.9	2.6
6	$(0, 0.1)$	0.12	–	6.5	10.4	5.3	11.5	21.8	2.3	5.4	1.3

Note. (1) Blob, (2) Position (arcsec, arcsec), (3) Distance from central mass (arcsec), (4) Keplerian velocity ($\mathrm{km\,s^{-1}}$), (5) Peak velocity ($\mathrm{km\,s^{-1}}$), (6x) Brightness at peak velocity of ^{12}CO$(3-2)$ (K), (7) Brightness at their own peak velocity given in column (5) (K).

Non-LTE best fit solutions were found by sampling the χ^2 surface defined as the quadratic sum of the difference between the measured brightness temperatures and the computed values, for ranges of H_2 density of $10^2 - 10^{10}\,\mathrm{cm^{-3}}$, ^{12}CO column density of $10^{13} - 10^{19}\,\mathrm{cm^{-2}}$, and kinetic temperature of $3 - 100\,\mathrm{K}$ using 50 steps of each parameter. We assume the standard isotopic ratios $^{12}\mathrm{C}/^{13}\mathrm{C}= 70$ (Milam et al., 2005) and $^{16}\mathrm{O}/^{18}\mathrm{O}= 550$ (Wilson, 1999) for the relative abundances of the isotopologues. ^{12}CO constrains the temperature, and ^{13}CO the column densities. Owing to its faintness, the C^{18}O$(3-2)$ data bring little additional information. Given the low critical densities of the observed transitions, we only obtain a lower limit to the density. The blob parameters are presented in Table 4.6.

Typically, we find high CO column densities around a few $\sim 10^{17}\,\mathrm{cm^{-2}}$ and temperatures in the range 40–80 K, with a lower limit on the density of the order of $10^5\,\mathrm{cm^{-3}}$.

For blob 6, the faintest region that we analyze with this method, the problem is marginally degenerated, with two separate solutions: i) a high column density ($\sim 10^{17}\,\mathrm{cm^{-2}}$), low temperature ($\sim 20\,\mathrm{K}$) and ii) a low column density ($\sim 10^{15}\,\mathrm{cm^{-2}}$) and high temperature ($> 80\,\mathrm{K}$). Since this region is between Aa and Ab, the material is wrapped up because of the stars rotation, the second solution (which is also that of lowest χ^2) is more likely. Table 4.6 summarizes all the results of blobs properties.

TABLE 4.6: Brighter blobs properties

Blob	Position	Radius	dv	H_2 density	N	T_{kin}	Mass (nLTE)	Mass ($F_{^{12}CO}$)	Mass ($F_{^{13}CO}$)
	(″,″)	(″)	($km\,s^{-1}$)	(cm^{-3})	(cm^{-2})	(K)	($M_\odot$)	($M_\odot$)	($M_\odot$)
(1)	(2)	(3)	(4)	(5)	(6)	(7)	(8)	(9)	(10)
1	(0.27, 0.36)	0.45	2.5	$> 5.0\,10^4$	$(2.1^{+0.6}_{-0.7})\,10^{17}$	40 ± 5	$(2.1^{+0.6}_{-0.7})\,10^{-6}$	$(3.1 \pm 0.1)\,10^{-7}$	$(1.9 \pm 0.1)\,10^{-6}$
2	(−0.09, 0.36)	0.37	2.7	$> 1.0\,10^4$	$(1.4^{+0.7}_{-0.5})\,10^{17}$	50 ± 5	$(1.3^{+0.7}_{-0.5})\,10^{-6}$	$(4.5 \pm 0.1)\,10^{-7}$	$(2.3 \pm 0.1)\,10^{-6}$
3	(−0.45, 0.36)	0.58	2.1	$> 5.0\,10^4$	$(2.6^{+1.0}_{-1.00})\,10^{17}$	40 ± 5	$(2.5^{+1.0}_{-1.0})\,10^{-6}$	$(3.2 \pm 0.2)\,10^{-7}$	$(1.1 \pm 0.1)\,10^{-6}$
4	(0.09, −0.15)	0.17	6.2	$> 1.0\,10^5$	$(6.3^{+2.1}_{-1.4})\,10^{16}$	80 ± 10	$(6.3^{+2.1}_{-1.4})\,10^{-7}$	$(6.9 \pm 0.1)\,10^{-7}$	$(2.5 \pm 0.2)\,10^{-6}$
5	(0.45, −0.18)	0.48	2.5	$> 1.0\,10^4$	$(2.2^{+1.0}_{-0.8})\,10^{17}$	40 ± 5	$(2.2^{+1.0}_{-0.8})\,10^{-6}$	$(3.9 \pm 0.1)\,10^{-7}$	$(1.7 \pm 0.1)\,10^{-6}$
6	(0, 0.1)	0.12	6.1	$> 1.0\,10^4$	$(4.0^{+1.4}_{-1.4})\,10^{16}$	80 ± 10	$(4.0^{+1.4}_{-1.4})\,10^{-7}$	$(3.4 \pm 0.1)\,10^{-7}$	$(2.8 \pm 0.1)\,10^{-6}$

Note. (1) Blob, (2) Offset from ring center, (3) Distance from center, (4) line-width ($km\,s^{-1}$), (5) H_2 density, (6) CO column density, (7) kinetic temperature, (8) H_2 mass derived from the CO column density which was derived from the non-LTE analysis, (9) H_2 mass derived from the ^{12}CO flux and (10) H_2 mass derived from the ^{13}CO flux. See also Section **??** for details of calculation.

4.2.3 Evaluation of the mass of gas contained in the cavity

Knowing the molecular column density in each blob, one can estimate the blob mass assuming a molecular abundance relative to H_2 (the lower limit on the H_2 density is not significant to directly constrain the mass).

One can also derive the total amount of gas in the cavity from the integrated flux of the optically thin lines of ^{13}CO(3–2) and C^{18}O(3–2). The ^{12}CO(3–2) emission, being partially optically thick, will yield a lower limit. In the optically thin approximation, the integrated flux and the column density of the upper level of a given transition are related by:

$$W = \frac{g_u}{\gamma_u} N_u \tag{4.1}$$

where, $W = \int T_b \, dv$ is the integrated brightness inside the cavity ($R < 160$ au), $g_u = 2J + 1$ is the statistical weight and N_u is the column density of the upper level, $\gamma_u = \frac{hc^3 A_{ul}}{8\pi k_B \nu^2}$ (the Einstein coefficient A_{ul} is taken from Lambda database[2]). I assume that the gas temperature T is 40 K everywhere inside the cavity and I calculate the total column density $N_{\rm total}$ of a given molecule:

$$N_{\rm total} = \frac{N_u}{Z} \exp\left(\frac{-E_u}{k_B\, T}\right) \tag{4.2}$$

where, Z is the partition function and E_u is the energy of the upper state.

The CO abundance was taken from those measured in the molecular cloud TMC-1 by Ohishi, Irvine, and Kaifu (1992), and I use standard isotopic ratios for the isotopologues (^{13}CO and C^{18}O). Table 4.7 summarizes the results.

TABLE 4.7: Mass of gas inside the cavity

Location	Integrated Flux (Jy km s^{-1}	H_2 mass ($M_\odot$)	Abundance (w.r.t H_2)
Cavity (^{12}CO)	11.4 ± 0.8	$6.1 \pm 0.4 \times 10^{-6}$	8.0×10^{-5}
Cavity (^{13}CO)	3.8 ± 0.1	$1.6 \pm 0.1 \times 10^{-4}$	†
Cavity (C^{18}O)	0.5 ± 0.2	$1.6 \pm 0.8 \times 10^{-4}$	‡

Note. † X[^{13}CO]=X[^{12}CO]/70 and ‡ X[C^{18}O]=X[^{12}CO]/550 (see text).

The H_2 masses derived from ^{13}CO(3–2) and C^{18}O(3–2) are similar which confirms that these lines are optically thin while the ^{12}CO emission is optically thick.

[2]https://home.strw.leidenuniv.nl/ moldata/

4.2.4 Discussion

Gas kinematics

From Figure 3.20, the rotation appears sub-Keplerian at radii smaller than about $0.8''$. This could be the signature of the tidal forces generated by the Aa/Ab binary. However, it is partly an effect of the intensity drop in the cavity, combined with the finite angular resolution. Since the signal intensity increases with radius in the cavity, the intensity weighted mean velocity is biased towards the values obtained at the largest radii, i.e. the gas apparently rotates at smaller velocities. A proper modelling of the angular resolution effect, accounting for the observed brightness distribution, would be required to remove this artefact and figure out whether the gas is rotating at the expected Keplerian speed or not. On the other hand, we find clear evidence for infall motions in the cavity, at velocities about $10 - 15\%$ of the Keplerian speed, proving that material is accreting onto the inner disks orbiting the central stars. This is consistent with the infall value found for L 1551 NE, a younger binary system (Takakuwa et al., 2017). However, our sensitivity is insufficient to make detailed comparison with hydro-dynamical models.

In summary, we find that the gas starts to exhibit non-Keplerian motion (at least infall motion, and/or slower than Keplerian rotation) at $r \approx 160$ au, somewhat smaller than the inner edge of the dust ring (193 au). This difference in radius is expected when dust trapped in the high pressure bump occurring in the dense ring is considered (e.g. Cazzoletti et al., 2017). The 160 au radius remains however much larger than the radius at which tidal disturbances are expected in a binary system, which is about 2.5-3 times the orbit semi-major axis (Artymowicz and Lubow, 1996). Given the current separations of Aa and Ab, about 35 au, we would expect deviations from Keplerian motions to only appear below about 100 au, unless the orbit is very eccentric. High eccentricity seems unlikely given the measured orbital parameters (Beust and Dutrey, 2005), who also mentioned that underestimated astrometric uncertainties could play an important role. Following Beust and Dutrey (2005), Köhler (2011) and Nelson and Marzari (2016) showed that this apparent contradiction could be solved if one assumes that the orbital plane of the stars is very different from the (common) plane of the ring and outer disks. A similar result was found by Aly, Lodato, and Cazzoletti (2018) who indicate that an inclination difference of 30° could remain stable over the (circumbinary) disk lifetime. However, Brauer et al. (2019) found the circumstellar disk around Aa and one of the disks around Ab1 or Ab2 must be co-planar with the circumbinary ring and disk, making the misaligned orbit proposition unlikely, since the alignment of the circumstellar disks is more controlled by the gravitational interactions with the stars than with the (much less massive) outer disk. The cavity size puzzle thus remains.

Gas temperature

Our non-LTE analysis, in agreement with the study by Dutrey et al. (2014), shows that the gas inside the cavity is warm, with temperatures ranging from 30 to 80 K. In the bright blobs, near the stars, we derived a kinetic temperature of the order of $40 - 50$ K at about $30 - 60$ au from the central stars. It is important to mention that such temperatures are well above the CO freeze out temperature.

Amount of gas

From the non-LTE analysis of the bright blobs, we measured a few 10^{17} cm^{-2} for the CO column density with the exception of blobs 4 and 6 which have a lower column density of $(3 - 6)\,10^{16}$ cm^{-2}. We also obtained a lower limit on the H_2 density of the order of $(1 - 10)\,10^4$ cm^{-3} for all blobs. However, a more stringent constraint can be obtained from the blob column density given in Table 4.6. Following the analysis presented in Section 4.1, we derived the thickness of the blobs ($h_{blob} = (r_{blob}/200\,au)$) to be of the order of the average value of $h(r)$, 5 to 10 au. The H_2 density, calculated from the measured column density using $\rho_{H2} = N_{H2}/\sqrt{2\pi \times h}$ (see more detail in Chapter 1, Eq (1.5)), is $\sim 10^7$ cm^{-3}.

The cumulative mass of the blobs is $\sim 1.2 \times 10^{-5}$ M$_\odot$. The total gas mass inside the cavity was estimated from the integrated flux of the optically thin CO isotopologues to be $\sim 1.6 \times 10^{-4}$ M$_\odot$, assuming standard CO abundance (see Table 9). The ^{13}CO and C^{18}O values perfectly agree suggesting that both the ^{13}CO and C^{18}O emissions are essentially optically thin. Therefore, the total mass of the gas inside the cavity appears a factor 10 larger than the cumulative blob mass. This only relies on the assumption of similar molecular abundances in these regions, which is reasonable given their similar temperatures. Thus a significant fraction of the gas in the cavity does not reside in the dense blobs but in diffuse features.

The values assumed for the CO abundance, taken equal to those observed in TMC-1, appear reasonable given the relatively high temperature in the cavity. However, lower values might result from C and O still being locked on grains in the form of more complex molecules such as CO_2 and CH_4 (Reboussin et al., 2015). A proper quantification of such a process would require a complete chemical study following the physical and chemical evolution of the gas and solid phases throughout the disk.

Nevertheless, an absolute minimum value for the gas mass in the cavity can be obtained if we accept that the CO abundance cannot exceed the Carbon cosmic abundance expected in cold molecular clouds (3.4×10^{-4} Hincelin et al., 2011a). In this case, we obtain the minimum mass by correcting the previous value by the factor of ~ 0.2. This leads to a lower limit of $\sim 0.3 \times 10^{-4}$ M$_\odot$ for the total gas mass inside the cavity.

In any case, the mass of gas in the cavity is only a very small fraction of the total disk mass (0.15 M$_\odot$) which is estimated from the dust emission.

Mass accretion rate

The gas in the cavity is unstable and will accrete onto the GG Tau A disks on a timescale of a few (∼4–5) orbital binary periods (Maddison's talk 2001[3]), that is estimated to be around 600 years, see Beust and Dutrey (2005).

A similar timescale, about 2500 yrs, is obtained independently from the ratio of the cavity radius to the measured infall velocity. This gives an accretion rate of $6.4 \times 10^{-8}\,M_\odot\,yr^{-1}$ if we assume the canonical mass value of $\sim 1.6 \times 10^{-4}\,M_\odot$.

The accretion rate on GG Tau Aa+Ab, measured in year 2000 using the H_α line, is about $\sim\ 2 \times 10^{-8}\,M_\odot\,yr^{-1}$ (Hartigan and Kenyon, 2003), a factor 3 lower than our estimate. The difference may be partly explained by variable accretion inside the cavity and onto the central star(s) associated to non steady state dynamics. In a binary star, the accretion rate process is modulated by the eccentricity, being more efficient at the pericenter with a delay which depends to first order on the eccentricity (Artymowicz and Lubow, 1996; Günther and Kley, 2002). The two values of the accretion rates reflect different aspects of a highly variable process depending how and when these rates are measured. The fair agreement between both results shows that the GG Tau A disk can be sustained by accretion through the cavity on a long timescale.

4.3 Summary

We report new observations of the emission of CO isotopologues from the close environment of GG Tau A. We study the ring by performing a LTE analysis and we perform a non-LTE analysis for the gas clumps observed inside the cavity. We investigate the gas kinematics in the outer disk and inside the cavity.

The outer disk doesn't not display a uniform brightness distribution but reveals the presence of sub-structures. The bright hot spot seen in ^{12}CO is marginally seen in ^{13}CO and C^{18}O suggesting a temperature effect. A northern depression of similar importance is observed in the ^{13}CO(3–2) data with an angular resolution of 50 au (see Chapter 3).

The gas temperature derived from the optically thick CO line displays a radial gradient similar to that of the dust (r^{-1}). The temperature of 20 K (CO snowline) is reached at $\sim$ 300 au.

The total amount of mass inside the cavity derived from ^{13}CO is $1.6 \times 10^{-4}\,M_\odot$, assuming standard CO abundance, and must exceed $0.4 \times 10^{-4}\,M_\odot$.

The gas streamers inside the cavity have been studied using 6 different blobs. A non-LTE analysis reveals physical conditions similar to those observed in warm molecular clouds: CO column densities around a few $10^{17}\,cm^{-2}$, temperatures in the range of $40 - 80$ K, and H_2 density in the dense parts of the order of $10^7\,cm^{-3}$.

[3]https://www.atnf.csiro.au/whats_on/workshops/mm_science2001/talks/Maddison.pdf

The kinematics of the outer disk is Keplerian beyond a radius of 180 au, enclosing a mass of the order of $1.36\,M_\odot$. The kinematics of the gas streamers is more complex than expected for such a binary system. In particular, the gas starts to display non-Keplerian motions for radii smaller than ~ 160 au.

The gas inside the cavity shows infall motion of about 10% of the Keplerian velocity allowing the central stars to accrete material from the dense ring.

The average mass flow rate of the gas through the cavity is $\sim 6 \times 10^{-8}\,M_\odot\,yr^{-1}$, a value compatible with the stellar accretion rate measured using the H_α line, and sufficient to replenish the circumstellar disks.

4.A Best ring model results reveal the emission inside the cavity

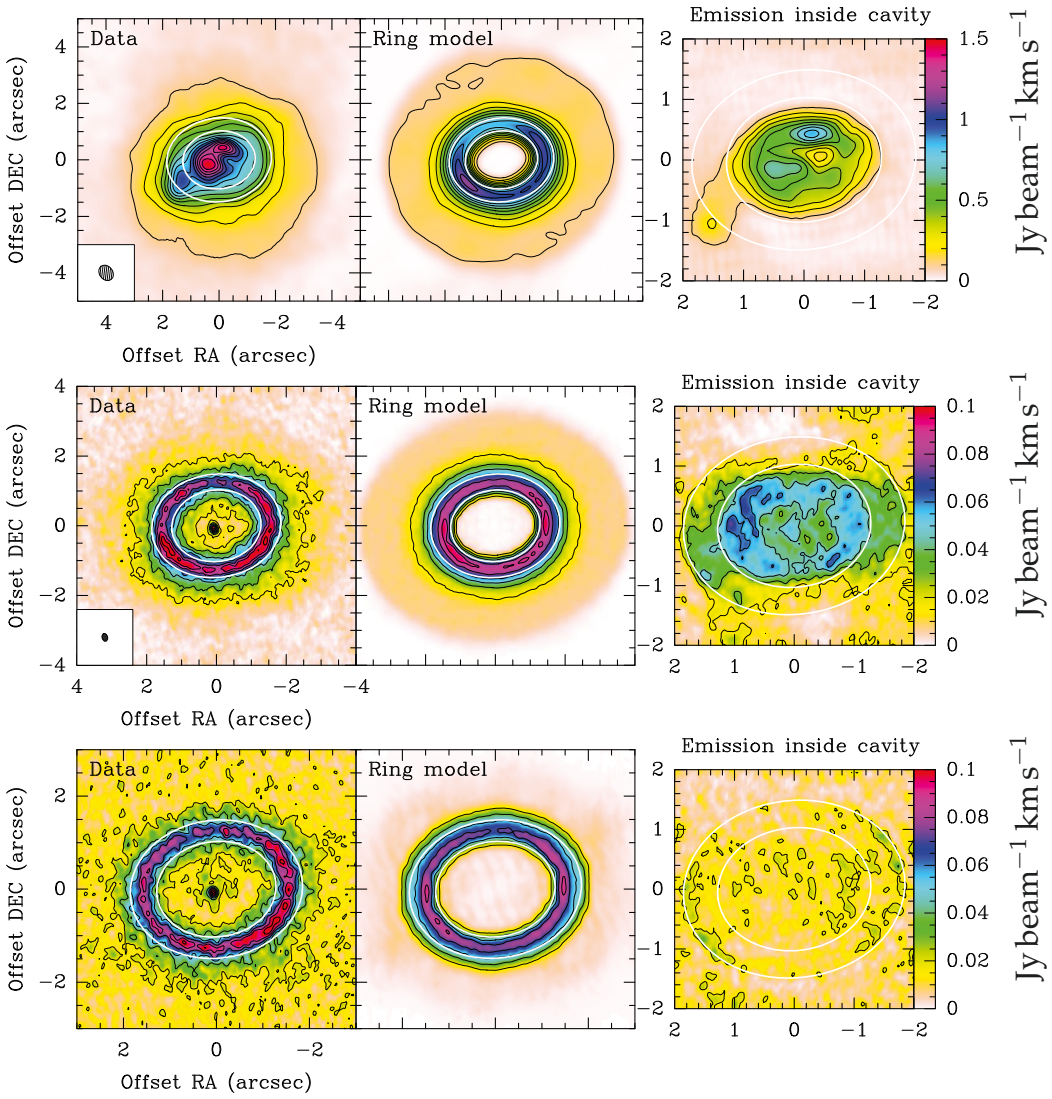

FIGURE 4.7: From top to bottom, ^{12}CO, ^{13}CO and C^{18}O J=3–2 maps. *Left:* Integrated intensity map. *Middle:* Best ring model intensity map. *Right:* Emission inside cavity measured as the difference between observations and ring model.

4.B χ^2 maps on excitation condition parameters plane

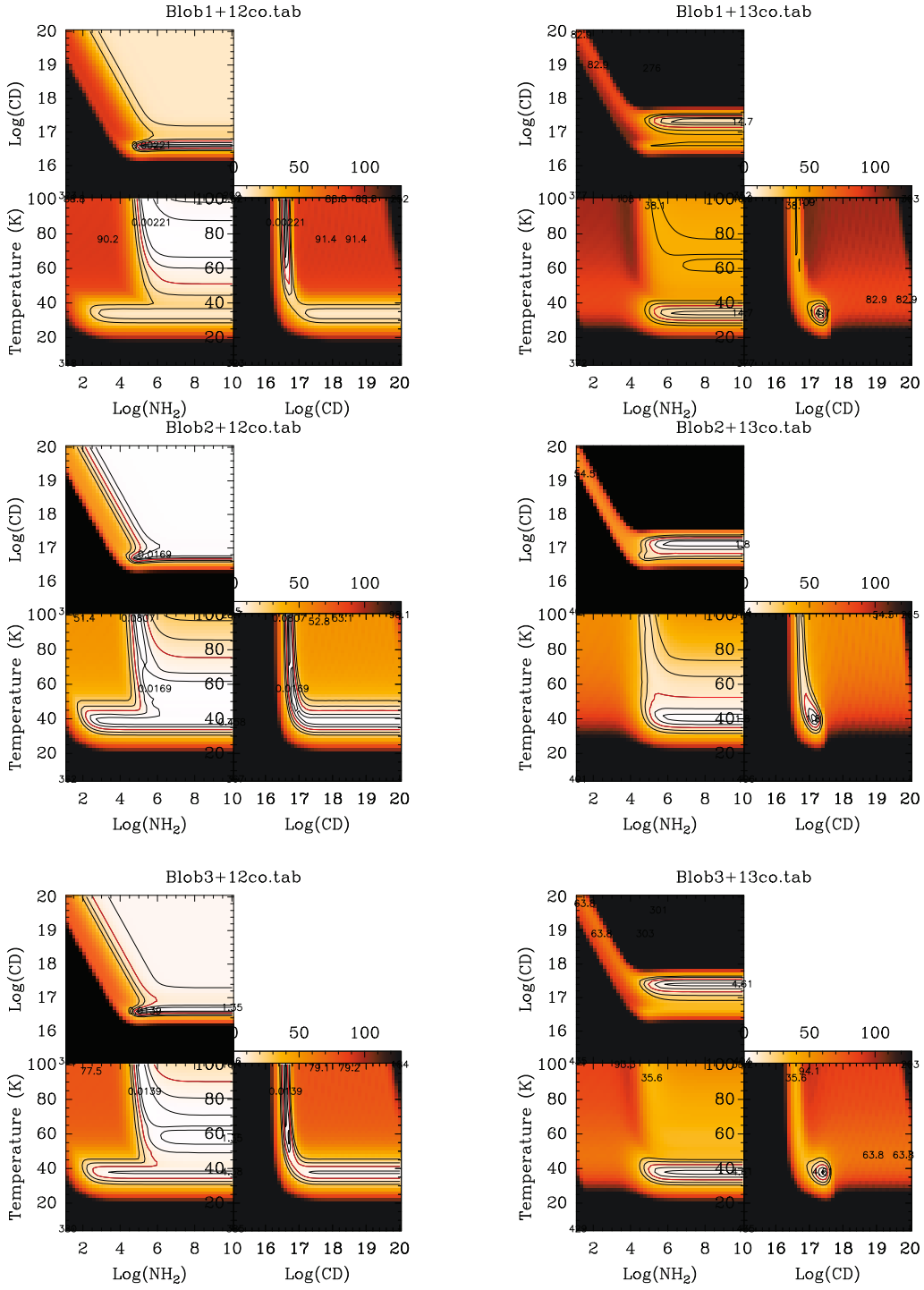

FIGURE 4.8: χ^2 maps in the (n_{H2}, CD), (n_{H2}, T_{ex}) and (CD, T_{ex}) planes calculated for ^{12}CO J=6–5 and J=3–2 *(left)*, for ^{12}CO J=6–5 and J=3–2 and ^{13}CO J=3–2 *(right)*. Upper panels are for blob B1, central panels for B2 and lower panels for B3.

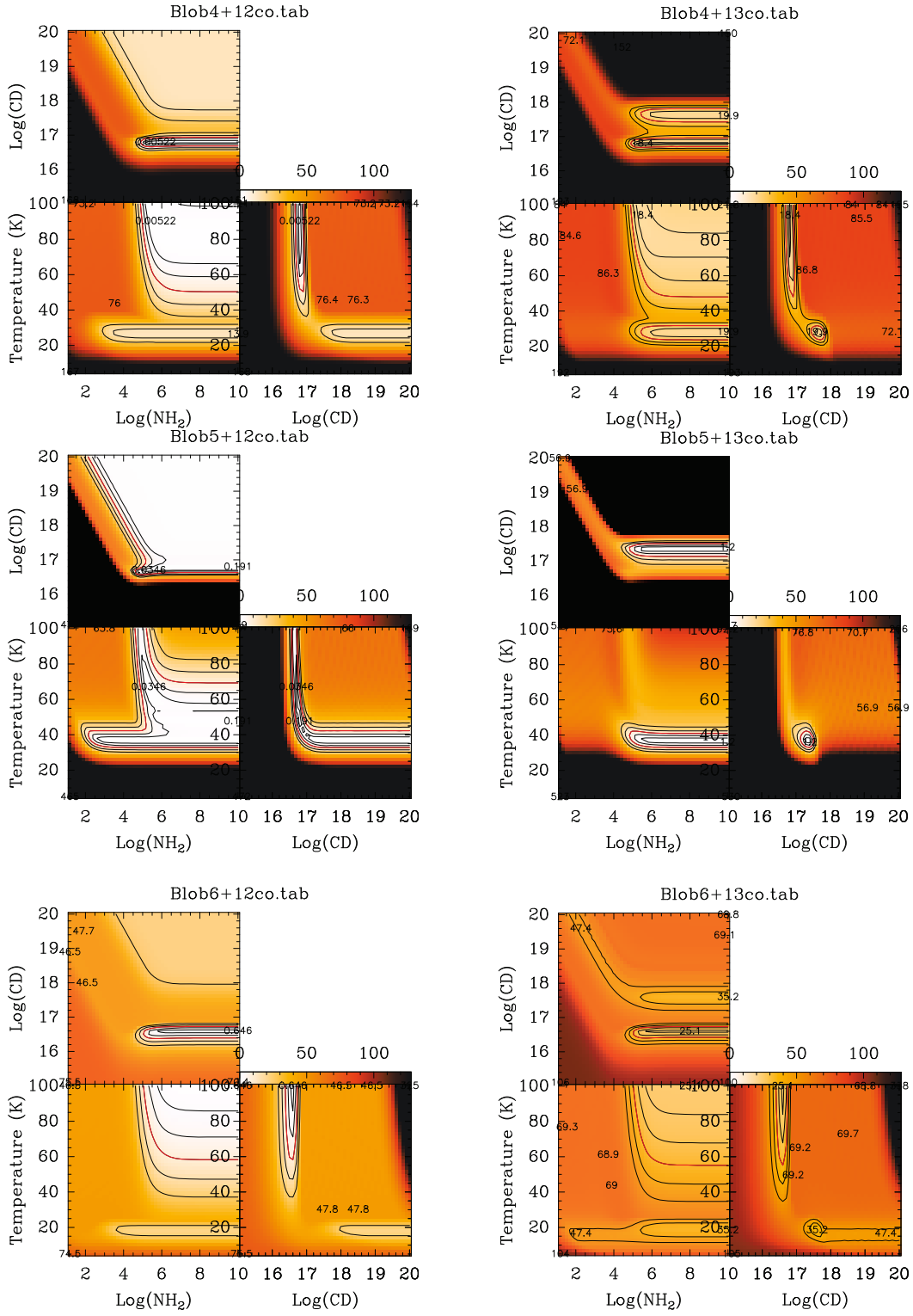

FIGURE 4.9: χ^2 maps in the (n_{H2}, CD), (n_{H2}, T_{ex}) and (CD, T_{ex}) planes calculated for ^{12}CO J=6–5 and J=3–2 *(left)*, for ^{12}CO J=6–5 and J=3–2 and ^{13}CO J=3–2 *(right)*. Upper panels are for blob B4, central panels for B5 and lower panels for B6.

Chapter 5

Chemical content of GG Tau A[1]

In a recent attempt to investigate the chemical content of protoplanetary disks, we observed several molecular emission lines at $\sim$ 2 mm wavelength. The present chapter presents the main results of this survey.

5.1 Published survey

In order to search for S-bearing species in protoplanetary disks, we observed H_2S, C_2S, SO_2 and SO emissions from GG Tau A. This resulted in the first detection of H_2S in a protoplanetary disk. The other molecules were not detected. We also observed C-bearing species and detected HCO^+, DCO^+, and $H^{13}CO^+$ molecular lines, while c-C_3H_2 and HC_3N remained undetected. However, the survey provided an estimated upper limit (3σ) to the surface densities of the undetected molecules (see Table 5.2 and 5.3).

5.1.1 Results

Figures 5.1 and 5.2 show integrated intensity maps and velocity maps of the detected lines, H_2S 1(1,0) – 1(0,1), $H^{13}CO^+$ (2–1), DCO^+(3–2), and HCO^+(1–0) respectively.

The velocity maps show a clear signature of rotation about the minor axis.

$H_2S\,1(1,0) - 1(0,1)$ is detected with a peak SNR$\geq$4 in several channels. Most of the line emission originates from the dense ring between 180 and 260 au and extends up to 500 au. The east-west asymmetry correspond to a difference of only 2σ.

HCO^+(1– 0) and $H^{13}CO^+$(2–1) emissions are detected with high SNR ($\geq$ 7). The emission of HCO^+(1–0) appear as extended as the CO emission out to $\sim$800 au (Guilloteau, Dutrey, and Simon, 1999). The optically thin emission from the J=2–1 line of

[1]The content of this chapter is published in Phuong, N. T.; Chapillon, E.; Majumdar, L.; Dutrey, A.; Guilloteau, S.; Piétu, V.; Wakelam, V.; Diep, P. N.; Tang, Y.-W.; Beck, T.; Bary, J., 2018A&A,616L,5P, DOI: 10.1051/0004-6361/201833766

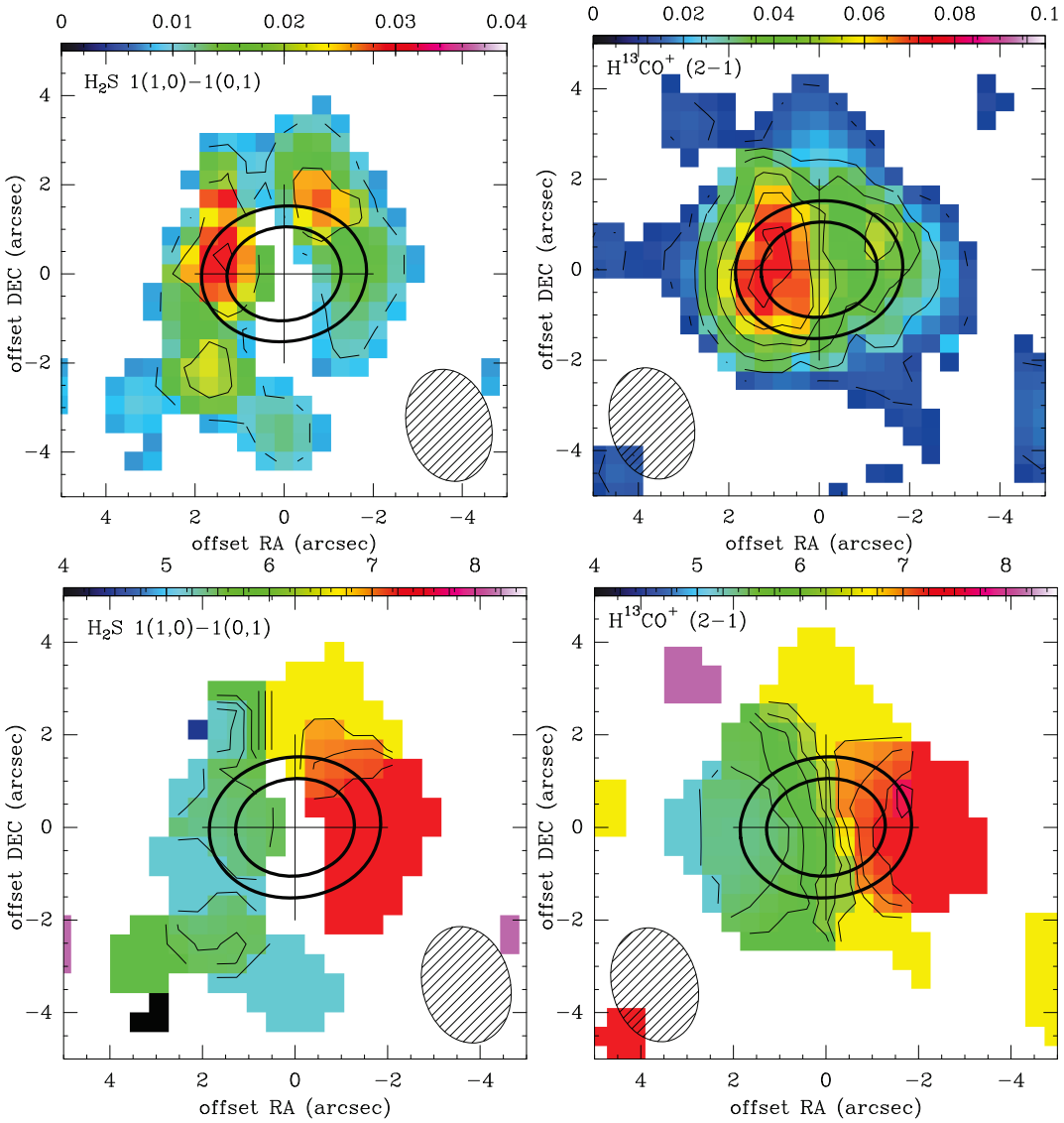

FIGURE 5.1: **Upper panels:** Integrated intensity map of H_2S 1(1,0)–1(0,1) (*left*) and $H^{13}CO^+$(2–1) (*right*) emissions. The colour scale at the top is in units of Jy beam^{-1} km s^{-1}, the contour levels step is 2σ. **Lower panels:** Velocity map of H_2S 1(1,0)–1(0,1) (*left*) and $H^{13}CO^+$(2–1) (*right*) emissions. The colour scale at the top is in units of km s^{-1}, the contour levels step is 0.5 km s^{-1}.

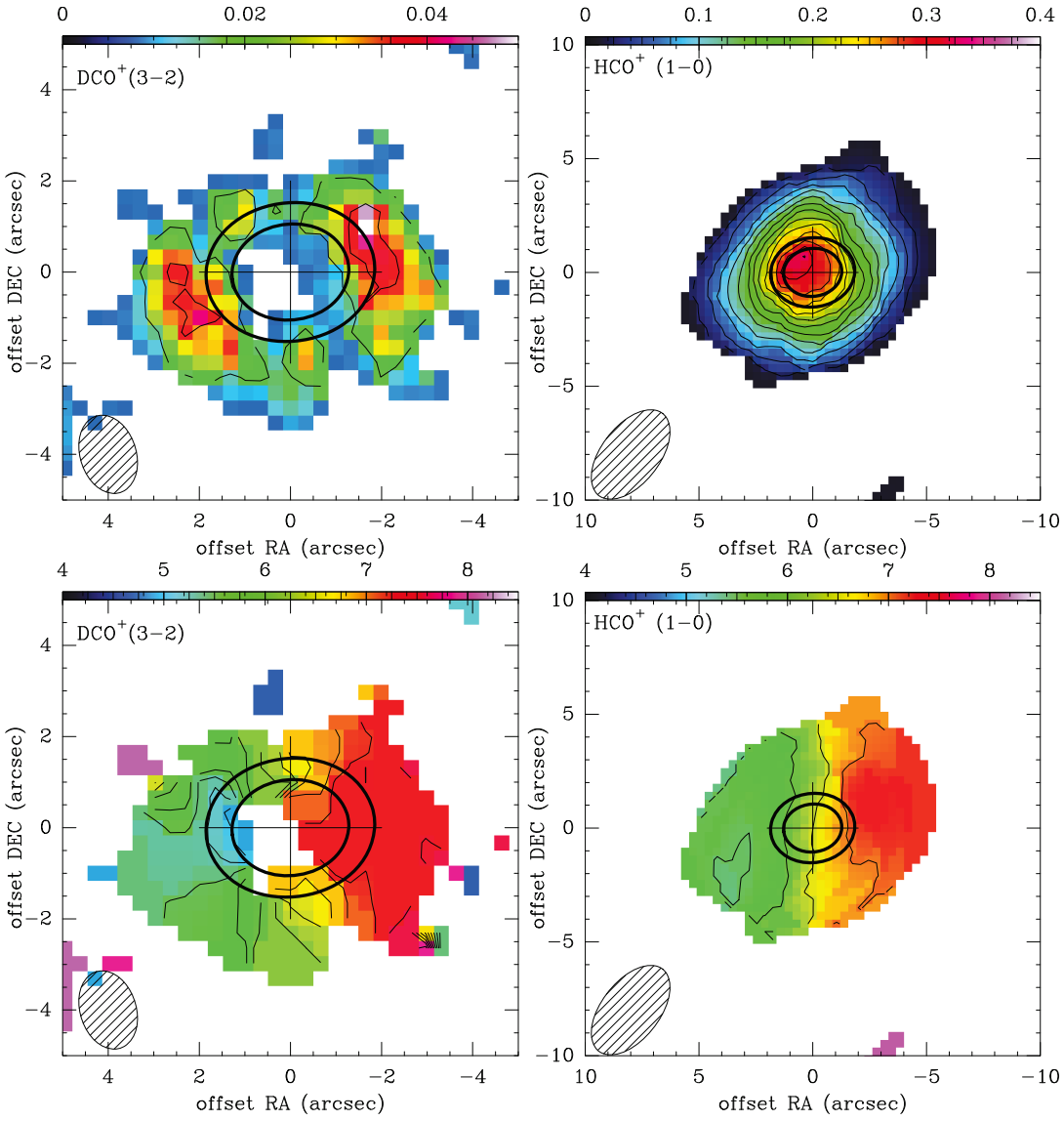

FIGURE 5.2: **Upper panels:** Integrated intensity map of DCO^+(3–2) (*left*) and HCO^+(1–0) (*right*) emissions. The colour scale at the top is in units of Jy beam^{-1} km s^{-1}, the contour levels step is 2σ. **Lower panels:** Velocity map of DCO^+(3–2) (*left*) and HCO^+(1–0) (*right*) emissions. The colour scale at the top is in units of km s^{-1}, the contour levels step is 0.5 km s^{-1}.

the $H^{13}CO^+$ isotopologue peaks on the dense ring and extends to ∼500 au. An east-west asymmetry is also seen in the $H^{13}CO^+$ integrated intensity map. In contrast, the DCO^+(3–2) emission, detected at SNR≥ 7, peaks just outside of the dense ring, near 280 au. This suggests some radially varying deuteration in the colder part of the outer disk.

5.1.2 Comparison between observations and chemical model predictions

Observed column density

The data were analyzed in the *uv* plane using the radiative transfer code DiskFit, which compares the observed visibilities with visibilities predicted by a model of the emission (Piétu, Dutrey, and Guilloteau, 2007, and Chapter 2). We use a power law radial dependence of the physical parameters that govern line emission (Dutrey, Guilloteau, and Simon, 1994; Piétu, Dutrey, and Guilloteau, 2007).

TABLE 5.1: GG Tau A parameters

Geometry		Law
Inclination	35°	$V(r) = 3.4\,(\frac{r}{100\,\mathrm{au}})^{-0.5}$ (km s^{-1})
Orientation	7°	$T(r) = 25\,(\frac{r}{200\,\mathrm{au}})^{-1}$ (K)
Systemic velocity	6.4 km s^{-1}	$\Sigma(r) = \Sigma_{250}\,(\frac{r}{250\,\mathrm{au}})^{-1.5}$ (cm^{-2})

Because of the relatively low SNR associated with these data, quantities such as inclination, orientation, velocity and temperature power laws are taken from previous studies (Dutrey, Guilloteau, and Simon, 1994; Dutrey et al., 2014; Guilloteau, Dutrey, and Simon, 1999, and our Table 5.1). We only vary the molecular surface density parameter Σ_{250}. Results are presented in Table 5.2 for the detected molecules and Table 5.3 lists the 3σ upper limits for undetected molecules.

Predicted column density from the chemical model

To model the chemistry in the dense and cold ring of GG Tau A, we use the gas-grain chemical model `Nautilus` (Ruaud, Wakelam, and Hersant, 2016). This model simulates chemistry in three phases, i.e. gas phase, grain surface and grain mantle, along with possible exchanges between the different phases. The reference chemical network is `deuspin.kida.uva.2016` (Majumdar et al., 2017), which includes ∼ 1100 species both in gas and solid phases linked together via ∼ 12000 reactions, with the updates in sulfur chemistry from Vidal et al., 2017. The disk structure is similar to that used in Wakelam et al., 2016. In addition to disk parameters from Table 5.1, we assume a stellar UV flux of $f_{UV200AU}$ = 375 χ_0 at 200 au, where χ_0 is in the units of the Draine (1978) interstellar UV field, based on what is observed in T Tauri

TABLE 5.2: Observed and predicted surface densities of detected molecules (cm^{-2})

Molecule	Observed⋆ (derived from DiskFit)	Predicted† (from Nautilus)
HCO^+(1-0)	$1.5 \pm 0.04 \times 10^{13}$	2.2×10^{12}
$H^{13}CO^+$ (2-1)	$5.3 \pm 0.3 \times 10^{11}$	(-)
DCO^+ (3-2)	$3.9 \pm 0.2 \times 10^{11}$	7.0×10^{10}
H_2S 1(1,0) - 1(0,1)	$1.3 \pm 0.1 \times 10^{12}$	3.4×10^{13}
CS(3-2)	2.2×10^{13}	1.4×10^{13}

⋆ Observed surface density at 250 au is derived using DiskFit.

† Species surface density in the gas phase at 250 au predicted with Nautilus.

$(-)$ Our model does not include carbon isotope chemistry.

TABLE 5.3: Observed and predicted surface densities of non-detected molecules (cm^{-2})

Molecule	Observed⋆ (derived from DiskFit)	Predicted† (from Nautilus)
CCS	$<1.7 \times 10^{12}$	7.2×10^{10}
SO_2	$<1.5 \times 10^{12}$	6.0×10^{12}
SO	$<1.1 \times 10^{12}$	1.5×10^{13}
HC_3N	$< 3.2 \times 10^{11}$	5.7×10^{11}
c-C_3H_2	$< 2.7 \times 10^{11}$	2.4×10^{12}

⋆ Observed surface density at 250 au is derived using DiskFit.

† Species surface density in the gas phase at 250 au predicted with Nautilus.

stars (Bergin et al., 2004). Previous observations (Tang et al., 2016) revealed a limited vertical temperature gradient at a radius of $\sim 250 - 300$ au, thus we introduced a small vertical temperature gradient with the mid-plane temperature equal to 20 K at 250 au, increasing to 30 K at three scale heights.

To compute the chemistry, we first calculated the chemical composition of the gas and ices of the parent cloud, assuming conditions for a dense cloud with an age of $\sim 10^6$ yr and then ran the model for another 10^6 yr following Wakelam et al. (2016). For the parent cloud, initially all the elements are in atomic form (see Table 1, Vidal et al., 2017) except for hydrogen and deuterium, which are initially in H_2 and HD forms, respectively (Majumdar et al., 2017).

To discuss the observations of H_2S, CS, DCO^+, and HCO^+ emissions, we compared the observed column densities with those predicted in the ring at a radius of 250 au.

We explored various initial C/O ratios, ortho to para ratios (OPR) for H_2, initial sulfur abundances X(S), grain sizes, and UV flux. According to Bergin et al. (2016), CCH emission can only be explained with a gas-phase C/O ratio larger than 1. This represents a scenario in which oxygen is depleted on the grains before the formation

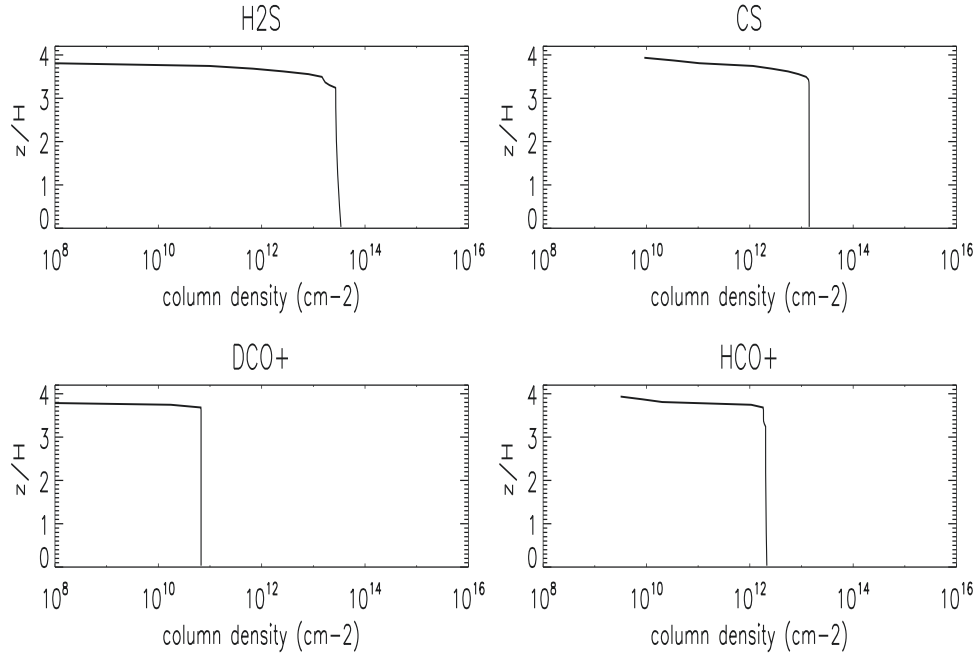

FIGURE 5.3: Best model of H_2S, CS, DCO^+, and HCO^+ in the GG Tau A ring derived from Nautilus. The z/H ratio (which measures the scale height) is shown vs. surface density.

of the disk and driven to the midplane of the disk. In other words, oxygen would not participate in the chemistry in the region where CCH is observed. Semenov et al. (2018) found that the column densities of SO and SO_2 drop by factors of ∼100 and 500, respectively, when C/O changes from 0.46 to 1.2, whereas column densities of H_2S do not change as the species contains neither C nor O. We stick to the standard C/O ratio of 0.7 in our model (Hincelin et al., 2011b; Wakelam et al., 2016; Majumdar et al., 2017), which gives a reasonably good agreement for DCO^+, CS, CCS, HC_3N, and SO_2.

Best model: Results are therefore presented for C/O = 0.7, OPR=3, X(S)=8 $\times 10^{-8}$ and a grain size of 0.1 μm. Other models lead to larger disagreement with the data. Figures 5.3 and 5.4 show the predicted vertical distribution of the molecules, and Tables 5.2 and 5.3 compares the predicted surface densities to the observational results derived using DiskFit.

5.1.3 Discussion

Relative molecular abundance in disks and in parent cloud: The measured H_2S column density is a factor of three greater than the upper limits quoted by Dutrey et al. (2011) for DM Tau, LkCa 15, MWC 480, and GO Tau, probably reflecting the larger disk mass of GG Tau A. However, the CS to H_2S abundance ratio of ∼20 in

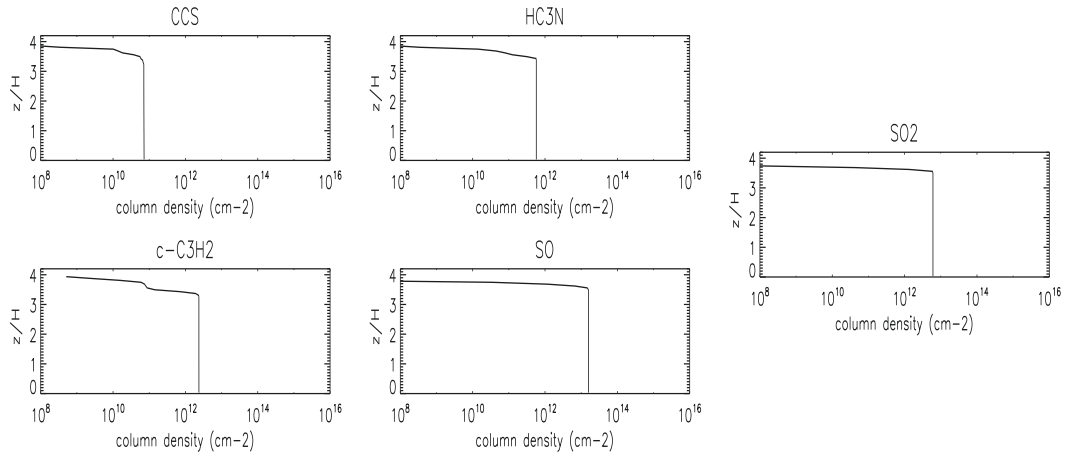

FIGURE 5.4: Best model of CCS, c-C_3H_2, HC_3N, SO, and SO_2 in the GG Tau A ring, derived from Nautilus, using our best knowledge of the GG Tau disk. The z/H ratio (which measures the scale height) is shown vs. surface density.

GG Tau A may be the same than in other similar disks. The upper limit on HC_3N is about half the values reported in LkCa 15, MWC 480, and GO Tau by Chapillon et al. (2012).

To make relevant abundance comparisons, we use ^{13}CO as a reference since H_2 column densities are difficult to measure accurately. The results for the disks of GG Tau A, LkCa15 and the dark cloud TMC-1 are given in Table 5.4. LkCa15 is a T Tauri star similar to GG Tau A: its disk exhibits a central cavity of radius 50 au (Piétu et al., 2006) and has a mass on the order of $\sim$ 0.028 $M_\odot$ (Guilloteau et al., 2011). Determining the uncertainties is difficult because the abundances were obtained from different studies. Therefore, we assume errors of 30% in the cases of LkCa 15 and TMC-1.

For GG Tau A, we take a ^{13}CO column density, derived from our observations, at 250 au of Σ_{250}=1.13 $\times$ 10^{16} cm^{-2} (Phuong et al., 2019 submitted). For LkCa 15, Punzi et al. (2015) found an HCO^+ abundance relative to ^{13}CO of 15 $\times$ 10^{-4}, Huang et al. (2017) gave abundance ratios of DCO^+/HCO^+ and $DCO^+/H^{13}CO^+$ of 0.024 and 1.1, respectively, and Dutrey et al. (2011) gave an upper limit of H_2S relative to CO of 10^{-6}, which we convert to ^{13}CO using an isotopic ratio $^{12}C/^{13}C \sim 60$ (Lucas and Liszt, 1998).

In the TMC-1 dark cloud, Ohishi, Irvine, and Kaifu (1992) determined a ^{12}CO abundance relative to H_2 of 8 $\times$ 10^{-5} or 1.3 $\times$ 10^{-6} for ^{13}CO. The abundance of HCO^+, H_2S (upper limit) (Omont, 2007), $H^{13}CO^+$, and DCO^+ (Butner, Lada, and Loren, 1995) relative to H_2 are then used to get the abundances relative to ^{13}CO. In L134N, the abundances of these species are similar, but H_2S has been detected with an abundance ratio of 60 $\times$ 10^{-5} (Ohishi, Irvine, and Kaifu, 1992), similar to the upper limit obtained in TMC-1. Thus, the disks appear to have very similar relative abundances, suggesting similar chemical processes at play, while the dense cores

TABLE 5.4: Molecular abundance relative to ^{13}CO ($X_{[mol]}/X_{[^{13}CO]} \times 10^5$)

	TMC-1*	LkCa 15	GG Tau
HCO^+	$600 \pm 180^{(1)}$	$150 \pm 35^{(3)}$	130 ± 12
H_2S	$< 45^{(1)}$	$< 7^{(4)}$	11 ± 3
$H^{13}CO^+$	15 ± 4 $^{(2)}$	5 ± 1.5 $^{(5)}$	4.7 ± 0.3
DCO^+	30 ± 9 $^{(2)}$	4.5 ± 1.4 $^{(5)}$	3.5 ± 0.15

* ^{13}CO abundance is derived from CO abundance in Ohishi, Irvine, and Kaifu (1992),
$^{(1)}$Omont (2007), $^{(2)}$Butner, Lada, and Loren (1995), $^{(3)}$Punzi et al. (2015), $^{(4)}$Dutrey et al. (2011), $^{(5)}$Huang et al. (2017).

differ significantly.

Chemistry of Sulfur-bearing species: In the chemical modelling, we found that H_2S peaks around three scale heights. The main reason behind this is the rapid formation of H_2S on the grain surface via the hydrogenation reaction of HS, i.e., grain-H + grain-HS→grain-H_2S. Once H_2S is formed on the surface, it is then chemically desorbed to the gas phase. Almost 80% of the H_2S comes from surface reactions. The contribution of the gas-phase reaction $H_3S^+ + e^- \rightarrow$ H + H_2S is about 20%. Below three scale heights, H_2S depletes rapidly on the grains because of the increase in density and decrease in temperature. At the same altitude, CS is formed in the gas phase via the dissociative recombination reactions of HCS^+, H_2CS^+, H_3CS^+, and $HOCS^+$.

The modeled CCS and SO_2 column densities (shown in Table 5.3 and in Figure 5.4) are low, explaining their non-detection but the SO column density is overpredicted. The CCS molecule peaking above z/H=3 is caused by the gas phase formation proceeding via S + CCH→ H + CCS and $HC_2S^+ + e^- \rightarrow$ H + CCS reactions. SO_2 is made from the OH + SO reaction around this location, whereas SO comes from the S + OH reaction.

We found that the UV field has a negligible impact on the H_2S desorption and mildly affects the SO/H_2S ratio. The key parameter in the model is the initial S abundance. Even with the low value of 8×10^{-8}, the chemical model overpredicts H_2S and SO by about an order of magnitude, but is compatible with CS and the current limits on SO_2 and CCS.

In our model, the molecular layer is very thin and located three scale heights above the disk plane. This is different from what is observed in CS in the Flying Saucer (Dutrey et al., 2017), where CS appears closer to one scale height. The difference may be due to the larger mass of the GG Tau disk (0.15 $M_\odot$). On one side, the high densities limit the UV radiation penetration (which drives the active chemistry) to the uppermost layers, while closer to the midplane, the even higher densities lead to more efficient sticking on dust grains.

Our results suggest that the H_2S chemistry on the surface of the grains is probably improperly accounted for, even with our three-phase model. They also suggest

that a significant amount of H_2S might transform in some more complex unobserved sulfur-bearing species (Dutrey et al., 2011; Wakelam et al., 2005). Indeed, measurements of S-bearing species in comet 67P performed by ROSETTA indicate a solar value for the S/O elemental ratio (Calmonte et al., 2016). H_2S accounts for about half of the S budget in the comet, suggesting that the transformation of H_2S into other compounds in ices is limited. The nearly constant H_2S/H_2O ratio also suggests that H_2S does not evaporate alone, but in combination with water (Jiménez-Escobar and Muñoz Caro, 2011).

Chemistry of DCO^+: The measured $HCO^+/H^{13}CO^+$ ratio is about 30, smaller than the standard isotopic ratio ($^{12}C/^{13}C$=70, Milam et al., 2005), suggesting partially optically thick emission for the $HCO^+(1-0)$ line. The measured DCO^+/HCO^+ ratio, ~ 0.03 over the disk, is comparable to the average value ($\sim$0.04; van Dishoeck, Thi, and van Zadelhoff, 2003) derived in the disk of TW Hydra of mass of $\sim 0.06\,M_\odot$ (Bergin et al., 2013), and in the disk of LkCa 15 (ratio of $\sim$0.024, Huang et al., 2017). These values are three orders of magnitude higher than the cosmic D/H ratio in the local ISM of 1.5×10^{-5} (Linsky et al., 2006), showing clear evidence for ongoing deuterium local enrichment in protoplanetary disks.

HCO^+ formation and deuteration is controlled by CO as well as by H_2D^+ and H_3^+ ions. These ions are mostly sensitive to the X-ray flux, while UV radiation and cosmic rays play a limited role. The balance of H_2D^+ and H_3^+ is controlled by the temperature sensitive reaction, $H_3^+ + HD \rightleftharpoons H_2D^+ + H_2 + 232\,K$ (Millar, Bennett, and Herbst, 1989). Upon fractionation of H_3^+, proton exchange reactions transfer the D enhancement to more complex gaseous species. One of the key reactions of this kind in protoplanetary disks is the interaction with CO to produce DCO^+ in the low temperature regime ($T \approx 10-30\,K$). Because of the temperature dependence, DCO^+ is expected to be enhanced around the CO snow-line interface, as illustrated by the ring structure observed in HD 163296 (Mathews et al., 2013b). Our model somewhat underpredicts the HCO^+ content. At 250 au, HCO^+ peaks at three scale heights, where the molecular layer is warm ($\sim 30\,K$) and forms mainly from the reaction of CO on ortho-H_3^+. At this altitude, DCO^+ forms from the isotope exchange reaction between HCO^+ and D because the gas temperature is still high. Closer to the disk midplane, the ortho-H_2D^+ + CO pathway remains inefficient because of the strong CO depletion that results from high densities and low temperature in the dense ring (180 au–260 au). DCO^+ emission is observed to peak just outside the dense ring ($\sim$300 au), at the CO snow-line location (we measured here $T_k = 20\,K$ from CO observations, see Chapter 4 for details). This behaviour is also observed by Mathews et al. (2013b) in HD 163296 disk. Higher angular resolution DCO^+ data are needed to go deeper into the analysis.

Other observed species: We also presented integrated column densities of HC_3N and c-C_3H_2 in Table 5.3 and Figure 5.4. The modeled column densities of HC_3N and $c-C_3H_2$ are overpredicted. The high column density of HC_3N above three

scale heights is due to its rapid formation via the $CN + C_2H_2 \rightarrow H + HC_3N$ reaction, whereas $c-C_3H_2$ forms from the $CH + C_2H_2$ reaction, photodissociation of CH_2CCH and dissociative recombination of $C_3H_5^+$.

5.2 Summary

Using NOEMA, we have observed the GG Tau A outer disk in several molecules. We report the first detection of H_2S in a protoplanetary disk.

We clearly detect HCO^+, $H^{13}CO^+$, DCO^+, and H_2S. HCO^+ emission is extended, $H^{13}CO^+$ and H_2S emissions peak inside the dense ring at $\sim$ 250 au, while DCO^+ emission arises from the outer disk beyond a radius of 300 au.

Our three-phase chemical model fails to reproduce the observed column densities of S-bearing molecules, even with low S abundance and C/O = 0.7, suggesting that our understanding of S chemistry on dust grains is still incomplete.

The detection of H_2S in GG Tau A is likely facilitated by the large disk mass in comparison with similar disks. When abundance ratios are measured, they appear similar to those found in other disks like LKCa 15.

5.A Channel maps

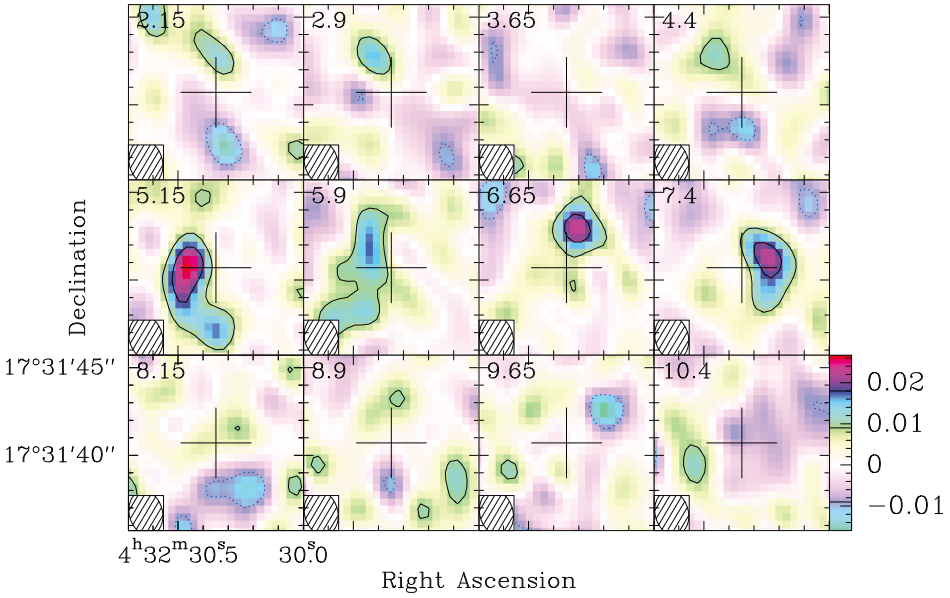

FIGURE 5.5: Channel maps of H_2S 1(1,0) - 1(0,1) emission. The colour scale is in units of Jy beam^{-1}. The contour spacing is 5 mJy beam^{-1} which corresponds to 1σ or 0.04 K. The beam (2.55″ × 1.90″, PA=14°) is shown in the lower corner of each channel map.

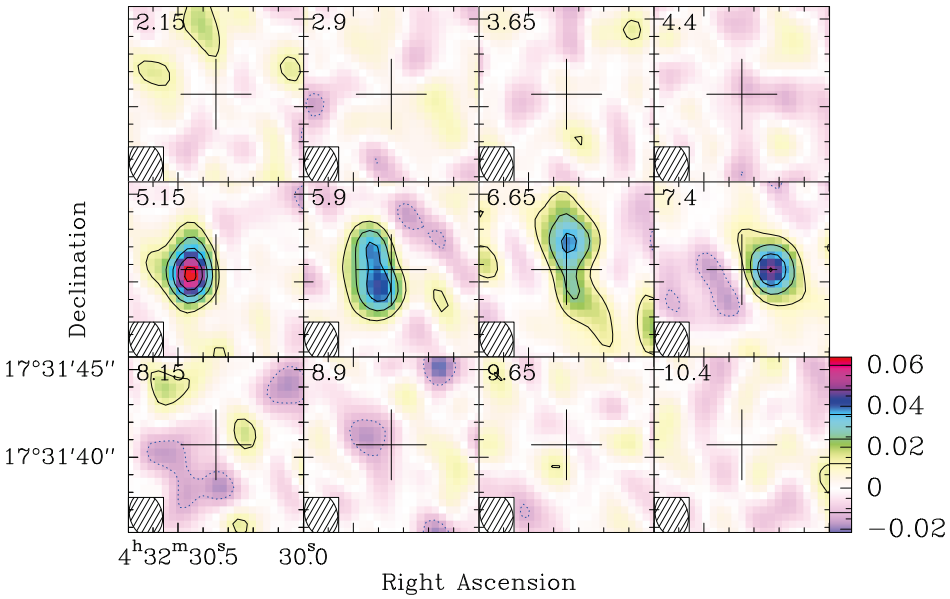

FIGURE 5.6: Channel maps of $H^{13}CO^+$ (2-1) emission. The colour scale is in units of Jy beam^{-1}. The contour spacing is 12 mJy beam^{-1} which corresponds to 2σ or 0.11 K. The beam (2.50″ × 1.85″, PA=15°) is shown in the lower conner of each channel map.

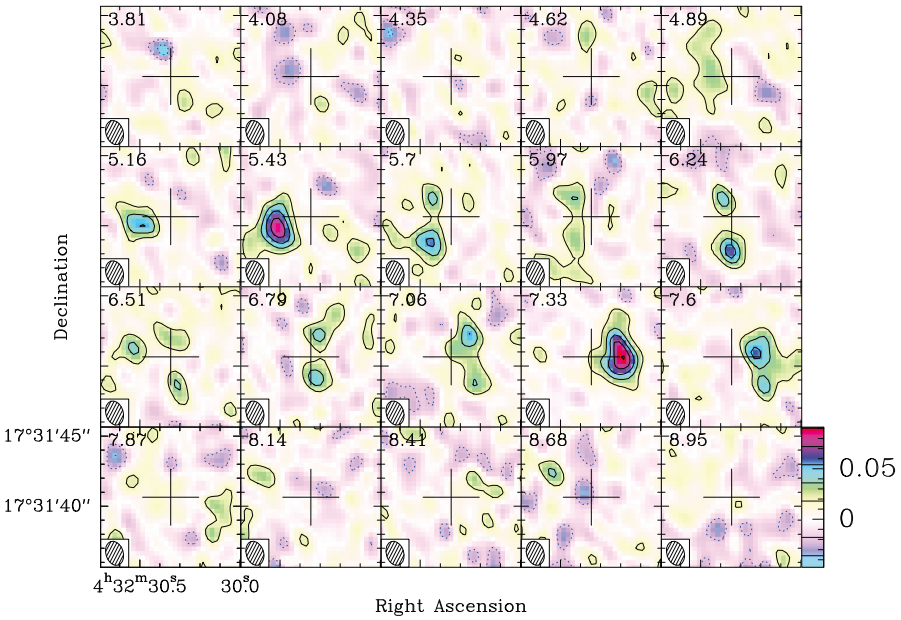

FIGURE 5.7: Channel maps of DCO^+ (3-2) emission. The colour scale is in units of Jy beam^{-1}. The contour spacing is 18 mJy beam^{-1} which corresponds to 2σ or 0.22 K. The beam (1.76″ × 1.23″, PA=17°) is shown in the lower conner of each channel map.

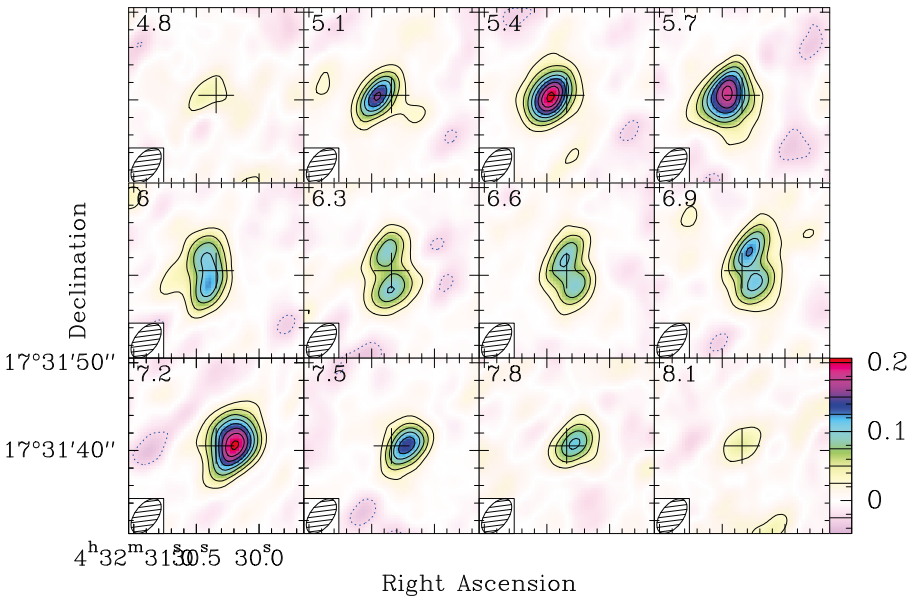

FIGURE 5.8: Channel maps of HCO^+ (1-0) emission. The colour scale is in units of Jy beam^{-1}. The contour spacing is 25 mJy beam^{-1} which corresponds to 2σ or 0.33 K. The beam (4.57″ × 2.55″, PA=−38°) is shown in the lower conner of each channel map.

Chapter 6

Conclusion and Perspectives

6.1 Conclusion

During my thesis, I have studied the gas and dust morphology of a protoplanetary disk surrounding a young triple protostar, GG Tau A. I investigated its kinematics and physical structure using the *mm* wavelength emission of molecular lines such as ^{12}CO, ^{13}CO, $C^{18}O$, HCO^+, $H^{13}CO^+$, DCO^+ and of H_2S observed by ALMA and NOEMA.

This analysis confirms the results of earlier studies of the morphology of the GG Tau A system to which it contributes significant additional information. The triple star system is surrounded by a dense gas and dust ring extending from 180 au to 260 au and a gas disk extending out to 800 au (in CO). The best angular resolution observations of $0.15''$ reveal that the circumbinary disk likely consists of unresolved ring(s) and sub-structures. I presented the analyses of the gas emitted by the circumbinary disk and by the cavity separately. 1) By removing the emission from the central cavity, I modelled the outer disk and evaluated its physical properties, such as surface density and temperature profiles. 2) Subtraction of the outer disk model prediction from the original data provides an image of emission inside the cavity that is not contaminated by the circumbinary disk emission and allows for a study of the dynamical and physical properties of the gas. 3) A first attempt at describing the chemistry at stake in the circumbinary disk has been presented.

The main results are summarised below.

6.1.1 Gas properties in the outer disk

I have evaluated the radial and azimuthal dependence of the morpho-kinematics and physical properties of the gas in the disk using a radiative transfer code.

The analysis reveals the presence of two concentric rings (one dominated by dust and the other dominated by gas) sharing a same axis projecting on the sky plane $\sim 7^\circ$ east of north and inclined with respect to the line of sight by respectively $32 \pm 4^\circ$ (dust) and $35 \pm 4^\circ$ (gas). While sharing approximately a same inner edge at

~180 au, their outer extensions are significantly different: 260 au for the dust and 800 au for the gas.

Variations of the integrated intensity across the disk area have been studied and found to confirm the presence of a "hot spot" in the south-eastern quadrant of the disk studied by Dutrey et al. (2014) and Tang et al. (2016).

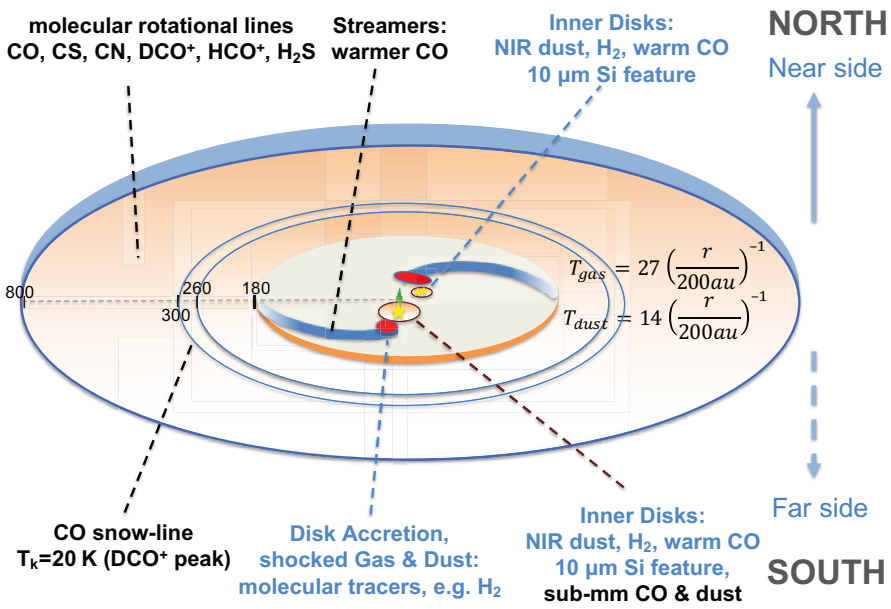

FIGURE 6.1: Schematic summary of the observations and analyses of the GG Tau A system presented in the thesis.

The study of the gas kinematics is dominated by Keplerian rotation around the disk axis. The Doppler velocity gradient along the disk major axis on the sky plane allows for a measurement of an upper limit of 9% on the ratio between a possible in-fall velocity and the rotation velocity (at 99% confidence level). The rotation velocity reaches 3.48 ± 0.04 km s^{-1} at 100 au, in agreement with previous, less precise determinations (e.g. Dutrey et al. (2014) quoted 3.4 ± 0.1 km s^{-1} at 100 au). This corresponds to a total stellar mass of 1.36 ± 0.07 M$_\odot$.

The dependence of the line width on r and ω has been also studied. It shows a little dependence on ω but increases from 0.18 km s^{-1} to 0.26 km s^{-1} when r decreases from 2.3″ to 1.5″. As the contributions of the Keplerian shear and the instrumental spectral resolution taken together should not exceed some 0.11 km s^{-1}, a possible explanation may be a factor 2 decrease of the disk surface temperature and opacity between these two locations.

The gas temperature derived from the optically thick CO line displays a steep decrease ($\propto r^{-1}$), as for the dust. I measured a gas temperature of 27 K at 200 au and the temperature of the CO snowline (20 K) is reached at $\sim$ 300 au, where we detect the maximum of emission of DCO^+. Mathews et al. (2013b) also observed a maximum of emission of DCO^+ from HD 163296 at the same snowline temperature.

Assuming constant flaring ($h(r)$ proportional to r) we obtain a scale height at $r = 200$ au of 24 au for ^{12}CO(3–2) and 23 au for ^{13}CO(3–2). In hydrostatic equilibrium, this corresponds to a temperature of $\sim$ 15 K, consistent with the dust temperature obtained by Dutrey et al. (2014).

The large mass of the GG Tau A disk, compared to that of other similar disks, has made it possible to reveal the presence of H_2S. When abundance ratios have been measured, they are similar to those found in other disks like that of LkCa 15. A chemical model has been used to predict the abundance of C-bearing and S-bearing species. Disagreements of a factor $\sim$ 7 in the former and a factor of $\sim$ 25 in H_2S have been found, suggesting that our understanding of the related chemistry is still incomplete.

A summary of the main results presented in the present thesis is sketched in Figure 6.1.

6.1.2 Gas inside the cavity

Subtracting the outer ring and disk model from the original data has produced images of the gas emission inside the cavity. These CLEANed images allowed for the study of the gas dynamics and properties (CO, ^{13}CO, and C^{18}O).

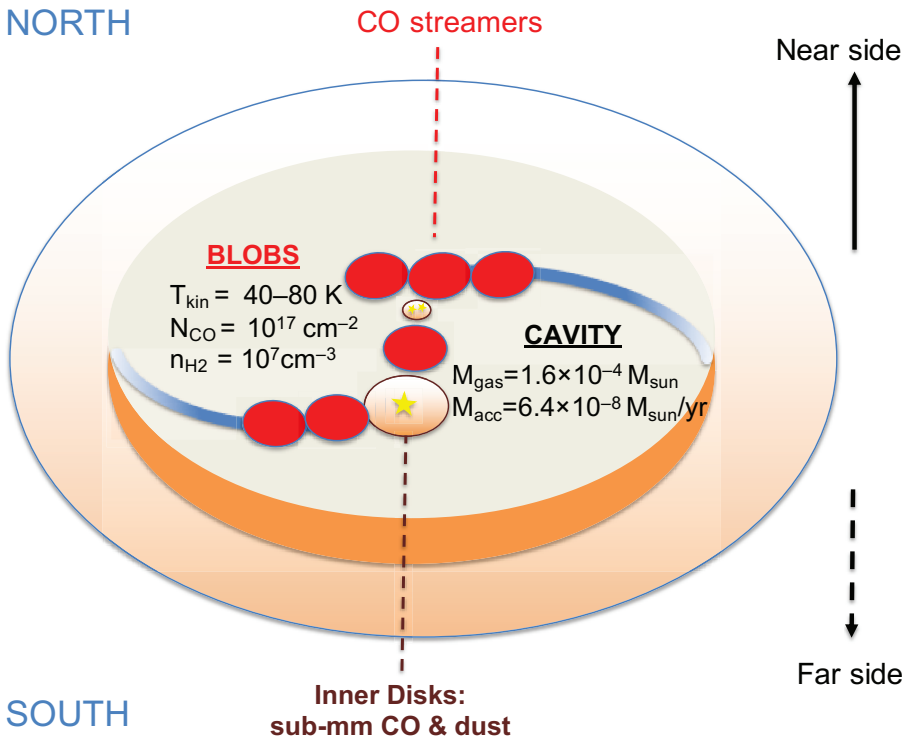

FIGURE 6.2: Schematic summary of the gas properties inside the GG Tau A cavity.

The CO emission inside the cavity appears brighter in the regions surrounding GG Tau Aa and Ab, which can be approximated by 6 blobs. A non-LTE analysis reveals physical conditions similar to those found in warm molecular clouds with CO column densities around a few $\sim 10^{17}\,\mathrm{cm}^{-2}$, temperatures in the range of $40 - 80\,\mathrm{K}$. The H_2 density in the dense part is estimated to be $10^7\,\mathrm{cm}^{-3}$.

Assuming an average temperature of 40 K inside the cavity, the total mass inside the cavity derived from the ^{13}CO observations is $1.6 \times 10^{-4}\,M_\odot$, assuming standard CO abundance and isotopic ratio.

The gas starts to exhibit non-Keplerian motion below $r \sim$160 au, where it reveals infall with a velocity of about 10% of the Keplerian velocity. The average mass accretion rate of the gas inside the cavity is $\sim 6 \times 10^{-8}\,M_\odot\,\mathrm{yr}^{-1}$, a value compatible with the stellar accretion rate measured using the H_α line, and sufficient to replenish the circumstellar disks.

Figure 6.2 summarizes the gas properties inside the GG Tau A cavity.

6.2 New Observations

New maps of the emission of CN, CO, and CS lines have been produced using ALMA Cycle 3 and Cycle 6 observations. Evidence for the "hot spot", as reported by Dutrey et al. (2014) and Tang et al. (2016) in CO emission, and indications of "spiral/ring" features have been revealed. I present here first images of these data which will be analysed in the future.

6.2.1 CO observations

CO(2–1) emission was observed in ALMA Cycle 6 with an angular resolution of $\sim 0.3''$, together with CS(5–4) and CN(2–1) line emissions. CO(2–1) intensity and velocity maps are shown in Figure 6.3. A region of strong emission is visible in the north-western quadrant, at opposite azimuth to the "hot spot"and at about the same radius. At larger distances from the star ($r > 250$ au), one may see some indication for the possible presence of two spiral arms, one originating from the "hot spot" and the other from its azimuthally opposite location, connecting the material of the ring to the outer disk. These features are better seen in the map of the peak brightness temperature shown in Figure 6.4. Confirmation of the presence of such features requires further analysis.

6.2.2 CN observations

CN(3–2) and CN(2–1) have been observed by ALMA in 2015 (Cycle 3) and 2018 (Cycle 6) with angular resolutions of $\sim 0.15''$ and $\sim 0.3''$ respectively. Figure 6.5 and Figure 6.6 display the related intensity and velocity maps. The intensity maps

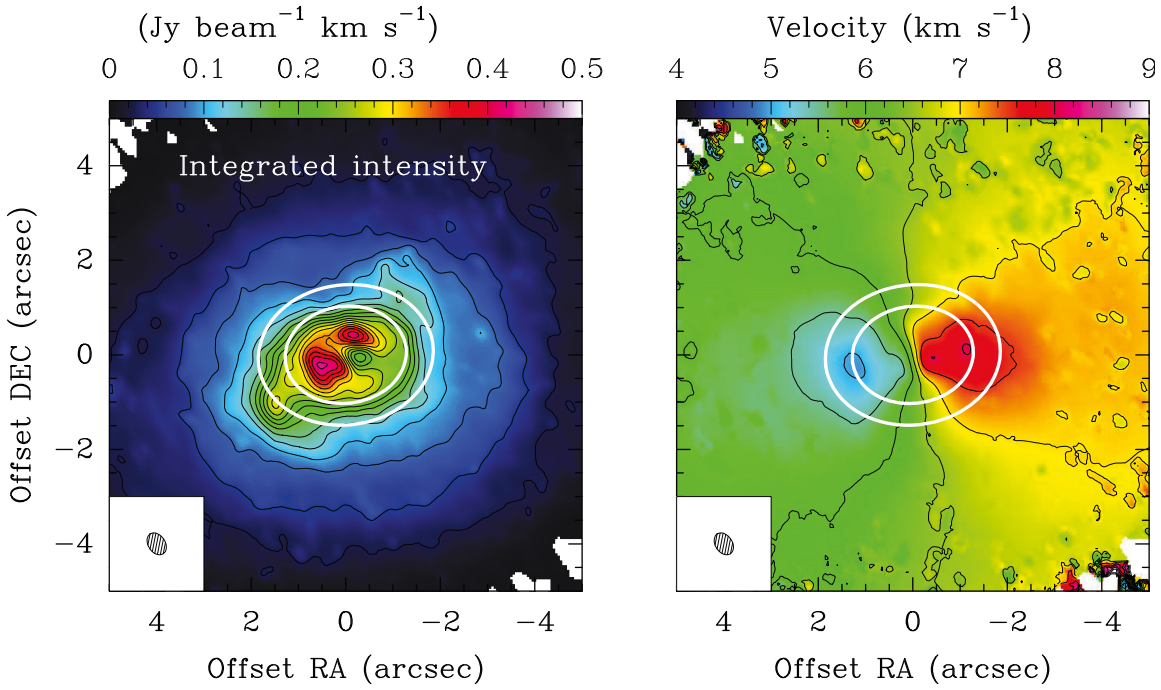

FIGURE 6.3: CO(2–1) line emission. *Left:* Integrated intensity map (Jy beam^{-1} km s^{-1}). The contour level is 25 mJy beam^{-1} km s^{-1}, which is about eight times the rms noise level of $\sim$ 3 mJy beam^{-1} km s^{-1}. *Right:* Velocity map (km s^{-1}). The contour spacing is 0.5 km s^{-1}. The colour scales are shown on the top.

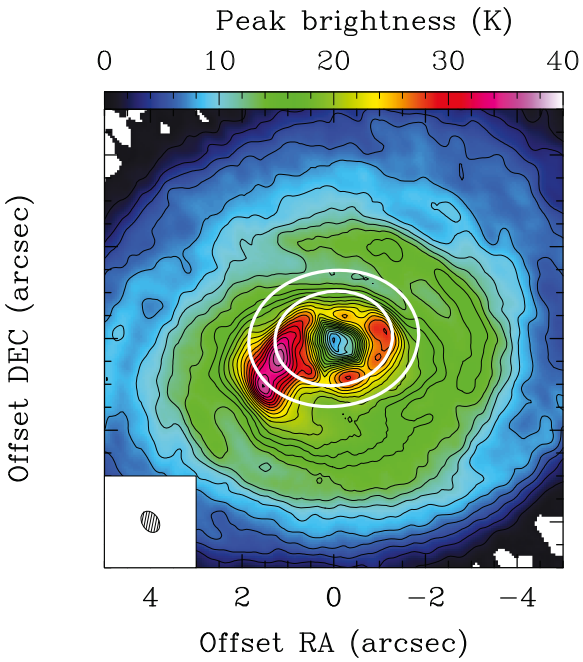

FIGURE 6.4: CO(2–1) line emission. Map of the peak brightness temperature (K). The colour scale is shown on the top and contour spacing is of 1.5 K

show enhanced emission in the dense ring from $\sim$ 180 au to $\leq$ 260 au. A possible "ring" pattern is revealed in the maps of the CN(2–1) extended emission, both for the integrated intensity (Figure 6.6 left) and for the peak brightness temperature (Figure 6.7). CN emission, being excited by UV photons, is likely to be confined to the upper molecular layer.

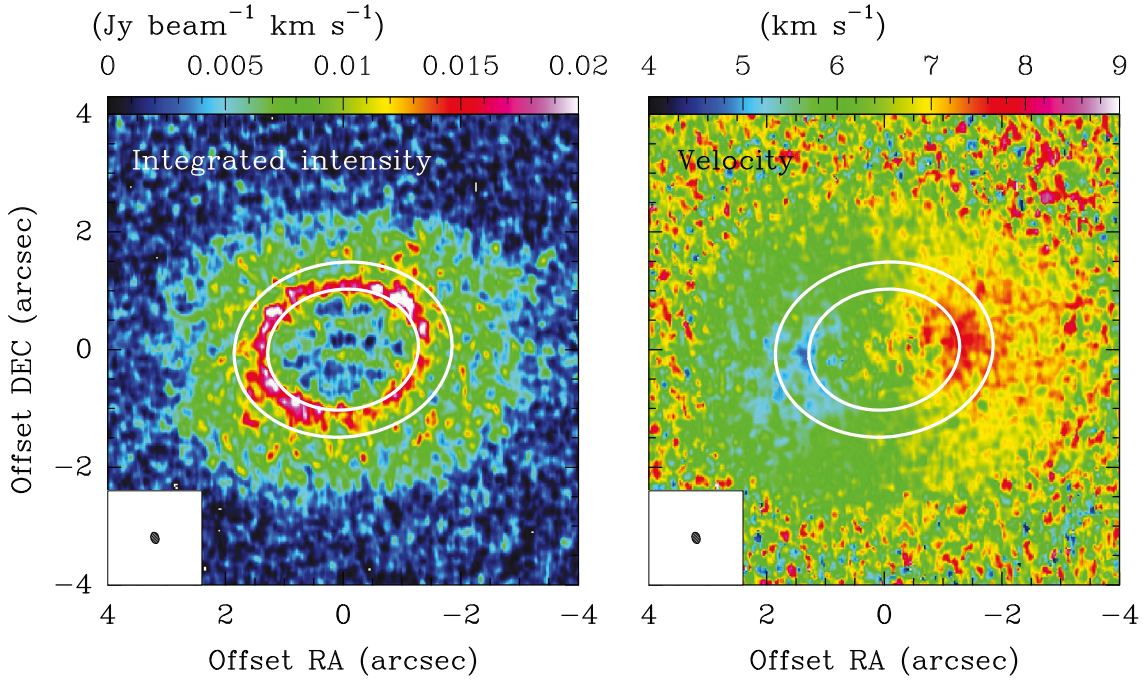

FIGURE 6.5: CN(3–2) line emission. *Left:* Integrated intensity map (Jy beam^{-1} km s^{-1}). *Right:* Velocity map (km s^{-1}).

6.2.3 CS observations

The emission of the CS(5–4) transition was observed by ALMA in 2018 (Cycle 6) with an angular resolution of 0.3″. Figure 6.8 shows intensity and velocity maps. CS(5–4) emission, like CN emission, peaks on the dense ring ($\sim$ 180 to 260 au). It is less extended than CS(3–2) emission but more extended than CS(7–6) emission (for which data exist but are not yet published). This is likely due to the excitation conditions in the disk. The peak brightness temperature map (Figure 6.9) also reveals possible ring-like structures. One ring is seen at radii between 1″ and 1.5″ (in the dense ring, $\sim$150 au to 230 au); another possible incomplete ring may be seen around $\sim$ 2″ (in the outer disk, $\sim$ 300 au).

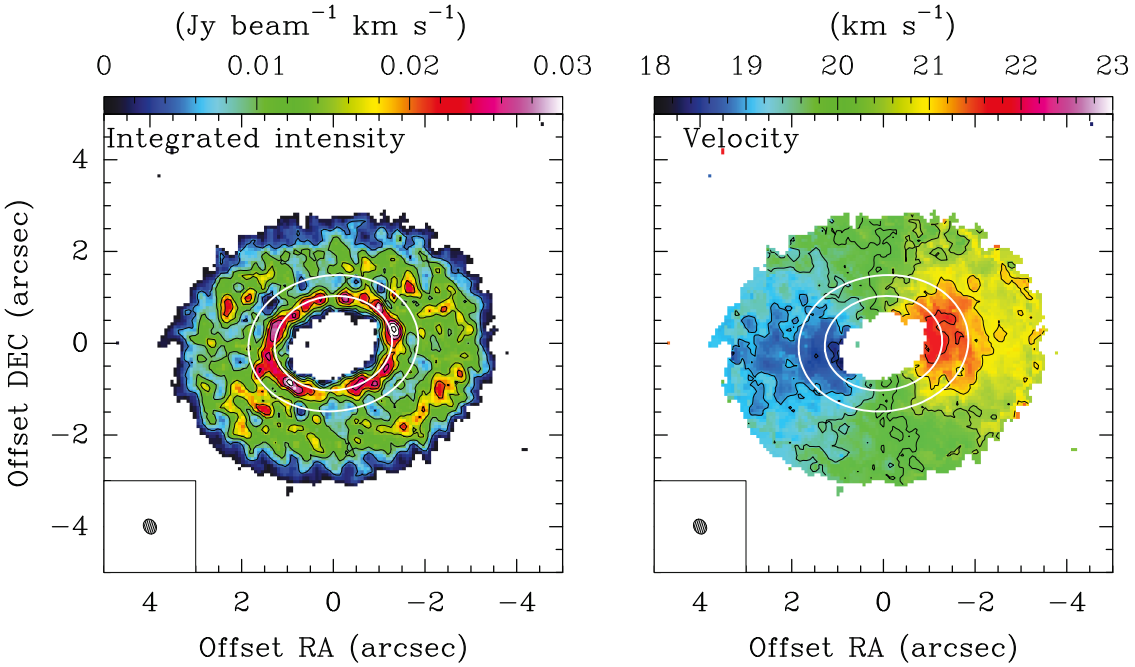

FIGURE 6.6: CN(2–1) line emission. *Left:* Integrated intensity map (Jy beam^{-1} km s^{-1}). The contour level is 5 mJy beam^{-1} km s^{-1}, about three times the rms noise level of $\sim$ 1.5 mJy beam^{-1} km s^{-1}. *Right:* Velocity map (km s^{-1}). The contour spacing is 0.5 km s^{-1}. Colour scales are shown on top.

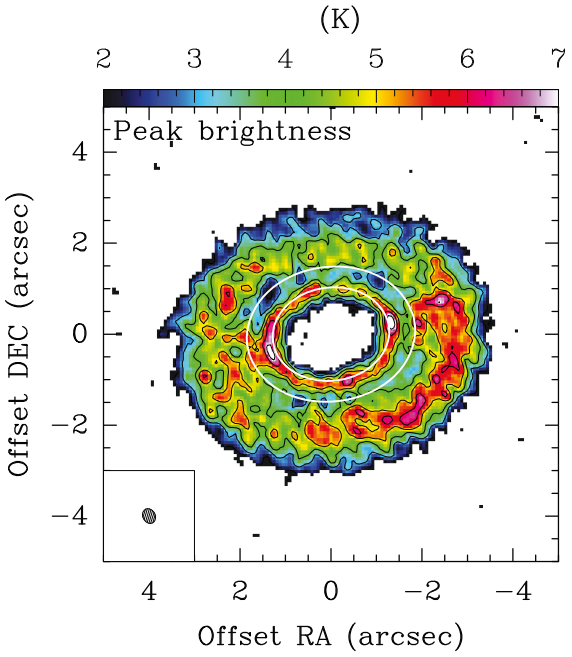

FIGURE 6.7: CN(2–1) line emission. Map of the peak brightness temperature (K). The colour scale is shown on top and the contour spacing is 1 K

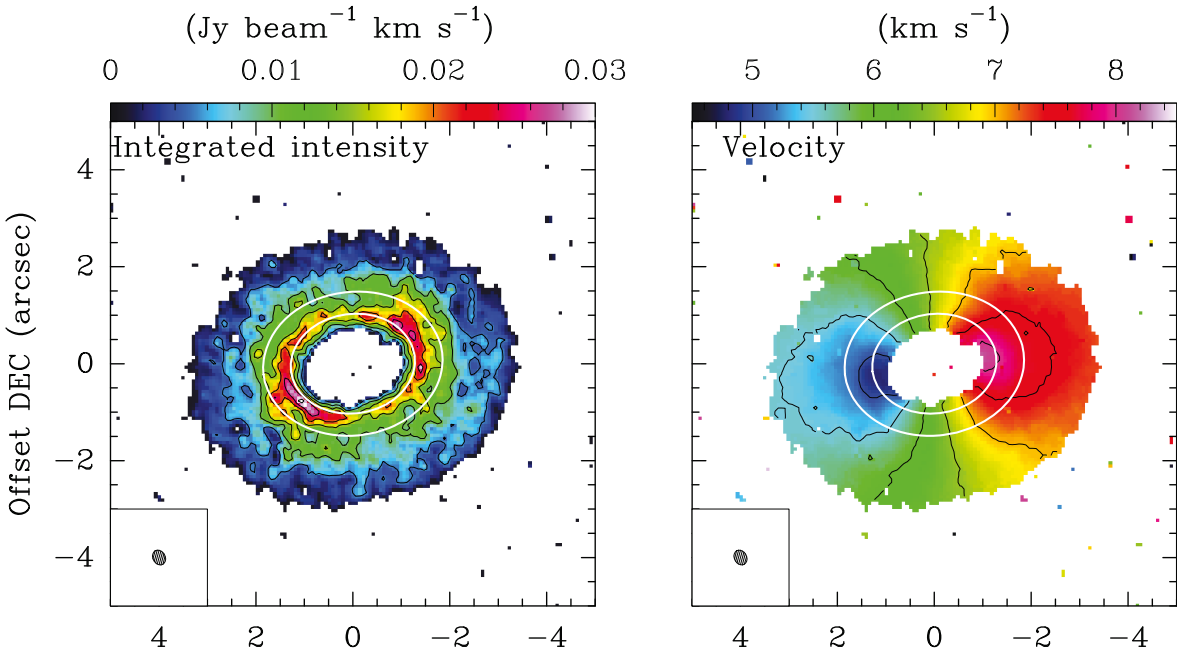

FIGURE 6.8: CS(5–4) line emission. *Left:* Integrated intensity map (Jy beam^{-1} km s^{-1}). The contour level is 5 mJy beam^{-1} km s^{-1}, about three times the rms noise level of $\sim$ 1.5 mJy beam^{-1} km s^{-1}. *Right:* Velocity map (km s^{-1}). The contour spacing is 0.5 km s^{-1}. Colour scales are shown on top.

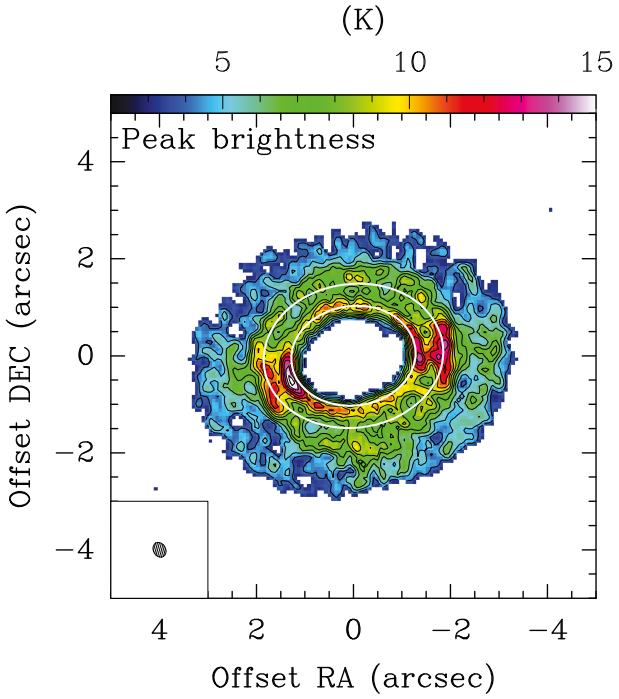

FIGURE 6.9: Peak brightness temperature (K) map of CS(5–4) emission. The colour scale is shown on top and the contour spacing is 1 K

6.3 Comparative study of the new observations and perspectives

Figure 6.10 shows the map of CO emission overlaid on the maps of CN (upper panel) and CS (lower panel) emissions.

Using CO observations, Dutrey et al. (2014) measured a "hot spot" temperature twice as high as in its surrounding. Here, the "hot spot" is also observed in CN emission, a molecule sensitive to photodissociation, and in CS emission, a molecule residing deeper inside the disk. Therefore, the "hot spot" is likely to host both a higher temperature and a higher density than its surrounding.

The "ring"/"possible spiral" patterns are seen in the emission of molecules tracing the uppermost layer of the protoplanetary disk (CN and CO) as well as of molecules tracing denser gas layers (CS) at lower altitude. The origin of the structures may be due to gravitational perturbations caused by an unseen planet (Dong et al., 2018), which would also explain the presence of the "hot spot".

This early look at the new data points to a number of analyses that will deserve to be made in depth and that promise to provide important new information.

I will apply the method developed in Chapter 4 to the study of the new CN and CS observations. This will allow for further investigation of the properties of the outer disk and of the gas inside the cavity. Additonal information on the physical and dynamical properties of the "hot spot" will be obtained, allowing for a refined understanding of its nature.

The new CS(5–4) observations will be analyzed together with the earlier CS(3–2) and CS(7–6) observations in order to further study the properties of the gas inside the dense ring. A non-LTE analysis will provide an estimate of the gas mass of the ring and of the gas-to-dust ratio.

In order to investigate the chemical composition of the cold disk of GG Tau A, I have submitted a NOEMA proposal to observe the gas at 3 mm wavelength. This survey will include emission from the following molecules: HNC, HC_3N, C_3H_2, N_2H^+, $N_2{}^+$, DCN, HCN, CS, CCH, DCO^+, $H^{13}CO^+$, and $C^{18}O$. The proposal was accepted and observations will soon be made. They will provide one of the most complete view of the chemistry in a cold T Tauri binary disk. This survey on a circumbinary disk will be an excellent addition to the ALMA Large program on (single) T Tauri and Herbig Ae disk chemistry (The Chemistry of Planet Formation, PI: Karin Oberg).

Finally, the Jame Webb Space Telescope, currently under construction at NASA, will mean major progress in the investigation of the gas properties in the inner disk(s) of GG Tau A at infrared wavelengths and in the search for possible planets. I will contribute to the preparation of a project dedicated to the study of the environment of GG Tau A using this instrument.

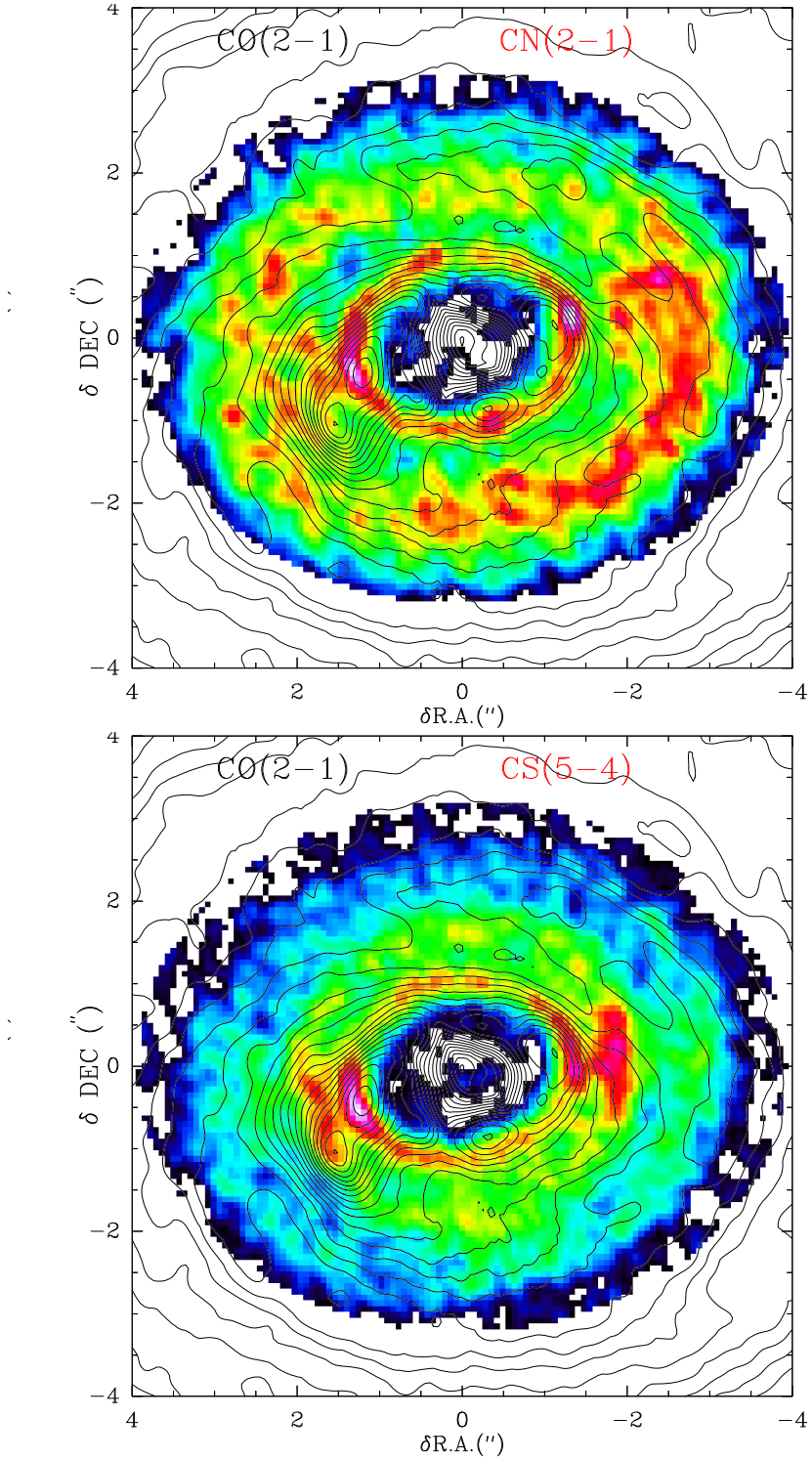

FIGURE 6.10: *Upper panel:* Map of the CN(2–1) peak brightness temperature (colour) overlaid over that of CO(2–1) shown as contours. *Lower panel:* Map of the CS(5–4) peak brightness temperature (colour) overlaid over that of CO(2–1) shown as contours

Appendix A

Papers and Accepted proposals

Research in Astronomy and Astrophysics

PAPER

Morphology of the ^{13}CO(3–2) millimetre emission across the gas disc surrounding the triple protostar GG Tau A using ALMA observations

To cite this article: Nguyen Thi Phuong *et al* 2018 *Res. Astron. Astrophys.* **18** 031

View the article online for updates and enhancements.

Related content

- MAPPING CO GAS IN THE GG TAURI A TRIPLE SYSTEM WITH 50 au SPATIAL RESOLUTION
Ya-Wen Tang, Anne Dutrey, Stéphane Guilloteau et al.
- Evolution of Molecular Clouds in the Superwind Galaxy NGC 1808 Probed by ALMA Observations
Dragan Salak, Yuto Tomiyasu, Naomasa Nakai et al.
- GAS DYNAMICS AND OUTFLOW IN THE BARRED STARBURST GALAXY NGC 1808 REVEALED WITH ALMA
Dragan Salak, Naomasa Nakai, Takuya Hatakeyama et al.

Recent citations

- Resolved Young Binary Systems and Their Disks
Rachel L. Akeson *et al.*

This content was downloaded from IP address 46.193.16.8 on 12/05/2019 at 16:45

RAA 2018 Vol. **18** No. **3**, 31(14pp) doi: 10.1088/1674–4527/18/3/31
© 2018 National Astronomical Observatories, CAS and IOP Publishing Ltd.
http://www.raa-journal.org *http://iopscience.iop.org/raa*

Research in Astronomy and Astrophysics

Morphology of the ^{13}CO(3–2) millimetre emission across the gas disc surrounding the triple protostar GG Tau A using ALMA observations

Nguyen Thi Phuong[1,2,3], Pham Ngoc Diep[1,2], Anne Dutrey[3], Edwige Chapillon[3,4], Pierre Darriulat[1], Stéphane Guilloteau[3], Do Thi Hoai[1], Pham Tuyet Nhung[1], Ya-Wen Tang[5], Nguyen Thi Thao[1] and Pham Tuan-Anh[1]

[1] Department of Astrophysics, Vietnam National Space Center, Vietnam Academy of Science and Technology, Hanoi, Vietnam; *ntphuong02@vnsc.org.vn*
[2] Graduate University of Science and Technology, Vietnam Academy of Science and Technology, Hanoi, Vietnam
[3] Laboratoire d'Astrophysique de Bordeaux, Université de Bordeaux, CNRS, F-33615 Pessac
[4] IRAM, F-38406 Saint Martin d'Hères Cedex, France
[5] Academia Sinica, Institute of Astronomy and Astrophysics, Taipei

Received 2017 November 7; accepted 2017 December 29

Abstract Observations by the Atacama Large Millimetre/sub-millimetre Array of the dust continuum and ^{13}CO(3–2) millimetre emissions of the triple stellar system GG Tau A are analysed, giving evidence for a rotating gas disc and a concentric and coplanar dust ring. The present work complements an earlier analysis (Tang et al.) by exploring detailed properties of the gas disc. A 95% confidence level upper limit of $0.24''$ (34 au) is placed on the disc scale height at a distance of $1''$ (140 au) from the central stars. Evidence for Keplerian rotation of the gas disc is presented, with the rotation velocity reaching $\sim$3.1 km s^{-1} at $1''$ from the central stars, and a 99% confidence level upper limit of 9% is placed on relative contribution from a possible in-fall velocity. Variations of the intensity across the disc area are studied in detail and confirm the presence of a hot spot in the south-eastern quadrant. However several other significant intensity variations, in particular a depression in the northern direction, are also revealed. Variations of the intensity are found to be positively correlated to variations of the line width. Possible contributions to the measured line width are reviewed, suggesting an increase of the disc temperature and opacity with decreasing distance from the stars.

Key words: protoplanetary disks — stars: low-mass — stars: individual (GG Tau A)

1 INTRODUCTION

GG Tau A is a triple stellar system, 1 to 5 million years old, located at 140 pc in a hole in the Taurus-Auriga star forming region. The separation between the main star GG Tau Aa and the close binary GG Tau Ab (Ab1-Ab2) is 35 au while the separation between GG Tau Ab1 and Ab2 is only 4.5 au (Di Folco et al. 2014). GG Tau A is surrounded by an envelope of gas and dust with a ring extending from $\sim$180 to 260 au and an outer disc extending up to $\sim$800 au from the central stars with an estimated mass of $\sim$0.15 solar masses (Dutrey et al. 1994). There is neither known molecular outflow nor jets associated with GG Tau A. Additional information about the system can be found in the review by Dutrey et al. (2016) and from references therein. In particular, high resolution Atacama Large Millimetre/sub-millimetre Array (ALMA) observations of ^{12}CO(6–5) emission and underlying continuum (Dutrey et al. 2014) have suggested possible planet formation. The present article uses ALMA data of the ^{13}CO(3–2) emission and underlying continuum that have been presented earlier by Tang et al. (2016) together with ^{12}CO(3–2) observations. Contrary to ^{12}CO(3–2) emission, which extends down to small distances from the

central stars, ^{13}CO(3–2) emission is limited to an outer ring having an inner edge radius of $\sim 1''$. The present analysis aims at complementing that of Tang et al. (2016) by providing new detailed information on the properties of the gas disc.

2 OBSERVATIONS AND DATA REDUCTION

The observations used in the present article were made in cycle 1 of ALMA operation (2012.1.00129.S) on 2013 November 18 and 19 in three blocks (Tang et al. 2016). The time spent on source was 1.84 hours. The number of antennas was 28, with the longest baseline being 1284.3 m. The three blocks of continuum data have been merged and calibrated by the ALMA staff and the ^{13}CO(3–2) data have been calibrated using CASA[1] and GILDAS[2]. The origin of coordinates at RA=$4^{\rm h}32^{\rm m}30.3^{\rm s}$ and DEC=$17^\circ\,31'\,40''$ corresponds to year 2000. Between 2000 and the time of observation, the source has moved by $0.24''$ east and $0.26''$ south (proper motion of [17, -19] mas per year taken from the SIMBAD[3] database); the data have been corrected accordingly.

The continuum emission was observed at $\sim$0.9 mm wavelength over frequencies covering from 330.655 to 344.426 GHz. The beam size (full width at half maximum, FWHM) is 0.39×0.29 arcsec^2 with a position angle (measured from north to east) of 56°. The ^{13}CO(3–2) emission was self-calibrated. The beam size (FWHM) is 0.37×0.31 arcsec^2 with a position angle of 80°. The present analysis is performed in the image plane and we evaluate the uncertainty on position measurements due to noise to be typically below $0.01''$, depending on the signal to noise ratio. However, it is often dominated by systematics and needs to be evaluated for each case separately. The spectral resolution (channel) has been smoothed to 0.11 km s^{-1} and the Doppler velocity covers between -2 and 15 km s^{-1}. Here, Doppler velocities are defined as the difference between the measured velocity and a systemic velocity of 6.38 ± 0.02 km s^{-1} as used by Dutrey et al. (2014) for ^{12}CO(6–5) about which the profile is symmetric.

[1] *http://casa.nrao.edu*
[2] *https://www.iram.fr/IRAMFR/GILDAS*
[3] *http://simbad.harvard.edu/simbad/sim-fbasic*

3 GENERAL FEATURES

3.1 Continuum Data

Figure 1 (left) maps the brightness of the continuum emission. It shows an elliptical ring surrounding a central source. The right panels show the projections on the x (right ascension offset) and y (declination offset) axes of the central source intensity integrated over y and x respectively. Gaussian fits give mean values of $0.06''$ and $-0.13''$ and FWHM values of $0.40''$ and $0.33''$ in x and y respectively, similar to the beam size: the central source is unresolved.

Figure 2 (left) displays the x and y projections of the continuum brightness integrated over y and x respectively. It requires the distance $R' = \sqrt{(x-0.06)^2 + (y+0.13)^2}$ to the central source to exceed $0.5''$, thereby excluding its contribution. The corresponding mean values of x and y are $-0.05''$ and $-0.09''$ respectively, showing that the ring is shifted north-west by $\sim$0.12$''$ with respect to the central source. The position and width measurements illustrated in Figure 1 and Figure 2 are accurate to better than $0.02''$, using the residuals of the fits to estimate measurement errors. They are dominated by systematics rather than simply by thermal noise. However, the angular separation between GG Tau Aa and Ab is $0.25''$: depending on what is being talked about, the position of the "centre" may vary by some $\pm 0.1''$.

Figure 2 (right) displays the dependence on $R = \sqrt{x^2+y^2}$ of the continuum brightness averaged over position angle $\varphi = 90^\circ - \tan^{-1}(y/x)$ (measured from north to east), again excluding the central source by requiring $R' > 0.5''$. A Gaussian fit to the peak gives a mean of $1.445'' \pm 0.015''$ and a σ of $0.266'' \pm 0.015''$ depending on the interval of R over which the fit is performed. Retaining a σ value of $0.266''$ and subtracting the beam size in quadrature gives a de-convolved FWHM of $0.528'' \pm 0.035''$. Tang et al. (2016) quote a value of $0.54''$ for the de-projected and de-convolved width of a uniform ring. The effect of de-projection is negligible and the correction factor for Gaussian to square box fit is $\sqrt{2\pi}/2\sqrt{2\ln 2} = 1.06$, bringing the Tang et al. (2016) value down to $0.51''$ to be compared with the present result of $0.528'' \pm 0.035''$. This is a very good agreement given that the ring is neither uniform nor perfectly Gaussian and that possible wings of faint emission be-

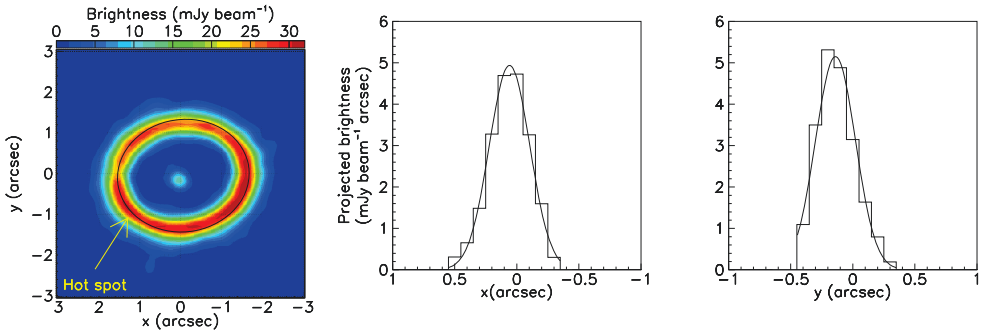

Fig. 1 Brightness of the dust ring continuum emission. *Left*: sky map; the *black ellipse* is the fit to $\langle R\rangle$ shown in Fig. 3; the *yellow arrow* points to the region of the hot spot observed by Dutrey et al. (2014) and Tang et al. (2016) in ^{12}CO(6–5) and ^{12}CO(3–2) emissions respectively. *Middle and right*: projections on the x and y axes of the central source brightness integrated over y and x respectively. The *lines* show Gaussian best fits.

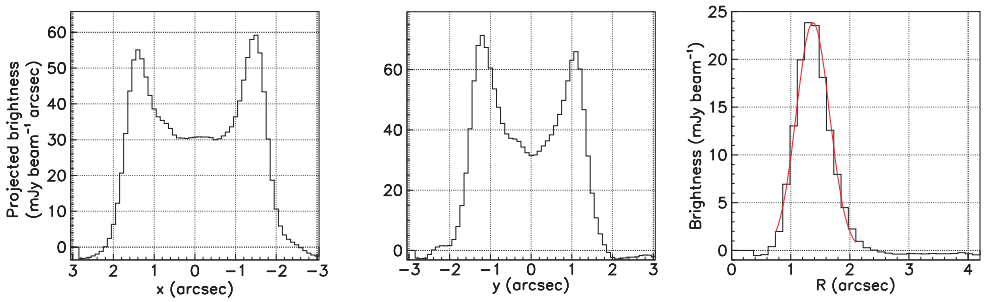

Fig. 2 Continuum brightness of the dust ring emission projected on the x (*left*) and y (*middle*) axes and integrated over y and x respectively. The *right panel* shows its distribution as a function of R, averaged over φ, together with the Gaussian best fit to the peak. In all three panels pixels having $R' < 0.5''$ are excluded.

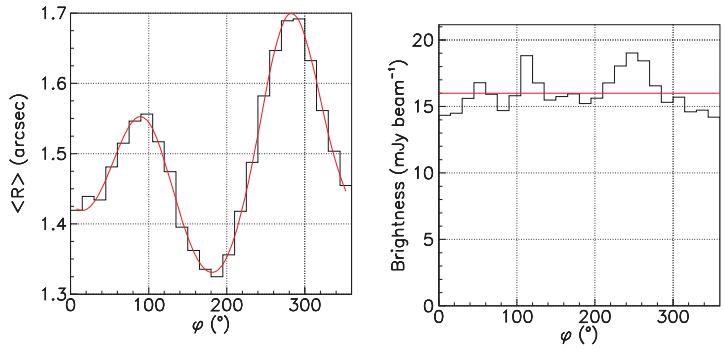

Fig. 3 Continuum emission. *Left:* Dependence on φ of $\langle R\rangle$ calculated in the interval $1'' < R < 2''$. The *red line* is the best fit to an elliptical tilted ring offset from the origin (see text). *Right:* Dependence on φ of the disc plane continuum brightness averaged over R in the interval $1'' < R < 2''$. The *red line* shows the mean value.

yond 1.8″ would affect differently the two fitting procedures.

Figure 3 (left) displays the mean value of R, $\langle R\rangle$, weighted by the radial average of the brightness across the ring over the interval $1'' < R < 2''$. A fit of the dependence of $\langle R\rangle$ on φ as an ellipse of semi-major and semi-minor axes a_0 and b_0 respectively and offset by Δx and Δy has been made to first order in the offsets and in the ellipticity:

$$r = \Big(\frac{\cos^2(\varphi-\varphi_0)}{a_0^2} - 2\frac{\Delta x}{\sqrt{a_0 b_0}}\frac{\cos(\varphi-\varphi_0)}{a_0^2} + \frac{\sin^2(\varphi-\varphi_0)}{b_0^2} - 2\frac{\Delta y}{\sqrt{a_0 b_0}}\frac{\sin(\varphi-\varphi_0)}{b_0^2}\Big)^{-1/2}. \quad (1)$$

It gives $a_0 = 1.62''$ and $b_0 = 1.38''$, position angle of the major axis $\varphi_0 = 97^\circ$ and small offsets $\Delta x = -0.07''$ and $\Delta y = -0.05''$, at the level of measurement uncertainties. This confirms the good centering of the ring on the origin of coordinates and the aspect ratio corresponds to a tilt with respect to the sky plane $\theta = \cos^{-1}(1.38/1.62) = 32^\circ \pm 4^\circ$ of a circular ring about the rotated (by 7.0°) x axis.

These results confirm the values quoted by Tang et al. (2016): 1.63″ instead of 1.62″ for a_0, 7.5° instead of 7.0° for the position angle and 36.4° instead of 32° for the tilt with respect to the sky plane, with the latter being measured to no better than ±4°. The values quoted for the tilt by Dutrey et al. (2014) are $37^\circ \pm 1^\circ$ for ^{12}CO(6–5) and $35.0^\circ \pm 0.2^\circ$ for the dust.

Figure 3 (right) displays the dependence on position angle φ of the continuum brightness averaged over R in the interval $1'' < R < 2''$. Here we have used the fact that the ratio between the beam area in the sky plane and its de-projected value in the disc plane is equal to $\langle R\rangle / a_0$. In the disc plane the brightness is uniform over the disc circumference and equal to 16.0 mJy beam^{-1} to within ±8.5% (rms).

3.2 ^{13}CO(3–2) Line Emission

Figure 4 (left) displays the brightness distribution over the data cube. A Gaussian fit to the noise peak gives a mean of -0.19 mJy beam^{-1} and a σ of 7.2 mJy beam^{-1} (0.56 K). Figure 4 (right) displays the Doppler velocity (V_z) spectrum integrated over 8×8 arcsec^2, with a double-horn profile typical of a rotating volume. It is centred to better than 0.1 km s^{-1}. In what follows, throughout the article, we restrict the Doppler velocity range to $|V_z| < 2$ km s^{-1} unless specified otherwise.

Figure 5 displays the sky maps of the velocity-integrated brightness, or integrated intensity, and of the mean Doppler velocity. The map of the integrated intensity shows a clear ring of gas surrounding the central stars and having morphology similar to the dust morphology, indicating a concentric circular gas disc having the same inclination as the dust ring on the sky plane. It displays no central emission, with an abrupt inner cut-off at $\sim 1''$; there is no significant emission inside an ellipse scaled down from the dust ellipse by a factor ∼3, meaning a de-projected radius of $\sim 1.62/3 = 0.54''$. The velocity map excludes the region inside the scaled-down ellipse where noise dominates. It displays a clear velocity gradient along the major axis of the ellipse, as expected from rotation of the tilted disc about its axis. Note that an infalling (rather than rotating) disc would display instead a gradient along the minor axis of the ellipse. In general adding some in-fall motion to rotation would cause the axis of the velocity gradient to deviate from the major axis, the more so the larger the relative contribution of in-fall.

Figure 6 is the equivalent for the line of Figure 2 for the continuum except that Figure 2 is for the continuum and Figure 6 is for the line: projections on the x and y axes and r-dependence, averaged over φ, of the integrated intensity, where r is now the de-projected value of R in the disc plane (see Fig. 8). Here, de-projection assumes a tilt angle of 32° and a position angle of the disc axis of 7°, as found for the dust. In all panels we exclude the central region where noise dominates by requiring $r > 0.54''$. When compared with the dust (continuum) ring, the gas (line) ring is broader and peaks at smaller radii. The mean values of x and y are $0.02''$ and $-0.10''$ respectively. A fit to the integrated intensity distribution as a function of r as a sum of three Gaussians is shown in the right panel of the figure. The means and widths of the Gaussians are fixed to the values obtained by Tang et al. (2016) when fitting the western half of the gas disc.

Figure 7 (left) displays the mean value of R, $\langle R\rangle$, weighted by the radial average of the brightness across the ring over the interval $0.54'' < r < 2''$. A fit of the dependence of $\langle R\rangle$ on φ as an ellipse gives semi-major and semi-minor axes $a_0 = 1.45''$ and $b_0 = 1.19''$ respectively, position angle of the major axis $\varphi_0 = 97.8^\circ$ and small offsets $\Delta x = 0.02$ and $\Delta y = 0.07''$. The position

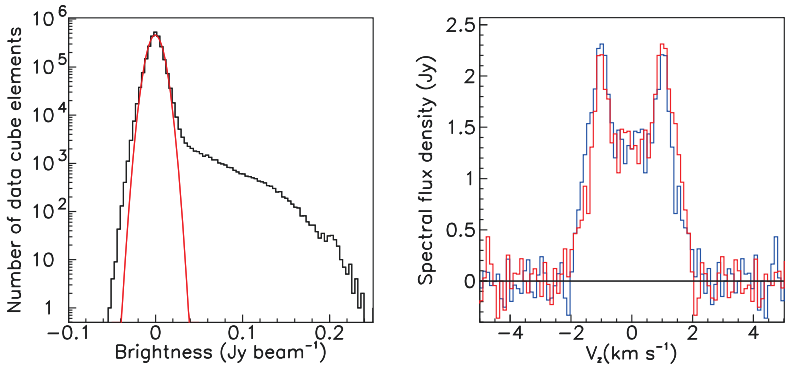

Fig. 4 *Left:* Line brightness distribution (Jy beam^{-1}); the *red curve* is a Gaussian fit to the noise peak. *Right:* Doppler velocity spectrum weighted by brightness and integrated over 8×8 arcsec^2 (*blue*); the *red histogram* is obtained from the original by symmetry about the origin.

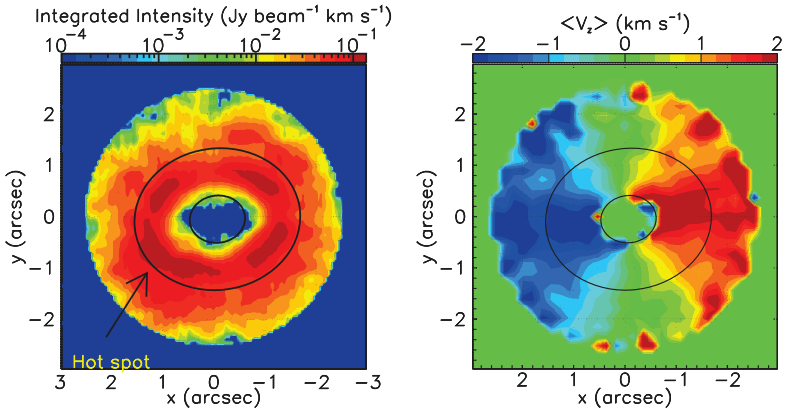

Fig. 5 *Left:* Sky map of the ^{13}CO(3–2) integrated intensity. The *black arrow* shows the position of the hot spot in ^{12}CO(6–5) (Dutrey et al. 2014) and ^{12}CO(3–2) (Tang et al. 2016). *Right:* Sky map of the mean Doppler velocity (weighted by brightness) excluding the region contained in the scaled-down ellipse shown in the *left panel*. In both panels, $R < 2.5''$ and the *black ellipses* are the best fits to the distribution of $\langle R \rangle$ in the continuum data and its scaled-down version (by a factor 3).

angle and aspect ratio (0.82 instead of 0.85) are very similar to the dust result, but the size of the ellipse is scaled down by a factor 87%. The tilt angle is now 35°, compared with 32° for the dust.

Another estimate of the tilt geometry is obtained from the map of the mean Doppler velocity (Fig. 7, middle). In a ring defined as $0.54'' < r < 2''$, a fit of the form $\langle V_z \rangle = V_0 - \Delta V \cos(\varphi - \varphi_0)$ gives $V_0 = 0.05\,\mathrm{km\,s^{-1}}$, $\Delta V = 1.73\,\mathrm{km\,s^{-1}}$ and $\varphi_0 = 97.8°$, again in excellent agreement with the value obtained from the dust fit, $\varphi_0 = 97.0°$; this provides evidence against a significant in-fall contribution. The values quoted by Dutrey et al. (2014) are $97° \pm 2°$ for ^{12}CO(6–5) and $96.5° \pm 0.2°$ for the dust. The value of ΔV, $1.73\,\mathrm{km\,s^{-1}}$, corresponds to a mean rotation velocity of $\sim \Delta V / \sin\theta \sim 3.3\,\mathrm{km\,s^{-1}}$.

Figure 7 (right) displays the dependence on φ of the disc plane integrated intensity averaged across the ring in the interval $0.54'' < r < 2''$. It has a mean value of 0.39 Jy beam^{-1} km s^{-1} and fluctuates around it with an rms of 17%. We summarise the geometry parameters of the dust and ^{13}CO(3–2) emission in Table 1.

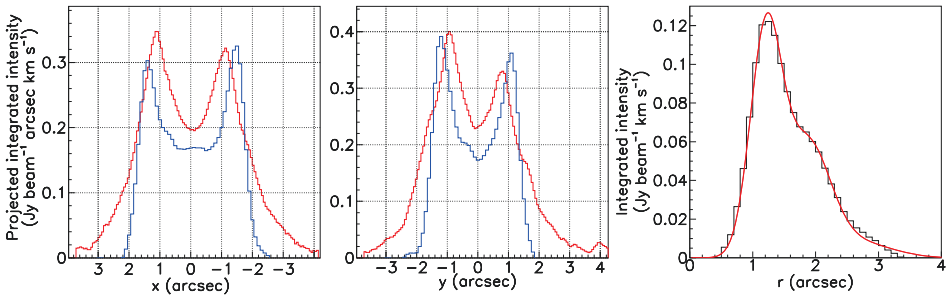

Fig. 6 Line emission. *Left* and *middle:* Continuum brightness (*blue*, arbitrary normalisation) and line integrated intensity (*red*) projected on the x (*left*) and y (*middle*) axes in the region of $r > 0.5''$. *Right:* r-dependence, averaged over φ, of the integrated intensity in the disc plane. The *red line* is a fit using the same three Gaussians as in Tang et al. (2016).

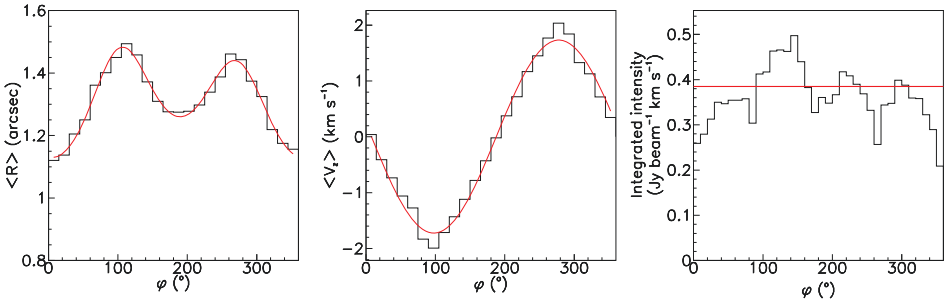

Fig. 7 Line emission. *Left:* Mean value of R, $\langle R\rangle$, weighted by the radial average of the brightness across the disc over the interval $0.54'' < r < 2''$. The *red line* is the result of the fit described in the text. *Middle:* Dependence on φ of the mean line Doppler velocity (brightness-weighted); the *red line* is the result of the fit described in the text. *Right:* Dependence on φ of the disc plane integrated intensity averaged across the disc ($0.54'' < r < 2''$). The *red line* shows the mean value.

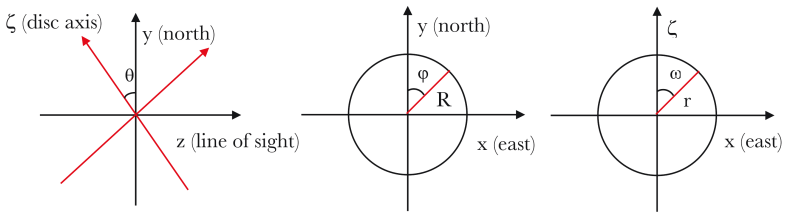

Fig. 8 Geometry. *Left*: in the (y, z) plane; *middle*: in the sky plane (x, y); *right*: in the disc plane (x, ζ).

4 DETAILED PROPERTIES OF THE GAS DISC

In the present section we use new coordinates obtained from those of the preceding sections by a rotation of an angle of $8°$ about the z axis. To within $1°$, this brings the new x axis on the major axes of the ellipses found in the preceding sections as best describing the φ dependences of both $\langle R\rangle$ and the Doppler velocity. Moreover, unless otherwise explicitly specified, we assume a tilt of $\theta = 35°$ for the disc plane as a reasonable compromise between values obtained in both earlier and the present studies, for both gas and dust observations. In practice, we use 99×81 pixels of 0.06×0.06 arcsec^2 on the sky

Table 1 Geometry Parameters

		Projection on x and y		Ellipse fitted to the $\langle R\rangle$ vs φ					
		$\langle x\rangle$ ($''$)	$\langle y\rangle$ ($''$)	a_0 ($''$)	b_0 ($''$)	φ_0 ($^\circ$)	Δx ($''$)	Δy ($''$)	θ ($^\circ$)
Dust	Central source	0.06	-0.13	-	-	-	-	-	-
	Ring	-0.05	-0.09	1.62	1.38	97.0	-0.07	-0.05	32
^{13}CO(3–2)	Disc	0.02	-0.01	1.45	1.19	97.8	0.02	0.07	35

map, covering $(99\times0.06)\times(81\times0.0733)\sim6\times6$ arcsec^2 in the disc plane ($0.0733 = 0.06/\cos35^\circ$). To each pixel (x, y) we associate disc coordinates $\zeta = y/\cos\theta$, $r = \sqrt{x^2+\zeta^2}$ and $\omega = 90^\circ - \tan^{-1}(\zeta/x)$. Here "disc plane" and "disc coordinates" are simply defined by this transformation, implying no assumption on the disc being actually thin and flat.

4.1 Estimate of the Disc Thickness Obtained from the Sharpness of the Disc Inner Edge

Tang et al. (2016) have commented on the sharpness of the inner edge of the ^{13}CO(3–2) emission and on the smallness of the vertical temperature gradient, with the inner edge of the disc being directly exposed to stellar light and casting a shadow on the outer disc. Here, we compare the value of the smearing of the inner edge of the disc map near the major axis of the ellipse with its value near the minor axis. To a good approximation, the effect of disc thickness essentially cancels for the former while, for the latter, it scales with the product of disc thickness by sine of the tilt angle. The optical thickness of the line is not expected to strongly affect this result. We consider four angular sectors in the disc plane, each 60° wide and centred on the axes of the ellipse. In each sector, we study the radial dependence of the integrated intensity, both in the disc plane (r) and in the sky plane (R). The result is displayed in Figure 9. In order to evaluate the sharpness of the inner edge of the gas disc, we fit a Gaussian to the rise of each distribution, between $0.5''$ and $1.5''$ in r. In R, we use the same interval of $0.5''$ to $1.5''$ for the sectors centred on the major axis of the ellipse but a scaled-down (by a factor $\cos35^\circ = 0.82$) interval of $0.41''$ to $1.23''$ for the sectors centred on the minor axes in order to account for the effect of tilt. The mean and σ values (dispersions, a factor 2.35 smaller than FWHM values also commonly quoted in the literature) obtained for the Gaussian best fits are listed in Table 2.

The distributions as a function of r show identical σ values, to within ±10 mas, in the four angular sectors. A contribution from the disc thickness would cause these values to be larger in the minor-axis sectors than in the major-axis sectors: it is already clear that a significant contribution from the disc thickness is excluded. At variance with the distributions as a function of r, the distributions as a function of R show significantly different σ values for the major-axis sectors, $\sim0.33''$, and the minor-axis sectors, $\sim0.28''$, a factor 85% smaller. Similarly, the ratio between the mean values of the Gaussians (listed as "scaling factor" in the table) are equal for the two sectors of a same axis of the ellipse, but again 85% smaller for sectors centred on the minor axis than for those centred on the major axis. The latter are very slightly smaller than unity, as expected from the 60° angular widths of the sectors. The consistency between these numbers suggests an interpretation of the σ values measured in the R distributions as the sum of three terms added in quadrature: i) a beam contribution of $0.14''$ on both the minor- and major-axis sectors (calculated from the known beam parameters); ii) a contribution from the intrinsic smearing of the disc emission, σ_0, caused by effects such as density variations and contributing in each sector a value σ_0 scaled down by the scaling factors listed in the table; iii) an additional contribution σ_1 due to the disc thickness and contributing only to the minor-axis sectors. After subtraction of the beam contribution and correction for de-projection, one obtains values for σ of $0.29''$ for the minor-axis sectors and $\sim0.30''$ for the major-axis sectors. A contribution σ_1 due to the disc thickness would cause the former to exceed the latter, at variance with what is observed. From the consistency between the numbers, we estimate an uncertainty of $\sim0.02''$ on the Gaussian σs. To a 95% confidence level (2σ) we obtain an upper limit for σ_1 of $\sqrt{(0.29+2\times0.02)^2-0.30^2}$=$0.14''$, corresponding to a scale height $H(r) \sim 0.14/\sin35^\circ = 0.24''$ (34 au)

Table 2 Estimating the thickness of the gas disc from the sharpness of its inner edge projected on the sky plane. All values (except the scaling factors) are in arcsec.

		North	East	South	West
r fit	$\langle r \rangle$	1.15	1.31	1.24	1.34
	σ	0.32	0.34	0.33	0.32
R fit	$\langle R \rangle$	0.99	1.29	1.08	1.32
	σ	0.28	0.34	0.28	0.32
R fit, beam subtracted	σ	0.24	0.31	0.24	0.29
R fit, de-projected	Scaling factor	0.86	0.98	0.87	0.99
	σ	0.29	0.31	0.29	0.29

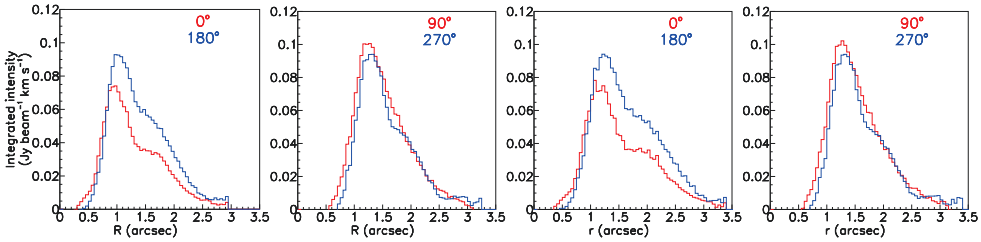

Fig. 9 Line emission. Dependence on R (*left panels*) and on r (*right panels*) of the line integrated intensity averaged in $60°$ wide angular sectors centred on the ellipse axes. In each case, the *leftmost panel* is for minor-axis sectors and the *rightmost panel* for major-axis sectors. The central values of ω are indicated in the inserts for each sector.

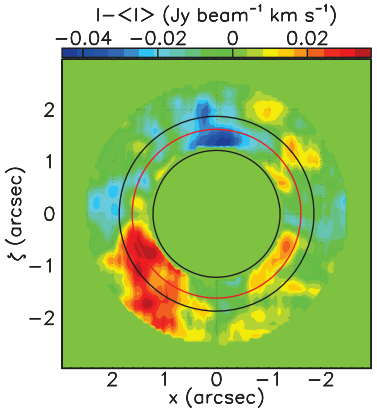

Fig. 10 Line emission. Map in the disc plane of the difference between the integrated intensity and its value averaged over ω at the same r. The *black circles* show the maxima of the Gaussians describing the mean radial integrated intensity distribution, $r = 1.22''$ and $1.87''$ respectively. The *red circle* corresponds to the mean value of r in the dust map ($1.62''$).

at $r \sim 1''$ (140 au) where the Keplerian velocity is $\sim 3\,\mathrm{km\,s^{-1}}$; at 30 K, the sound velocity is $\sim 0.5\,\mathrm{km\,s^{-1}}$ and hydrostatic equilibrium implies $H(r) = 0.5/3 = 0.17''$ compared with the $0.24''$ upper limit obtained above. We have checked that this result is independent of the width of the angular sectors (using $40°$ instead of $60°$ lowers the Gaussian σs by $\sim 0.01''$). Depending on the interval chosen for calculation, the Gaussian σ's lower values of the σ_1 upper limit may be obtained, as low as $0.10''$ instead of $0.14''$. We conservatively prefer to retain the latter value as our final result.

4.2 Integrated Intensity Variations across the Disc

In order to better understand the nature of the integrated intensity variations displayed in Figure 7 (right), we display in Figure 10 the map in the disc plane of the difference between measured integrated intensity and its value averaged over ω at the same value of r (as obtained from Fig. 6, right). This map provides a measure of the lack of rotational symmetry of the integrated intensity in the disc plane. It gives strong evidence for an excess associated with the hot spot observed by Dutrey et al. (2014) and Tang et al. (2016) and for a northern depression of similar amplitude. Both excess and depression reach their maxima at a distance from the central stars corresponding to the gap between the maxima of the two first Gaussians describing the mean radial distribution of the integrated intensity (these Gaussians peak at $r = 1.22''$ and $1.87''$ respectively). It is also in this gap that the continuum dust emission peaks (at $r = 1.62''$). However, both excess and depression extend to larger values of r, particularly the former that extends out to $r \sim 2.5''$.

4.3 Gas Kinematics

Calling $V_{\rm rot}$ and $V_{\rm fall}$ the components of the disc plane velocity respectively perpendicular and parallel to the disc radius, the Doppler velocity reads $V_z = \sin\theta(V_{\rm rot}\sin\omega - V_{\rm fall}\cos\omega)$ for each data-cube element (x, y, V_z). To a good approximation, $V_{\rm fall}$ can be neglected and we can calculate $V_{\rm rot} = V_z(\sin\theta\sin\omega)^{-1}$ for each data-cube element, leaving for later the task of revealing a possible small $V_{\rm fall}$ contribution. $V_{\rm rot}$ becomes trivially singular along the ζ axis. We require accordingly $|\sin\omega|$ to exceed 0.3 when calculating $V_{\rm rot}$. As $\sin^{-1}(0.3) = 17.5°$, this is not much of a loss.

Figure 11 displays the dependence on ω and r of V_z averaged (using brightness as weight) over $0.8'' < r < 2.5''$ and over ω respectively. Averaging V_z requires some care in dealing with the noise: the interval used for averaging must be symmetric with respect to the mean value obtained as a result, which requires relaxing the condition $|V_z| < 2\,{\rm km\,s^{-1}}$ usually applied in the analysis. The ω-dependence is perfectly described by a sine wave of amplitude $-1.43\,{\rm km\,s^{-1}}$. Adding a cosine term does not change the coefficient of the sine term and insignificantly improves the value of χ^2. Its amplitude is $-0.05\,{\rm km\,s^{-1}}$, only 2.6% of the amplitude of the $\sin\omega$ term, corresponding to a shift of $-1.9°$ in ω. As a check of the correctness of the procedure, we compare this result with what is obtained when requiring a 3σ cut on each data-cube element; the amplitudes of the sine and cosine waves become -1.40 and $-0.04\,{\rm km\,s^{-1}}$ respectively.

The negative sign of the best-fit cosine term means radial expansion, and in-fall would give a positive sign. Assuming a 3° uncertainty on ω, corresponding to half a beam sigma at a distance of $1.3''$, we obtain a 3σ upper limit (99% confidence level) of 9% on the ratio $V_{\rm fall}/V_{\rm rot}$. As a function of r, averaging over ω would cause $\langle V_z\rangle$ to cancel if symmetry with respect to the ζ axis were perfect. It is indeed found to be very small, at the level of $-0.05\,{\rm km\,s^{-1}}$ as soon as r exceeds the peak of the radial integrated intensity distribution at $r \sim 1.3''$.

Similarly, the dependence on ω and r of $V_{\rm rot}$ averaged respectively (using brightness as weight) over $0.8'' < r < 2.5''$ and over ω ($|\sin\omega| > 0.3$) is displayed in Figure 12. The left panel shows the distribution of $\langle V_{\rm rot}\, r^{1/2}\rangle$ on r, which would be constant if the rotation were Keplerian. A fit in the interval $1.1'' < r < 2.5''$ gives a power index of -0.63 instead of the Keplerian -0.5 and $\langle V_{\rm rot}\rangle = 3.0\,{\rm km\,s^{-1}}$ at $r = 1''$. The middle panel illustrates the difficulty in measuring $V_{\rm rot}$ reliably due to its singularity on the ζ axis. As remarked earlier, the binarity of the central star prevents the position of the "centre" from being defined to better than some $\pm 0.1''$ (more exactly such a definition requires modelling properly the binary configuration). Shifting the origins of x and y on the sky map by ± 1 pixel size ($\pm 0.06''$) changes the value of ω and therefore of $V_{\rm rot}$. The result displayed in the middle panel shows the importance of the effect. As a result, increasing the $|\sin\omega|$ cut from 0.3 to 0.707 ($\sin 45°$) makes the $\langle V_{\rm rot}\, r^{1/2}\rangle$ distribution Keplerian with a power index of -0.51 instead of -0.63, and the rotation velocity at $r = 1''$ increases from 3.0 to $3.1\,{\rm km\,s^{-1}}$ (left panel). We display, in the right panel, the map of $V_{\rm rot}\, r^{1/2}$ in the disc plane. It is uniform except for increases near the ω limits in the north-west and south-east directions. These are largely artefacts due to the difficulty in calculating a reliable $V_{\rm rot}$ near the ζ axis. Note that Dutrey et al. (2014) quote a $V_{\rm rot}$ value of $3.4 \pm 0.1\,{\rm km\,s^{-1}}$ for ^{12}CO(6–5) emission with an index of -0.5 ± 0.1 at $r = 100\,{\rm au}$; this corresponds to $2.9\,{\rm km\,s^{-1}}$ at $r = 1''$, consistent with the $3.0\,{\rm km\,s^{-1}}$ observed here for ^{13}CO(3–2) emission.

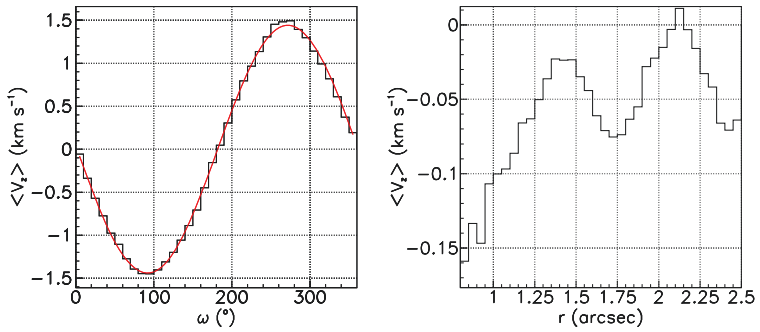

Fig. 11 Distributions on ω (*left*) and r (*right*) of the Doppler velocity respectively averaged over $0.8'' < r < 3.2''$ and over ω. In the *left panel*, the *line* shows the best fit result of the form $-1.43\sin\omega + 0.05\cos\omega = -1.43\sin(\omega - 1.9°)\,\mathrm{km\,s^{-1}}$.

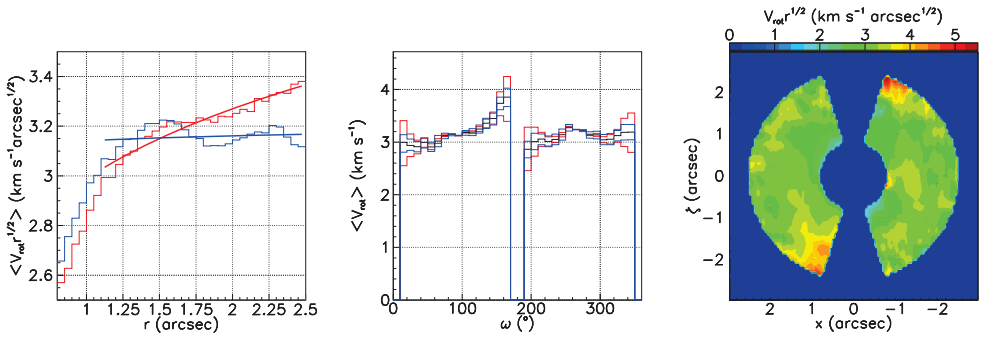

Fig. 12 *Left:* Dependence on r of $\langle V_{\rm rot}\, r^{1/2}\rangle$ (brightness-weighted average); the *lines* are the best power law fits with indices -0.63 for $|\sin\omega| > 0.3$ (*red*) and -0.51 for $|\sin\omega| > 0.707$ (*blue*). *Middle:* Dependence on ω of $\langle V_{\rm rot}\rangle$ (averaged in the interval $0.8'' < r < 2.5''$) calculated using the nominal origin of coordinates on the sky plane (*black histogram*) or by shifting the origin by $\pm 0.06''$ in either x or y (*red* and *blue histograms* respectively). *Right:* De-projected map of $\langle V_{\rm rot}\, r^{1/2}\rangle$ ($|\sin\omega| > 0.3$).

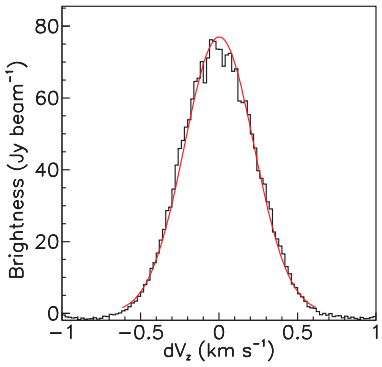

Fig. 13 Dependence of the brightness on the difference dV_z between measured values of V_z and their mean value in the associated pixel. Summing is over all pixels in the interval $0.8'' < r < 2.5''$. The curve is a Gaussian fit.

4.4 Line Width

Figure 13 displays the dependence of the brightness on the difference dV_z between the values of V_z measured in a given pixel and their mean values in that same pixel. The mean is calculated using brightness as a weight and the histogram is summed over all pixels in the interval $0.8'' < r < 2.5''$. A Gaussian fit gives a σ-value of $0.23\,\mathrm{km\,s^{-1}}$.

Several quantities, added in quadrature, are expected to contribute to σ_{vz}: Keplerian shear σ_K associated with both beam size and disc thickness, the instrumental resolution σ_I and the thermal broadening σ_T, possibly including a turbulence contribution (Teague et al. 2016), and opacity broadening, σ_τ.

Averaged over ω, the Keplerian shear at $r = 1.5''$ reads, from the derivative of a power law, $\sigma_K = 0.6\,\langle|V_z|\rangle\,\sigma_r/r$ where 0.6 stands for the power index of the radial $V_{\rm rot}$ distribution (it would be 0.5 in a pure Keplerian case). Here, σ_r is the sum in quadrature of the σs of the beam, $0.21''$, and of the disc thickness multiplied by $\tan\theta = 0.7$, $0.11''$. Hence, $\sigma_r \sim \sqrt{0.21^2 + 0.11^2} = 0.24''$ and $\sigma_K = 0.6 \times \sin(35^\circ) \times 3.1 \times 1.5^{-0.6} \times (2/\pi) \times \sigma_r/1.5 = 0.09\,\mathrm{km\,s^{-1}}$. Taking the FWHM of the instrumental resolution as one velocity bin gives $\sigma_I \sim 0.05\,\mathrm{km\,s^{-1}}$. Thermal broadening proper reads $\sqrt{2kT/M_{\rm co}}$ where k is Boltzmann constant, T the temperature and $M_{\rm co}$ the mass of the ^{13}CO molecule; at $T = 18\,\mathrm{K}$ (Tang et al. 2016) it amounts again to some $0.10\,\mathrm{km\,s^{-1}}$. Opacity tends to flatten the line profile and its effect is an effective broadening of $\sim \sqrt{\ln(\tau)}$, where τ is the line opacity (Piétu et al. 2007). Tang et al. (2016) show that ^{13}CO(3–2) and ^{12}CO(3–2) have similar brightness, implying that $\tau(^{13}\mathrm{CO})$ is significantly above unity. Using both ^{13}CO(3–2) and ^{12}CO(3–2), we estimate its value to be $\tau \sim 10$, meaning an effective broadening of $\sim$1.5 and a joint contribution of $\sim 0.15\,\mathrm{km\,s^{-1}}$ for thermal and opacity broadening. A possible additional source of broadening could be the effect of noise. However, using a 3σ cut to select the data, which must underestimate the measured value of σ_{vz}, we obtain 0.20 instead of $0.23\,\mathrm{km\,s^{-1}}$, showing that noise can be neglected within our estimated uncertainty of $\pm 0.03\,\mathrm{km\,s^{-1}}$.

Adding the estimated contributions in quadrature gives a total contribution of $\sqrt{0.05^2 + 0.09^2 + 0.15^2} = 0.18\,\mathrm{km\,s^{-1}}$ compared with $0.23 \pm 0.03\,\mathrm{km\,s^{-1}}$ measured: there is not much room left for additional contributions and turbulence is small (highly subsonic) in this disc.

Important additional information on the line width can be obtained from a study of the variations of σ_{vz} over the disc plane. To this end we consider three r intervals, $0.4''$ wide, covering between $1.3''$ and $2.5''$ and 24 ω-intervals, 15° wide, covering between 0° and 360°. The dependence on ω of the integrated intensity is shown in Figure 14 (left) for each r-interval separately. The hot spot sticks out at values of ω that increase from $\sim 120^\circ$ in the low r-interval to $\sim 150^\circ$ in the high r-interval. The middle panel shows the dependence on ω of the normalized value of V_z averaged in each r-ω bin separately; more precisely a fit of the form $\langle V_z\rangle = -a\sin\omega - b\cos\omega$ is performed in each r-ω bin separately and the normalization is made by dividing each of the three distributions by the corresponding value of a (respectively 1.46, 1.27 and $1.18\,\mathrm{km\,s^{-1}}$, namely $\sim 1.78\,\mathrm{km\,s^{-1}}$ divided by $\langle r\rangle^{1/2}$). The values of b are between 0.02 and $0.03\,\mathrm{km\,s^{-1}}$ and can be neglected. All three normalized histograms are described well by a sine wave. The right panel displays the dependence on ω of σ_{vz}: in each r-ω interval the σ of a Gaussian fit to the peak of the Doppler velocity spectrum is plotted after normalization to its value averaged over ω in the corresponding r-interval (0.258, 0.210, and $0.181\,\mathrm{km\,s^{-1}}$ respectively).

As a function of ω, the line width fluctuates relatively less than the integrated intensity. Moreover, there is no sign of a sine wave contribution that would signal the effect of Keplerian shear, confirming the conclusion that was reached above. While the hot spot dominates the variations of the integrated intensity, its presence is barely visible as an increase of the line width; conversely, sharper line width excesses at $\omega \sim 60^\circ$ and 320° are visible on the velocity-integrated distribution as less marked excesses. The depressions at $\omega \sim 0^\circ$, 90° and 270° are also associated with lower values of the line width. The correlation between σ_{vz} and fluctuations of the integrated intensity f is illustrated in Figure 15. In each (r,ω) bin we define $\Delta\sigma$ and Δf as the difference between the values of σ_{vz} and f and their mean in the r interval: $\Delta\sigma = \sigma_{vz}/\langle\sigma_{vz}\rangle - 1$ and $\Delta f = f/\langle f\rangle - 1$. A clear positive correlation is evidenced from the best linear fit, $\Delta\sigma = 0.32\,\Delta f$. Note that the correlation is even slightly stronger if one excludes the hot spot region, with the corresponding Pearson coefficients being respectively 0.25 and 0.32. From the low-r interval to the

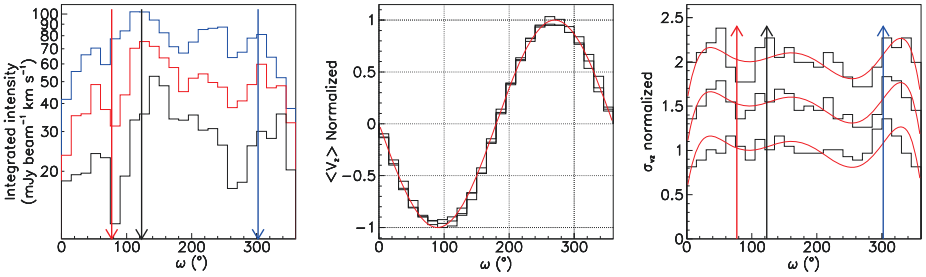

Fig. 14 *Left:* Dependence on ω of the integrated intensity for $1.3'' < r < 1.7''$ (*blue*), $1.7'' < r < 2.1''$ (*red*) and $2.1'' < r < 2.5''$ (*black*); *Middle:* dependence on ω of the value of $\langle V_z \rangle$ in each of the three r-intervals (*black histograms*); here, $\langle V_z \rangle$ has been divided by 1.46, 1.27 and 1.18 km s^{-1} respectively, making the three histograms nearly identical; the *red curve* is a sine wave. *Right:* dependence of σ_{vz} on ω, for each r-interval separately; in each r-ω bin, a Gaussian fit is performed to the peak of the V_z spectrum, giving a σ-value that averages to respectively 0.258, 0.210 and 0.181 km s^{-1}; the plotted histograms are normalized to these respective average values; in addition, for clarity, they are shifted up by respectively 0, 0.5 and 1. The *red curve*, a sixth degree polynomial fit to the distribution of the central r-interval, is shown to guide the eye. In the *left* and *right panels* the *arrows* point in the direction of increasing r and indicate remarkable features: the *black arrow* shows the hot spot as defined from the *left panel*; the *blue* and *red arrows* show peaks of the line width as defined from the *right panel*.

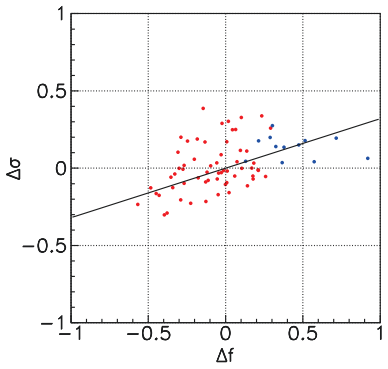

Fig. 15 Correlation between the normalized relative fluctuations of the line width $\Delta\sigma$ and the integrated intensity Δf (see text). The *line* is the best fit to the data, $\Delta\sigma = 0.32\Delta f$. The *blue points* are for $105^\circ < \omega < 165^\circ$ (*hot spot*).

high-r interval the ω-averaged line width (σ) decreases by a factor 0.70 while the amplitude of the V_z sine wave decreases only by a factor 0.81. A possible explanation may be an increase of the temperature and opacity with decreasing r. An increase of temperature and opacity from (T, τ)=(18 K, 5) at $r \sim 2.3''$ to (36 K, 10) at $r \sim 1.5''$ would imply an effective thermal broadening increasing from ~ 0.13 km s^{-1} to about 0.21 km s^{-1}. Adding in quadrature σ_K and σ_I contributions of respectively 0.09 and 0.05 km s^{-1} would give respectively 0.15 and 0.23 km s^{-1}, compared with 0.18 and 0.26 km s^{-1} being measured.

The fact that the ω-dependence of $\langle V_z \rangle$ is very well described by a simple sine wave in each of the three intervals implies that the observations are consistent with $V_{\rm rot}$ being independent of ω. It shows again that the fluctuations of $V_{\rm rot}\, r^{1/2}$ observed in Figure 11 are affected by very large uncertainties. Indeed, very good fits to the measured V_z sky map are obtained by assuming a purely Keplerian rotation velocity. On the contrary, we estimate that the uncertainty attached to both $\langle V_z \rangle$ and σ_{vz} is of the order of only 0.02 km s^{-1}, making the discussion of the line width in terms of σ_{vz} more reliable than in terms of $V_{\rm rot}$ dispersion.

5 SUMMARY

In summary, the present analysis confirms the results obtained earlier by Tang et al. (2016). It reveals the presence of concentric dust and gas rings sharing the same axis projecting on the sky plane $\sim 7^\circ$ east of north. In the approximation where both rings are flat and thin, their inclination angles with respect to the sky plane are respectively 32° and 35°. The gas ring is broader than the dust ring and peaks at smaller distance (typically 87%) to the central stars. The de-projected radial dependence of the line emission displays maxima at $\sim 1.2''$ and $1.9''$ from the central stars, bracketing the mean dust ring radius of $\sim 1.6''$. It cuts-off sharply at a mean distance of $\sim 1''$, cancelling completely below $\sim 0.54''$. Azimuthal rms variations of the dust and gas emissions in the disc planes are measured at the respective levels of $\sim \pm 9\%$ and $\pm 17\%$. Strong evidence is obtained for the rotation of the tilted gas disc about its axis dominating the kinematics.

A detailed study of the properties of the gas disc has been presented, adding significant new contributions to the earlier analysis of Tang et al. (2016). From the azimuthal dependence of the sharpness of the inner edge of the disc, a 95% confidence level upper limit of $0.24''$ (34 au) has been placed on its scale height $H(r)$ at a distance of $1''$ (140 au) from the central stars. At 30 K, hydrostatic equilibrium would imply $H(r)/r \sim 0.17$, consistent with this observation.

Variations of the integrated intensity across the disc area have been studied in detail and found to confirm the presence of a hot spot in the south-eastern quadrant. However several other significant fluctuations, in particular a depression in the northern direction, have also been revealed. On average, the rms relative variation of the integrated intensity reaches only $\sim 17\%$. The radial dependence of the integrated intensity is modulated with enhancements at $r \sim 1.2''$ and $1.9''$, bracketing the dust ring ($\sim 1.6''$). It is also between these radial integrated intensity enhancements that both the hot spot and the northern depression are observed to peak (their effects nearly cancelling each other when averaged over ω).

The study of the gas kinematics has given evidence for a strong dominance of rotation about the disc axis. The Doppler velocity gradient being perpendicular to the projection of the disc axis on the sky plane allows placing a 99% confidence upper limit of 9% on the ratio between a possible in-fall velocity and the rotation velocity. The difficulty of evaluating reliably the rotation velocity close to the sky plane projection of the disc axis has been illustrated and commented upon. Taking this in proper account, the rotation is observed to be Keplerian with a power index of ~ -0.51 across most of the disc area. At $r = 1''$, the rotation velocity reaches $\sim 3.1\,\mathrm{km\,s^{-1}}$, in agreement with the value measured by Dutrey et al. (2014) for ^{12}CO(6–5). No significant anomaly can be revealed in regions of important integrated intensity variation such as the hot spot and the northern depression.

Finally, the dependence of the line width on r and ω has been studied. It shows little dependence on ω and increases as r decreases: the σ of the line, σ_{vz}, increases from $\sim 0.18\,\mathrm{km\,s^{-1}}$ to $\sim 0.26\,\mathrm{km\,s^{-1}}$ when r decreases from $2.3''$ to $1.5''$. As the contributions of Keplerian shear and instrumental spectral resolution taken together should not exceed some $0.11\,\mathrm{km\,s^{-1}}$, a possible explanation may be a factor ~ 2 decrease of the disc surface temperature and opacity, reaching respectively 36 K and 10 at $r = 1.5''$. Relative variations of the line width over the disc area have been found to be strongly correlated with relative variations of the integrated intensity, the former being about a third of the latter. At least qualitatively, this result would also support the presence of a temperature gradient, the CO(3–2) emission ladder peaking at temperatures higher than the average disc temperature.

These new results contribute significant additional information and complement the earlier conclusions reached by Dutrey et al. (2014) and Tang et al. (2016). However, considerations on optical thickness, which are discussed in detail by Tang et al. (2016), are not repeated here. Moreover, interpretations of the observed variations of the integrated intensity as signalling the formation of a planet or of a new companion star remain valid suggestions that would require detailed modelling to be validated. However, this is beyond the scope of the present work.

Acknowledgements This paper makes use of the following ALMA data: ADS/JAO.ALMA#2012.1.00129.S. ALMA is a partnership of ESO (representing its member states), NSF (USA) and NINS (Japan), together with NRC (Canada), NSC and ASIAA (Taiwan), and KASI (Republic of Korea), in cooperation with the Republic of Chile. The Joint ALMA Observatory is operated by ESO, AUI/NRAO and NAOJ. This research has made use of the SIMBAD database, operated at CDS, Strasbourg, France, and of the NASA ADS Abstract

Services. We thank the anonymous referee for useful comments that helped in improving the presentation of this work. We thank the members of the initial "GG Tau team" for early contributions, Jeff Bary, Tracy Beck, Hervé Beust, Yann Boehler, Frederic Gueth, Jean-Marc Huré, Vincent Piétu, Arnaud Piérens and Michal Simon. This research is funded by the Vietnam National Foundation for Science and Technology Development (NAFOSTED) (No. 103.99–2016.50). The Department of Astrophysics (VNSC/VAST) acknowledges support from the World Laboratory, Rencontres du Viet Nam, the Odon Vallet fellowships, Vietnam National Space Center and Graduate University of Science and Technology. Anne Dutrey and Stéphane Guilloteau thank the French CNRS programs PNP, PNPS and PCMI.

References

Di Folco, E., Dutrey, A., Le Bouquin, J.-B., et al. 2014, A&A, 565, L2

Dutrey, A., Di Folco, E., Beck, T., & Guilloteau, S. 2016, A&A Rev., 24, 5

Dutrey, A., Guilloteau, S., & Simon, M. 1994, A&A, 286, 149

Dutrey, A., di Folco, E., Guilloteau, S., et al. 2014, Nature, 514, 600

Piétu, V., Dutrey, A., & Guilloteau, S. 2007, A&A, 467, 163

Tang, Y.-W., Dutrey, A., Guilloteau, S., et al. 2016, ApJ, 820, 19

Teague, R., Guilloteau, S., Semenov, D., et al. 2016, A&A, 592, A49

A&A 616, L5 (2018)
https://doi.org/10.1051/0004-6361/201833766
© ESO 2018

Astronomy & Astrophysics

LETTER TO THE EDITOR

First detection of H_2S in a protoplanetary disk

The dense GG Tauri A ring

N. T. Phuong[1,2,3], E. Chapillon[1,4], L. Majumdar[5], A. Dutrey[1], S. Guilloteau[1], V. Piétu[4], V. Wakelam[1], P. N. Diep[2,3], Y.-W. Tang[6], T. Beck[7], and J. Bary[8]

[1] Laboratoire d'Astrophysique de Bordeaux, Université de Bordeaux, CNRS, B18N, Allée Geoffroy Saint-Hilaire, 33615 Pessac, France
e-mail: thi-phuong.nguyen@u-bordeaux.fr
[2] Department of Astrophysics, Vietnam National Space Center, Vietnam Academy of Science and Techonology, 18 Hoang Quoc Viet, Cau Giay, Hanoi, Vietnam
[3] Graduate University of Science and Technology, Vietnam Academy of Science and Techonology, 18 Hoang Quoc Viet, Cau Giay, Hanoi, Vietnam
[4] IRAM, 300 rue de la piscine, 38406 Saint Martin d'Hères Cedex, France
[5] Jet Propulsion Laboratory, California Institute of Technology, 4800 Oak Grove Drive, Pasadena, CA 91109, USA
[6] Academia Sinica Institute of Astronomy and Astrophysics, PO Box 23-141, Taipei 106, Taiwan
[7] Space Telescope Science Institute, 3700 San Martin Drive, Baltimore, MD 21218, USA
[8] Department of Physics and Astronomy, Colgate University, 13 Oak Drive, Hamilton, NY 13346, USA

Received 3 July 2018 / Accepted 27 July 2018

ABSTRACT

Context. Studying molecular species in protoplanetary disks is very useful to characterize the properties of these objects, which are the site of planet formation.
Aims. We attempt to constrain the chemistry of S-bearing molecules in the cold parts of circumstellar disk of GG Tau A.
Methods. We searched for H_2S, CS, SO, and SO_2 in the dense disk around GG Tau A with the NOrthem Extended Millimeter Array (NOEMA) interferometer. We analyzed our data using the radiative transfer code DiskFit and the three-phase chemical model Nautilus.
Results. We detected H_2S emission from the dense and cold ring orbiting around GG Tau A. This is the first detection of H_2S in a protoplanetary disk. We also detected HCO^+, $H^{13}CO^+$, and DCO^+ in the disk. Upper limits for other molecules, CCS, SO_2, SO, HC_3N, and c-C_3H_2 are also obtained. The observed DCO^+/HCO^+ ratio is similar to those in other disks. The observed column densities, derived using our radiative transfer code DiskFit, are then compared with those from our chemical code Nautilus. The column densities are in reasonable agreement for DCO^+, CS, CCS, and SO_2. For H_2S and SO, our predicted vertical integrated column densities are more than a factor of 10 higher than the measured values.
Conclusions. Our results reinforce the hypothesis that only a strong sulfur depletion may explain the low observed H_2S column density in the disk. The H_2S detection in GG Tau A is most likely linked to the much larger mass of this disk compared to that in other T Tauri systems.

Key words. protoplanetary disks – molecular data – astrochemistry – stars: individual: GG Tau

1. Introduction

Understanding the physical and chemical structure of protoplanetary disks is needed to determine the initial conditions of planet formation. Studies of protoplanetary disks have led to a global picture in which disks are flared and layered with important vertical, radial density, and temperature gradients. The uppermost layer is directly illuminated by stellar UV and dominated by photodissociation reactions, while molecules stick to dust grains in the very cold midplane. In between there is a rich molecular layer (Kenyon & Hartmann 1987; van Zadelhoff et al. 2001). Studies of the gas content rely on trace molecules because H_2 is not detectable at the temperatures of disks. So far, the molecules that have been detected in T Tauri disks are CO, ^{13}CO, $C^{18}O$, $C^{17}O$, CN, CS, H_2CO, CCH, DCN, HCO^+, $H^{13}CO^+$, DCO^+, N_2H^+, HC_3N, CH_3CN, HD, C_3H_2, C_2H_2, OH, SO, CH^+, N_2D^+, NH_3, CH_3OH, $H^{13}CN$, $HC^{15}N$, $C^{15}N$, and HCOOH (Dutrey et al. 1997, 2011; Thi et al. 2001; Qi et al. 2008, 2013; Chapillon et al. 2012; Bergin et al. 2013; Huang & Öberg 2015; Öberg et al. 2015; Walsh et al. 2016; Guilloteau et al. 2016; Salinas et al. 2016; Guzmán et al. 2015; Hily-Blant et al. 2017; Favre et al. 2018).

More than a dozen S-bearing species have been observed in dense cloud cores; they are chemically active and often used as chemical clocks in low-mass star forming regions (Buckle & Fuller 2003; Wakelam et al. 2004a,b). Some S-bearing species, CS, SO, SO_2, and H_2S, are observed in Class 0 and Class I sources (Dutrey et al. 2011; Guilloteau et al. 2013, 2016) while CS, the second main reservoir of sulfur in the gas

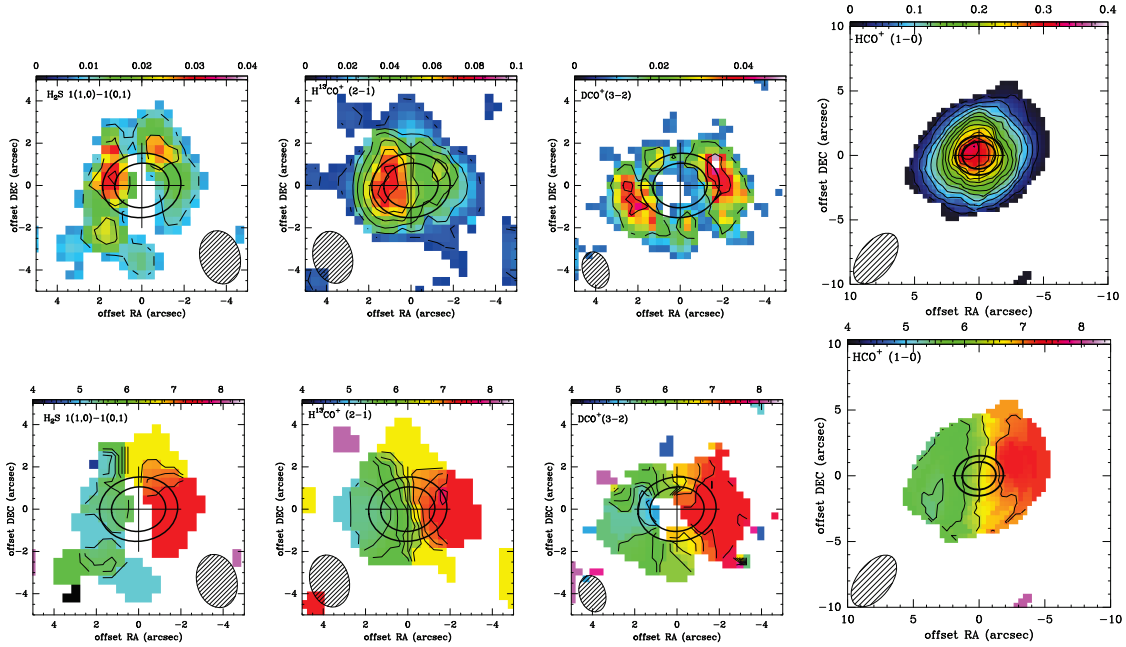

Fig. 1. *Upper*: Integrated intensity maps. The color scale is in the unit of Jy beam^{-1} km s^{-1}. Contour level step is 2σ. *Lower*: Velocity maps. Contour level steps is 0.5 km s^{-1}. Beam sizes are indicated. The ellipses show the location of inner (~180 au) and outer (~260 au) radii of the dust ring.

Table 2. Observed and predicted surface densities (cm^{-2})

Molecule	Observed	Predicted	Predicted
	Detection (derived from DiskFit)	(derived from DiskFit)	(from Nautilus)
H_2CO (3–2)	$4.5 \pm 0.04 \times 10^{12}$	2.2×10^{12}	7.2×10^{12}
$H^{13}CO^+$ (2–1)	$5.3 \pm 0.3 \times 10^{10}$	(a)	(a)
DCO^+ (3–2)	$3.9 \pm 0.2 \times 10^{12}$	7.0×10^{12}	1.2×10^{12}
H_2S 1(1,0)–1(0,1)	$1.3 \pm 0.1 \times 10^{13}$	5.4×10^{13}	1.4×10^{13}
CCS (5–4)	2.2×10^{12}	1.4×10^{13}	2.4×10^{12}
DCO^+ (3–2)	$3.9 \pm 0.2 \times 10^{12}$	7.0×10^{12}	1.2×10^{12}
SO_2	$<1.5 \times 10^{11}$	6.0×10^{11}	$<1.7 \times 10^{11}$
SO	$<4.1 \times 10^{12}$	1.5×10^{13}	$<1.7 \times 10^{12}$
HC_3N	5.2×10^{10}	3.7×10^{11}	$<2.7 \times 10^{10}$
c-C_3H_2	$<2.7 \times 10^{11}$	2.4×10^{12}	$<1.7 \times 10^{11}$

Notes. (a) Observed surface density at 250 au is derived using DiskFit.

of species surface density in the gas phase at 250 au predicted with Nautilus. (1) Our model does not include carbon isotope chemistry.

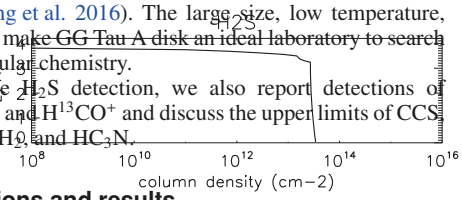

Fig. 2. Best model of H_2S, CCS, DCO^+, and HCO^+ in the GG Tau A ring derived from Nautilus. The surface density is shown vs. the z/H ratio (z/H=1 means 1 scale height).

phase (Vidal et al. 2017) is the only S-bearing molecule detected in disks around T Tauri stars.

We report the first detection of H_2S in a disk around a Pre-Main-Sequence star, GG Tau A. GG Tau, located at 150 pc in the Taurus-Auriga star forming region (Gaia Collaboration 2016, 2018), is a hierarchical quintuple system with the GG Tau A triple star (separation ~5 and 38 au; Di Folco et al. 2014) surrounded by a dense ring located between 180 and 260 au and a large disk extending out to 800 au (see Dutrey et al. 2016, and references therein). The disk is massive (0.15 $M_\odot$) and cold; it has a dust temperature of 14 K at 200 au, a kinetic temperature derived from CO analysis of ≤ 20 K at the same radius (Dutrey et al. 2014; Guilloteau et al. 1999), and little or no vertical temperature gradient in the molecular layer (Tang et al. 2016). The large size, low temperature, and large mass make GG Tau A disk an ideal laboratory to search for cold molecular chemistry.

Besides the H_2S detection, we also report detections of HCO^+, DCO^+, and $H^{13}CO^+$ and discuss the upper limits of CCS, SO_2, SO, c-C_3H_2, and HC_3N.

2. Observations and results

2.1. Observations

The H_2S 1(1,0)–1(0,1) observations were carried out with the NOrthern Extended Millimeter Array (NOEMA) on 23, December 2017 using D configuration with nine antennas. The total on source integration time is 5.2 h. Baselines ranging between 24 m and 176 m provide an angular resolution of 2.50″ × 1.9″, PA = 15°. Phase and amplitude calibrations were performed using 0507+179 and 0446+112. Flux calibration was carried out using MWC349 as a reference (flux 1.6 Jy at 170.3 GHz). The full 7.74 GHz upper and lower sidebands of the new PolyFiX correlator were covered at 2 MHz channel spacing, and high spectral resolution (62.5 kHz) windows covered lines of interest. Two windows covered lines of H_2S 1(1,0)–1(0,1), $H^{13}CO^+$(2–1), CCS, SO_2, DCO^+(3–2), HC_3N, and c-C_3H_2.

DCO^+(3–2) was observed with PdBI interferometer (now known as NOEMA) in December 2013 and April 2014 with six antennas at an angular resolution of 1.76″ × 1.23″, PA = 17°. Phase and amplitude calibrations were performed using 0507+179 and 0446+112, while the flux calibration was carried out using 3C84 and MWC 349.

The HCO^+(1–0) data are from Guilloteau et al. (1999) and are processed in this work with a resolution of 4.57″ × 2.55″, at PA = −38°. We used the GILDAS[1] software package to reduce the data. Images were produced using natural weighting and *Hogbom* algorithm. The continuum emission is subtracted from the line maps.

2.2. Results

Figure 1 shows integrated intensity maps (upper panels) and velocity maps (lower panels) of the detected lines, H_2S 1(1,0)–1(0,1), $H^{13}CO^+$(2–1), DCO^+(3–2), and HCO^+(1–0). The velocity maps show a clear signature of Keplerian rotation. Channel maps are presented in Appendix A.

H_2S 1(1,0)–1(0,1) is clearly detected with a peak $S/N \geq 4$ in several channels. Most of the line emission originates from the dense ring between 180 and 260 au and extends up to ≤500 au. The weak east-west asymmetry is unlikely to be significant given the limited signal-to-noise ratio (S/N).

HCO^+(1–0) and $H^{13}CO^+$(2–1) are detected with high S/N(≥7). HCO^+(1–0) is as extended as the CO emission out

[1] https://www.iram.fr/IRAMFR/GILDAS/

Table 1. GG Tau parameters.

Geometry		Law
Inclination	35°	$V(r) = 3.4\,(\frac{r}{100\,\mathrm{au}})^{-0.5}$ (km s^{-1})
Orientation	7°	$T(r) = 25\,(\frac{r}{200\,\mathrm{au}})^{-1}$ (K)
Systemic velocity	6.4 km s^{-1}	$\Sigma(r) = \Sigma_{250}\,(\frac{r}{250\,\mathrm{au}})^{-1.5}$ (cm^{-2})

to ~800 au (Guilloteau et al. 1999). The optically thin emission from the $J = 2$–1 line of the $H^{13}CO^+$ isotopolog peaks on the dense ring and extends to ~500 au. On the contrary, the DCO^+(3–2) emission, detected at $S/N \geq 7$, peaks just outside of the dense ring, near 280 au, suggesting radially varying deuteration. Other sulfur-bearing species, SO, SO_2, CCS, and carbon-bearing species HC_3N and c-C_3H_2, are not detected.

3. Data analysis

3.1. DiskFit modeling

We assume the physical parameters that govern line emission to vary as power laws of the radii (Dutrey et al. 1994; Piétu et al. 2007). The data were analyzed inside the uv plane using the radiative transfer code DiskFit, which uses χ^2 minimization technique, comparing the observed visibilities to visibilities predicted by ray tracing (Piétu et al. 2007).

The source parameters such as geometry (inclination, orientation, and systemic velocity), velocity, and temperature power laws are kept constant as they are well known from previous studies (Dutrey et al. 1994, 2014; Guilloteau et al. 1999 and our Table 1). Only the molecule surface density parameter Σ_{250} was varied during the minimization process. Results are presented in Table 2 with 3σ upper limits for undetected molecules.

3.2. Nautilus modeling

To model the chemistry in the dense and cold ring of GG Tau A, we used the gas-grain chemical model `Nautilus` (Ruaud et al. 2016). This model simulates chemistry in three phases, i.e., gas phase, grain surface, and grain mantle, along with possible exchanges between the different phases. The reference chemical network is `deuspin.kida.uva.2016` (Majumdar et al. 2017) with the updates in sulfur chemistry from Vidal et al. (2017). The disk structure is similar to that used in Wakelam et al. (2016). In addition to disk parameters from Table 1, we assume a stellar UV flux of $f_{UV200AU} = 375\,\chi_0$ at 200 au, where χ_0 is in the units of the Draine (1978) interstellar UV field, based on what is observed in T Tauri stars (Bergin et al. 2004). Based on the observation (Tang et al. 2016), we introduced a small vertical temperature gradient with $T_k = 30$ K at three scale heights.

To compute the chemistry, we first calculated the chemical composition of the gas and ices of the parent cloud, assuming conditions for a dense cloud with an age of $\sim 10^6$ yr and then ran the model for another 10^6 yr (Wakelam et al. 2016). For the parent cloud, initially all the elements are in atomic form (see Table 1, Vidal et al. 2017) except for hydrogen and deuterium, which are initially in H_2 and HD forms, respectively (Majumdar et al. 2017).

We present the trends of the chemistry inside the ring at a radius of 250 au in order to explain the observed column densities of H_2S, CS, DCO^+, and HCO^+. We explored various initial C/O ratios, ortho to para ratios for H_2 (OPR), initial sulfur abundances X(S), grain sizes, and UV flux. According to Bergin et al. (2016), CCH emission can only be explained with a gas-phase C/O ratio larger than 1. This represents a scenario in which oxygen is depleted on the grains before the formation of the disk and driven to the midplane of the disk. In other words, oxygen would not participate in the chemistry in the region where they observe CCH. Semenov et al. (2018) found that the column densities of SO and SO_2 drop by factors of ~100 and 500, respectively, when C/O changes from 0.46 to 1.2, whereas column densities of H_2S do not change as the species contains neither C nor O. We stick to the standard C/O ratio of 0.7 in our model (Hincelin et al. 2011; Wakelam et al. 2016; Majumdar et al. 2017), which gives a reasonably good agreement for DCO^+, CS, CCS, HC_3N, and SO_2.

Results are therefore presented for C/O = 0.7, OPR = 3, $X(S) = 8 \times 10^{-8}$ and a grain size of 0.1 μm. Other models lead to larger disagreement with the data. Figure 2 and Appendix B show the predicted vertical distribution of the molecules, and Table 2 compares the predicted surface densities to the observational results derived using DiskFit.

4. Discussion

4.1. Comparison with other sources

The measured H_2S column density is a factor of three greater than the upper limits quoted by Dutrey et al. (2011) for DM Tau, LkCa 15, MWC 480, and GO Tau, probably reflecting the larger disk mass of GG Tau A. However, the CS to H_2S abundance ratio of ~20 in GG Tau A may still be similar in all sources. The upper limit on HC_3N is about two times lower than the detections reported in LkCa 15, MWC 480, and GO Tau by Chapillon et al. (2012).

To make relevant abundances comparisons, we use ^{13}CO as a reference since H_2 column densities are difficult to accurately determine. The results for the disks of GG Tau A and LkCa15 and the dark cloud TMC-1 are given in Table 3. LkCa15 is a T Tauri star similar to GG Tau A: its disk exhibits a central cavity of radius 50 au (Piétu et al. 2006) and has a mass on the order of ~0.028 $M_\odot$ (Guilloteau et al. 2011). Determining the uncertainties is difficult because the abundances were obtained from different studies. Therefore, we assume errors of 30% in the cases of LkCa 15 and TMC-1.

For GG Tau A, we take a ^{13}CO column density, derived from observations, at 250 au of $\Sigma_{250} = 1.13 \times 10^{16}$ cm^{-2} (Phuong et al., in prep). For LkCa 15, Punzi et al. (2015) found HCO^+ abundance relative to ^{13}CO of 15×10^{-4}, Huang et al. (2017) gave abundance ratios of DCO^+/HCO^+ and $DCO^+/H^{13}CO^+$ of 0.024 and 1.1, respectively, and Dutrey et al. (2011) gave an upper limit of H_2S relative to CO of 10^{-6}, which we convert to ^{13}CO using an isotopic ratio $^{12}C/^{13}C$ ~60 (Lucas & Liszt 1998).

In the TMC-1 dark cloud, Ohishi et al. (1992) determined ^{12}CO abundance relative to H_2 of 8×10^{-5} or 1.3×10^{-6} for ^{13}CO. The abundance relative to H_2 of HCO^+, H_2S (upper limit; Omont 2007), $H^{13}CO^+$, and DCO^+ (Butner et al. 1995) are then used to get the abundances relative to ^{13}CO. In L134N, the abundances of these species are similar, but H_2S has been detected with an abundance ratio of 60×10^{-5} (Ohishi et al. 1992), similar to the upper limit obtained in TMC-1. Thus, the disks appear to have very similar relative abundances, suggesting similar chemical processes at play, while the dense core differs significantly.

4.2. Sulfur-bearing species

In the chemical modeling, we found that H_2S peaks around three scale heights. The main reason behind this is rapid formation of H_2S on the grain surface via the hydrogenation

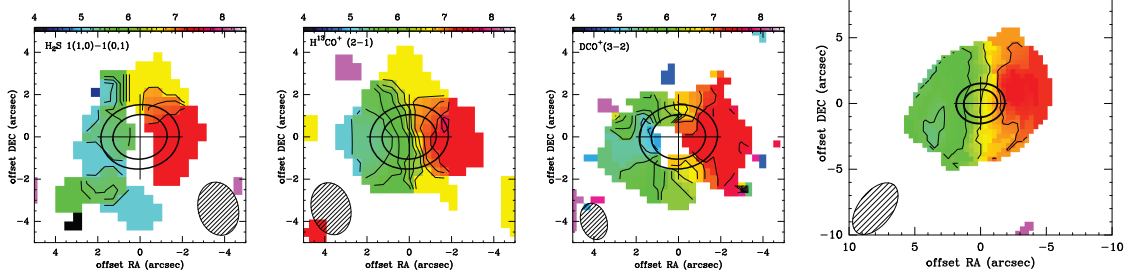

Fig. 1. *Upper:* Integrated intensity maps. The color scale is in the unit of (Jy beam^{-1} km s^{-1}). Contour level step is 2σ. *Lower:* Velocity maps. Contour level step is 0.5 km s^{-1}. Beam sizes are indicated. The ellipses show the location of inner (~180 au) and outer (~260 au) radii of the dust ring.

Table 2. Observed and predicted surface densities (cm^{-2}).

Table 2. Observed and predicted surface densities (cm^{-2})

Molecule	Detection Observed^{a*} (derived from DiskFit)	Detection Predicted^{c†} (from Nautilus)	Molecule	Non-detection Observed^{a*} (derived from DiskFit)	Non-detection Predicted^{c†} (from Nautilus)
HCO^+(1–0)	$1.5 \pm 0.04 \times 10^{13}$	2.2×10^{12}	CCS	$<1.7 \times 10^{12}$	7.2×10^{10}
$H^{13}CO^+$ (2–1)	$5.3 \pm 0.3 \times 10^{11}$	(–)	SO_2	$<1.5 \times 10^{12}$	6.0×10^{12}
DCO^+ (3–2)	$3.9 \pm 0.2 \times 10^{11}$	7.0×10^{10}	SO	$<1.1 \times 10^{12}$	1.5×10^{13}
H_2S 1(1,0)–1(0,1)	$1.3 \pm 0.1 \times 10^{12}$	3.4×10^{13}	HC$_3$N	$<3.2 \times 10^{11}$	5.7×10^{11}
CS(3–2)	2.2×10^{13}#	1.4×10^{13}	c-C_3H_2	$<2.7 \times 10^{11}$	2.4×10^{12}

Notes. [a]Observed surface density at 250 au is derived using DiskFit. [b]Phuong et al., in prep. [c]Species surface density in the gas phase at 250 au predicted with Nautilus. (–) Our model does not include carbon isotope chemistry.

Notes. ⋆ Observed surface density at 250 au is derived using DiskFit. # Phuong et al., in prep. † Species surface density in the gas phase at 250 au predicted with Nautilus. (–) Our model does not include carbon isotope chemistry.

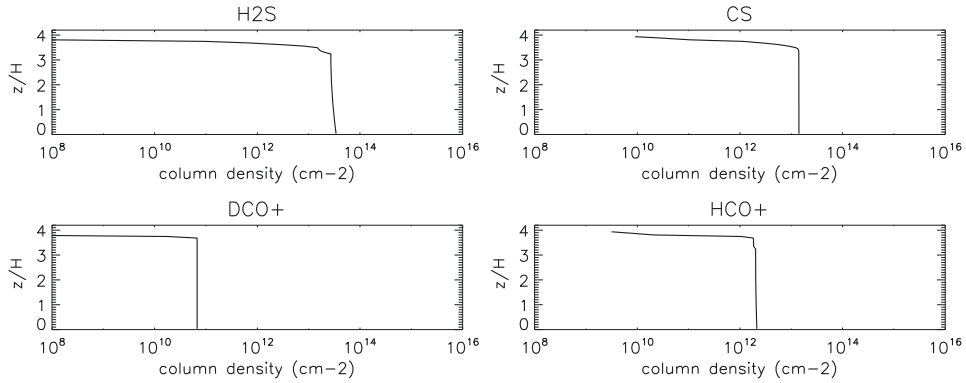

Fig. 2. Best model of H_2S, CS, DCO^+, and HCO^+ in the GG Tau A ring derived from Nautilus. The surface density is shown vs. the z/H ratio (z/H=1 means 1 scale height).

Fig. 2. Best model of H_2S, CS, DCO^+, and HCO^+ in the GG Tau A ring derived from Nautilus. The surface density is shown vs. the z/H ratio (z/H=1 means 1 scale height).

reaction of HS, i.e., grain-H + grain-HS → grain-H_2S. Once H_2S is formed on the surface, it is then chemically desorbed to the gas phase. Almost 80% of the H_2S comes from the surface reactions, whereas the contribution of the gas-phase reaction $H_3S^+ + e^- \rightarrow H + H_2S$ is about 20%. Below three scale heights, H_2S depletes rapidly on the grains because of the increase in density and decrease in temperature. At the same altitude, CS is formed in the gas phase via the dissociative recombination reactions of HCS^+, H_2CS^+, H_3CS^+, and $HOCS^+$.

The modeled CCS and SO_2 column densities (shown in Table 2 and in Appendix B) are low, explaining their non-detection but the SO column density is overpredicted. The CCS molecule shows its peak above $z/H = 3$ and is due to the gas phase formation via $S + CCH \rightarrow H + CCS$ and $HC_2S^+ + e^- \rightarrow H + CCS$ reactions. SO_2 is made from the OH + SO reaction around this location, whereas SO comes from the S + OH reaction.

We found that the UV field has a negligible impact on the H_2S desorption and mildly affects the SO/H_2S ratio. The key parameter in the model is the initial S abundance. Even with the low value, 8×10^{-8}, the chemical model overpredicts H_2S and SO by about an order of magnitude, but is compatible with CS and the current limits on SO_2 and CCS.

In our models, the molecular layer is very thin and situated high above the disk plane at three scale heights. This is at odds with the observations of CS in the Flying Saucer (Dutrey et al. 2017), where CS appears closer to one scale height. The difference may be due to the larger mass of the GG Tau disk (0.15 $M_\odot$). On one side, the high densities limit the UV radiation penetration (which drives the active chemistry) to the uppermost layers, while closer to the midplane, the even higher densities lead to more efficient depletion on dust grains.

Our results suggest that chemistry for H_2S on the grain surfaces is likely not properly taken into account even with our three-phase model and that a significant amount of H_2S should change in some more complex sulfur-bearing species, limiting the overall desorption of S-bearing molecules (Dutrey et al. 2011; Wakelam et al. 2005). Indeed, measurements of S-bearing species in comets 67P performed by ROSETTA indicate a solar value for the S/O elemental ratio within 2σ errors (Calmonte et al. 2016). H_2S accounts for about half of the S budget in the comet, suggesting that transformation of H_2S to other compounds in ices is limited. The nearly constant H_2S/H_2O ratio also suggests that H_2S does not evaporate alone, but in combination with water (Jiménez-Escobar & Muñoz Caro 2011).

4.3. Chemistry of DCO^+ and other observed species

Chemistry of DCO^+. The measured $HCO^+/H^{13}CO^+$ ratio is about 30, suggesting partially optically thick emission for HCO^+(1–0) line. The measured DCO^+/HCO^+ ratio, ~0.03 over the disk, is comparable to the averaged value (~0.04; van Dishoeck et al. 2003) derived in the disk of TW Hydra of mass of ~0.06 $M_\odot$ (Bergin et al. 2013), and in the disk of LkCa 15 (ratio of ~0.024, Huang et al. 2017.) This shows clear evidence of ongoing deuterium enrichment.

HCO^+ formation and deuteration is controlled by CO as well as H_2D^+ and H_3^+ ions. These ions are mostly sensitive

Table 3. Molecular abundance relative to ^{13}CO ($X_{[mol]}/X_{[^{13}CO]} \times 10^5$).

	TMC-1[a]	LkCa 15	GG Tau
HCO^+	$600 \pm 180^{(1)}$	$150 \pm 35^{(3)}$	130 ± 12
H_2S	$<45^{(1)}$	$<7^{(4)}$	11 ± 3
$H^{13}CO^+$	15 ± 4 [(2)]	5 ± 1.5 [(4)]	4.7 ± 0.3
DCO^+	30 ± 9 [(2)]	4.5 ± 1.4 [(4)]	3.5 ± 0.15

Notes. [(a)] ^{13}CO abundance is derived from CO abundance in Ohishi et al. (1992), [(1)]Omont (2007), [(2)]Butner et al. (1995), [(3)]Punzi et al. (2015), [(4)]Dutrey et al. (2011), [(5)]Huang et al. (2017).

to the X-ray flux, while UV radiation and cosmic rays play a limited role, and their balance is controlled by the temperature sensitive reaction $H_3^+ + HD \rightleftharpoons H_2D^+ + H_2$. Because of the temperature dependences, DCO^+ is expected to be enhanced around the CO snow-line, as illustrated by the ring structure in HD 163296 (Mathews et al. 2013). Our model somewhat underpredicts the HCO^+ content. At 250 au, HCO^+ peaks at three scale heights, where the molecular layer is warm (~30 K) and forms mainly from the reaction of CO + ortho-H_3^+. At this altitude, DCO^+ forms from the isotope exchange reaction between HCO^+ and D because the gas temperature is still high. Closer to the disk midplane, the ortho-H_2D^+ + CO pathway remains inefficient because of the strong CO depletion that results from high densities. Lower densities just outside the dense ring may lead to lower CO depletion and a more efficient DCO^+ formation, explaining the DCO^+ peak there.

Other observed species. We also presented integrated column densities of HC_3N and c-C_3H_2, in Table 2 and Appendix B. The modeled column densities of HC_3N and c-C_3H_2 are overpredicted. The high column density of HC_3N above three scale heights is due to its rapid formation via $CN + C_2H_2 \rightarrow H + HC_3N$ reaction, whereas c-C_3H_2 forms from the $CH + C_2H_2$ reaction, photodissociation of CH_2CCH and dissociative recombination of $C_3H_5^+$.

5. Summary

Using NOEMA, we have observed the GG Tau A outer disk in several molecules. We report the first detection of H_2S in a protoplanetary disk.

We clearly detect HCO^+, $H^{13}CO^+$, DCO^+, and H_2S. HCO^+ emission is extended, $H^{13}CO^+$ and H_2S emissions peak inside the dense ring at ~250 au, while DCO^+ emission arises from the outer disk beyond a radius of 300 au, perhaps as a result of competition between CO depletion and high temperatures.

Our three-phase chemical model fails to reproduce the observed column densities of S-bearing molecules, even with low S abundance and C/O = 0.7, suggesting that our understanding of S chemistry on dust grains is still incomplete.

Comparisons with other disks indicate that the detection of H_2S appears to be facilitated by the large disk mass, but that the relative abundance ratios remain similar. This indicates that GG Tau A could be a good test bed for chemistry in disks.

Acknowledgements. We thank the referee for useful comments that helped improve the quality of the manuscript. This work is based on observations carried out with the IRAM NOEMA Interferometer. IRAM is supported by INSU/CNRS (France), MPG (Germany) and IGN (Spain). This work has made use of data from the European Space Agency (ESA) mission *Gaia* (https://www.cosmos.esa.int/gaia), processed by the *Gaia* Data Processing and Analysis Consortium (DPAC, https://www.cosmos.esa.int/web/gaia/dpac/consortium). Funding for the DPAC has been provided by national institutions, in particular the institutions participating in the *Gaia* Multilateral Agreement. A. Dutrey and S. Guilloteau thank the French CNRS programs PNP, PNPS, and PCMI. N. T. Phuong and P. N. Diep acknowledge financial support from NAFOSTED under grant number 103.99-2016.50, World Laboratory, Rencontres du Viet Nam, the Odon Vallet fellowships, Vietnam National Space Center, and Graduate University of Science and Technology. V. Wakelam's research is funded by an ERC Starting Grant (3DICE, grant agreement 336474). L. Majumdar acknowledges support from the NASA postdoctoral program. A portion of this research was carried out at the Jet Propulsion Laboratory, California Institute of Technology, under a contract with the National Aeronautics and Space Administration.

References

Bergin, E., Calvet, N., Sitko, M. L., et al. 2004, ApJ, 614, L133
Bergin, E. A., Cleeves, L. I., Gorti, U., et al. 2013, Nature, 493, 644
Bergin, E. A., Du, F., Cleeves, L. I., et al. 2016, ApJ, 831, 101
Buckle, J. V., & Fuller, G. A. 2003, A&A, 399, 567
Butner, H. M., Lada, E. A., & Loren, R. B. 1995, ApJ, 448, 207
Calmonte, U., Altwegg, K., Balsiger, H., et al. 2016, MNRAS, 462, S253
Chapillon, E., Dutrey, A., Guilloteau, S., et al. 2012, ApJ, 756, 58
Di Folco, E., Dutrey, A., Le Bouquin, J.-B., et al. 2014, A&A, 565, L2
Draine, B. T. 1978, ApJS, 36, 595
Dutrey, A., Guilloteau, S., & Simon, M. 1994, A&A, 286, 149
Dutrey, A., Guilloteau, S., & Guelin, M. 1997, A&A, 317, L55
Dutrey, A., Wakelam, V., Boehler, Y., et al. 2011, A&A, 535, A104
Dutrey, A., di Folco, E., Guilloteau, S., et al. 2014, MNRAS, 514, 600
Dutrey, A., Di Folco, E., Beck, T., & Guilloteau, S. 2016, A&ARv, 24, 5
Dutrey, A., Guilloteau, S., Piétu, V., et al. 2017, A&A, 607, A130
Favre, C., Fedele, D., Semenov, D., et al. 2018, ApJ, 862, L2
Gaia Collaboration (Prusti, T., et al.) 2016, A&A, 595, A1
Gaia Collaboration (Brown, A. G. A., et al.) 2018, A&A, 616, A1
Guilloteau, S., Dutrey, A., & Simon, M. 1999, A&A, 348, 570
Guilloteau, S., Dutrey, A., Piétu, V., & Boehler, Y. 2011, A&A, 529, A105
Guilloteau, S., Di Folco, E., Dutrey, A., et al. 2013, A&A, 549, A92
Guilloteau, S., Reboussin, L., Dutrey, A., et al. 2016, A&A, 592, A124
Guzmán, V. V., Öberg, K. I., Loomis, R., & Qi, C. 2015, ApJ, 814, 53
Hily-Blant, P., Magalhaes, V., Kastner, J., et al. 2017, A&A, 603, L6
Hincelin, U., Wakelam, V., Hersant, F., et al. 2011, A&A, 530, A61
Huang, J., & Öberg, K. I. 2015, ApJ, 809, L26
Huang, J., Öberg, K. I., Qi, C., et al. 2017, ApJ, 835, 231
Jiménez-Escobar, A., & Muñoz Caro, G. M. 2011, A&A, 536, A91
Kenyon, S. J., & Hartmann, L. 1987, ApJ, 323, 714
Lucas, R., & Liszt, H. 1998, A&A, 337, 246
Majumdar, L., Gratier, P., Ruaud, M., et al. 2017, MNRAS, 466, 4470
Mathews, G. S., Klaassen, P. D., Juhász, A., et al. 2013, A&A, 557, A132
Öberg, K. I., Furuya, K., Loomis, R., et al. 2015, ApJ, 810, 112
Ohishi, M., Irvine, W. M., & Kaifu, N., 1992, IAU Symp., 150, 171
Omont, A. 2007, Rep. Prog. Phys., 70, 1099
Piétu, V., Dutrey, A., Guilloteau, S., Chapillon, E., & Pety, J. 2006, A&A, 460, L43
Piétu, V., Dutrey, A., & Guilloteau, S. 2007, A&A, 467, 163
Punzi, K. M., Hily-Blant, P., Kastner, J. H., Sacco, G. G., & Forveille, T. 2015, ApJ, 805, 147
Qi, C., Wilner, D. J., Aikawa, Y., Blake, G. A., & Hogerheijde, M. R. 2008, ApJ, 681, 1396
Qi, C., Öberg, K. I., Wilner, D. J., et al. 2013, Science, 341, 630
Ruaud, M., Wakelam, V., & Hersant, F. 2016, MNRAS, 459, 3756
Salinas, V. N., Hogerheijde, M. R., Bergin, E. A., et al. 2016, A&A, 591, A122
Semenov, D., Favre, C. & Fedele, D. 2018, A&A, in press, DOI 10.1051/0004-6361/201832980
Tang, Y.-W., Dutrey, A., Guilloteau, S., et al. 2016, ApJ, 820, 19
Thi, W. F., van Dishoeck, E. F., Blake, G. A., et al. 2001, ApJ, 561, 1074
van Dishoeck, E. F., Thi, W.-F., & van Zadelhoff, G.-J. 2003, Ap&SS, 285, 691
van Zadelhoff, G.-J., van Dishoeck, E. F., Thi, W.-F., & Blake, G. A. 2001, A&A, 377, 566
Vidal, T. H. G., Loison, J.-C., Jaziri, A. Y., et al. 2017, MNRAS, 469, 435
Wakelam, V., Caselli, P., Ceccarelli, C., Herbst, E., & Castets, A. 2004a, A&A, 422, 159
Wakelam, V., Castets, A., Ceccarelli, C., et al. 2004b, A&A, 413, 609
Wakelam, V., Ceccarelli, C., Castets, A., et al. 2005, A&A, 437, 149
Wakelam, V., Ruaud, M., Hersant, F., et al. 2016, A&A, 594, A35
Walsh, C., Loomis, R. A., Öberg, K. I., et al. 2016, ApJ, 823, L10

Appendix A: Channel maps

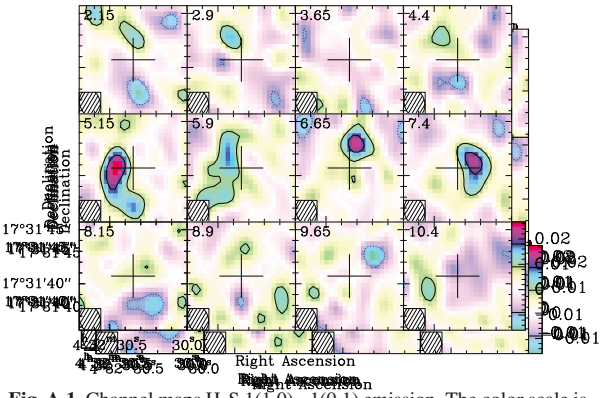

Fig. A.1. Channel maps H_2S 1(1,0) - 1(0,1) emission. The color scale is in the unit of Jy/beam. The contour spacing is 10 mJy/beam, which corresponds to 2σ or 0.08 K. The beam (2.55″ × 1.90″; PA = 14°) is inserted in the lower corner of each channel map.

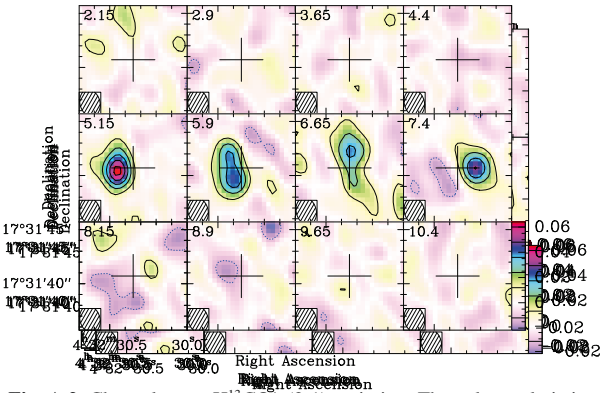

Fig. A.2. Channel maps $H^{13}CO^+$ (2-1) emission. The color scale is in the unit of Jy/beam. The contour spacing is 12 mJy/beam, which corresponds to 2σ or 0.11 K. The beam (2.50″ × 1.85″; PA = 15°) is inserted in the lower corner of each channel map.

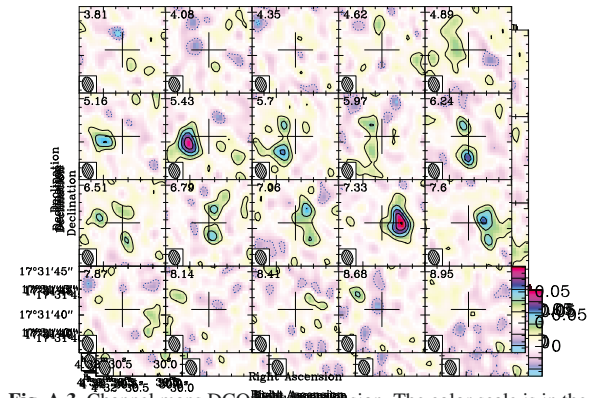

Fig. A.3. Channel maps DCO^+ (2-1) emission. The color scale is in the unit of Jy/beam. The contour spacing is 15 mJy/beam, which corresponds to 2σ or 0.22 K. The beam (1.76″ × 1.23″; PA = 17°) is inserted in the lower corner of each channel map.

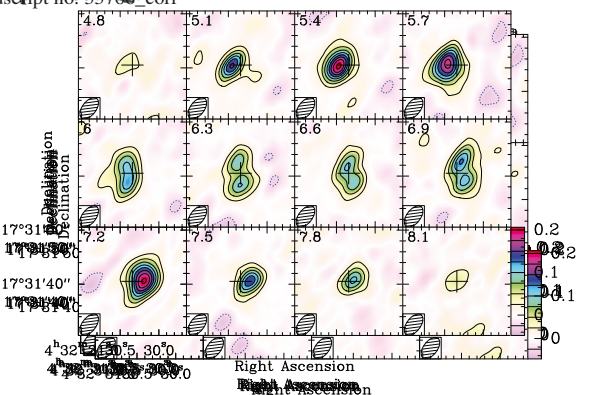

Fig. A.4. Channel maps HCO^+ (1-0) emission. The color scale is in the unit of Jy/beam. The contour spacing is 25 mJy/beam, which corresponds to 2σ or 0.33 K. The beam (4.57″ × 2.53″; PA = 38°) is inserted in the lower corner of each channel map.

Appendix B: Vertical integrated molecule column densities

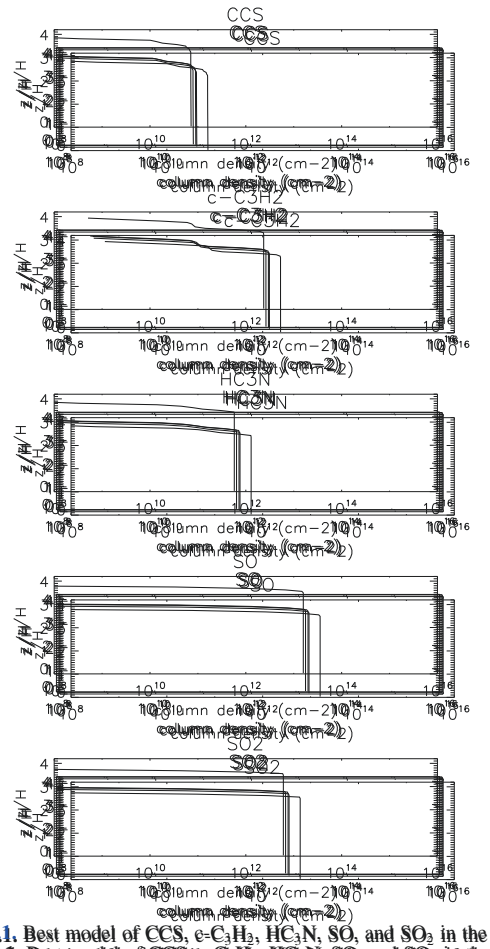

Fig. B.1. Best model of CCS, c-C_3H_2, HC_3N, SO, and SO_2 in the GG Tau disk, derived from Nautilus, using our best knowledge of the GG Tau disk.

Astronomy & Astrophysics manuscript no. ggtau-revised-R1
September 17, 2019
© ESO 2019

GG Tau A: gas properties and dynamics from the cavity to the outer disk

N.T. Phuong[1⋆,2,3], A. Dutrey[1], P. N. Diep[2,3], S. Guilloteau[1], E. Chapillon[1,4], E. Di Folco[1], Y-W. Tang[5], V. Piétu[4], J. Bary[6], T. Beck[7], F. Hersant[1], D.T Hoai[2], J.M. Huré[1], P.T. Nhung[2], A. Pierens[1], and P. Tuan-Anh[2]

[1] Laboratoire d'Astrophysique de Bordeaux, Université de Bordeaux, CNRS, B18N, Allée Geoffroy Saint-Hilaire, F-33615 Pessac; ⋆ thi-phuong.nguyen@u-bordeaux.fr
[2] Department of Astrophysics, Vietnam National Space Center, Vietnam Academy of Science and Techonology, 18 Hoang Quoc Viet, Cau Giay, Hanoi, Vietnam
[3] Graduate University of Science and Technology, Vietnam Academy of Science and Techonology, 18 Hoang Quoc Viet, Cau Giay, Hanoi, Vietnam
[4] IRAM, 300 rue de la piscine, F-38406 Saint Martin d'Hères Cedex, France
[5] Academia Sinica Institute of Astronomy and Astrophysics, PO Box 23-141, Taipei 106, Taiwan
[6] Department of Physics and Astronomy, Colgate University, 13 Oak Drive, Hamilton, New York 13346, USA
[7] Space Telescope Science Institute, 3700 San Martin Drive, Baltimore, Maryland 21218, USA

2019 / 2019

ABSTRACT

Context. GG Tau A is the prototype of the young triple T Tauri star surrounded by a massive and extended Keplerian outer disk. The central cavity is not devoid of gas and dust and at least GG Tau Aa exhibits its own mm disk of gas and dust. Its observed properties make this source an ideal laboratory to investigate planet formation in multiple young solar-type stars.
Aims. We use new ALMA ^{13}CO and C^{18}O(3–2) observations obtained at high angular resolution ($\sim 0.2''$) together with previous CO(3–2) and (6–5) ALMA data and continuum maps at 1.3 and 0.8 mm to determine the gas properties (temperature, density, kinematics) in the outer ring and in the cavity.
Methods. By deprojecting, we study the radial and azimuthal gas distribution and its kinematics. We also apply a new method to improve the deconvolution of the CO data and in particular better quantify the gas emission inside the cavity. Using DiskFit, we finally perform LTE and non-LTE studies in order to determine the excitation conditions and relevant physical parameters inside the ring and in the central cavity.
Results. Residual emission after removing a smooth disk model indicates unresolved structures at our angular resolution, probably in the form of irregular rings or spirals. The outer disk is cold, with a temperature < 20 K beyond 250 au, and dropping quickly ($\propto r^{-1}$). The kinematics of the gas inside the cavity reveals infall motions at about 10% of the Keplerian speed. We derive the amount of gas in the cavity, and find that the brightest clumps, which contain about 10% of this mass, have kinetic temperatures 40 – 80 K, CO column densities of a few 10^{17} cm^{-2}, and H_2 densities around 10^7 cm^{-3}.
Conclusions. Although the gas in the cavity is only a small fraction of the disk mass, the mass accretion rate throughout the cavity is comparable or higher than the stellar accretion rate, and thereby sufficient to sustain the circumstellar disks on a long timescale.

Key words. Stars: circumstellar matter – Protoplanetary disks – Stars: individual (GG Tau A) – Radio-lines: stars

1. Introduction

In more than two decades of studying exoplanets, nearly 4,000 exoplanets have been found. More than 10% of these planets are detected in binary or higher hierarchical systems (Roell et al. 2012). The general picture of planet formation is well agreed that they are formed in a protoplanetary disk surrounding its protostar within a few million years after the collapse phase. However, the detailed formation conditions and mechanisms are still debated.

Welsh et al. (2012) observations with the Kepler space telescope reveal that planets can form and survive in binary systems, in circumbinary or circumstellar orbits. The formation conditions in these systems differ from those around single stars. Theoretical studies of disk evolution predicts that the stars in a T Tauri binary of about 1 Myr should be surrounded by two inner disks, located inside the Roche lobes and an outer ring or disk located outside the outer Lindblad resonances (Artymowicz et al. 1991). For a binary system of low or moderate eccentricity, the stable zone is typically located beyond the 3:1 or 4:1 resonance (Artymowicz & Lubow 1994). The outer radii of these inner disks, as well as the inner radius of the circumbinary (outer) disk, are defined by tidal truncation. At (sub)mm wavelengths, circumbinary disks have been observed in many systems, and in some of these, e.g. L 1551 NE, UY Aur and GG Tau A (Takakuwa et al. 2014; Tang et al. 2014; Dutrey et al. 2014), the circumstellar disk(s) are also detected. Studying the gas and dust properties in these environments is a necessary step to understand the formation of planets in the binary/multiple systems.

The subject of this paper is a detailed study of gas and dust properties of the GG Tau A system. GG Tau A, located in the Taurus-Auriga star forming region consists of a single star GG Tau Aa and a close binary GG Tau Ab1/Ab2 with separations of 35 au and 4.5 au on the plane of the sky respectively (Dutrey et al. 2016; Di Folco et al. 2014). Although the GAIA results

Send offprint requests to: Nguyen Thi Phuong,
e-mail: thi-phuong.nguyen@u-bordeaux.fr

suggest a value of 150 pc (Gaia Collaboration et al. 2016, 2018), we use a distance of 140 pc for comparison with previous works.

The triple star is surrounded by a Keplerian disk that which is innerly tidally truncated at ∼180 au, and comprises a dense gas and dust ring extending from about 180 au up to 260 au and an outer disk extending out to ∼ 800 au (Dutrey et al. 1994). The disk is inclined at about 35°, with a rotation axis at PA 7°, and the Northern side towards us (Guilloteau et al. 1999). The disk is one of the most massive of the Taurus region, ∼0.15 $M_\odot$, ∼10% of the total mass of the stars. A 10% mass ratio should lead to small deviation (about 5%) to the Keplerian law (Huré et al. 2011).

The outer disk is relatively cold with the dust and gas (derived from ^{13}CO analysis) temperatures of 14 K and 20 K at 200 au, respectively (Dutrey et al. 2014; Guilloteau et al. 1999). More information about the triple system can be found in Dutrey et al. (2016) and the references therein.

In this paper, we present a study about the gas properties in the ring, the outer disk and inside the cavity of GG Tau A using sub-mm observations carried out by the ALMA. The paper is organized as follows. Section 2 describes the observations and data reduction. The observation results are presented in Section 3, while the radiative transfer modelling of the outer disk is presented in Section 4. The properties of the cavity (excitation conditions, mass, dynamics) are derived in Section 5. The gas and dust properties in the circumbinary disk and inside the tidal cavity are discussed in Section 6. Section 7 summarizes the main results.

2. Observations and data reduction

Table 1 lists the observational parameters of our data sets, spectral sampling, angular resolution and brightness sensitivity, for all observed molecular lines.

GG Tau A was observed with the ALMA Band 9 during Cycle 0 (2011.0.00059.S) and Band 7 during Cycle 1 (2012.1.00129.S) and Cycle 3 (2015.1.00224.S). Anne Dutrey is the PI of the 3 projects.

Cycle 0 Observations were made on August 13$^{\rm th}$, 2012. The spectral windows covered the ^{12}CO(6–5) line (see Dutrey et al. 2014, for details of the data reduction). This data was processed here with a restoring beam of $0.35'' \times 0.31''$, PA=104°.

Cycle 1 Observations were taken on November 18$^{\rm th}$ and 19$^{\rm th}$, 2013. The spectral windows covered the lines of ^{12}CO(3–2), ^{13}CO(3–2) at high spectral resolution (0.11 km s^{-1}). The details of data reduction are given in Tang et al. (2016). The ^{12}CO(3–2) images were obtained here with a restoring beam of $0.34'' \times 0.28''$, PA=−89° while the ^{13}CO(3–2) data are merged with new data acquired in Cycle 3.

Cycle 3 Observations were carried on September 25$^{\rm th}$ and 30$^{\rm th}$, 2016 with 37 and 38 useful antennas in configuration C40-6. The projected baselines range from 16 m to 3049 m, and the total time on source is 1.4 hours. The spectral set up covered the lines of ^{13}CO(3–2) and C^{18}O(3–2) at 330.588 and 329.330 GHz in two windows, each covering 58.89 MHz bandwidth with a high spectral resolution of 141 kHz (∼ 0.11 km s^{-1}).

The continuum was observed in two separate windows, one centred at 330.15 GHz with 1875 MHz bandwidth and the other centred at 342.00 GHz with 117 MHz bandwidth. Data was calibrated in CASA[1] software (Version 4.7.0). The quasar J0510+1800 is used for phase and bandpass calibration. The absolute amplitude calibration was done using J0522-3627 (flux ∼ 3.84 Jy at 343.5 GHz at the time of observations). The calibrated data was regrided in velocity to the LSR frame using the "cvel" task, and exported through UVFITS format to the GILDAS[2] package for further data processing.

The origin of coordinates at RA=4h 32m 30.3s and DEC=17° 31′ 40″ corresponds to year 2000. GG Tau has significant proper motions: Ducourant et al. (2005) cite [17, −19] mas per year, while Frink et al. (1997) give [11, −28] mas per year. These measurements are however affected by the multiplicity of the star. To re-align our observations, we assumed the continuum ring is centered on the center of mass of the system. We fitted the continuum emission with the sum of a circular Gaussian (for the circumstellar disk around Aa) and an elliptical ring (for the dust ring) in the *uv* plane (Guilloteau et al. 1999; Piétu et al. 2011). The apparent motion of the ring gives a proper motion of [9, −23] mas per year, that we applied to all our data set.

The imaging and deconvolution was done with natural weighting, *hogbom* algorithm and the images are cleaned down to the rms noise level. Channel maps of the observed lines are presented in Appendix A, Figs.A.1-A.2.

3. Results

3.1. Continuum emission

Fig.1 shows the continuum emission at 330 GHz derived from the Cycle 3 data. It reveals emission from the Aa disk and the ring structure detected in previous observations (see Dutrey et al. 2016, and references therein), but the ring is now clearly resolved. The ring is not azimuthally symmetric (after taking into account the limb brightening effect along the major axis), but displays a ∼ 15 − 20% stronger emission at PA ≈ 240° − 260°. The outer edge is clearly shallower than the steep inner edge, confirming that some dust remains beyond the ∼ 260 au outer edge of the ring, as initially mentionned by Dutrey et al. (1994). As in previous studies (e.g. Guilloteau et al. 1999; Piétu et al. 2011), a compact, unresolved emission is detected in the direction of the single star Aa, but no emission originates from the Ab1/Ab2 close binary system.

A detailed study of the continuum emission is beyond the scope of this paper and deferred to subsequent work.

3.2. Images of line emission

Figure 2 shows the integrated intensity and the velocity maps of ^{13}CO(3–2) (left) and C^{18}O(3–2) (right). In these figures, the continuum has been subtracted. The velocity fields suggest Keplerian rotation inside the disk.

The ^{13}CO(3–2) emission extends out to 550 au, while the C^{18}O(3–2) is mostly visible in the dense ring.

3.2.1. Intensity variations

Figure 3 (upper panels) shows the radial profiles of the integrated brightness of the lines and of the peak brightness of the continuum emission, averaged over the entire azimuthal direction, after de-projection to the disk plane. The de-projection has been done assuming a position angle of the minor disk axis of 7° and an inclination of 35° (Dutrey et al. 2014; Phuong et al. 2018b).

[1] https://casa.nrao.edu/

[2] https://www.iram.fr/IRAMFR/GILDAS/

Table 1. List of observations

Spectral line	Frequency (GHz)	Energy level (K)	Channel spacing (km/s)	Beamsize	Noise (K)	ALMA project
^{12}CO J = 6→5	691.473	33.2	0.106	0.35″ × 0.31″, PA=104°	1.8	2011.0.00059.S
^{12}CO J = 3→2	345.795	16.6	0.106	0.34″ × 0.28″, PA=91°	0.7	2012.1.00129.S
^{13}CO J = 3→2	330.588	15.9	0.110	0.22″ × 0.16″, PA=15°	0.7	2012.1.00129.S, 2015.1.00224.S
C^{18}O J = 3→2	329.330	15.8	0.110	0.19″ × 0.14″, PA=19°	1.9	2015.1.00224.S
Continuum	330.15	–	–	0.19″ × 0.14″, PA=190°	0.03	2015.1.00224.S

Notes. Col.3 gives the upper state Energy level.

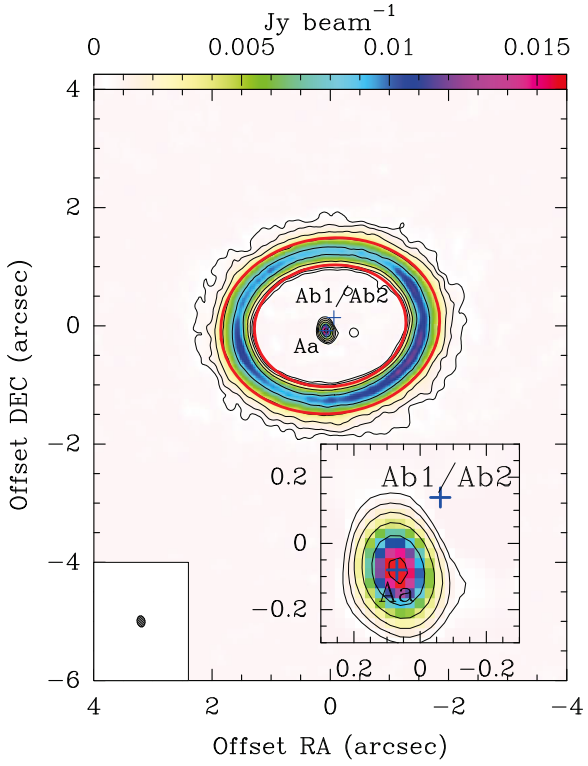

Fig. 1. Continuum image at 330 GHz. The beam size of 0.19″ × 0.14″, PA = 190° is indicated in the lower left corner. The contour levels are 0.5, 1, 2, 4, 8 and 16 mJy beam^{-1}. The noise level is 0.06 mJy beam^{-1}. The red ellipses indicate the inner and outer edges of the dense dust ring at 180 au and 260 au, respectively (e.g. Guilloteau et al. 1999). The positions of the Aa star and Ab close binary are indicate by the crosses. The inset shows an enlarged view of the Aa/Ab surroundings.

See also Phuong et al. (2018b) for the detail information of deprojection description.

The ^{12}C^{16}O emission covers a broad region around the central binary, $r \lesssim 6''$ (800 au), peaking at the centre. Some of the differences between the three transitions of CO may result from calibration effects and different *uv* coverage. In particular, short spacings are missing in the CO(6–5) transition data because of its high frequency, making it less sensitive to extended structures.

Figure 3 (lower panels) displays the azimuthal dependence (in the disk plane) of the peak brightness and velocity integrated brightness in the ring ($1.2'' \leq r \leq 2''$) for CO, ^{13}CO, C^{18}O and the 0.85 mm continuum emissions. The azimuth ω in the disk mid-plane is measured counterclockwise from the minor axis (north). The significant enhancement in the south-eastern quadrant for ^{12}C^{16}O corresponds to the "hot spot" discovered by Dutrey et al. (2014), that may reveal a possible planet in formation (labelled "hp" for "hypothetical planet" in the figure). It is much less visible in the other CO isotopologues.

3.2.2. CO gas kinematics in the outer disk

For a thin disk, the line of sight velocity is given by $V_z = \sin i(V_{rot} \sin\omega + V_{fall} \cos\omega)$ where i is the disk inclination, V_{rot} the rotation velocity and V_{fall} the infall velocity, and ω is the azimuth in the disk plane. We can neglect the infall motions, as Phuong et al. (2018b) studies at angular resolution of $\sim 0.35''$ have placed an upper limit of 9% on it with respect to the rotation. We used the intensity weighted images of the line of sight velocity V_z shown in Fig.2 and for each pixel calculate $V_z(\sin i \sin\omega)^{-1}$. We then azimutally averaged these values for all pixels at the same radius (using a 0.15″ radial binning) such that $|\sin\omega|$ to > 0.7 (i.e. avoiding pixels around the minor axis) to derive V_{rot}.

Figure 4 shows the dependence of $\langle V_{rot}\,(r/1'')^{1/2}\rangle$ on r, which would be constant for the three CO isotopologues if the rotation is Keplerian.

There is a good overall agreement between the three isotopes, showing that the outer ring and disk are in Keplerian rotation beyond about 180 au. A constant fit to these histograms gives $V_{rot} \approx 2.94$ km s^{-1}, with a standard deviation (σ) of 0.14 km s^{-1} of the residuals from the mean for CO, 2.98 km s^{-1} (σ = 0.04 km s^{-1}) for ^{13}CO and 2.81 km s^{-1} (σ = 0.07 km s^{-1}) for C^{18}O, at $\approx 1.0''$ (the integration ranges are illustrated in Fig.4).

The formal errors on these mean values will be 2 to 3 times smaller, depending on the number of independent points, which is not a simple value given our averaging method. However, the CO data show deviations from the mean which are not random, since they occur on a radial scale of $\approx 0.8''$, more than twice the resolution. We thus conservatively use the standard deviation as the error on the mean. Using the 3 independent measurements from CO, ^{13}CO and C^{18}O, we derive a mean weighted value of 2.94 ± 0.03 km s^{-1} for the Keplerian rotation speed at 1″, i.e. 3.48 ± 0.04 km s^{-1} at 100 au, in agreement with previous, less precise determinations (e.g. Dutrey et al. (2014) found 3.4 ± 0.1 km s^{-1}). Taking into account the uncertainty on the inclination, ±2°, this corresponds to a total stellar mass of 1.36 ± 0.07 M$_\odot$.

The apparent lower than Keplerian velocities at radii smaller than about 0.8″ will be discussed in Sec.6.3.

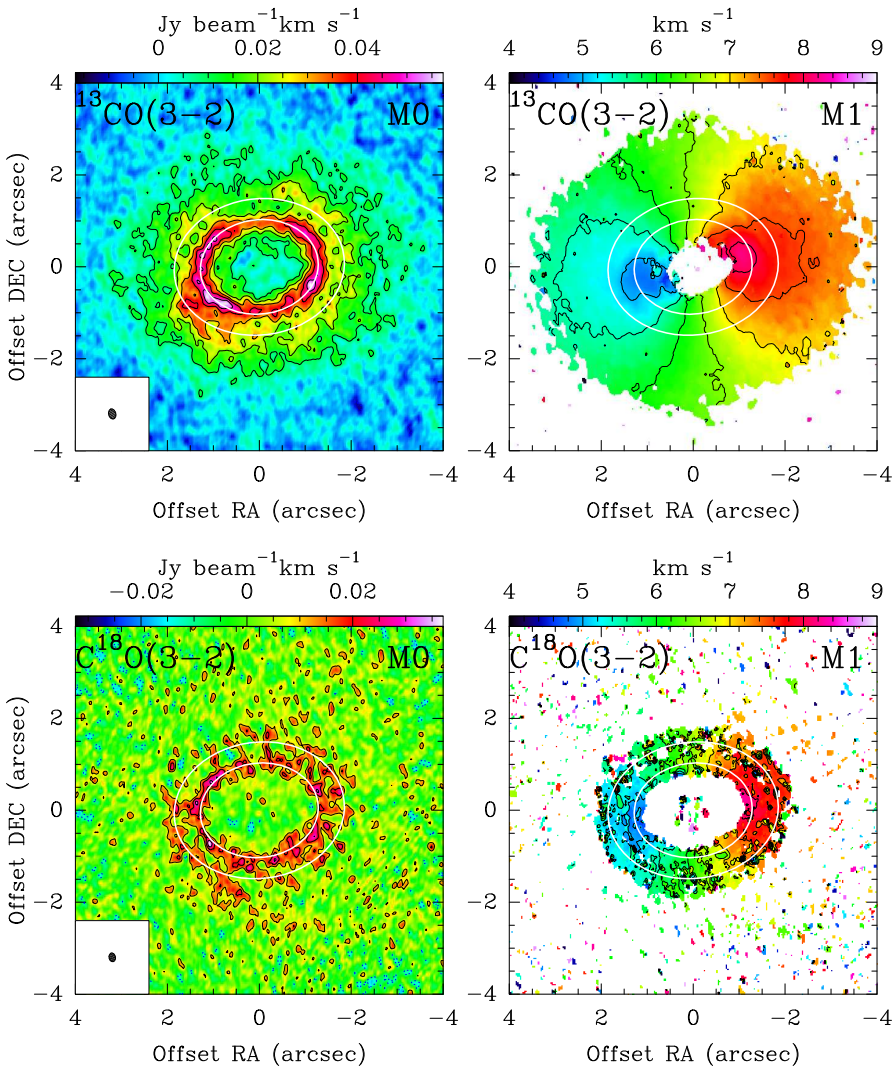

Fig. 2. *Upper:* ^{13}CO(3–2) integrated intensity map (left, contour spacing 0.01 Jy/beam km s^{-1} (3 σ) with zero level omitted) and velocity map (right). *Lower:* C^{18}O(3–2) integrated intensity map (left, contour spacing 0.01 Jy/beam km s^{-1}, 2 σ) and velocity map (right). The beams are indicated at lower left corner in each intensity map. The contour level spacing in velocity maps is 0.5 km s^{-1}. The continuum has been subtracted. The white ellipses indicate the inner and outer edges of the dust ring.

4. Disk Modelling

We use the DiskFit tool (Piétu et al. 2007) to derive the bulk properties of the ring and outer disk. The disk model is that of a flared disk with piece-wise power laws for the temperatures and surface densities. We assume sharp inner and outer radii. The temperature is vertically isothermal, and the vertical density profile is a Gaussian, $n(r,z) = n_0(r)\exp(-(z/H(r))^2)$, with a scale height following a simple power law $H(r) = h_0(r/R_0)$. For spectral lines, we assume that the velocity field is Keplerian, $v(r) = V_0(r/R_0)^{-0.5}$, and use a constant local linewidth δV. The lines are assumed to be at LTE: the derived temperatures thus indicate excitation temperatures. The emission from the disk is computed using a ray-tracing method. The difference between the predicted model visibilities and the observed ones is minimized using a Levenberg–Marquardt method, and the error bars are derived from the covariance matrix.

A more detailed description of the DiskFit tool and our adopted fitting method is given in Appendix B. The fit parameters are summarized in Table B.1.

4.1. Continuum fit

The CO emission being at least partially optically thick, we cannot simply separate the contribution of CO and continuum (Weaver et al. 2018). To determine the continuum properties, we fitted the continuum using the broad-band, line-free, spectral window data. We followed the procedure described in Dutrey et al. (2014), who derived dust properties using 1.3 mm and 0.45 mm continuum. We first subtracted a Gaussian source

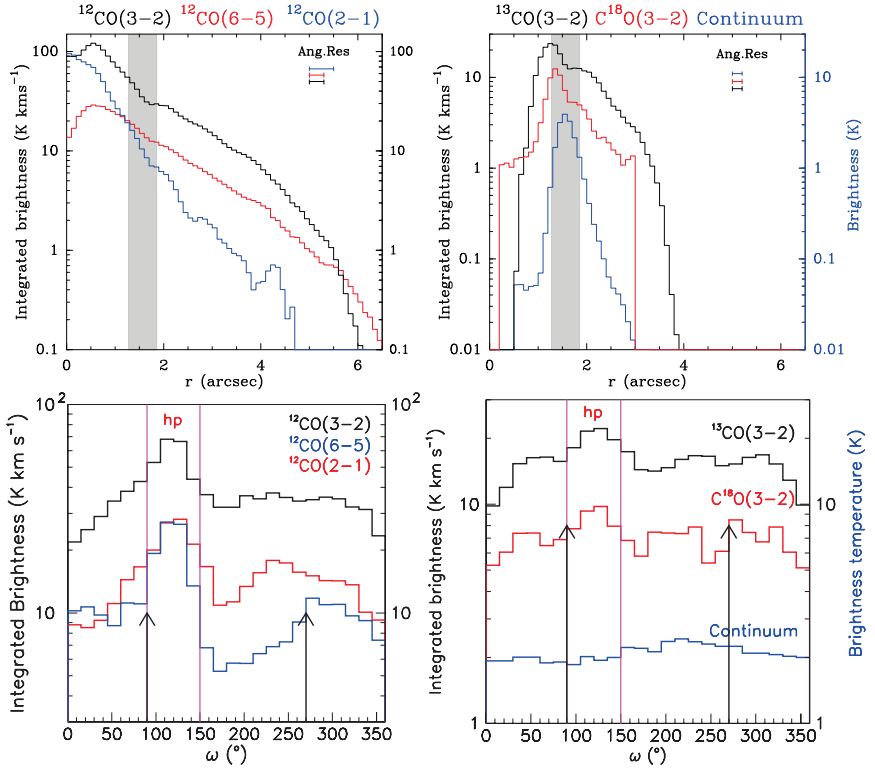

Fig. 3. *Upper:* The radial dependence of the integrated brightness temperature (for lines) and brightness temperature (for continuum emission) in the disk plane. The horizontal sticks indicate the angular resolutions. *Lower:* The azimuthal dependence of the same quantities averaged over the ring of $1.2'' < r < 2.0''$. The left panels show the plot of the three ^{12}CO emissions (J=6–5, 3–2 and 2–1) (see Dutrey et al. 2014; Tang et al. 2016, for the intensity maps of these emissions), the right panels show the less abundant CO isotopologues (J=3–2) emissions. The grey region delineates the dust ring in the upper panels. In the lower panels, black arrows show the location of the limb brightening peaks and the magenta lines show the hot spot location.

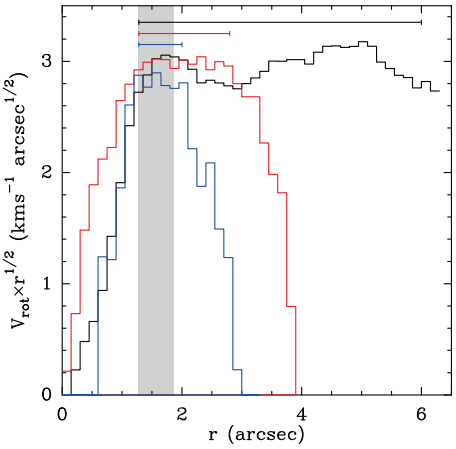

Fig. 4. Dependence on r of $V_{rot} \times r^{1/2}$ (weighted by the brightness and averaged in bins of 0.15″) of ^{12}CO(3–2) (black), ^{13}CO(3–2) (red) and C^{18}O(3–2) (blue) emissions. The horizontal bars indicate over which radius range the mean value is computed for each transition. The grey shaded area indicates the dense dust ring boundaries.

model of the emission from the circumstellar disk of Aa. The emission from the ring was then fit by a simple power law distribution for the surface density and temperature, with sharp inner and outer edges (see also Appendix B), assuming a spatially constant dust absorption coefficient that scales with frequency ν as ν^{β}. We simultaneously fit the 1.3 and 0.8 mm data (the 1.3 mm dust emission is from Dutrey et al. 2014). The results of the continuum fit are given in Table 3.

Table 2. System geometric and kinematic parameters

Parameter	Value	
(x_0, y_0)	(0,0)	Center of dust ring
$PA(^\circ)$	7	PA of disk rotation axis
$i(^\circ)$	−35	Inclination
$V_{\rm LSR}$	6.40	Systemic velocity
V_0 (km s^{-1})	3.37	Keplerian Rotation velocity at 100 au
dV (km s^{-1})	0.3	Local line width

Notes. Values derived from previous papers and verified with these new CO isotopologues data.

Table 3. Dust ring parameters

Parameter	Value/Law	
Inner radius (au)	193	fixed
Outer radius (au)	285	fixed
Abs. Coefficient κ_ν (cm$^2/g$)	$0.02 \times (\nu/230\mathrm{GHz})^{+1}$	fixed
Temperature (K)	$14 \times (r/200\,\mathrm{au})^{-1}$	fixed
Surface density (cm^{-2})	$5.6\ 10^{24} \times (r/200\,\mathrm{au})^{-1.4}$	Fitted

Notes. Fixed values are taken from Dutrey et al. (2014).

4.2. CO isotopologues

We analyze the CO isotopologue data without removing the continuum. The parameters specified in Tables 2 - 3 are used as fixed input parameters for our modelling.

While the outer disk is well represented by a Keplerian disk, the emission from the cavity does not follow such a simple model. Yet it contributes to a significant fraction of the total emission from CO. However, since the fit is made by minimizing in the visibility (Fourier) plane, we cannot separate the cavity from the outer disk contributions in this process.

Thus, to avoid biasing our results for the ring and disk parameters, we adopted a specific strategy. We first subtracted the Clean components located inside the cavity (up to a radius of 160 au) from the original *uv* tables (this also removes the continumum from Aa). The residual *uv* tables are then analyzed using an innerly truncated Keplerian disk model as described in details in Appendix B.

Since the radial profiles of the emission from CO and ^{13}CO are not well represented by a power law (see Fig.3, and Fig.3 of Tang et al. 2016), our disk model assumes piece-wise, continuous power laws (linear in log-log space) for the surface density and temperature. We used knots at 160, 200, 260, 300 and 400 au. The knots are chosen to reflect both slope changing in the radial profile of the line emissions and the sharp edges of the dust ring based on our previous studies (Dutrey et al. 1994; Guilloteau et al. 1999), and to allow a good estimate for the properties of the bulk of the gas in the ring and outer disk.

The following strategy has been adopted to fit in parallel the ^{12}CO and ^{13}CO data. In a first step, we determine the temperature by fitting the ^{12}CO line. The surface density of CO is not a critical value here: as CO is largely optically thick, we just need to use a high enough CO surface density to ensure this. We then used this temperature profile to fit the ^{13}CO data and determine the ^{13}CO surface density, since this line is partially optically thin. The derived surface density is then multiplied by the isotopic ratio ^{12}CO/^{13}CO (70, Milam et al. 2005) to specify the CO surface density to iterate on the temperature determination using the ^{12}CO data. The process converges quickly (in 2 iterations).

Our method makes the underlying assumption that the ^{12}CO and ^{13}CO layers are at the same temperature. This hypothesis is consistent with the results from Tang et al. (2016), who found that the vertical temperature gradient around 200−400 au should be small to reproduce the observed ^{12}CO/^{13}CO line ratio.

A fixed inner radius of 169 au provided a good compromise to represent all molecular distributions. This radius is here only to obtain a good model for the ring and outer disk: it should not be over-interpreted as the physical edge of the cavity. We also determined independently the outer radii for each CO isotopologue, and verified the best fit value for the inclination and systemic velocity. The small difference between our adopted Keplerian rotation law and that suggested by the analysis in Sec.3.2.2 has negligible impact on the fitted parameters. For the C^{18}O, we used only 4 knots to derive the surface density profile.

With this process, we find a reasonable model of the ring and outer disk in all CO isotopologues. Figure 5 shows the residuals from the original *uv* data after removal of the best fit outer disk models and of Aa continuum source. As expected, most of the left-over emission is coming from the cavity, but some azimuthal asymmetries are still visible in the dense ring. The best fit results and formal errors are summarized in Table 4. Since significant deviations from the best fit model do exist (e.g. azimuthal variations), the results must be interpreted with caution. The formal errors underestimate the uncertainties on the physical parameters. We thus also quote a confidence interval for the temperatures in Table 4, based on the dispersion of values found during our minimization studies: surface densities are typically uncertain by 20 − 30%, but the steep decrease in temperature between 200 and 300 au, and then to 400 au and beyond is a robust result. The surface density profile around 180 − 200 au is poorly constrained, due to the removal of emission inside 160 au, and the insufficient angular resolution at this level. However, the variations in the fitted surface densities between 169 au (the inner truncation radius) and 180 au suggests a very dense inner edge.

In spite of its limitations, our approach leads to some robust conclusions. Beyond a radius of about 200 au, we confirm that the CO gas is cold with temperatures dropping from about 27 K at 180 au to 11 K at 400 au (see Fig.6).

We note that the scale height of 24 au at 200 au which was found to represent well the CO isotopologue emissions (see Appendix B) corresponds to a kinetic temperature of 15 K under the hydrostatic equilibrium hypothesis. This is in reasonable agreement with the dust temperature derived by Dutrey et al. (2014).

The outer radius of the disk is 370 au in C^{18}O, about 550 au in ^{13}CO and greater than 600 au in ^{12}CO. The last two radii are less constrained than that of C^{18}O because the temperature drops steeply with radius. The primary beam attenuation does not affect significantly these results.

Table 4. Temperature derived from ^{12}CO(3–2) and surface density from ^{13}CO(3–2) and C^{18}O(3–2)

(1)	(2)	(3)	(4)	(5)	(6)	(7))
r	T_k			^{13}CO	C^{18}O	Ratio
(au)	(K)	(K)	(K)	10^{15} cm^{-2}		
160	27.2	0.17	[26,28]	39 ± 2	6.7 ± 0.6	5.8 ± 0.8
200	27.4	0.11	[25,28]	18 ± 1	5.5 ± 0.4	3.3 ± 0.4
260	19.7	0.07	[19,21]	9.7 ± 0.3	2.1 ± 0.1	4.6 ± 0.4
300	18.0	0.03	[17,19]	6.8 ± 0.1	0.39 ± 0.02	17 ± 1
400	10.7	0.02	[10,11]	2.8 ± 0.03	–	–

Notes. Nominal model fit after removal of Clean Components for $r <$ 160 au. (1) Knot radius. (2) Temperature derived from ^{12}CO(3–2) and (3) its formal error from the fit and (4) estimated confidence interval from the minimizations. (5-6) molecular surface density, (7) ^{13}CO/C^{18}O surface density ratio.

5. Analysis of the gas inside the cavity

With a good first order model for the spectral line emission in the ring and outer disk (i.e. beyond 169 au), we can now find a better representation of the emission coming from the gas in the cavity. For this purpose, we subtract our best ring+disk model (presented in Sec. 4) from the original visibilities. CLEANed images

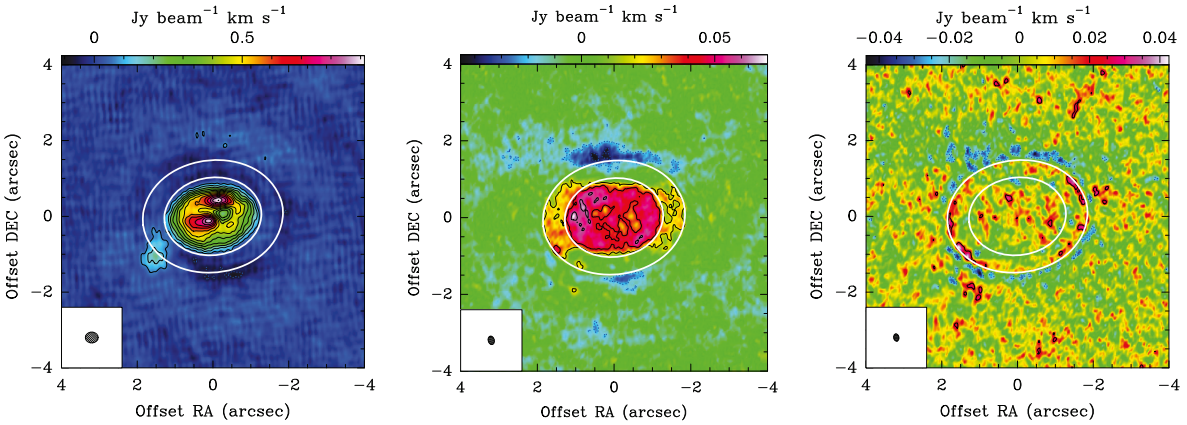

Fig. 5. The integrated intensity of (residual) emissions after subtracting the best ring+disk models. *Left:* ^{12}CO(3–2). The restoring beam of 0.34″ × 0.28″, PA = −89° is indicated in the lower left corner. *Middle:* ^{13}CO(3–2). The restoring beam is 0.22″ × 0.16″, PA = 16°. *Right:* C^{18}O(3–2). The restoring beam is 0.19″ × 0.14″, PA = −167°. The contour level is 0.07 Jy beam^{-1} (5σ) for ^{12}CO(3–2) map and ∼0.2 Jy beam^{-1} (3σ) for ^{13}CO(3–2) and C^{18}O(3–2) maps, the zero level is omitted. The ellipses show the inner and outer edges of the dust ring at 180 and 260 au.

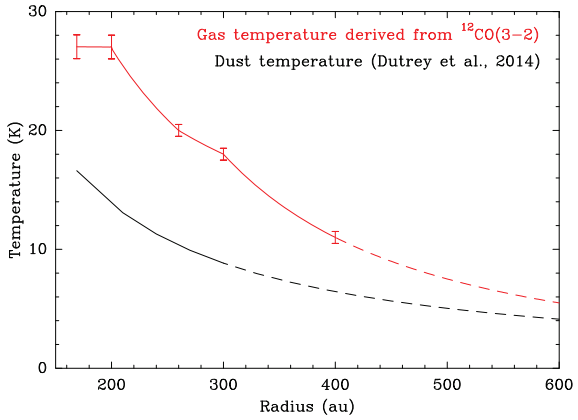

Fig. 6. Radial dependence of CO gas (red) and dust (black) temperature. The gas temperature is derived from ^{12}CO(3–2) analysis. Beyond 400 au, CO temperature is extrapolated from the fitted law in the range of 300−400 au. The dust temperature is taken from Dutrey et al. (2014). Beyond a radius of 285 au, the dust temperature corresponds to an extrapolation.

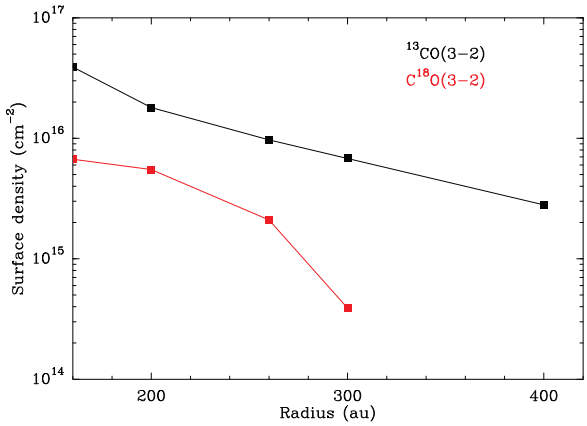

Fig. 7. Comparison of the surface densities from the LTE analysis.

of this residual emission, which mostly comes from the cavity, were produced for the three CO isotopologues (^{12}CO, ^{13}CO and C^{18}O J=3–2). Figure 5 presents the residual maps obtained. In this section, we study the properties of the gas inside the cavity using these residual maps.

5.1. The dynamics inside the cavity

To study the gas dynamics inside the cavity, we plot in Fig.8 the azimuthal dependence of $\langle V_z/\sin(i)\rangle$ in 5 rings of width 0.25″ each of ^{12}CO(3–2) (black), ^{13}CO(3–2) (red) and C^{18}O(3–2) (blue) emissions in the region $0 < r < 1.25''$. Azimuth and radius are defined in the disk plane, i.e. deprojected from the disk inclination. In each ring, we fitted the azimuthal dependency of $\langle V_z/\sin(i)\rangle$ of the ^{13}CO with a sine function $V_z/\sin(i) = V_{z0}\sin\omega$. This sine function is presented as the smooth red curve and the amplitude V_{z0} is mentioned on top of each panel. The good fit for the ^{13}CO(3–2) indicates that the gas inside the cavity is dominated by rotation. The amplitude is however smaller than that of the Keplerian rotation, but this is most likely a result of the finite resolution of the observations combined with the very inhomogeneous brightness distribution. The dynamics of the three lines are in very good agreement for $1'' < r < 1.25''$, but differ in the region with $r < 1''$. In particular, the ^{12}CO(3–2) departs from the ^{13}CO(3–2) in the region $0.25'' < r < 1''$ (boxes (b,c,d) in Fig.8) because of the bright localized emission regions seen in CO.

However, a better fit is obtained by taking into account the contribution of a radial (from the disk center) velocity $V_z/\sin(i) = V_{fall}\cos\omega + V_{rot}\sin\omega$ as shown in the lower right panel of Fig.8. The results are presented in Table 5: $V_{fall} > 0$ corresponds to infall motions. Table 5 thus indicates that the gas in the cavity is moving inwards to the center at velocities about 0.3 km s^{-1}, which is about 10 − 15% of the Keplerian velocity. Since infall and rotation motions have different radial and azimuthal dependencies, the finite beamsize has a different impact on the infall velocity than on the apparent rotation velocity.

Table 5. Infall and rotation the gas inside the cavity.

Ring	V_{Kep} ($\mathrm{km\,s^{-1}}$)	V_{rot} ($\mathrm{km\,s^{-1}}$)	V_{fall} ($\mathrm{km\,s^{-1}}$)	$\frac{V_{fall}}{V_{rot}}$	$\frac{V_{fall}}{V_{Kep}}$
(a)	-	0.34	0.04	12%	-
(b)	-	0.79	0.21	27%	-
(c)	3.63	0.98	0.30	31%	8%
(d)	3.07	1.08	0.38	28%	12%
(e)	2.71	1.27	0.48	38%	18%

Notes. The rings (a)...(e) are defined in the Figure 8

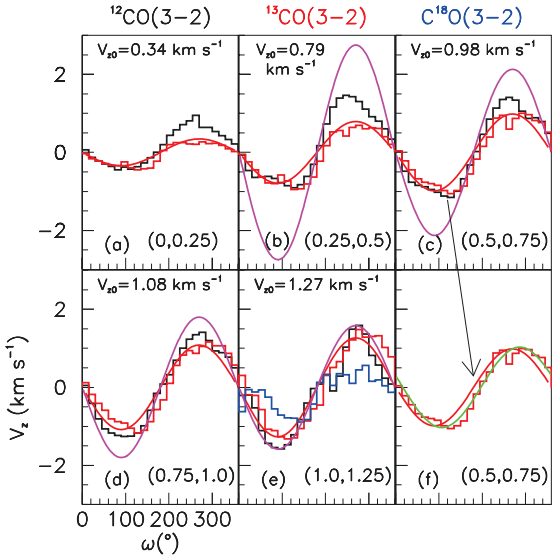

Fig. 8. Dependence of $\langle V_z \rangle$ ($\mathrm{km\,s^{-1}}$) on the azimuth ω (°) in the cavity. ^{12}CO (3–2) is in black, ^{13}CO (3–2) in red and C^{18}O (3–2) in blue. The red curve is a fit of a sine function to the ^{13}CO (3–2) data (see text). We use a blanking if there is no good data available (no emission) in the ring. The magenta curves show the expected Keplerian velocity around a single star of 1.36 $M_\odot$. The green curve in the panel (f) shows the best fit velocity curve when infall motions are allowed, superimposed on the ^{13}CO velocity.

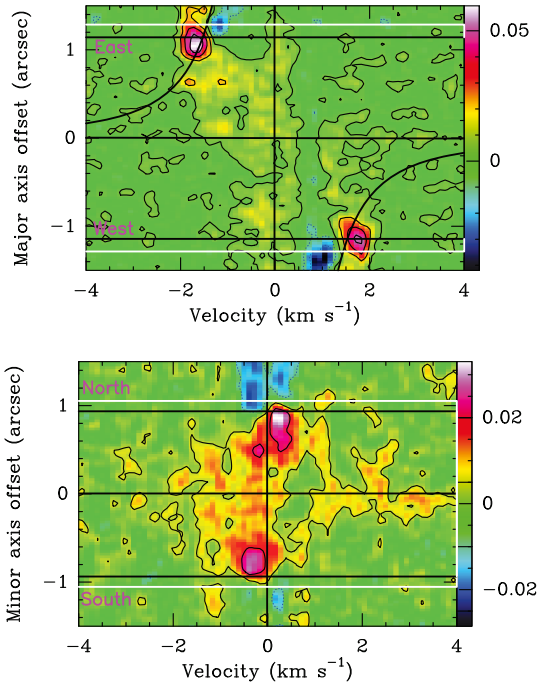

Fig. 9. Position-velocity diagrams of the ^{13}CO(3–2) emission in the cavity along the major axis (upper panel) and minor axis (lower panel). The black curves show the expected Keplerian velocity around a single star of 1.36 $M_\odot$. Contour levels are spaced by 10 mJy/beam, with the zero contour omitted. The white lines indicate the position of the dust ring inner edge (180 au) and the black ones that of the gas disk inner radius (169 au). Note that the data has been rotated by 7° to align with the disk axis, so that cardinal directions are approximate.

A direct illustration of the infall motions is given in Fig.9 that shows position-velocity (PV) diagrams of the ^{13}CO(3–2) emission in the cavity along the major and minor axis of the disk. The PV diagram along the major axis shows the Keplerian rotation until the inner edge of the ^{13}CO(3–2) emission, at $\sim$ 1.1″ (160 au). The PV diagram along the minor axis shows an asymmetry between the north and the south consistent with the derived infall motion of $\sim$ 0.3−0.4 $\mathrm{km\,s^{-1}}$ at the same (deprojected) radius (the PV diagrams being presented in the sky plane).

5.2. Gas properties

Using the (residual) ^{12}CO(3–2) data and the ^{12}CO(6–5) data from Dutrey et al. (2014), for which the emission outside of the cavity is negligible, smoothed to a similar angular resolution (0.35″ × 0.30″), we identify 2 dominant features that we arbitrarily separate in 5 bright "blobs" to simplify the analysis and the 6th one connecting blobs 2 and 4, brighter in CO(6–5) (see Fig.10). The blobs are likely unresolved at this spatial resolution. Integrated line flux and line widths were derived for each blob by fitting a Gaussian into the line profile. Velocities and line width derived from the CO (3–2) were used to determine the ^{13}CO and C^{18}O line intensities.

To determine the physical conditions, we use a non-LTE escape probability radiative transfer code implemented in DiskFit. It uses escape probability formulation of Elitzur (1992), $\beta = [1 - \exp(-\tau)]/\tau$, a single collision partner, H_2, and Gaussian line profiles. Non-LTE best fit solutions were found by sampling the χ^2 surface defined as the quadratic sum of the difference between the measured brightness temperatures and the computed values of the CO (6–5), CO (3–2), ^{13}CO (3–2) and C^{18}O (3–2) transitions, for ranges of H_2 density of $10^2 - 10^{10}\,\mathrm{cm^{-3}}$, ^{12}CO column density of $10^{13} - 10^{19}\,\mathrm{cm^{-2}}$, and kinetic temperature of 3 – 100 K using 50 steps of each parameter. We assume the standard isotopic ratios ^{12}C/^{13}C= 70 (Milam et al. 2005) and ^{16}O/^{18}O= 550 (Wilson 1999) for the relative abundances of the isotopologues. ^{12}CO constrain the temperature, and ^{13}CO the column densities. Owing to its faintness, the C^{18}O(3–2) data bring little information. Given the low critical densities of the observed transitions, we only obtain a lower limit to the density. The blob parameters are presented in Table 6.

Typically, we find high CO column densities around a few $\sim 10^{17}\,\mathrm{cm^{-2}}$ and temperatures in the range 40–80 K, with a lower limit on the density of the order of $10^5\,\mathrm{cm^{-3}}$. For the blob 6, the faintest region we analyze with this method, the problem is marginally degenerate, with two separate solutions: i) a high column density ($\sim 10^{17}\,\mathrm{cm^{-2}}$), low temperature ($\sim$ 20 K) and (ii) a low column density ($\sim 10^{15}\,\mathrm{cm^{-2}}$) and high temperature

Table 6. Brighter blobs properties

Blob	Position	Radius	dv	H_2 density	N	T_{kin}	Mass (nLTE)	Mass (^{12}CO Flux)	Mass (^{13}CO Flux)
	(″,″)	(″)	(km s^{-1})	(cm^{-3})	(cm^{-2})	(K)	(M$_\odot$)	(M$_\odot$)	(M$_\odot$)
(1)	(2)	(3)	(4)	(5)	(6)	(7)	(8)	(9)	(10)
1	(0.27, 0.36)	0.45	2.5	$> 5.0\,10^4$	$(2.1^{+0.6}_{-0.7})\,10^{17}$	40 ± 5	$(2.1^{+0.6}_{-0.7})\,10^{-6}$	$(3.1 \pm 0.1)\,10^{-7}$	$(1.9 \pm 0.1)\,10^{-6}$
2	(−0.09, 0.36)	0.37	2.7	$> 1.0\,10^4$	$(1.4^{+0.7}_{-0.5})\,10^{17}$	50 ± 5	$(1.3^{+0.7}_{-0.5})\,10^{-6}$	$(4.5 \pm 0.1)\,10^{-7}$	$(2.3 \pm 0.1)\,10^{-6}$
3	(−0.45, 0.36)	0.58	2.1	$> 5.0\,10^4$	$(2.6^{+1.0}_{-1.00})\,10^{17}$	40 ± 5	$(2.5^{+1.0}_{-1.0})\,10^{-6}$	$(3.2 \pm 0.2)\,10^{-7}$	$(1.1 \pm 0.1)\,10^{-6}$
4	(0.09, −0.15)	0.17	6.2	$> 1.0\,10^5$	$(6.3^{+2.1}_{-1.4})\,10^{16}$	80 ± 10	$(6.3^{+2.1}_{-1.4})\,10^{-7}$	$(6.9 \pm 0.1)\,10^{-7}$	$(2.5 \pm 0.2)\,10^{-6}$
5	(0.45, −0.18)	0.48	2.5	$> 1.0\,10^4$	$(2.2^{+1.0}_{-0.8})\,10^{17}$	40 ± 5	$(2.2^{+1.0}_{-0.8})\,10^{-6}$	$(3.9 \pm 0.1)\,10^{-7}$	$(1.7 \pm 0.1)\,10^{-6}$
6	(0, 0.1)	0.12	6.1	$> 1.0\,10^4$	$(4.0^{+1.4}_{-1.4})\,10^{16}$	80 ± 10	$(4.0^{+1.4}_{-1.4})\,10^{-7}$	$(3.4 \pm 0.1)\,10^{-7}$	$(2.8 \pm 0.1)\,10^{-6}$

Notes. (1) Blob, (2) Offset from ring center, (3) Distance from center, (4) line-width (km s^{-1}), (5) H_2 density, (6) CO column density, (7) kinetic temperature, (8) H_2 mass derived from the CO column density (nLTE analysis), (9) H_2 mass derived from the ^{12}CO flux and (10) H_2 mass derived from the ^{13}CO flux.

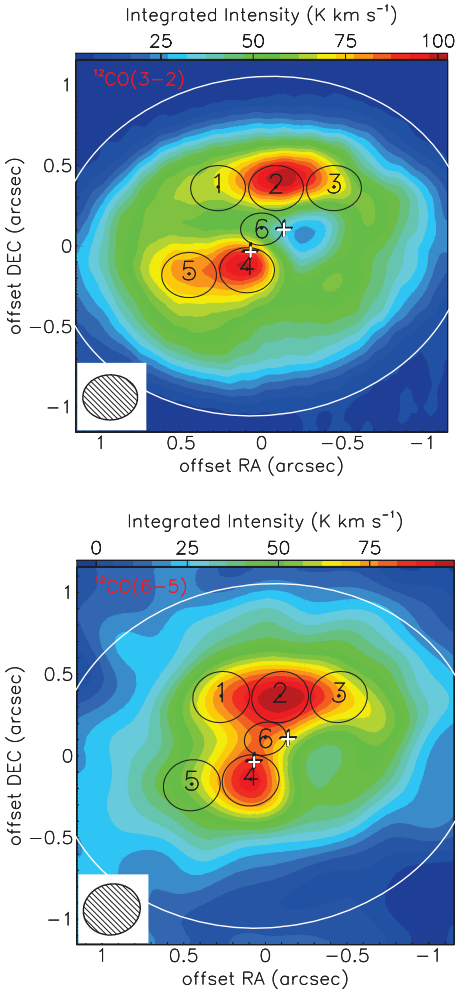

Fig. 10. Integrated intensity map of ^{12}CO(3–2) *(upper) (this work and Tang et al. 2016)* and ^{12}CO(6–5) *(lower)* (from Dutrey et al. 2014) and blobs position and sizes. The crosses mark the position of Aa and Ab1+Ab2, and the ellipse is the inner edge of the dust ring (180 au).

(> 80 K). Given that this region is between Aa and Ab, the second solution (which is also that of lowest χ^2) is more probable.

5.3. Gas masses

The lower limit on the density obtained from the non-LTE analysis being insufficient to provide any useful constraint on the blob masses, we use another method to do so. We estimate the blob mass from the derived molecular column density and blob size, assuming a molecular abundance relative to H_2, as described below.

In the same way, we also derive the total amount of gas in the cavity, from the integrated flux of the optically thin lines of the ^{13}CO(3–2) and C^{18}O(3–2). For this purpose, we integrate the emission out to a radius of 160 au.

In the optically thin approximation, the integrated flux and the column density of the upper level of a given transition are related by:

$$W = \frac{g_u}{\gamma_u} N_u \tag{1}$$

where, $W = \int T_b\, dv$ is the integrated brightness inside the cavity ($R < 160$ au), $g_u = 2J + 1$ is the statistics weight and N_u is the column density of the upper level, $\gamma_u = \frac{hc^3 A_{ul}}{8\pi k_B \nu^2}$ (the Einstein coefficient A_{ul} is taken from Lamda database[3]). Guided by the results of the non-LTE analysis, we assume the gas temperature T is 40 K everywhere inside the cavity and calculate the total column density $N_{\rm total}$ of a given molecule:

$$N_{\rm total} = \frac{N_u}{Z} \exp\left(\frac{-E_u}{k_B T}\right) \tag{2}$$

where, Z is the partition function and E_u is the energy of the upper state. The ^{12}CO(3–2) emission, being partially optically thick, will yield a lower limit.

CO abundance was taken from those measured in TMC-1 by Ohishi et al. (1992), and we assumed a standard isotopic ratio for the isotopologues (^{13}CO and C^{18}O). Results are in Cols 9-10 of Table 6 for the blobs, and Table 7 summarizes the results for the cavity.

The H_2 mass derived from ^{13}CO(3–2) and C^{18}O(3–2) are similar which confirms that these lines are optically thin while the ^{12}CO emission is optically thick.

[3] https://home.strw.leidenuniv.nl/ moldata/

Table 7. Mass of gas inside the cavity

Location	Integrated Flux (Jy km s^{-1})	H_2 mass ($M_\odot$)	Abundance (w.r.t H_2)
Cavity (^{12}CO)	11.4 ± 0.8	$6.1 \pm 0.4 \times 10^{-6}$	8.0×10^{-5}
Cavity (^{13}CO)	3.8 ± 0.1	$1.6 \pm 0.1 \times 10^{-4}$	†
Cavity (C^{18}O)	0.5 ± 0.2	$1.6 \pm 0.8 \times 10^{-4}$	‡

Notes. † X[^{13}CO]=X[^{12}CO]/70 and ‡ X[C^{18}O]=X[^{12}CO]/550 (see text).

6. Discussion

Fig.11 is a schematic layout summarizing the properties of the GG Tau A system. Numbers quoted in this schematic view are discussed in the following section.

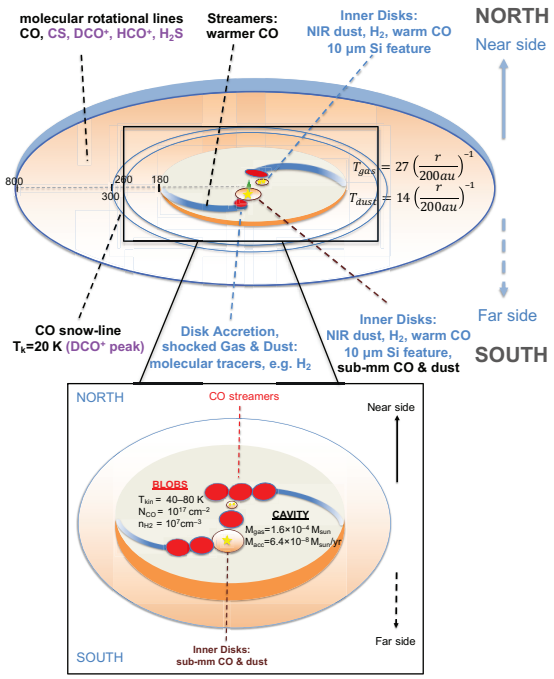

Fig. 11. A schematic view of the GG Tau system. Colored text indicates results obtained from other publications, in particular magenta is from Phuong et al. (2018a); see Dutrey et al. (2016) for a review of other references. Black text are for results from this work.

6.1. Temperature distribution in the outer disk

Our analysis confirms that most of the outer disk of GG Tau A is very cold (see Fig.6). The gas temperature derived here agrees with the value found by Guilloteau et al. (1999) from ^{13}CO only, 20 K at 300 au. The agreement between values derived independently from ^{12}CO and ^{13}CO supports our assumption of a limited vertical temperature gradient in the CO layer, as already mentioned by Tang et al. (2016). A power law fit to this temperature profile gives a radial dependency of $r^{-1} - r^{-1.3}$, confirming the previous exponent value of -1 derived by Guilloteau et al. (1999). Dutrey et al. (2014) also found a similar exponent for the dust temperature from the analysis of dust images between 3 and 0.45 mm using a simple power law. Since this study is based on multi-wavelength continuum resolved observations from 3 up to 0.45 mm, the derived dust temperature is characteristic of the large grains which have likely settled down around the mid-plane. It is then reasonable to consider that this temperature traces the mid-plane dust temperature. This steep radial slope of the temperatures is most likely due to the stellar light being blocked by the inner dense ring, while the rest of the disk remains then in its shadow.

6.2. Gas distribution and smoothness of the outer ring

Global properties Our canonical (smooth) model (Sec.4.2) shows that the ratio of the ^{13}CO and C^{18}O column densities beyond $r > 300$ au is of the order of 17 (see Table 4) above the standard isotopic ratio of 7, suggesting selective photodissociation (e.g. van Dishoeck & Black 1988), but also confirming that in the outer disk the emissions are optically thin.

On the contrary, inside the densest part of the ring (200 – 260 au), the measured ratio is of the order of 3 – 5. Chemical effects such as selective photodissociation and fractionation that occurs through isotope exchange between CO and C^+ (Watson et al. 1976) and enhances ^{13}CO at temperatures about 20-30 K, would both tend to enhance this ratio above the double isotopic (^{16}O/^{18}O)/(^{12}C/^{13}C) ratio. Thus the simplest explanation for a low value is partially optically thick ^{13}CO(3–2) emission. However, our model should account for the opacity if the disk was as smooth as assumed. Hence, we conclude that the GG Tau disk and ring deviates significantly from the smooth, non stratified, azimuthally symmetric structure we adopted.

Smoothness versus unresolved structures The radial profile (see Fig.3 upper panels) of the observed molecular lines, ^{12}CO(3–2), ^{13}CO(3–2), C^{18}O(3–2) does not appear smooth. After subtracting the best (smooth) outer disk model, Figure 5 reveals some extra emission located in rings, at specific azimuths. This is particularly clear for the optically thinner transitions of the C^{18}O(3–2), suggesting radial density variations in the molecular layer (at about 1 scale height). Contrary to the gas, the dust emission is hardly seen in the outer disk (radius > 260 au), but mostly concentrated in the ring (radius 200 – 260 au).

The azimuthal dependence of the integrated brightness of the ^{12}C^{16}O emission (Fig.3 lower left panel) shows strong excesses at specific azimuth. The excess seen in the south-east quadrant is consistent with the hot spot location quoted by Dutrey et al. (2014). This "hot spot" remains visible, though less clearly in ^{13}CO and C^{18}O. This indicates that it is mostly a temperature enhancement, rather than an overdensity region.

In the residual maps (Fig.5), other azimuthal variations are also visible. Our smooth model removes any azimuthally symmetric emission so that apparent effects resulting from velocity coherence length and convolution with elongated beam-shape are properly eliminated. The observed residuals thus reveal intrinsic structures.

All these evidences point to the existence of radial and azimuthal sub-structures that remain unresolved (at least radially) at our 30 au linear resolution.

6.3. Properties of the gas inside the cavity

Kinematics From Fig.4, the rotation appears sub-Keplerian at radii smaller than about 0.8″. This could be the signature of the tidal forces generated by the Aa/Ab binary. Unfortunately, this

is largely an effect of the intensity drop in the cavity, combined with the finite angular resolution. Since the signal intensity increases with radius in the cavity, the intensity weighted mean velocity is biased towards the values obtained at the largest radii, i.e. the gas apparently rotates at smaller velocities. A proper modeling of the angular resolution effect, accounting for the observed brightness distribution, would be required to remove this artefact and figure out whether the gas is rotating at the expected Keplerian speed or not.

On the other hand, we find clear evidence for infall motions in the cavity (see Sec.5.1), at velocities about $10-15\%$ of the Keplerian speed, proving that material is accreting onto the inner disks orbiting the central stars. This is consistent with the infall value found for L 1551 NE, a younger binary system (Takakuwa et al. 2017). However, our sensitivity is insufficient to make detailed comparison with hydro-dynamics models.

In summary, we find that the gas starts to exhibit non-Keplerian motions (at least infall motions, and perhaps slower than Keplerian rotation) at $r \approx 160$ au, somewhat smaller than the inner edge of the dust ring (193 au). This difference in radii is expected when dust trapping in the high pressure bump occuring in the dense ring is considered (e.g. Cazzoletti et al. 2017). The 160 au radius remains however much larger than the radius at which tidal disturbances are expected in a binary system, which is about 2.5-3 times the orbit semi-major axis (Artymowicz & Lubow 1996). Given the current separations of Aa and Ab, about 35 au, we would expect deviations from Keplerian motions would only appear inside about 100 au, unless the orbit is very eccentric. High eccentricity appears unlikely given the measured orbital parameters (Beust & Dutrey 2005), who also mentioned than underestimated astrometric errorbars could play an important role. Following Beust & Dutrey (2005), Köhler (2011) and Nelson & Marzari (2016) showed that this apparent contradiction could be solved if one assumes that the orbital plane of the stars is very different from the (common) plane of the ring and outer disks. A similar result was found by Aly et al. (2018) who indicate that an inclination difference of 30° could remain stable over the (circumbinary) disk lifetime. However, Brauer et al. (2019) found the circumstellar disk around Aa and one of the disks around Ab1 or Ab2 must also be co-planar with the circumbinary ring and disk, making the mis-aligned orbit proposition unlikely, since the alignment of the circumstellar disks is more controlled by the gravitational interactions with the stars than with the (much less massive) outer disk. The cavity size puzzle thus remains.

Gas temperature Our non-LTE analysis, in agreement with the study from Dutrey et al. (2014), shows that the gas inside the cavity is warm, with temperatures ranging from 30 to 80 K. In the bright blobs, near the stars, we derived a kinetic temperature of the order of $40-50$ K at about $30-60$ au from the central stars. It is important to mention that such temperatures are well above the CO freeze out temperature.

Amount of gas From our non-LTE analysis of the bright blobs, we found $\sim$ a few 10^{17} cm^{-2} for the CO column density with the exception for blobs 4 and 6 which have a lower column density of $\sim (3-6)\,10^{16}$ cm^{-2}. We also obtained a lower limit on the H_2 density of the order of $\sim (1-10)\,10^4$ cm^{-3} for all blobs. However, a more stringent constraint can be obtained from the blob masses given in Table 6, because the thickness of the blobs is of the order of the scale height $H(r)$, 5 to 10 au at this distance to the stars. This leads to densities about 10^7 cm^{-3}.

The cumulative mass of the blobs is $\sim 1.2\times10^{-5}$ M$_\odot$. We also estimated the total gas mass inside the cavity from the integrated flux of the optically thin CO isotopologues. We found a mass of $\sim 1.6\times10^{-4}$ M$_\odot$, assuming standard CO abundance (see Table 7). The ^{13}CO and C^{18}O values perfectly agree suggesting that both the ^{13}CO and C^{18}O emissions are essentially optically thin in the cavity.

Therefore, the total mass of the gas inside the cavity appears a factor 10 larger than the cumulative blob mass. This only relies on the assumption of similar molecular abundances in these regions, which is reasonable given their similar temperatures. Thus a significant fraction of the gas in the cavity does not reside in the dense blobs but in diffuse features.

Determining the absolute value of the gas mass inside the cavity is more challenging. On one hand, our assumed value for the CO abundance, that observed in TMC-1, appears reasonable given the relative high temperature in the cavity. However, lower values might result from C and O still being locked on grains in the form of more complex or less volatile molecules (CO_2 and CH_4, see Reboussin et al. (2015)). A proper quantification of such a process would require a complete chemical study following the physical and chemical evolution of the gas and solid phases throughout the disk.

Nevertheless, an absolute minimum value for the gas mass in the cavity can be obtained if we assume the CO abundance cannot exceed the Carbon cosmic abundance expected in cold molecular clouds (3.4×10^{-4} Hincelin et al. 2011). In this case, we obtain the minimum mass by correcting the previous value by the factor of ~ 0.2. This leads to $\sim 0.3\times10^{-4}$ M$_\odot$ for the total gas mass inside the cavity.

In any case, the mass of gas in the cavity is only a very small fraction of the total disk mass (0.15 M$_\odot$) which is estimated from the dust emission.

Mass accretion rate The gas in the cavity is unstable and will accrete onto the GG Tau A disks on a timescale of a few ($\sim$4) orbital binary periods, that is estimated to be around 600 years, see Beust & Dutrey (2005). A similar timescale, about 2500 yrs, is given independently by the ratio of cavity radius to the measured infall velocities. This gives an accretion rate of $\sim 6.4\times10^{-8}$ M$_\odot$ yr^{-1} if we assume the canonical mass value.

The accretion rate on GG Tau Aa+Ab, measured in year 2000 using the H_α line, is about $\sim 2\times10^{-8}$ M$_\odot$ yr^{-1} (Hartigan & Kenyon 2003), a factor 3 lower than our estimate. The small difference may be partly explained by variable accretion inside the cavity and onto the central star(s) associated to non steady state dynamics. In a binary star, the accretion rate process is modulated by the eccentricity, being more efficient at the pericenter with a delay which depends at zero order of the eccentricity (Artymowicz & Lubow 1996; Günther & Kley 2002). The two values of the accretion rates reflect different aspects of a highly variable process depending how and when these rates are measured. The fair agreement between both results shows that the GG Tau A disk can be sustained by accretion through the cavity on a long timescale.

7. Summary

We report new observations of CO isotopologues with ALMA of the close environment of GG Tau A. We study the ring by performing a LTE analysis and we perform non-LTE analysis for the gas clumps observed inside the cavity, we also investigate the gas kinematics in the outer disk and inside the cavity.

– The ring and outer disks do not exhibit a smooth distribution but likely consist of a series of unresolved substructures with some azimuthal variations, particularly in the dense inner ring. The bright hot spot seen in ^{12}CO is marginally seen in ^{13}CO and in C^{18}O, suggesting a temperature effect.
– The gas temperature derived from the optically thick CO line has a sharp decrease (r^{-1}), as for the dust. The temperature of 20 K (CO snowline) is reached at $\sim$ 300 au.
– The total amount of mass inside the cavity derived from ^{13}CO is $(1.6 \pm 0.1) \times 10^{-4}$ M$_\odot$, assuming standard CO abundance.
– The gas streamers inside the cavity can be essentially defined by 6 blobs. A non-LTE analysis reveals that their conditions are similar with CO column densities around a few $\sim 10^{17}$ cm^{-2}, temperatures in the range 40 − 80 K, and H_2 density in the dense parts of the order of 10^7 cm^{-3}.
– The kinematics of the whole structure (outer ring + cavity) appears in Keplerian rotation around a 1.36 M$_\odot$ system for radii beyond $\sim$ 1.2" or 180 au. The kinematics of the gas streamers and blobs appear more complex than it is expected for such a binary system. In particular, the gas starts to exhibit non-Keplerian motions for radii smaller than $\sim$ 160 au.
– The gas inside the cavity shows infall motions of about 10% of the Keplerian velocity allowing the central stars to accrete material from the dense ring.
– The average mass flow rate of the gas through the cavity is $\sim 6 \times 10^{-8}$ M$_\odot$ yr^{-1}, a value compatible with the stellar accretion rate measured using the H_α line, and sufficient to replenish the circumstellar disks.

Acknowledgements. N. T. Phuong warmly thanks P. Darriulat for his guidance and supports. A. Dutrey also thanks him for making the collaboration possible. A. Dutrey and S. Guilloteau acknowledge M. Simon who started to study this wonderful object with them in another millennium. This work was supported by "Programme National de Physique Stellaire" (PNPS) and "Programme National de Physique Chimie du Milieu Interstellaire" (PCMI) from INSU/CNRS. This research made use of the SIMBAD database, operated at the CDS, Strasbourg, France. This paper makes use of the following ALMA data: ADS/JAO.ALMA#2011.1.00059.S, #2012.1.00129.S and #2015.1.00224.S ALMA is a partnership of ESO (representing its member states), NSF (USA), and NINS (Japan), together with NRC (Canada), NSC and ASIAA (Taiwan), and KASI (Republic of Korea) in cooperation with the Republic of Chile. The Joint ALMA Observatory is operated by ESO, AUI/NRAO, and NAOJ. N. T. Phuong and P. N. Diep acknowledge financial support from World Laboratory, Rencontres du Viet Nam, the Odon Vallet fellowships, Vietnam National Space Center, and Graduate University of Science and Technology. N. T. Phuong thanks the financial support from French Embassy Excellence Scholarship Programme, P. Darriulat and from the Laboratoire d'Astrophysique de Bordeaux. This research is funded by Vietnam National Foundation for Science and Technology Development (NAFOSTED) under grant number 103.99-2018.325.

References

Aly, H., Lodato, G., & Cazzoletti, P. 2018, MNRAS, 480, 4738
Artymowicz, P., Clarke, C. J., Lubow, S. H., & Pringle, J. E. 1991, ApJ, 370, L35
Artymowicz, P. & Lubow, S. H. 1994, ApJ, 421, 651
Artymowicz, P. & Lubow, S. H. 1996, Interaction of Young Binaries with Protostellar Disks, ed. S. Beckwith, J. Staude, A. Quetz, & A. Natta, Vol. 465, 115
Beust, H. & Dutrey, A. 2005, A&A, 439, 585
Brauer, R., Pantin, E., Di Folco, E., et al. 2019, arXiv e-prints, arXiv:1906.11582
Cazzoletti, P., Ricci, L., Birnstiel, T., & Lodato, G. 2017, A&A, 599, A102
Chiang, E. I. & Goldreich, P. 1997, ApJ, 490, 368
Di Folco, E., Dutrey, A., Le Bouquin, J.-B., et al. 2014, A&A, 565, L2
Ducourant, C., Teixeira, R., Périé, J. P., et al. 2005, A&A, 438, 769
Dutrey, A., Di Folco, E., Beck, T., & Guilloteau, S. 2016, A&A Rev., 24, 5
Dutrey, A., di Folco, E., Guilloteau, S., et al. 2014, Nature, 514, 600
Dutrey, A., Guilloteau, S., & Simon, M. 1994, A&A, 286, 149
Elitzur, M. 1992, Science, 257, 112
Frink, S., Röser, S., Neuhäuser, R., & Sterzik, M. F. 1997, A&A, 325, 613
Gaia Collaboration, Brown, A. G. A., Vallenari, A., et al. 2018, ArXiv e-prints [[arXiv]1804.09365]
Gaia Collaboration, Prusti, T., de Bruijne, J. H. J., et al. 2016, A&A, 595, A1
Guilloteau, S., Dutrey, A., & Simon, M. 1999, A&A, 348, 570
Günther, R. & Kley, W. 2002, A&A, 387, 550
Hartigan, P. & Kenyon, S. J. 2003, ApJ, 583, 334
Hincelin, U., Wakelam, V., Hersant, F., et al. 2011, A&A, 530, A61
Huré, J.-M., Hersant, F., Surville, C., Nakai, N., & Jacq, T. 2011, A&A, 530, A145
Köhler, R. 2011, A&A, 530, A126
Milam, S. N., Savage, C., Brewster, M. A., Ziurys, L. M., & Wyckoff, S. 2005, ApJ, 634, 1126
Nelson, A. F. & Marzari, F. 2016, ApJ, 827, 93
Ohishi, M., Irvine, W. M., & Kaifu, N. 1992, in IAU Symposium, Vol. 150, Astrochemistry of Cosmic Phenomena, ed. P. D. Singh, 171
Phuong, N. T., Chapillon, E., Majumdar, L., et al. 2018a, A&A, 616, L5
Phuong, N. T., Diep, P. N., Dutrey, A., et al. 2018b, Research in Astronomy and Astrophysics, 18, 031
Piétu, V., Dutrey, A., & Guilloteau, S. 2007, A&A, 467, 163
Piétu, V., Gueth, F., Hily-Blant, P., Schuster, K.-F., & Pety, J. 2011, A&A, 528, A81
Reboussin, L., Wakelam, V., Guilloteau, S., Hersant, F., & Dutrey, A. 2015, A&A, 579, A82
Roell, T., Neuhäuser, R., Seifahrt, A., & Mugrauer, M. 2012, A&A, 542, A92
Takakuwa, S., Saigo, K., Matsumoto, T., et al. 2017, ApJ, 837, 86
Takakuwa, S., Saito, M., Saigo, K., et al. 2014, ApJ, 796, 1
Tang, Y.-W., Dutrey, A., Guilloteau, S., et al. 2016, ApJ, 820, 19
Tang, Y.-W., Dutrey, A., Guilloteau, S., et al. 2014, ApJ, 793, 10
van Dishoeck, E. F. & Black, J. H. 1988, ApJ, 334, 771
Watson, W. D., Anicich, V. G., & Huntress, W. T., J. 1976, ApJ, 205, L165
Weaver, E., Isella, A., & Boehler, Y. 2018, ApJ, 853, 113
Welsh, W. F., Orosz, J. A., Carter, J. A., et al. 2012, Nature, 481, 475
Wilson, T. L. 1999, Reports on Progress in Physics, 62, 143

Appendix A: Channel maps

We present in Figs.A.1-A.2 the Cleaned channel maps produced without subtracting the continuum emission.

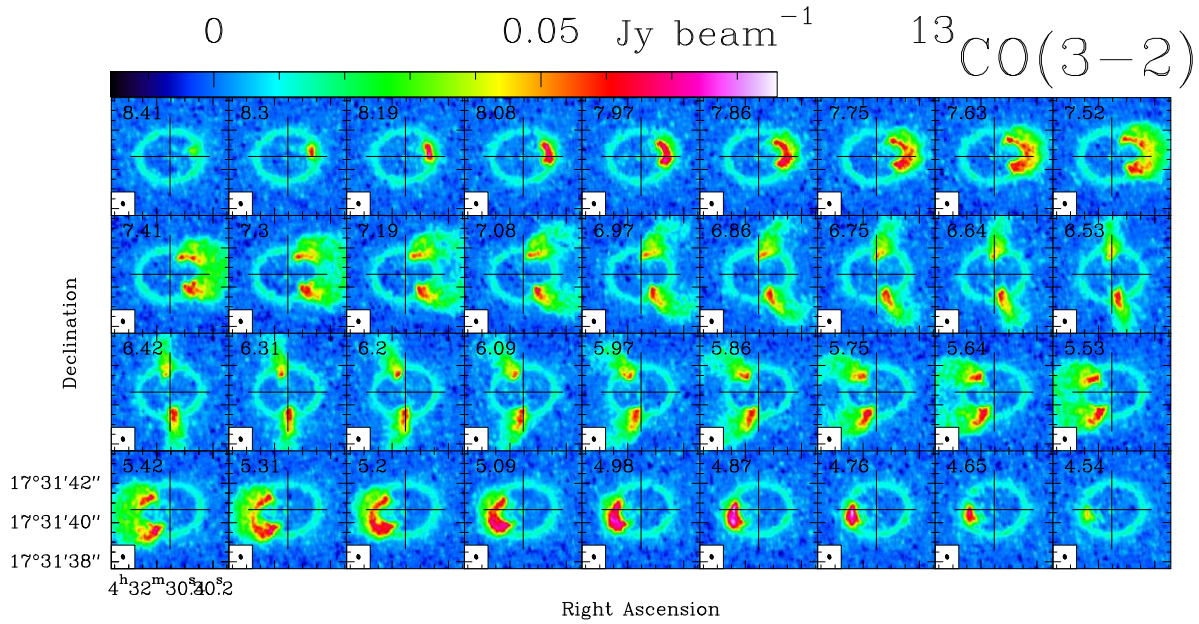

Fig. A.1. Channel maps of ^{13}CO(3–2), Beam 0.22" × 0.16", PA=16°. The noise level is 2.4 mJy beam^{-1}. The colour scale is indicated in the upper right panel. The cross is centred on the centre of the map.

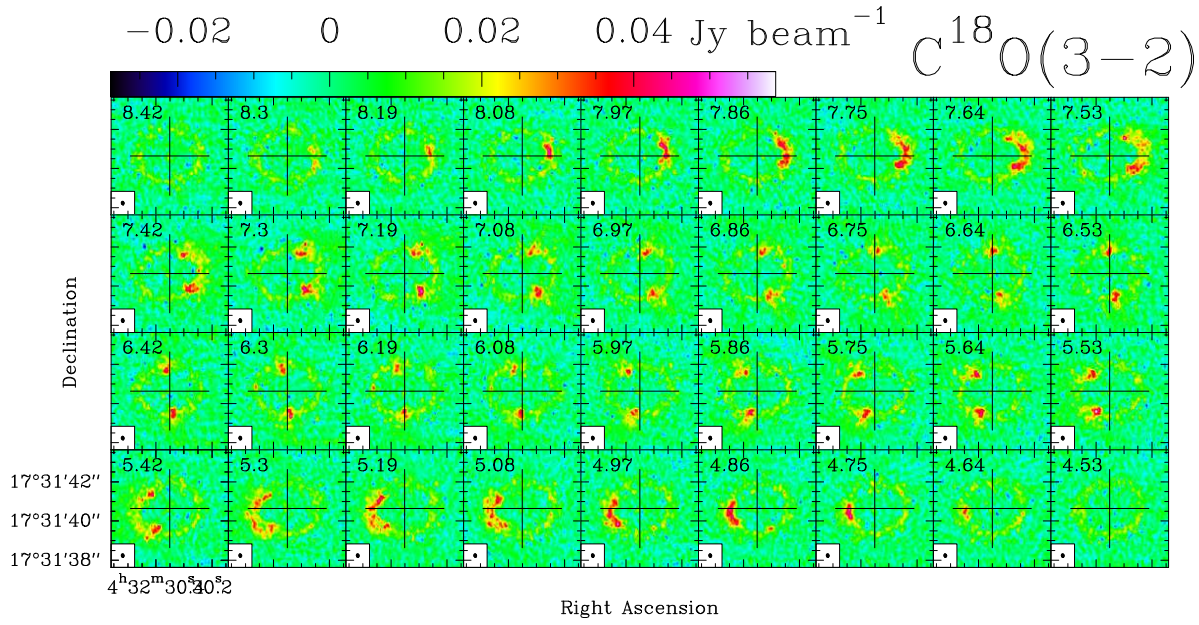

Fig. A.2. Channel maps of C^{18}O(3–2), Beam 0.19" × 0.14", PA=19°. The noise level is 4.8 mJy beam^{-1}. The colour scale is indicated in the upper right panel. The cross is centred on the centre of the map.

Appendix B: Disk model fitting

We use the DiskFit tool (Piétu et al. 2007) to derive physical parameters of rotating circumstellar disks.

Principles: DiskFit computes the spatial distribution of the emission coming from spectral lines (and dust) as a function of frequency (related to the line rest frequency and source Doppler velocity) for a given azimutally symmetric disk model.

In its basic form, as described in Piétu et al. (2007), the disk model assumes that the relevant physical quantities which control the line emission vary as power law as function of radius, and, except for the density, do not depend on height above the disk plane. The exponent is taken as positive if the quantity decreases with radius:

$$a(r) = a_0(r/R_a)^{-e_a}$$

If dust emission is negligible, for each molecular line, the disk is thus described by the following parameters :

- X_0, Y_0, the star position, and $V_{\rm disk}$, the systemic velocity.
- PA, the position angle of the disk axis, and i the inclination.
- V_0, the rotation velocity at a reference radius R_v, and v the exponent of the velocity law. With our convention, $v = 0.5$ corresponds to Keplerian rotation. Furthermore, the disk is oriented so that the V_0 is always positive. Accordingly, PA varies between 0 and 360°, while i is constrained between −90° and 90°.
- T_m and q_m, the temperature value at a reference radius R_T and its exponent.
- dV, the local line width, and its exponent e_v.
- Σ_m, the molecular surface density at a radius R_Σ and its exponent p_m
- $R_{\rm out}$, the outer radius of the emission, and $R_{\rm in}$, the inner radius.
- h_m, the scale height of the molecular distribution at a radius R_h, and its exponent e_h: it is assumed that the density distribution is Gaussian, with

$$n(r,z) = \frac{\Sigma(r)}{h(r)\sqrt{\pi}} \exp\left[-(z/h(r))^2\right] \quad \text{(B.1)}$$

(note that with this definition, $e_h < 0$ in realistic disks)

thus giving a grand total of 17 parameters to describe a pure spectral line emission.

All these parameters can actually be constrained for each observed line, under the above assumption of power laws. This comes from two specific properties of proto-planetary disks: i) the rapid decrease of the surface density with radius, and ii) the known kinematic pattern. In particular, we can derive both the temperature law (T_m, q_m) and the surface density law (Σ_m, p_m) when there is a region of optically thick emission (in the inner parts) while the outer parts is optically thin.

If dust emission is not negligible, it can also be accounted for in the emission process. Again assuming simple power laws, this adds up 6 new parameters, namely 2 for the dust temperature, 2 for the dust surface density, plus the inner and outer radii of the dust distribution. Note that the absolute value of the dust surface density is degenerate with that of the dust absorption coefficient. Surface density and temperature may also be degenerate if the dust emission is optically thin and in the Rayleigh Jeans regime. Dust emission being in general weak compared to the observed spectral lines, an inaccurate model of the dust will have limited effects.

Power laws are good approximation for the velocity, temperature (see, e.g. Chiang & Goldreich 1997), and thus to the scale height prescription. For molecular surface density, the approximation may be less good because of chemical effects.

We refer to Piétu et al. (2007) for a more thorough discussion about the interpretation of the model parameters. We recall however that the temperature derived in such a way for a molecule is the excitation temperature of the transition, and that the surface density is derived assuming this temperature also represents the rotation temperature of the rotational level population.

From the disk model, an output data cube representing the spatial distribution of the emitted radiation as a function of velocity is generated by ray-tracing. From this model data cube, DiskFit computes the model visibilities on the same (u, v) sampling as the observed data, and derives the corresponding χ^2:

$$\chi^2 = \Sigma_i \left(M(u_i, v_i) - O(u_i, v_i)\right)^2 / W_i$$

where M is the model visibility at the (u_i, v_i) Fourier plane coordinate, O the observed visibility, and W_i the visibility weight, computed from the observed system temperature, antenna efficiency, integration time and correlation losses.

A Levenberg-Marquardt method (with adaptive steps adjusted according to the estimated parameter error bars) is then used to minimize the χ^2 function upon the variable parameters.

Error bars are computed from the covariance matrix. As described by Piétu et al. (2007), although there are many parameters in the model, they are in general well decoupled provided the angular resolution is sufficient. Thus the covariance matrix is well behaved, but assymetric error bars are not handled (assymetric error bars often happen for the outer radius, even leading to lower limits only in case of insufficient sensitivity).

Broken power laws The basic power law model above is insufficient to represent the emission from the GG Tau A disk, because of strong and non monotonic radial variations of the line brightness in CO and ^{13}CO.

Instead of representing the whole emission by unique temperature and surface density power laws over the whole extent of the disk, we thus break them into multiple power laws, each applying to different annuli. Such a broken power law is fully characterized

by the values of the temperature and surface density at the knot radii, i.e. the radii that separate consecutive annuli. Given the knot position, the power law exponent can be derived from the ratio of values at consecutive knots. For the innermost annulus (between the inner radius and the first knot) and outermost annulus (between the last knot and the outer radius), we simply assume the same exponent as in their respective neighbors.

This representation gives us more flexibility in the shape of the distribution. However, the finite spatial resolution (even accouting for the super-resolution provided by the Keplerian nature of the rotation), as well as sensitivity issues, limit the possible number of knots. In practice, we could use 4 or 5 knots to represent the narrow dense ring and the shallower outer disk in CO and other molecules.

This finer radial profile representation also breaks our ability to determine both the temperature and the surface density in each annulus, as these two quantities are degenerate if the line is optically thin (unless the annulus is very wide). [4]

We thus used the CO J=3-2 line to derive the temperature, and used this temperature law as fixed input parameters to derive molecular surface densities.

B.1. Best fit model

We obtained our best fit model using the following method. Figure B.1 displays the integrated intensity maps derived from Figs.A.1-A.2 and from the best fit model, as well as that of the residuals, that are dominated by emission in the cavity. Note that the continuum emission from Aa has been removed in these residuals.

Geometric parameters All data sets were recentered on the dust ring center.

We verified by fitting that the geometric parameters are consistent with values derived from previous studies. In particular, we verified that the ring center position ($X_0 = 0, Y_0 = 0$) is also consistent with the kinematic center of the Keplerian rotating disk.

The typical errors on these parameters (± 0.01" for the position, $\pm 1 - 2^\circ$ for PA and i, ± 0.03 km s^{-1} for $V_{\rm sys}$ and V_0) are much too small to affect in any substantial way the derived temperatures and surface densities. Similarly, the small difference between the rotation velocity derived in Sec.3.2.2 and the adopted value has no significant impact.

Dust model The dust properties and dust temperature law were adopted from Dutrey et al. (2014). Only the dust surface density was adjusted, to compensate to first order flux calibration errors. Although the model is not perfect (in particular it does not represent the $\sim 15\%$ azimutal brightness variations), the residuals are small enough to have negligible influence on the results derived for the observed molecules.

Temperature law The temperature law is derived from the fit to the CO data, and used for other molecules as fixed input parameters. To better model the ensemble, we assumed the CO column density (which is not well constrained by the CO data because of the high optical depth) is equal to 70 times the ^{13}CO column density.

Scale height We assumed the scale height exponent was $e_h = -1$, i.e. $h(r) = H_m(r/r_h)$. The scale height was fitted independently for CO and ^{13}CO data, leading to a consistent value of 23 au at $r_h = 100$ au, which was used as a fixed parameter in the final fit for all spectral lines.

Nominal fit Table B.1 summarizes the adopted fixed parameters for our final best fit. Since the coupling between these parameters and the fitted ones (temperatures and surface densities) are small, fixing these parameters does not affect the derived values and errorbars of the fitted parameters.

[4] In the optically thick case, the temperature is well constrained, but the surface density can only be constrained from the opticall thin line wings.

Table B.1. Fitting parameters

Geometric parameters			
Parameter	Value		Status
(x_0, y_0)	(0,0)	Center of dust ring	Verified
$PA(^\circ)$	7	PA of disk rotation axis	Verified
$i(^\circ)$	−35	Inclination	Verified
$V_{\rm LSR}$	6.40	Systemic velocity	Verified
V_0 (km s^{-1})	3.37	Keplerian Rotation velocity at 100 au	Verified
dV (km s^{-1})	0.3	Local line width	Fixed
H_0	24	Scale height at 200 au	Verified
Dust ring parameters			
$R_{\rm in}$	193 au	Inner radius	fixed
$R_{\rm out}$	285 au	Outer radius	fixed
K_ν (cm$^2/g$)	$0.02 \times (\nu/230{\rm GHz})^{+1}$	Abs. Coefficient	fixed
$T(r)$ (K)	$14 \times (r/200\,{\rm au})^{-1}$	Temperature	fixed
$\Sigma(H_2)(r)$ (cm^{-2})	$5.6\ 10^{24} \times (r/200\,{\rm au})^{-1.4}$	Surface density	Fitted
Line parameters			
$R_{\rm in}$	169 au	Inner radius	Verified
$R_{\rm knots}$	see results	Knot positions	Fixed
$T(r)$ (K)	see results	Temperature law	fitted from CO
$\Sigma((X))(r)$ (cm^{-2})	see results	Molecule X surface density	Fitted
$R_{\rm out}(X)$	see results	Outer radius for Molecule X	Fitted

Notes. Fixed values are taken from Dutrey et al. (2014). Verified values were used as fixed parameters in the last fitting step, but as free parameters in intermediate fits to verify their impact.

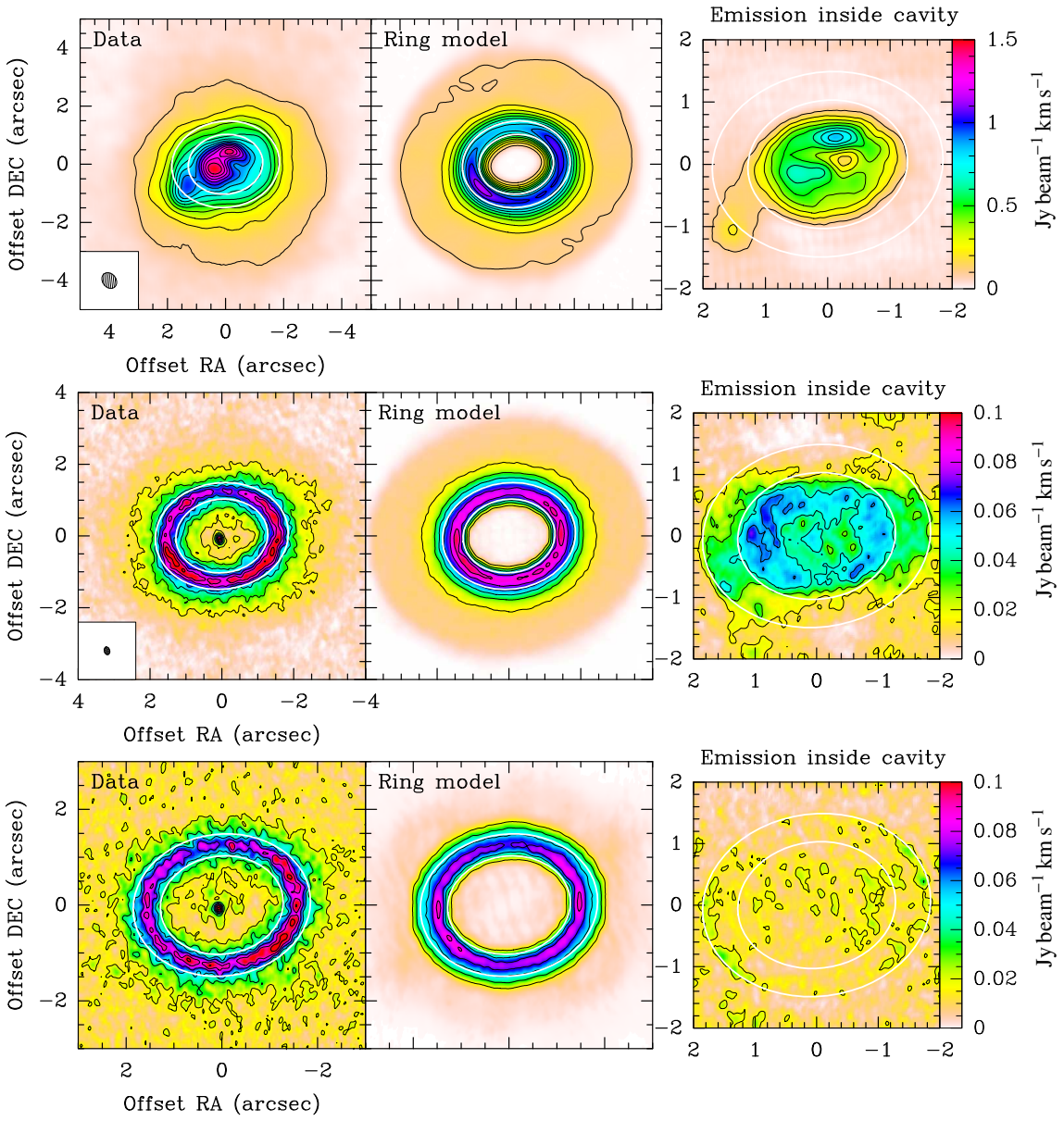

Fig. B.1. From top to bottom, ^{12}CO(3–2), ^{13}CO(3–2) and C^{18}O(3–2). *Left:* The integrated intensity map. *Middle:* The best ring and outer disk model intensity map. *Right:* Residual emission inside cavity (original data minus best fit model).

GG Tau ring: Dust trap or not Dust trap, that is the question... 2018.1.00532.S

ABSTRACT

We propose to observe the gas and dust ring orbiting the triple TTauri star GG Tauri. Located about 180 to 260 au from the star, this ring has a total mass of 0.13 Msun, estimated from 1.3 mm continuum measurements and a gas-to-dust ratio of 100. However, hydrodynamical models reveal that large dust particles can remain trapped at gas pressure maxima (dust traps), forming dust rings as those recently observed by ALMA around many transition disks. If the GG Tau ring is a dust trap, its total mass can be lower by a factor of 3-5. To check this, we propose to directly measure the gas mass by observing the ring in CS J=5-4 at the resolution of 0.3 arcsec because with its high dipole moment, CS is a high density tracer. We will analyse these new data with the existing images in CS J=3-2 (NOEMA) and CS J=7-6 (ALMA projects 2012.1.00129.S and 2015.1.00224.S at 0.4 and 0.1 arcsec). By performing non-LTE analysis, with these 3 transitions we will be able to determine the H2 density and temperature in the ring, and thus measure the gas mass and the gas-to-dust ratio.

PI NAME:	Otoniel Denis Alpizar			**SCIENCE CATEGORY:**	Circumstellar disks, exoplanets and the solar system
ESTIMATED 12M TIME:	**6.2 h**	**ESTIMATED ACA TIME:**	**0.0 h**	**ESTIMATED NON-STANDARD MODE TIME (12-M):**	**0.0 h**
CO-PI NAME(S): (Large & VLBI Proposals only)					
CO-INVESTIGATOR NAME(S):	Anne Dutrey; Diep Pham; Edwige Chapillon; Stephane Guilloteau; Vincent Pietu; Liton Majumdar; Ya-Wen Tang; Phuong Nguyen				
DUPLICATE OBSERVATION JUSTIFICATION:					

REPRESENTATIVE SCIENCE GOALS (UP TO FIRST 30)

SCIENCE GOAL	POSITION	BAND	ANG.RES.(")	LAS.(")	ACA?	NON-STANDARD MODE
CS J=5-4 from GG_Tau A	ICRS 04:32:30.3460, 17:31:40.640	6	0.300	8.000	N	N
Total # Science Goals : 1						

SCHEDULING TIME CONSTRAINTS	NONE	TIME ESTIMATES OVERRIDDEN ?	No

1 Scientific Justification

Dust Traps in young Disks With the advent of ALMA, detailed observations of the dust emission around TTauri stars have revealed the presence of dust rings around many systems, which are sometimes asymmetric such as that of Oph IRS 48 (Van der Marel et al., 2013). These systems exhibit a central cavity where the dust is strongly depleted, while CO gas is still present (Van der Marel et al., 2015). Most of the mm continuum emission is confined in a ring encircling the central cavity. This is seen in transition disks (Andrews et al., 2011) but also around binary systems such as HD142527 (Casassus et al., 2015). The existence of such cavities is expected to result from gravitational tidal interactions due to the central binary or to an unseen planet residing inside the cavity. The presence of the dust ring is reinforced by the fact that large dust grains which dominate the mm continuum can remain trapped at large distance from the central star, at the outer gas pressure maximum resulting from these tidal interactions (Pinilla et al., 2012). Hydrodynamical models have also shown that asymmetric pressure bumps can form due to anticyclonic vortices or Rossby instabilities (Zhu and Stone, 2014, Lovelace et al., 1999). Quantifying the amount of dust trapping would provide a clear test of our understanding of these mechanisms. This has been attempted so far by comparing the distribution of optically thin tracers, such as CO isotopologues, to that of dust.

For example, Boehler et al., 2017 have performed a study of the asymmetric bumps observed in the circumbinary ring of HD 142527. After correcting for the opacity of the CO lines, and assuming a CO/H_2 abundance ratio of $6\,10^{-5}$, they found a gas-to-dust ratio at the maximum of the 'mm' dust emission of about 1.65 while the mean value across the ring is of the order 3-5.

Tracing the gas mass in protoplanetary disks: The method presented above has a major problem: the CO line opacity is very high meaning that the method only traces the CO near the disk surface. Studying TW Hya, Zhang et al 2017 have shown that to really characterize the bulk of the gas near the mid-plane, rarer optically thinner isotopologues, such as $^{13}C^{18}O$, have to be observed. With the exception of TW Hya located at 56 pc, this necessitates very long integration times. Moreover, assuming that the CO-to-dust ratio can be properly determined at the location of the CO layer, the CO-to-H_2 ratio can be still uncertain by a factor 2 to 10 (Favre et al., 2013, Reboussin et al., 2014) due to chemical effects. This can significantly affect the gas-to-dust ratio and the mass determination, at the end. **In a recent study of the Flying Saucer edge-on disk, Dutrey et al 2017 directly confirmed, by tomography that in a disk, the CO layer is typically located 3-5 scale heights above the mid-plane.** If we want to characterize the bulk of the dense gas, we need to find an abundant, easy to detect, gas tracer which emission peaks deeper in the disk, relatively protected from the UV flux to minimize chemical effects. This is exactly the case of CS: in the Flying Saucer disk, the optically thin CS J=5-4 layer is observed around 1 scale height or less. This makes CS the best molecule to trace the high density H_2 gas in a disk. This is not surprising because due to its high dipole moment, CS is recognized and utilized as a high density tracer to study molecular clouds and dense cores. This is opposite to CO that, because of its very low dipole moment, is easily thermalized and thus only a good tracer of the gas temperature (Dartois et al 2003). As CS is relatively strong in protoplanetary disks (Guilloteau et al 2016), its use as a density tracer will become an important tool in the near future.

Therefore, we propose here an approach that does not rely on molecular abundances, but directly measure the density and mass from the excitation conditions of the CS molecule. Studying the CS excitation conditions using several lines of CS will allow us to recover the mass of gas and in a second step the gas-to-dust ratio.

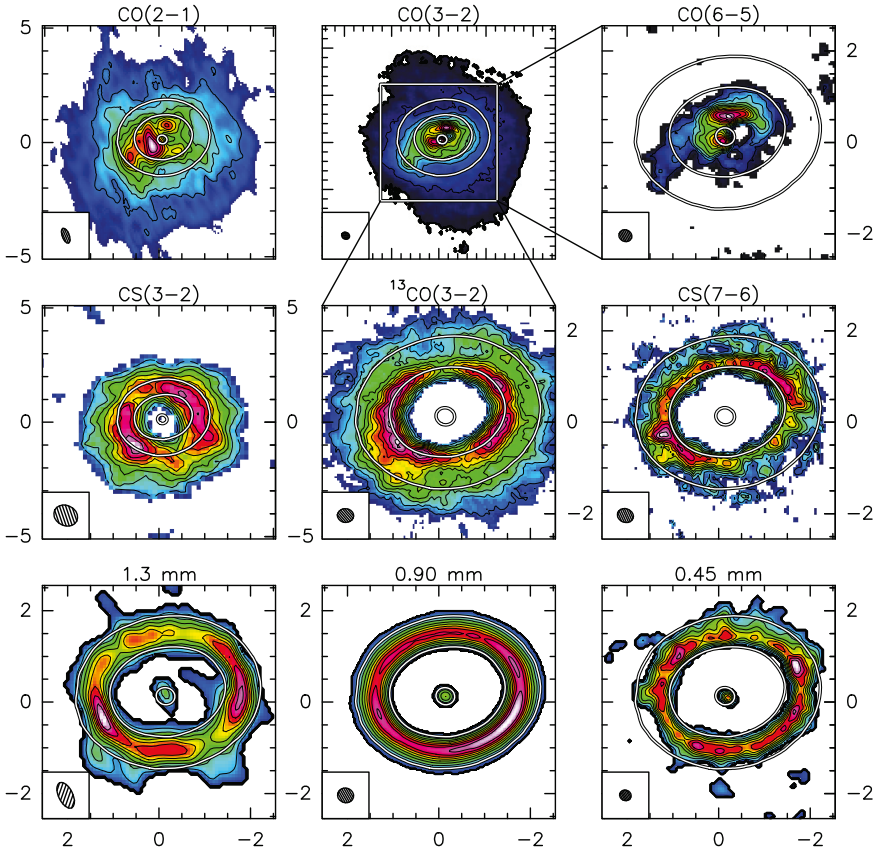

Figure 1: **ALMA and IRAM images of GG Tau A** (Dutrey et al., 2016) **IRAM data:** CO J=2-1 (Guilloteau and Dutrey 2001) and CS J=3-2 integrated areas and 1.3mm map. **ALMA data:** CO and ^{13}CO J=3-2 and CO J=6-5 (Dutrey et al., 2014) and CS J=7-6 (Phuong et al., 2018, in prep) integrated areas, 0.8 and 0.45mm maps. The ellipses display the location of Aa, the inner (180 au) and outer (260 au) radii of dust emission.

GG Tau A, a unique target: Located at 140 pc in Taurus cloud, GG Tau A is a young (about 1-3 Myr old) hierarchical triple system consisting of a single star GG Tau Aa and a close binary GG Tau Ab (named Ab1 and Ab2 and separated by 4.5 au , DiFolco et al., 2014). GG Tau Aa and Ab are separated by 35 au in the plane of sky. The triple star is surrounded by an outer Keplerian disk of gas and dust which consists of a ring extending from ∼180 au up to ∼260 au and a larger disk of outer radius ∼ 800 au (Dutrey et al., 1994). The central cavity is not completely devoid of dust as suggested by scattered light images (e.g. Roddier et al., 1996) and contains gas as revealed by observation of ^{12}CO J=2-1 (Guilloteau and Dutrey 2000). Beck et al., 2012 also reported the existence of very hot (∼ 1000 K) H_2 gas around the stars. ALMA Band 9 (CO and continuum images at angular resolution 0.2″) analyzed with existing PdBI observations (Dutrey et al., 2014, and Fig.1) revealed the presence into the cavity of a streamer of CO gas resolved in several fragments and falling onto the central stars. Moreover, the Band 7 CO observations (project 2012.1.00129.S, Tang et al., 2016) also reveal the presence of a local hot spot while the ^{13}CO J=3-2 data strongly suggests the existence of an unresolved/embedded gap at the ring outer edge (∼ 260 au) which also corresponds to the radius of the hot spot. Together with evidence for local heating at the hot spot location, this reinforces the hypothesis of an accreting planet at the hot spot location (Tang et al, 2016).

Thus the dense and massive dust ring, extending from 180 to 260 au, appears to be confined by gravitational tidal interactions due to the proto-planet on one side and to the central triple star on the other side. Simultaneous modeling of the 3, 1.3 and 0.5mm images provides the determination

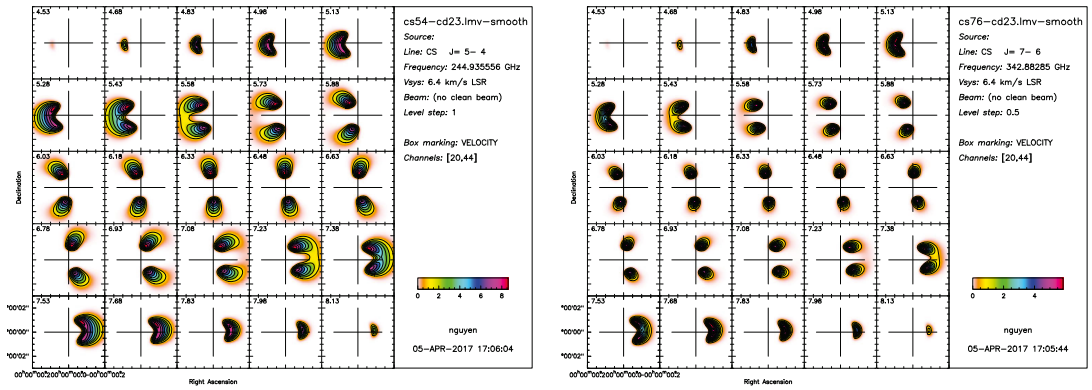

Figure 2: **ALMA simulated non-LTE CS emissions of the GG Tau A ring** CS J=5-4 (left) and CS J=7-6 (right) brightness distributions (K) simulated using DiskFit, assuming the best model derived from CO, CS and dust existing images. The angular resolution is set to 0.3″. The CS J=7-6 samples the inner ring while the CS J=5-4 is observed in the whole ring, as expected from the observed physical conditions.

of the dust (mid-plane) temperature. The disk is cold with a dust temperature of 14 K at 200 au and about 8 K at 300 au (Dutrey et al., 2014). Its total mass (gas and dust) estimated from the mm dust images is 0.13 $M_\odot$ and assuming standard dust absorption coefficient (Beckwith et al., 1990) with a gas-to-dust ratio of 100 (although Andrews et al., 2014, using additional 7-cm VLA data, suggest different dust properties that lead to lower dust masses). Such a mass is high compared to the stellar mass of 1.28 $M_\odot$ and the ring may be partly self-gravitating.

The properties mentioned above make the ring a perfect candidate for an almost perfectly symmetric 'mm' dust trap. **We propose to use a multi-line study of CS to derive the gas density, and thus study potential variations of the dust-to-gas ratio as a function of radius in this azimuthally symmetric disk.**

2 Immediate objectives and Proposal:

Our primary goal is to image the disk and ring in CS J=5-4 at an angular resolution of 0.3″. These data will perfectly complement the existing CS J=7-6 data from ALMA at 0.4″ (project 2012.1.129.S) and 0.1″ (2015.1.00224.S) and the CS J=3-2 data at 1″ resolution from NOEMA. Figure 1 presents the observations, and clearly reveals that the emissions of the two transitions have different spatial distributions. The J=3-2 line extends up to a radius of 400 au, while the high excitation transition of J=7-6 is mostly seen in the dense inner ring at radius less than 300 au. This is confirmed by the modeling of the CS J=3-2 and CS J=7-6 (Phuong et al 2018, in prep.) and our preliminary study of the excitation conditions of the CS lines inside the ring+disk (see Fig. 2 our first non-LTE models). The three transitions sample different excitation conditions, and have different critical densities ranging from a few 10^5 to about 10^8 cm^{-3}. The high J transitions of CS (J=5-4 and J=7-6) are located around one scale height above mid-plane. They can be sub-thermally excited in the outer disk and are mostly observed in the inner, denser part of the ring (Dutrey et al., 2017, Phuong et al., 2018 in prep). On the contrary, the CS J=3-2 is observed in the ring and in the outer disk.

With the CS J=5-4 observed at about the same angular resolution as that of the CS J=7-6, we will be able to fully characterize the gas density inside the ring (see Fig.2) while with the CS J=3-2, we will be able to study the outer disk (see also Fig.1). Figure 2 presents a non-LTE simulation of the CS J=5-4 emission of the ring using our current knowledge of the gas ring+disk system (obtained using the nLTE version of DiskFit, Pietu et al (2007)). A good estimate from the gas temperature has been already derived from previous CO and ^{13}CO analyses (Tang et al., 2016 andGuilloteau et

al., 1999). More recently, using new ^{12}CO, ^{13}CO and C^{18}O ALMA (2015.1.00224.S) observations, Phuong et al 2018 (in prep.) have analyzed the ring+outer disk properties. They confirmed that beyond a radius of 230 au, the gas disk is very cold, with a steep slope in r^{-1}. Tang et al., 2016 also found that there is no vertical temperature gradient in the molecular layer. The CO gas is at 20 K at 300 au, compared to a dust temperature of 14 K. As a consequence, the kinetic temperature of the CS emitting layer is expected to be around or slightly below 20 K. The dust temperature of 14 K can be seen as an absolute lower limit, being the temperature of 'mm' dust emitting layer lying onto the mid-plane because of dust settling. These two values will allow us to bracket the excitation conditions of CS. Even getting a lower limit on the density would allow us to exclude low gas-to-dust ratios. Since this method measures the density, the result does not rely on any assumption about the molecular abundances, and hence on chemical modeling.

Finally, last but not least, the choice of CS is also dictated by the fact that new accurate collisions rates with H_2 have been calculated by Denis-Alpizar et al., 2012, 2013, 2018.

We also include in the setup the CN J=2-1 which has been already detected by Dutrey et al., 1997 in GG Tau. CN is ubiquitous in TTauri disks (Guilloteau et al., 2013), presumably coming from the photo-dissociation layer above the mid-plane (Cazzoletti et al 2018). Because of its sensitivity to the UV field, it should provide a clear determination of the inner edge of the ring, where the gas is directly exposed to the UV radiation from the central triple star.

The setup also includes the CO J=2-1 line that can be observed for free, and would improve our knowledge of the temperature along the gas streamers in the cavity (Dutrey et al., 2014).

For CO, CN and CS lines, a final spectral resolution of 0.1-0.2 km/s will be enough to retrieve the kinematic information (but the observations will be obtained with ∼0.05 km/s sampling to allow study of turbulence using the method of Guilloteau et al., 2012) while an angular resolution of 0.3″ is needed. We request a total observing time of about 6.2 hours.

Team Strengths Our team includes experts in millimeter interferometry working on observations of protoplanetary disks and relevant modeling (gas and dust). We have developed tools dedicated to the analysis of mm observations (molecules and dust) of protoplanetary disks, such as DiskFit (Pietu et al., 2007, Boehler et al., 2013).

Potential for Publicity This project will provide the first robust measurement of the gas-to-dust ratio inside a disk. Moreover, ALMA observations of GG Tau made by our team have already provided attractive images: see http://www.eso.org/public/news/eso1434/.

References Andrews et al., 2011, ApJ, 742, 5. Andrews et al., 2014, ApJ, 787, 148. Beck et al., 2012, ApJ, 754, 72. Beckwith et al., 1990 AJ, 99, 924. Boehler et al., 2013, MNRAS, 431, 1573. Boehler et al., 2017, ApJ, in press. Casassus et al., 2015, ApJ, 812, 126. Cazzoletti et al., 2018, AA, 609, 93. Dartois et al., 2003, AA, 399, 773. Denis-Alpizar et al., 2012, 2013, J. Chem. Physics, 137 & 139. Denis-Alpizar et al 2018, MNRAS, submitted DiFolco et al., 2014, AA, 565, 2. Dutrey et al., 1994, AA, 286, 149. Dutrey et al., 1997, AA, 317, L55. Dutrey et al., 2014, Nature , 514, 600. Dutrey et al., 2016, AA Review, 24, 5. Favre et al., 2013, ApJ, 776, 38. Guilloteau et al., 1999, AA, 348, 570. Guilloteau and Dutrey 2000, ASPCS, 219, 645. Guilloteau and Dutrey 2001, Proceedings of IAU symposium 200. Guilloteau et al., 2012, AA, 548, 70. Guilloteau et al., 2013, AA, 549, 92. Guilloteau et al., 2016, AA, 592, 124. Lovelace et al., 1999, ApJ, 513, 805. Phuong et al 2018, in prep. Pietu et al., 2007, AA, 467, 163. Pinilla et al., 2012, AA, 538, 114. Roddier et al., 1996, ApJ, 463, 326. Reboussin et al., 2014, MNRAS, 440, 3557. Tang et al., 2016, ApJ, 820, 19. Van der Marel et al., 2013, AA, 556, 76. Van der Marel et al., 2015, ApJ, 810, 7. Zhu and Stone 2014, APJ, 759.

ID Not Assigned

SG : 1 of 1 CS J=5-4 from GG_Tau A Band 6

Observation of CS J=5-4 in GG Tau A

Science Goal Parameters

Ang.Res.	LAS	Requested RMS	RMS Bandwidth	Rep.Freq.	Cont. RMS	Cont. Bandwidth	Poln.Prod.	Non-standard mode
0.3000"	8.0"	2.208 mJy, 500 mK	200 m/s, 163.4 kHz	244.935556 GHz	17.912 µJy, 4.1 mK	2.461 GHz	XX,YY	No

Use of 12m Array (43 antennas)

t_total(all configs)	t_science(C43-5)	t_total(C43-2)	Imaged area	#12m pointing	12m Mosaic spacing	HPBW	t_per_point	Data Vol	Avg. Data Rate
6.2 h	3.1 h	1.3 h	7.9 "	1	offset	23.8 "	11127.9 s	581.7 GB	31.6 MB/s

Use of ACA 7m Array (10 antennas) and TP Array

t_total(ACA)	t_total(7m)	t_total(TP)	Imaged area	#7m pointing	7m Mosaic spacing	HPBW	t_per_point	Data Vol	Avg. Data Rate

Spectral Setup : Spectral Line

BB	Center Freq Rest GHz	spw name	Eff #Ch p.p.	Bandwidth	Resolution	Vel. Bandwidth	Vel. Res.	Res. El. per FWHM
1	227.418905	HC3N v=0 J=25-24	960	58.59 MHz	0.141 MHz	77.2 km/s	0.186 km/s	27
1	226.885000	CN v=0 N=2-1, J=5/2-3/2, F=7/...	960	58.59 MHz	0.122 MHz	77.4 km/s	0.161 km/s	31
1	226.655000	CN v=0 N=2-1, J=3/2-1/2, F=5/...	1920	117.19 MHz	0.122 MHz	155.0 km/s	0.161 km/s	31
2	231.321828	CH3OH v t=0 3(-2,2)-4(-1,4)	960	58.59 MHz	0.141 MHz	75.9 km/s	0.183 km/s	27
2	231.220686	13CS v=0 5-4	960	58.59 MHz	0.141 MHz	76.0 km/s	0.183 km/s	27
2	230.538000	CO v=0 2-1	960	58.59 MHz	0.122 MHz	76.2 km/s	0.159 km/s	31
2	229.533062	NH2CHO 2(2,0)-1(1,1)	960	58.59 MHz	0.141 MHz	76.5 km/s	0.184 km/s	27
3	246.404588	SO 3Σ v=0 2(3)-3(2)	1920	58.59 MHz	0.121 MHz	71.3 km/s	0.147 km/s	34
3	244.935556	CS v=0 5-4	1920	58.59 MHz	61.035 kHz	71.7 km/s	0.075 km/s	67
4	243.500000	cont-SO2-H2CO-H2CS	3840	1875.00 MHz	0.977 MHz	2308.6 km/s	1.202 km/s	4

1 Target

No.	Target	Ra,Dec (ICRS)	V,def,frame --OR--z
1	1-GG_Tau	04:32:30, 17:31:40	6.40 km/s,lsrk,RADIO

Expected Source Properties

	Peak Flux	SNR	Linewidth	RMS (over 1/3 linewidth	linewidth / bandwidth used for sensitivity	Pol.	Pol. SNR
Line	200.00 mJy	262.6	5 km/s	761.48 µJy, 172...	25.00	0.0%	0.0
Continuum	100.00 mJy	5582.9				0.0%	0.0

Dynamic range (cont flux/line rms): 45.5

1 Tuning

Tuning	Target	Rep. Freq. Sky GHz	RMS (Rep. Freq.)	RMS Achieved
1	1	244.930327	2.2 mJy, 497.8 mK	2.07 mJy - 2.64 mJy

Justification for requested RMS and resulting S/N (and for spectral lines the bandwidth selected) for the sensitivity ca...

We use a spectral resolution of 0.2 km/s to calculate the sensitivity.
We request a rms of 0.5 K based on the observed brightness of the CS 7-6 and 3-2 which are partly optically thin, even in the ring and sub-thermally excited.

The CO, CS and CN lines use a spectral averaging of 1, to allow further studies of turbulence.
The wideband pseudo-continuum mode is left in FDM with spectral average 1 to allow serendipitous measurements of possible emission from lines of H2CO or SO2 in this frequency range.
The remaining spectral line windows use an averaging a factor of 2 or 4 to limit the overall data rate.

Justification of the chosen angular resolution and largest angular scale for the source(s) in this Science Goal.

The angular resolution 0.3'' is enough to resolve out the ring which has a width of about 0.7''.

Justification of the correlator set-up with particular reference to the number of spectral resolution elements per line ...

The choice of the spectral correlator has been done to ensure enough spectral resolution for CS. Spectral windows have been optimized to cover lines that are potentially detectable in this long integration.
A wide band continuum window is available for calibration.

IRAM

300, rue de la Piscine
38406 Saint-Martin-d'Hères (France)
Fax: (33/0) 476 42 54 69

Registration n°: **P351980**
Date: **12-MAR-2019**

PROPOSAL FOR THE NOEMA INTERFEROMETER

Title: GG Tau A: a 3mm Large spectral Survey in the densest binary TTauri disk

PIs: Anne Dutrey (FR), Thi Phuong Nguyen (FR)
CoIs: Edwige Chapillon (IRAMF), Stephane Guilloteau (FR), Vincent Pietu (IRAMF), Tracy Beck (US) (invited), Ya-Wen Tang (TW), Jeffrey Bary (US) (invited), Audrey Coutens (FR), DIEP PHAM NGOC (VN), Liton Majumdar (US), Emmanuel Di Folco (FR), Otoniel Denis-Alpizar (CL)

Proposal category: Standard
Scientific category: Disks around low-mass stars

Total requested time: 24.0 (PolyFiX)

Abstract:
Multiple systems represent a substantial fraction of stars and exo-planets can form and evolve either in circumstellar or circumbinary orbits. Contrary to disks around single stars, the accretion in a binary star proceeds through the warm dynamically unstable zone which delineates the area inside the circumbinary disk and outside the Roche Lobes.

Continuation: W17BA
Proposal history:
This proposal is partly the continuation of project W17BA

Sources:

Id	Epoch	RA	DEC	Vlsr (km/s)	Setups	
GG_Tau	J2000	04:32:30.346	17:31:40.642	6.4	1, 2, 3	edit/delete

Technical sheet "70GHz":

Summary

Point source detection with lines & continuum on 1 source(s).
Total observing time: 8.00 hours
Track fractions: Any: 100.0 %

Instrumental tuning

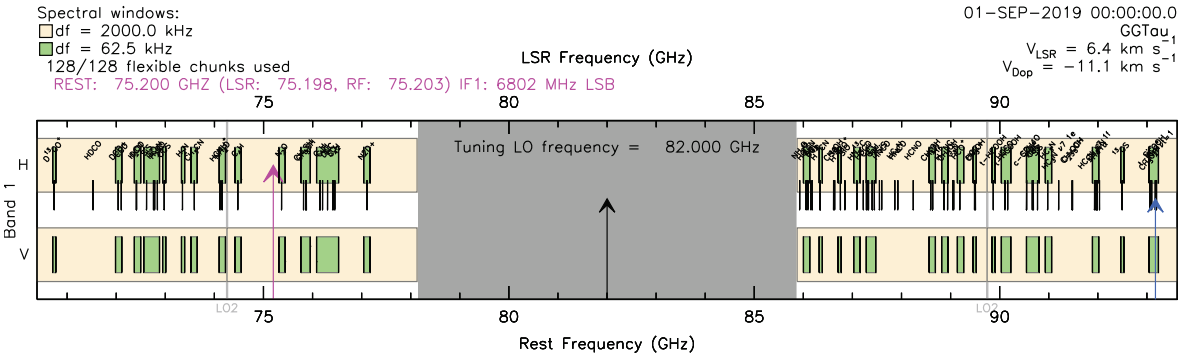

Half the most narrow SPW is equivalent to an offset of 127.567 km/s in source LSR velocity

Source properties for lines

Expected signal: 80.0 mJy/beam Sensitivity: 4.4 mJy/beam (0.250 km/s) → SNR: 18

Expected line width: 3.0 km/s

Source properties for continuum

Expected signal: 1000.0 mJy/beam Sensitivity: 11.2 microJy/beam (15488.0 MHz x 2 polar) → SNR: 89273

Technical sheet "80GHz":

Summary

Point source detection with lines & continuum on 1 source(s).
Total observing time: 8.00 hours
Track fractions: Any: 100.0 %

Instrumental tuning

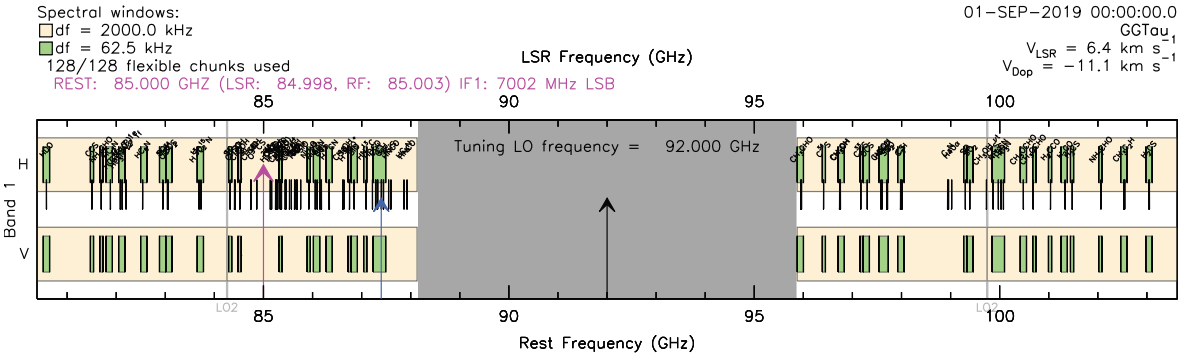

Half the most narrow SPW is equivalent to an offset of 112.859 km/s in source LSR velocity

Source properties for lines

Expected signal: 80.0 mJy/beam Sensitivity: 4.5 mJy/beam (0.250 km/s) → SNR: 18

Expected line width: 2.54248235 km/s

Source properties for continuum

Expected signal: 1000.0 mJy/beam Sensitivity: 10.1 microJy/beam (15488.0 MHz x 2 polar) → SNR: 99179

Technical sheet "90GHz":

Summary

Point source detection with lines & continuum on 1 source(s).
Total observing time: 8.00 hours
Track fractions: Any: 100.0 %

Instrumental tuning

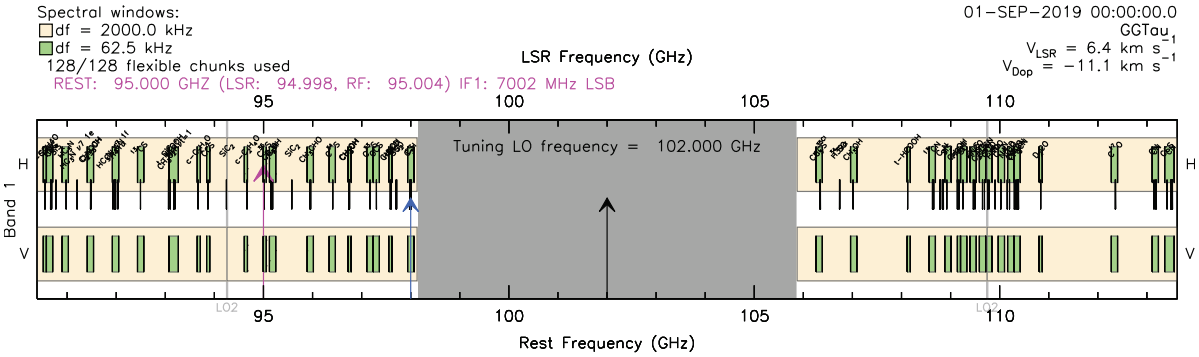

Half the most narrow SPW is equivalent to an offset of 100.979 km/s in source LSR velocity

Source properties for lines

Expected signal: 80.0 mJy/beam Sensitivity: 4.8 mJy/beam (0.211 km/s) → SNR: 17

Expected line width: 3.0 km/s

Source properties for continuum

Expected signal: 1000.0 mJy/beam Sensitivity: 11.6 microJy/beam (15488.0 MHz x 2 polar) → SNR: 86400

BLANK PAGE

GG Tau A: a 3mm large spectral survey in the densest binary TTauri disk

P.I.: Anne Dutrey, Thi Phuong Nguyen

1 Science Context

Multiple systems represent a substantial fraction of stars and exo-planets can form and evolve either in circumstellar or circumbinary orbits (e.g. Welsh et al. 2012). Theory of disk evolution (Artymowicz et al. 1991) predicts that a binary TTauri star about 1 Myr old should be surrounded by two inner disks, located inside the Roche lobes and an outer ring or disk located outside the outer Lindblad resonances. The outer radii of inner disks, as well as the inner radius of circumbinary (outer) disk, are delineated by tidal truncation while the survival of inner accretion disks on a timescale allowing for planet formation necessitates that matter inflows from the outer to the inner circumstellar disks through streaming gas and dust (the so-called streamers). **Determining the physical and chemical gas properties throughout their pathway from the outer disk to the inner disks is a necessary step to understand how planets can form in such gravitationally disturbed environnement, and eventually how they can differ from planets formed around single stellar systems.** So far, outer disks and streamers have only been imaged in a few objects such as GG Tau A, L1551 NE or UY Aur (Dutrey et al. 2014, Takakuwa et al. 2014, Tang et al. 2014).

The GG Tauri A system: With a spectacular large and dense outer disk, GG Tau A appears as a unique laboratory. It consists of a triple star (Aa-Ab1/b2) with respective separation of 35 and 4.5 au (Di Folco et al. 2014). The outer CO and dust disk which surrounds GG Tau A is in Keplerian rotation (Dutrey et al. 1994. The outer disk consists of a ring extending from radius r $\sim$ 180 to 260 au surrounded by a large gaseous outer disk extending up to $\sim$ 800 au. NOEMA and ALMA CO images show a puzzling hot spot at the outer edge of the dust ring (Fig.2) presumably an indirect evidence for an embedded companion that is still accreting material from the outer disk (Dutrey et al 2014, Tang et al. 2016). Moreover, the inner disk orbiting Aa, detected with ALMA in CO 6-5 and in continuum, is massive enough to form a Jupiter-like planet ($10^{-3}\,M_\odot$, Dutrey et al. 2014).

Gas and Dust properties from the inner disks to the outer ring: Figure 1 is a schematic of the GG Tau system. The cavity is not completely devoid of gas and dust as shown by scattered light and ^{12}CO J=2-1 images (Roddier et al. 1996, Guilloteau and Dutrey 2000). The CO J=6-5 gas (Fig.2) mostly resides inside the cavity, and is fragmented in several clumps transiting from the outer disk onto the central stars. Using Subaru, Yang et al. 2016 have recently observed an arc connecting the outer ring and the central star in polarized dust image that corresponds to the CO streamer. Non-LTE analysis of the CO fragments reveal a warm cavity with a kinetic temperature ranging from 30 -70 K (Dutrey et al. 2014, Phuong et al. 2019, in prep.). These temperatures are well above the CO freeze out temperature of 17 K. Beck et al. 2012 also reported the existence of very hot ($\sim$ 1000-1500 K) H_2 filaments near the stars (within 0.1″). On the contrary, the outer disk is very cold with temperatures of the order of $T \sim 10 - 26$ K for the CO gas (Fig.2, Phuong et al. 2019) and dust temperature of $T_D(r) = 14 \times (r/200au)^{-1}$ K around the mid-plane, where the large 'mm' dust particles are located. With NOEMA, we started investigating the molecular content of the system, detecting H_2S for the first time in a disk (Phuong et al 2018). Fig.4 shows that the H_2S emission arises from the ring. This new detection is an argument for a massive ring, significantly more massive than other TTauri disks with a mass of $\sim 0.15\,M_\odot$ (Dutrey et al 1994, Guilloteau et al 1999, Phuong et 2018). For example, the well known TW Hya disk has a total mass of the order of $0.06\,M_\odot$.

Dynamically, part of the matter transiting from the cold and dense outer disk, where chemical coupling between the dust and the gas is important, is then injected into a warm cavity, where thermal desorption can occur, before being incorporated into the inner disk of Aa.

2 Proposal

Investigating how the gas and dust transiting from the outer disk onto the inner disks is chemically processed and changed during its transit towards the central disks is a key problem to evaluate how planets formed

in multiple systems can differ from those formed around single stars. This is a long term project and as a first step, we propose here to make an unbiased spectral survey of the molecules observed in the outer disk in order to measure their molecular abundances. This survey will provide a robust molecular database which 1/ can be compared to abundances observed in disks orbiting single stars (e.g. using the ALMA Large Program led by K. Öberg) and 2/ can serve as a reference to study the gas properties in the cavity and in the inner disk orbiting Aa (using ALMA).

The choice of the 3mm band is scientifically motivated because it covers the J=1-0 transitions of many molecules, which are critical in determining the relative abundances at the low temperatures prevailing in the GG Tau disk. By comparison with previously detected transitions, it will provide excitation conditions for the most abundant species.

Being the most massive disk and fairly extended, GG Tau A is the best candidate for such a study. With its specific geometry and (well known) temperatures, there is no mixing of areas presenting strong chemical variations due to different physical conditions. This allows a proper derivation of molecular (relative) abundances even at moderate angular resolution.

So far, the molecules detected in the GG Tau disk are CO, ^{13}CO, C^{18}O, CN, CS, H_2CO, CCH, HCO^+, $H^{13}CO^+$, DCO^+, HCN and H_2S (Dutrey et al 1997, Phuong et al 2018). Good upper limits on CCS, SO_2, SO, HC_3N and c-C_3H_2 are also reported (Phuong et al 2018). Phuong et al 2018 have started to measure molecular abundances relative to ^{13}CO (Table 1). The GG Tau ring appears similar to the cold outer disk of LkCa15. The disk surrounding LkCa15 is in fact a transition disk with an inner cavity of radius about 25 au, i.e. it has the same geometry than the GG Tau A disk, but on a smaller scale. This may partly explain their chemical similarities. A deeper comparison requests the detection of other species.

Other molecules detected around single TTauri or Herbig Ae disks are HNC, HC_3N, CH_3CN, HD, C_3H_2, C_2H_2, OH, SO, CH^+, N_2D^+, NH_3, CH_3OH, $H^{13}CN$ and N_2H^+.

After H_2S, it is unlikely to expect the detection of new species with NOEMA but several species observed in disks such as HNC, HC_3N, C_3H_2, N_2H^+ and maybe N_2D^+ and DCN could be detected in GG Tau. This will provide one of the most (if not the most) complete view of the chemistry in a cold TTauri disk. This will be an excellent complement, on a different kind of object (circumbinary disk), of the ALMA Large program on (single)TTauri and Herbig A disk chemistry currently running on ALMA.

Searching for deuterated species such as DCN or N_2D^+ is very well suited because the disk is very cold. DCO^+ has been already observed at 2mm using NOEMA by Phuong et al. 2018 (Fig.4) who found ratios of DCO^+/HCO^+ and $DCO^+/H^{13}CO^+$ of the order of 0.024, as in the case of LkCa15 and TW hydra.

Finally, observations of HCN, CS, CCH, DCO^+, $H^{13}CO^+$ and C^{18}O in the 3mm band will allow a proper determination of the excitation conditions since all these species have been resolved either in the 2, 1.3 or 0.9 mm bands with ALMA or NOEMA/PdBI.

3 Technical justification

Using Polyfix with 3 tunings, the 3mm band can offer a wide frequency coverage, allowing for detections of species already detected in the GG Tau disk at higher frequency or in other disks. Our setups also overlap in frequency in order to obtain a sqrt(2) gain in sensitivity for particularly promising species.

At 2mm, the H_2S line was detected during summer period in about 5 hours on source. We propose to make three transits (one for each tuning), either C or D. Additional integration time could also be obtained under conditions of unstable phases, since self-calibration is possible on the dust disk at this frequency.

The final angular resolution of about $3-5''$ is also well suited, being comparable to the size of the dust disk and that of the H_2S emission.

The detection of H_2S, with a column density of 1.3×10^{12}cm^{-2} at radius 300 au demonstrates that this project is feasible with NOEMA. Using Nautilus, Majumdar et al have started to investigate the outer disk chemistry (see also Phuong et al 2018). Their predicted column densities for HCN, HC_3N, c-C_3H_2, SO and CCS are of the order of a few 10^{12}cm^{-2}, making the project feasible.

4 Supporting material

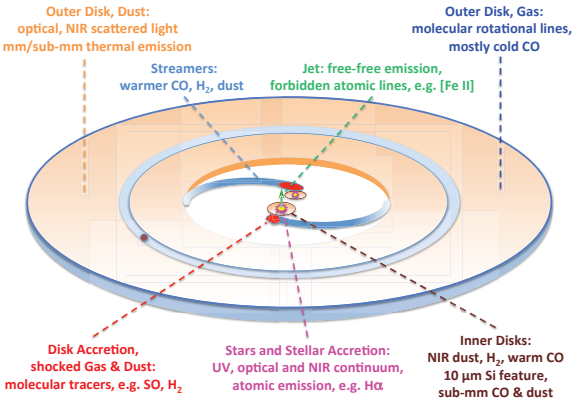

Figure 1: From Dutrey et al. 2016, a scheme showing the dust and gas distribution around a young low-mass binary star similar to GG Tau A.

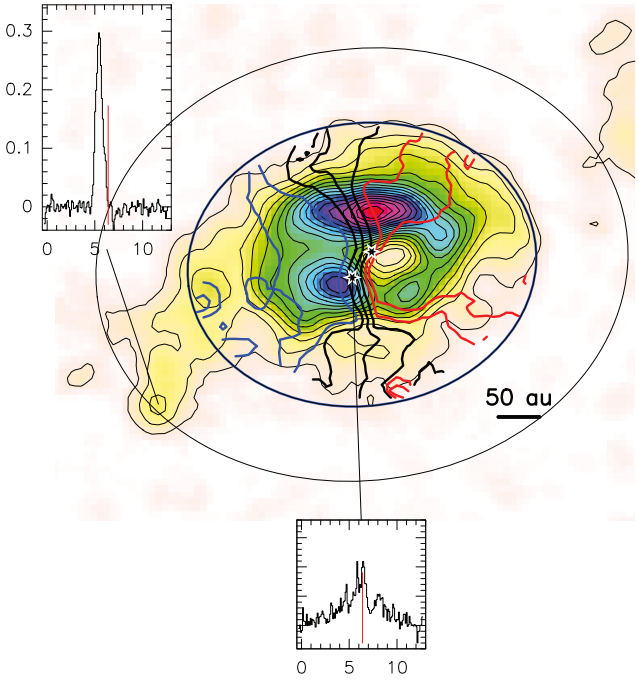

Figure 2: **ALMA ^{12}CO J=6-5 data:** From Dutrey et al. (2014, 2016). The locations of Aa and Ab are indicated by stars. The two ellipses show the position of the dust ring. The CO J=6-5 velocity gradient in contours (blue, black and red) is superimposed to the CO integrated area (color scale). From east to west, black velocity contours correspond to 6-6.4 and 6.8 km/s. The first blue contour near Aa is at 5.6 km/s. This corresponds to the centroid velocity of the CO J=6-5 accretion shock, the CS J=3-2 and H_2S emissions shown Fig.3. The two spectra display the CO J=6-5 at the hot spot location (east) and onto Aa. This spectrum shows that there is a contribution from the circumstellar disk but also a broad line emission maybe resulting from the accretion shock or a weak contribution from an outflow associated to the southern jet (Fig.3).

References

Artymowicz et al., 1991, ApJ. Let. 1086 - Di Folco et al. 2014, AA, 565 - Dutrey et al., 1994, AA, 286 - Dutrey et al., 2014, Nat. 514 - Dutrey et al. 2016, A&ARv 24 - Guilloteau et al., 1999, Aa, 348 - Guilloteau and Dutrey 2001, Symp. 200 " the formation of binary stars" , IAU symp. vol. 200 - Majumdar et al., 2019, in prep. - Phuong et al. 2018, AA. Let. 616 - Phuong et al. 2019, in prep. - Roddier et al., 1996, ApJ, 1086 - Takakuwa et al. 2014, ApJ, 1409 - Tang et al. 2014, ApJ, 1407 - Tang et al., 2016, ApJ, 820 - Welsh et al. 2012, Nat. 481 - Yang et al., 2016, AJ, 153 -

Table 1: Molecular abundance relative to ^{13}CO ($X_{[mol]}/X_{[^{13}CO]} \times 10^5$) from Phuong et al 2018.

	TMC-1⋆	LkCa 15	GG Tau
HCO^+	$600 \pm 180^{(1)}$	$150 \pm 35^{(3)}$	130 ± 12
H_2S	$< 45^{(1)}$	$< 7^{(4)}$	11 ± 3
$H^{13}CO^+$	15 ± 4 $^{(2)}$	5 ± 1.5 $^{(4)}$	4.7 ± 0.3
DCO^+	30 ± 9 $^{(2)}$	4.5 ± 1.4 $^{(4)}$	3.5 ± 0.15

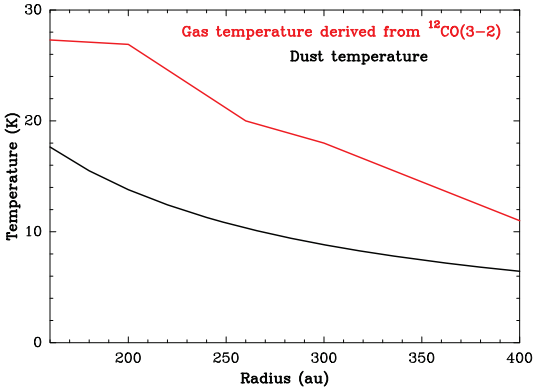

Figure 3: From Phuong et al 2019, in prep. Radial dependence of CO gas (red) and dust (black) temperature. The gas temperature is derived from the CO analyses. The dust temperature is taken from Dutrey et al 2014.

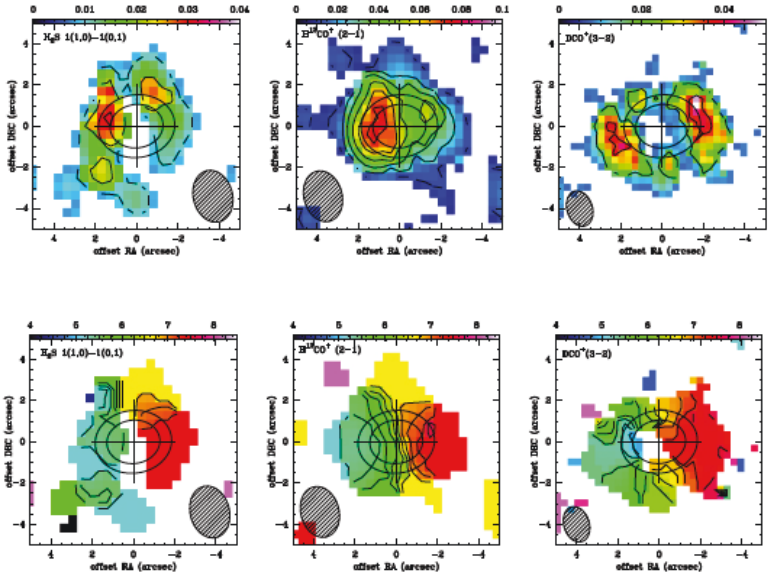

Figure 4: From Phuong et al 2018. *Upper:* Integrated intensity maps of NOEMA observations. The colour scale is in the unit of (Jy beam^{-1} km s^{-1}). Contour level step is 2σ. *Lower:* Velocity maps. Contour level step is 0.5 km s^{-1}. Beam sizes are indicated. The ellipses display the location of inner (∼180 au) and outer (∼260 au) radii of the dust ring.

Bibliography

Aly, Hossam, Giuseppe Lodato, and Paolo Cazzoletti (2018). "On the secular evolution of GG Tau A circumbinary disc: a misaligned disc scenario". In: *MNRAS* 480.4, pp. 4738–4745. DOI: 10.1093/mnras/sty2179. arXiv: 1809.06383 [astro-ph.SR].

Andre, P., D. Ward-Thompson, and M. Barsony (1993). "Submillimeter continuum observations of Rho Ophiuchi A - The candidate protostar VLA 1623 and prestellar clumps". In: *ApJ* 406, pp. 122–141. DOI: 10.1086/172425.

Andrews, Sean M. et al. (2018). "The Disk Substructures at High Angular Resolution Project (DSHARP). I. Motivation, Sample, Calibration, and Overview". In: *ApJ* 869.2, L41, p. L41. DOI: 10.3847/2041-8213/aaf741. arXiv: 1812.04040 [astro-ph.SR].

Armitage, Philip J. and Diana Valencia (2010). "Astrophysics of Planet Formation". In: *Physics Today* 63.12, p. 63. DOI: 10.1063/1.3529004.

Artymowicz, P. and S. H. Lubow (1996). "Interaction of Young Binaries with Protostellar Disks". In: *Disks and Outflows Around Young Stars, Proceedings of a Conference Held at Heidelberg, Germany 6 - 9 September 1994, 361 pp., with CD-ROM, and booklet with approx. 400 pp.. Springer-Verlag Berlin Heidelberg New York. Edited by Steven Beckwith, Jakob Staude, Axel Quetz, and Antonella Natta. Also Lecture Notes in Physics, volume 465, 1996, p.115*. Ed. by Steven Beckwith et al. Vol. 465, p. 115. DOI: 10.1007/BFb0102630.

Artymowicz, P. et al. (1991). "The Effect of an External Disk on the Orbital Elements of a Central Binary". In: *ApJ* 370, p. L35. DOI: 10.1086/185971.

Artymowicz, Pawel and Stephen H. Lubow (1994). "Dynamics of Binary-Disk Interaction. I. Resonances and Disk Gap Sizes". In: *ApJ* 421, p. 651. DOI: 10.1086/173679.

Beck, T. L. et al. (2012). "Circumbinary Gas Accretion onto a Central Binary: Infrared Molecular Hydrogen Emission from GG Tau A". In: *ApJ* 754, 72, p. 72. DOI: 10.1088/0004-637X/754/1/72. arXiv: 1205.1526 [astro-ph.SR].

Beckwith, Steven V. W. et al. (1990). "A Survey for Circumstellar Disks around Young Stellar Objects". In: *AJ* 99, p. 924. DOI: 10.1086/115385.

Bergin, E. et al. (2004). "A New Probe of the Planet-forming Region in T Tauri Disks". In: *ApJ* 614, pp. L133–L136. DOI: 10.1086/425865. eprint: astro-ph/0409308.

Bergin, E. A. et al. (2013). "An old disk still capable of forming a planetary system". In: *Nature* 493, pp. 644–646. DOI: 10.1038/nature11805. arXiv: 1303.1107 [astro-ph.SR].

Bergin, E. A. et al. (2016). "Hydrocarbon Emission Rings in Protoplanetary Disks Induced by Dust Evolution". In: *ApJ* 831, 101, p. 101. DOI: 10.3847/0004-637X/831/1/101. arXiv: 1609.06337 [astro-ph.EP].

Beust, H. and A. Dutrey (2005). "Dynamics of the young multiple system <ASTROBJ>GG Tauri</ASTROBJ>. I. Orbital fits and inner edge of the circumbinary disk of <ASTROBJ>GG Tau</ASTROBJ> A". In: *A&A* 439, pp. 585–594. DOI: 10.1051/0004-6361:20042441.

Brauer, Robert et al. (2019). "GG Tau A: Dark shadows on the ringworld". In: *arXiv e-prints*, arXiv:1906.11582, arXiv:1906.11582. arXiv: 1906.11582 [astro-ph.SR].

Bruderer, S. et al. (2012). "The warm gas atmosphere of the HD 100546 disk seen by Herschel. Evidence of a gas-rich, carbon-poor atmosphere?". In: *A&A* 541, A91, A91. DOI: 10.1051/0004-6361/201118218. arXiv: 1201.4860 [astro-ph.SR].

Butner, H. M., E. A. Lada, and R. B. Loren (1995). "Physical Properties of Dense Cores: DCO + Observations". In: *ApJ* 448, p. 207. DOI: 10.1086/175953.

Calmonte, U. et al. (2016). "Sulphur-bearing species in the coma of comet 67P/Churyumov-Gerasimenko". In: *MNRAS* 462, S253–S273. DOI: 10.1093/mnras/stw2601.

Cazzoletti, P. et al. (2017). "Testing dust trapping in the circumbinary disk around GG Tauri A". In: *A&A* 599, A102, A102. DOI: 10.1051/0004-6361/201629721. arXiv: 1610.08381 [astro-ph.SR].

Chapillon, E. et al. (2012). "Chemistry in Disks. VII. First Detection of HC_3N in Protoplanetary Disks". In: *ApJ* 756, 58, p. 58. DOI: 10.1088/0004-637X/756/1/58. arXiv: 1207.2682 [astro-ph.SR].

Chiang, E. I. and P. Goldreich (1997). "Spectral Energy Distributions of T Tauri Stars with Passive Circumstellar Disks". In: *ApJ* 490, pp. 368–376. DOI: 10.1086/304869. eprint: astro-ph/9706042.

Cleeves, L. Ilsedore, Edwin A. Bergin, and Fred C. Adams (2014). "Exclusion of Cosmic Rays in Protoplanetary Disks. II. Chemical Gradients and Observational Signatures". In: *ApJ* 794.2, 123, p. 123. DOI: 10.1088/0004-637X/794/2/123. arXiv: 1408.2835 [astro-ph.SR].

Close, L. M. et al. (1998). "Adaptive Optics Imaging of the Circumbinary Disk around the T Tauri Binary UY Aurigae: Estimates of the Binary Mass and Circumbinary Dust Grain Size Distribution". In: *ApJ* 499.2, pp. 883–888. DOI: 10.1086/305672.

Crida, A. and A. Morbidelli (2007). "Cavity opening by a giant planet in a protoplanetary disc and effects on planetary migration". In: *MNRAS* 377.3, pp. 1324–1336. DOI: 10.1111/j.1365-2966.2007.11704.x. arXiv: astro-ph/0703151 [astro-ph].

Dartois, E., A. Dutrey, and S. Guilloteau (2003). "Structure of the DM Tau Outer Disk: Probing the vertical kinetic temperature gradient". In: *A&A* 399, pp. 773–787. DOI: 10.1051/0004-6361:20021638.

Dauphas, N. and M. Chaussidon (2011). "A Perspective from Extinct Radionuclides on a Young Stellar Object: The Sun and Its Accretion Disk". In: *Annual Review of Earth and Planetary Sciences* 39, pp. 351–386. DOI: 10.1146/annurev-earth-040610-133428. arXiv: 1105.5172 [astro-ph.EP].

Di Folco, E. et al. (2014). "GG Tauri: the fifth element". In: *A&A* 565, L2, p. L2. DOI: 10.1051/0004-6361/201423675. arXiv: 1404.2205 [astro-ph.SR].

Dong, Ruobing et al. (2018). "Multiple Disk Gaps and Rings Generated by a Single Super-Earth. II. Spacings, Depths, and Number of Gaps, with Application to Real Systems". In: *ApJ* 866.2, 110, p. 110. DOI: 10.3847/1538-4357/aadadd. arXiv: 1808.06613 [astro-ph.EP].

Draine, B. T. (1978). "Photoelectric heating of interstellar gas". In: *ApJS* 36, pp. 595–619. DOI: 10.1086/190513.

Duchêne, G. et al. (2004). "A Multiwavelength Scattered Light Analysis of the Dust Grain Population in the GG Tauri Circumbinary Ring". In: *ApJ* 606.2, pp. 969–982. DOI: 10.1086/383126. arXiv: astro-ph/0401560 [astro-ph].

Ducourant, C. et al. (2005). "Pre-main sequence star Proper Motion Catalogue". In: *A&A* 438, pp. 769–778. DOI: 10.1051/0004-6361:20052788.

Dutrey, A., S. Guilloteau, and M. Guelin (1997). "Chemistry of protosolar-like nebulae: The molecular content of the DM Tau and GG Tau disks.". In: *A&A* 317, pp. L55–L58.

Dutrey, A., S. Guilloteau, and M. Simon (1994). "Images of the GG Tauri rotating ring". In: *A&A* 286, pp. 149–159.

Dutrey, A. et al. (2011). "Chemistry in disks. V. Sulfur-bearing molecules in the protoplanetary disks surrounding LkCa15, MWC480, DM Tauri, and GO Tauri". In: *A&A* 535, A104, A104. DOI: 10.1051/0004-6361/201116931. arXiv: 1109.5870 [astro-ph.SR].

Dutrey, A. et al. (2014). "Possible planet formation in the young, low-mass, multiple stellar system GG Tau A". In: *Nature* 514, pp. 600–602. DOI: 10.1038/nature13822.

Dutrey, A. et al. (2016). "GG Tau: the ringworld and beyond. Mass accretion and planetary formation in young multiple stellar systems". In: *A&A Rev.* 24, 5, p. 5. DOI: 10.1007/s00159-015-0091-5.

Dutrey, A. et al. (2017). "The Flying Saucer: Tomography of the thermal and density gas structure of an edge-on protoplanetary disk". In: *A&A* 607, A130, A130. DOI: 10.1051/0004-6361/201730645. arXiv: 1706.02608 [astro-ph.SR].

Duvert, G. et al. (1998). "Disks in the UY Aurigae binary". In: *A&A* 332, pp. 867–874.

Elitzur, M. (1992). "Book-Review - Astronomical Masers". In: *Science* 257, p. 112.

Favre, C. et al. (2018). "First Detection of the Simplest Organic Acid in a Protoplanetary Disk". In: *ApJ* 862, L2, p. L2. DOI: 10.3847/2041-8213/aad046. arXiv: 1807.05768 [astro-ph.SR].

Fedele, D. et al. (2012). "Warm H_2O and OH in the disk around the Herbig star HD 163296". In: *A&A* 544, L9, p. L9. DOI: 10.1051/0004-6361/201219615. arXiv: 1207.3969 [astro-ph.SR].

Forrest, W. J. et al. (2004). "Mid-infrared Spectroscopy of Disks around Classical T Tauri Stars". In: *ApJS* 154.1, pp. 443–447. DOI: 10.1086/423138. arXiv: astro-ph/0605464 [astro-ph].

Frank, Juhan, Andrew King, and Derek J. Raine (2002). *Accretion Power in Astrophysics: Third Edition*.

Frink, S. et al. (1997). "New proper motions of pre-main sequence stars in Taurus-Auriga". In: *A&A* 325, pp. 613–622. arXiv: astro-ph/9704281 [astro-ph].

Furlan, E. et al. (2006). "A Survey and Analysis of Spitzer Infrared Spectrograph Spectra of T Tauri Stars in Taurus". In: *ApJS* 165.2, pp. 568–605. DOI: 10.1086/505468. arXiv: astro-ph/0608038 [astro-ph].

Gaia Collaboration et al. (2016). "The Gaia mission". In: *A&A* 595, A1, A1. DOI: 10.1051/0004-6361/201629272. arXiv: 1609.04153 [astro-ph.IM].

Gaia Collaboration et al. (2018). "Gaia Data Release 2. Summary of the contents and survey properties". In: *A&A* 616, A1, A1. DOI: 10.1051/0004-6361/201833051. arXiv: 1804.09365 [astro-ph.GA].

Greene, Thomas (2001). "Protostars". In: *American Scientist* 89.4, p. 316. DOI: 10.1511/2001.4.316.

Guilloteau, S., A. Dutrey, and M. Simon (1999). "GG Tauri: the ring world". In: *A&A* 348, pp. 570–578.

Guilloteau, S. et al. (2011). "A dual-frequency sub-arcsecond study of proto-planetary disks at mm wavelengths: first evidence for radial variations of the dust properties". In: *A&A* 529, A105, A105. DOI: 10.1051/0004-6361/201015209. arXiv: 1103.1296.

Guilloteau, S. et al. (2016). "Chemistry in disks. X. The molecular content of protoplanetary disks in Taurus". In: *A&A* 592, A124, A124. DOI: 10.1051/0004-6361/201527088. arXiv: 1604.05028 [astro-ph.EP].

Günther, R. and W. Kley (2002). "Circumbinary disk evolution". In: *A&A* 387, pp. 550–559. DOI: 10.1051/0004-6361:20020407. arXiv: astro-ph/0204175 [astro-ph].

Guzmán, V. V. et al. (2015). "Cyanide Photochemistry and Nitrogen Fractionation in the MWC 480 Disk". In: *ApJ* 814, 53, p. 53. DOI: 10.1088/0004-637X/814/1/53. arXiv: 1511.03313 [astro-ph.SR].

Hartigan, Patrick and Scott J. Kenyon (2003). "A Spectroscopic Survey of Subarcsecond Binaries in the Taurus-Auriga Dark Cloud with the Hubble Space Telescope". In: *ApJ* 583.1, pp. 334–357. DOI: 10.1086/345293. arXiv: astro-ph/0209608 [astro-ph].

Hayashi, C. (1981). "Structure of the Solar Nebula, Growth and Decay of Magnetic Fields and Effects of Magnetic and Turbulent Viscosities on the Nebula". In: *Progress of Theoretical Physics Supplement* 70, pp. 35–53. DOI: 10.1143/PTPS.70.35.

Henning, T. and D. Semenov (2013). "Chemistry in Protoplanetary Disks". In: *Chemical Reviews* 113, pp. 9016–9042. DOI: 10.1021/cr400128p. arXiv: 1310.3151 [astro-ph.GA].

Hily-Blant, P. et al. (2017). "Direct evidence of multiple reservoirs of volatile nitrogen in a protosolar nebula analogue". In: *A&A* 603, L6, p. L6. DOI: 10.1051/0004-6361/201730524. arXiv: 1706.10095.

Hincelin, U. et al. (2011a). "Oxygen depletion in dense molecular clouds: a clue to a low O_2 abundance?". In: *A&A* 530, A61, A61. DOI: 10.1051/0004-6361/201016328. arXiv: 1104.1530 [astro-ph.SR].

— (2011b). "Oxygen depletion in dense molecular clouds: a clue to a low O_2 abundance?". In: *A&A* 530, A61, A61. DOI: 10.1051/0004-6361/201016328. arXiv: 1104.1530 [astro-ph.SR].

Hogbom, J. A. and W. N. Brouw (1974). "The Synthesis Radio Telescope at Westerbork. Principles of Operation, Performance and Data Reduction". In: *A&A* 33, p. 289.

Huang, J. and K. I. Öberg (2015). "Detection of N_2D^+ in a Protoplanetary Disk". In: *ApJ* 809, L26, p. L26. DOI: 10.1088/2041-8205/809/2/L26. arXiv: 1508.03637 [astro-ph.SR].

Huang, J. et al. (2017). "An ALMA Survey of DCN/$H^{13}CN$ and $DCO^+/H^{13}CO^+$ in Protoplanetary Disks". In: *ApJ* 835, 231, p. 231. DOI: 10.3847/1538-4357/835/2/231. arXiv: 1701.01735 [astro-ph.SR].

Itoh, Yoichi et al. (2002). "Near-Infrared Coronagraphy of the GG Tauri A Binary System". In: *Publications of the Astronomical Society of Japan* 54, pp. 963–967. DOI: 10.1093/pasj/54.6.963.

Jiménez-Escobar, A. and G. M. Muñoz Caro (2011). "Sulfur depletion in dense clouds and circumstellar regions. I. H_2S ice abundance and UV-photochemical reactions in the H_2O-matrix". In: *A&A* 536, A91, A91. DOI: 10.1051/0004-6361/201014821. arXiv: 1112.3240 [astro-ph.EP].

Kawabe, R. et al. (1993). "Discovery of a Rotating Protoplanetary Gas Disk around the Young Star GG Tauri". In: *ApJ* 404, p. L63. DOI: 10.1086/186744.

Köhler, R. (2011). "The orbit of GG Tauri A". In: *A&A* 530, A126, A126. DOI: 10.1051/0004-6361/201016327. arXiv: 1104.2245 [astro-ph.SR].

Kraus, S. et al. (2009). "Revealing the sub-AU asymmetries of the inner dust rim in the disk around the Herbig Ae star R Coronae Austrinae". In: *A&A* 508, pp. 787–803. DOI: 10.1051/0004-6361/200912990. arXiv: 0911.3653 [astro-ph.SR].

Lada, C. J. (1987). "Star formation - From OB associations to protostars". In: *Star Forming Regions*. Ed. by M. Peimbert and J. Jugaku. Vol. 115. IAU Symposium, pp. 1–17.

Lada, C. J. and B. A. Wilking (1984). "The nature of the embedded population in the Rho Ophiuchi dark cloud - Mid-infrared observations". In: *ApJ* 287, pp. 610–621. DOI: 10.1086/162719.

Le Gal, Romane et al. (2019). "Sulfur Chemistry in Protoplanetary Disks: CS and H_2CS". In: *ApJ* 876.1, 72, p. 72. DOI: 10.3847/1538-4357/ab1416. arXiv: 1903.11105 [astro-ph.GA].

Leinert, Ch. et al. (1991). "Lunar occultation and near-infrared speckle observations of DG Tauri, FV Tauri, FW Tauri and GG Tauri.". In: *A&A* 250, p. 407.

Linsky, Jeffrey L. et al. (2006). "What Is the Total Deuterium Abundance in the Local Galactic Disk?". In: *ApJ* 647.2, pp. 1106–1124. DOI: 10.1086/505556. arXiv: astro-ph/0608308 [astro-ph].

Lubow, S. H. and P. Artymowicz (1997). "Young Binary Star/Disk Interactions". In: *IAU Colloq. 163: Accretion Phenomena and Related Outflows*. Ed. by D. T. Wickramasinghe, G. V. Bicknell, and L. Ferrario. Vol. 121. Astronomical Society of the Pacific Conference Series, p. 505.

Lucas, R. and H. Liszt (1998). "Interstellar isotope ratios from mm-wave molecular absorption spectra". In: *A&A* 337, pp. 246–252.

Majumdar, L. et al. (2017). "Chemistry of TMC-1 with multiply deuterated species and spin chemistry of H_2, H_2^+, H_3^+ and their isotopologues". In: *MNRAS* 466.4, pp. 4470–4479. DOI: 10.1093/mnras/stw3360. arXiv: 1612.07845 [astro-ph.GA].

Mathews, G. S. et al. (2013a). "ALMA imaging of the CO snowline of the HD 163296 disk with DCO^+". In: *A&A* 557, A132, A132. DOI: 10.1051/0004-6361/201321600. arXiv: 1307.3420 [astro-ph.SR].

Mathews, G. S. et al. (2013b). "ALMA imaging of the CO snowline of the HD 163296 disk with DCO^+". In: *A&A* 557, A132, A132. DOI: 10.1051/0004-6361/201321600. arXiv: 1307.3420 [astro-ph.SR].

Meeus, G. et al. (2012). "Observations of Herbig Ae/Be stars with Herschel/PACS. The atomic and molecular contents of their protoplanetary discs". In: *A&A* 544, A78, A78. DOI: 10.1051/0004-6361/201219225. arXiv: 1206.3413 [astro-ph.GA].

Milam, S. N. et al. (2005). "The $^{12}C/^{13}C$ Isotope Gradient Derived from Millimeter Transitions of CN: The Case for Galactic Chemical Evolution". In: *ApJ* 634, pp. 1126–1132. DOI: 10.1086/497123.

Millar, T. J., A. Bennett, and Eric Herbst (1989). "Deuterium Fractionation in Dense Interstellar Clouds". In: *ApJ* 340, p. 906. DOI: 10.1086/167444.

Nelson, Andrew F. and F. Marzari (2016). "Dynamics of Circumstellar Disks. III. The Case of GG Tau A". In: *ApJ* 827.2, 93, p. 93. DOI: 10.3847/0004-637X/827/2/93. arXiv: 1605.02764 [astro-ph.SR].

Öberg, K. I. et al. (2015). "Double DCO^+ Rings Reveal CO Ice Desorption in the Outer Disk Around IM Lup". In: *ApJ* 810, 112, p. 112. DOI: 10.1088/0004-637X/810/2/112. arXiv: 1508.07296.

Ohishi, M., W. M. Irvine, and N. Kaifu (1992). "Molecular Abundance Variations among and Within Cold, Dark Molecular Clouds(rp)". In: *Astrochemistry of Cosmic Phenomena*. Ed. by P. D. Singh. Vol. 150. IAU Symposium, p. 171.

Omont, A. (2007). "Molecules in galaxies". In: *Reports on Progress in Physics* 70, pp. 1099–1176. DOI: 10.1088/0034-4885/70/7/R03. arXiv: 0709.3814.

Phuong, N. T. et al. (2018a). "First detection of H_2S in a protoplanetary disk. The dense GG Tauri A ring". In: *A&A* 616, L5, p. L5. DOI: 10.1051/0004-6361/201833766. arXiv: 1808.00652 [astro-ph.SR].

Phuong, N. T. et al. (2018b). "Morphology of the $^{13}CO(32)$ millimetre emission across the gas disc surrounding the triple protostar GG Tau A using ALMA observations". In: *Research in Astronomy and Astrophysics* 18, 031, p. 031. DOI: 10.1088/1674-4527/18/3/31. arXiv: 1801.00861 [astro-ph.SR].

Pierens, A. and R. P. Nelson (2013a). "Migration and gas accretion scenarios for the Kepler 16, 34, and 35 circumbinary planets". In: *A&A* 556, A134, A134. DOI: 10.1051/0004-6361/201321777. arXiv: 1307.0713 [astro-ph.EP].

— (2013b). "Migration and gas accretion scenarios for the Kepler 16, 34, and 35 circumbinary planets". In: *A&A* 556, A134, A134. DOI: 10.1051/0004-6361/201321777. arXiv: 1307.0713 [astro-ph.EP].

Piétu, V., A. Dutrey, and S. Guilloteau (2007). "Probing the structure of protoplanetary disks: a comparative study of DM Tau, LkCa 15, and MWC 480". In: *A&A* 467, pp. 163–178. DOI: 10.1051/0004-6361:20066537. eprint: astro-ph/0701425.

Piétu, V. et al. (2006). "Resolving the inner dust disks surrounding LkCa 15 and MWC 480 at mm wavelengths". In: *A&A* 460, pp. L43–L47. DOI: 10.1051/0004-6361:20065968. eprint: astro-ph/0610200.

Piétu, V. et al. (2011). "High resolution imaging of the GG Tauri system at 267 GHz". In: *A&A* 528, A81, A81. DOI: 10.1051/0004-6361/201015682. arXiv: 1102.4029 [astro-ph.SR].

Punzi, K. M. et al. (2015). "An Unbiased 1.3 mm Emission Line Survey of the Protoplanetary Disk Orbiting LkCa 15". In: *ApJ* 805, 147, p. 147. DOI: 10.1088/0004-637X/805/2/147. arXiv: 1504.00061 [astro-ph.SR].

Qi, C. et al. (2008). "Resolving the Chemistry in the Disk of TW Hydrae. I. Deuterated Species". In: *ApJ* 681, pp. 1396–1407. DOI: 10.1086/588516. arXiv: 0803.2753.

Qi, C. et al. (2013). "Imaging of the CO Snow Line in a Solar Nebula Analog". In: *Science* 341, pp. 630–632. DOI: 10.1126/science.1239560. arXiv: 1307.7439 [astro-ph.SR].

Qi, Chunhua et al. (2011). "Resolving the CO Snow Line in the Disk around HD 163296". In: *ApJ* 740.2, 84, p. 84. DOI: 10.1088/0004-637X/740/2/84. arXiv: 1107.5061 [astro-ph.SR].

Reboussin, L. et al. (2015). "Chemistry in protoplanetary disks: the gas-phase CO/H_2 ratio and the carbon reservoir". In: *A&A* 579, A82, A82. DOI: 10.1051/0004-6361/201525885. arXiv: 1505.01309 [astro-ph.SR].

Reipurth, Bo et al. (2007). "Visual Binaries in the Orion Nebula Cluster". In: *AJ* 134.6, pp. 2272–2285. DOI: 10.1086/523596. arXiv: 0709.3824 [astro-ph].

Riviere-Marichalar, P. et al. (2012). "HD 172555: detection of 63 μm [OI] emission in a debris disc". In: *A&A* 546, L8, p. L8. DOI: 10.1051/0004-6361/201219745. arXiv: 1210.0089 [astro-ph.SR].

Riviere-Marichalar, P. et al. (2013). "Gas and dust in the TW Hydrae association as seen by the Herschel Space Observatory". In: *A&A* 555, A67, A67. DOI: 10.1051/0004-6361/201321506. arXiv: 1306.0328 [astro-ph.SR].

Robitaille, T. P. et al. (2006). "Interpreting Spectral Energy Distributions from Young Stellar Objects. I. A Grid of 200,000 YSO Model SEDs". In: *ApJS* 167, pp. 256–285. DOI: 10.1086/508424. eprint: astro-ph/0608234.

Roddier, C. et al. (1996). "Adaptive Optics Imaging of GG Tauri: Optical Detection of the Circumbinary Ring". In: *ApJ* 463, p. 326. DOI: 10.1086/177245.

Ruaud, M., V. Wakelam, and F. Hersant (2016). "Gas and grain chemical composition in cold cores as predicted by the Nautilus three-phase model". In: *MNRAS* 459, pp. 3756–3767. DOI: 10.1093/mnras/stw887. arXiv: 1604.05216.

Salinas, V. N. et al. (2016). "First detection of gas-phase ammonia in a planet-forming disk. NH_3, N_2H^+, and H_2O in the disk around TW Hydrae". In: *A&A* 591, A122, A122. DOI: 10.1051/0004-6361/201628172. arXiv: 1604.00323 [astro-ph.SR].

Sargent, B. et al. (2006). "Dust Processing in Disks around T Tauri Stars". In: *ApJ* 645.1, pp. 395–415. DOI: 10.1086/504283. arXiv: astro-ph/0605415 [astro-ph].

Semenov, D. et al. (2018). "Chemistry in disks. XI. Sulfur-bearing species as tracers of protoplanetary disk physics and chemistry: the DM Tau case". In: *ArXiv e-prints*. arXiv: 1806.07707.

Simon, M. and S. Guilloteau (1992). "Dusty Disks in the Multiple Systems UZ Tauri and GG Tauri". In: *ApJ* 397, p. L47. DOI: 10.1086/186541.

Skemer, Andrew J. et al. (2011). "Dust Grain Evolution in Spatially Resolved T Tauri Binaries". In: *ApJ* 740.1, 43, p. 43. DOI: 10.1088/0004-637X/740/1/43. arXiv: 1107.3161 [astro-ph.SR].

Skrutskie, M. F. et al. (1993). "Detection of Circumstellar Gas Associated with GG Tauri". In: *ApJ* 409, p. 422. DOI: 10.1086/172675.

Takakuwa, S. et al. (2014). "Angular Momentum Exchange by Gravitational Torques and Infall in the Circumbinary Disk of the Protostellar System L1551 NE". In: *ApJ* 796, 1, p. 1. DOI: 10.1088/0004-637X/796/1/1. arXiv: 1409.4903 [astro-ph.SR].

Takakuwa, Shigehisa et al. (2017). "Spiral Arms, Infall, and Misalignment of the Circumbinary Disk from the Circumstellar Disks in the Protostellar Binary System L1551 NE". In: *ApJ* 837.1, 86, p. 86. DOI: 10.3847/1538-4357/aa6116. arXiv: 1702.05562 [astro-ph.GA].

Tang, Y.-W. et al. (2014). "Circumbinary Ring, Circumstellar Disks, and Accretion in the Binary System UY Aurigae". In: *ApJ* 793, 10, p. 10. DOI: 10.1088/0004-637X/793/1/10. arXiv: 1407.4561.

Tang, Y.-W. et al. (2016). "Mapping CO Gas in the GG Tauri A Triple System with 50 au Spatial Resolution". In: *ApJ* 820, 19, p. 19. DOI: 10.3847/0004-637X/820/1/19. arXiv: 1511.05687.

Teague, R. et al. (2016). "Measuring turbulence in TW Hydrae with ALMA: methods and limitations". In: *A&A* 592, A49, A49. DOI: 10.1051/0004-6361/201628550. arXiv: 1606.00005 [astro-ph.SR].

Thi, W. F. et al. (2001). "H_2 and CO Emission from Disks around T Tauri and Herbig Ae Pre-Main-Sequence Stars and from Debris Disks around Young Stars: Warm and Cold Circumstellar Gas". In: *ApJ* 561, pp. 1074–1094. DOI: 10.1086/323361. eprint: astro-ph/0107006.

van Dishoeck, E. F., W.-F. Thi, and G.-J. van Zadelhoff (2003). "Detection of DCO^+ in a circumstellar disk". In: *Ap&SS* 285, pp. 691–698. DOI: 10.1023/A:1026113327303.

van Dishoeck, Ewine F. (2014). "Astrochemistry of dust, ice and gas: introduction and overview". In: *Faraday Discussions* 168, p. 9. DOI: 10.1039/C4FD00140K. arXiv: 1411.5280 [astro-ph.GA].

van Dishoeck, Ewine F. and John H. Black (1988). "The Photodissociation and Chemistry of Interstellar CO". In: *ApJ* 334, p. 771. DOI: 10.1086/166877.

Vidal, T. H. G. et al. (2017). "On the reservoir of sulphur in dark clouds: chemistry and elemental abundance reconciled". In: *MNRAS* 469, pp. 435–447. DOI: 10.1093/mnras/stx828. arXiv: 1704.01404.

Wakelam, V. et al. (2005). "Sulphur chemistry and molecular shocks: The case of NGC 1333-IRAS 2". In: *A&A* 437.1, pp. 149–158. DOI: 10.1051/0004-6361:20042566. arXiv: astro-ph/0503462 [astro-ph].

Wakelam, V. et al. (2016). "Importance of the H_2 abundance in protoplanetary disk ices for the molecular layer chemical composition". In: *A&A* 594, A35, A35. DOI: 10.1051/0004-6361/201628748. arXiv: 1609.01471.

Walsh, C. et al. (2016). "First Detection of Gas-phase Methanol in a Protoplanetary Disk". In: *ApJ* 823, L10, p. L10. DOI: 10.3847/2041-8205/823/1/L10. arXiv: 1606.06492 [astro-ph.EP].

Watson, W. D., V. G. Anicich, and Jr. Huntress W. T. (1976). "Measurement and significance of the reaction $^{13}C^{+}+^{12}CO$ ü $^{12}C^{+}+^{13}CO$ for alteration of the $^{13}C/^{12}C$ ratio in interstellar molecules.". In: *ApJ* 205, pp. L165–L168. DOI: 10.1086/182115.

Weaver, E., A. Isella, and Y. Boehler (2018). "Empirical Temperature Measurement in Protoplanetary Disks". In: *ApJ* 853, 113, p. 113. DOI: 10.3847/1538-4357/aaa481. arXiv: 1801.03478 [astro-ph.EP].

Welsh, W. F. et al. (2012). "Transiting circumbinary planets Kepler-34 b and Kepler-35 b". In: *Nature* 481, pp. 475–479. DOI: 10.1038/nature10768. arXiv: 1204.3955 [astro-ph.EP].

Wetzstein, M. et al. (2009). "Vine—A Numerical Code for Simulating Astrophysical Systems Using Particles. I. Description of the Physics and the Numerical Methods". In: *The Astrophysical Journal Supplement Series* 184.2, pp. 298–325. DOI: 10.1088/0067-0049/184/2/298. arXiv: 0802.4245 [astro-ph].

White, Russel J. et al. (1999). "A Test of Pre-Main-Sequence Evolutionary Models across the Stellar/Substellar Boundary Based on Spectra of the Young Quadruple GG Tauri". In: *ApJ* 520, pp. 811–821. DOI: 10.1086/307494. arXiv: astro-ph/9902318 [astro-ph].

Williams, J. P. and L. A. Cieza (2011). "Protoplanetary Disks and Their Evolution". In: *ARA&A* 49, pp. 67–117. DOI: 10.1146/annurev-astro-081710-102548. arXiv: 1103.0556 [astro-ph.GA].

Wilson, T. L. (1999). "Isotopes in the interstellar medium and circumstellar envelopes". In: *Reports on Progress in Physics* 62, pp. 143–185. DOI: 10.1088/0034-4885/62/2/002.

Wilson, Thomas L., Kristen Rohlfs, and Susanne Hüttemeister (2009). *Tools of Radio Astronomy*. DOI: 10.1007/978-3-540-85122-6.

Windmark, F. et al. (2012). "Planetesimal formation by sweep-up: how the bouncing barrier can be beneficial to growth". In: *A&A* 540, A73, A73. DOI: 10.1051/0004-6361/201118475. arXiv: 1201.4282 [astro-ph.EP].

Woitke, P. et al. (2010). "Continuum and line modelling of discs around young stars - I. 300000 disc models for HERSCHEL/GASPS". In: *MNRAS* 405.1, pp. L26–L30. DOI: 10.1111/j.1745-3933.2010.00852.x. arXiv: 1003.2323 [astro-ph.EP].

Yang, Y. et al. (2017). "Near-infrared Imaging Polarimetry of Inner Region of GG Tau A Disk". In: *AJ* 153, 7, p. 7. DOI: 10.3847/1538-3881/153/1/7. arXiv: 1610.09134 [astro-ph.EP].

Zhang, Shangjia et al. (2018). "The Disk Substructures at High Angular Resolution Project (DSHARP). VII. The Planet-Disk Interactions Interpretation". In: *ApJ* 869.2, L47, p. L47. DOI: 10.3847/2041-8213/aaf744. arXiv: 1812.04045 [astro-ph.EP].